Particle-modified Surface Plasmon Resonance Biosensor

Yao Du

Department of Chemical Engineering and Biotechnology

University of Cambridge

This dissertation is submitted for the degree of

Doctor of Philosophy

Trinity College 2018

I would like to dedicate this thesis to my loving family.

Declaration

I hereby declare that except where specific reference is made to the work of others, the contents of this dissertation are original and have not been submitted in whole or in part for consideration for any other degree or qualification in this, or any other University. This dissertation is the result of my own work and includes nothing which is the outcome of work done in collaboration, except where specifically indicated in the text. This dissertation contains less than 65,000 words including appendices, bibliography, footnotes, tables and equations and has less than 150 figures.

Yao Du

2018

Acknowledgements

First, I would like to thank my supervisor Prof. Elizabeth Hall for her invaluable guidance throughout my four year in Cambridge in the pursuit of a PhD degree. Her meticulous attitude towards scientific excellence has driven me to new heights day after day. I am truly enlightened by many of her brilliant ideas and deeply motivated by her drive in the pursuit of knowledge.

I would also like to express my gratitude to Prof. Alex Routh from the BP institute for advices on DLS particle sizing theory and the use of their equipment. My thanks also go to Dr Ronan Daly for his discussion and advices for my first-year report. I also appreciate the help and guidance provided by my advisor Dr Colin Davidson on lasers.

Many thanks to the technical team in the Chemical Engineering and Biotechnology Department. They have dutifully helped with my daily work by troubleshooting and providing directions along the way. Marta Lapsley has also been tremendously helpful when I started my project and I am grateful to her.

I would also like to express my pleasure in the collaboration with Qian Sun from the BP Institute. Many thanks to all the members from the Hall group for useful discussions and helping hands when in need. I am also thankful to all the friends I made in the department for they made my time here enjoyable and memorable.

Special thanks to my loving family especially my wife for their constant support and unconditional love.

Finally, I would like to acknowledge Agency for Science, Technology and Research (ASTAR) Singapore for financial support. My work is supported by the ASTAR National Science Scholarship (NSS-PhD).

Abstract

Surface plasmon resonance (SPR) biosensors have attracted great attention in scientific research in the past three decades. Extensive studies on the immobilisation of biorecognition elements have been conducted in pursuit of higher sensitivity, but trialled formats have focussed on a thin layer modification next to the plasmon film, which usually requires in situ derivatization. This thesis investigates an 'off-chip' immobilisation strategy for SPR biosensing using silica particles and considers the implications of a particle-modified evanescent field on the signal amplitude and kinetics, for an exemplar affinity binding between immobilised IgG and its anti-IgG complement.

Submicron silica particles were synthesized as carriers for the bio-recognition elements. They were then immobilised to form a sub-monolayer on the gold film of an SPR biosensor using two methods: thiolsilane coupling and physical adsorption aided by mechanical pressure. The bio-sensitivity towards an antigen/antibody interaction was lower than an SPR biosensor with an alkanethiolate SAM due to the difference in ligand capacity and position in the evanescent field. The binding kinetics of antigen/antibody pair was found to follow the Langmuir model closely in a continuous flow configuration but was heavily limited by the mass transport from the bulk to the sensor surface in a stop-flow configuration.

A packed channel configuration was designed with larger gel particles as ligand carriers, packed on top of a gold film to create a column-modified SPR biosensor. This sensor has comparable bio-sensitivity to the previous sub-monolayer particle-modified systems, but the binding and dissociation of the analyte was heavily dependent on mass transport and binding equilibria across the column. A bi-directional diffusion mechanism was proposed based on a two-compartment mass transport model and the expanded model fitted well with the experimental data. The column-modified sensor was also studied by SPR imaging and analyte band formation was observed and analysed. Using the lateral resolution, a multiplexing particle column configuration was explored, and its potential in distinguishing a multicomponent analyte.

Publications

[1] E. A. H. Hall, S. Chen, J. Chun, Y. Du, and Z. Zhao, “A molecular biology approach to protein coupling at a biosensor interface,” *TrAC - Trends Anal. Chem.*, pp. 1–10, 2016.

Candidate’s contribution is not part of this thesis.

[2] Q. Sun *et al.*, “Functional Silver-Coated Colloidosomes as Targeted Carriers for Small Molecules,” *Langmuir*, vol. 33, no. 15, pp. 3755–3764, 2017.

Candidate’s contribution is an extension of the work in this thesis but not included here.

[3] Q. Sun, Y. Du, E. A. H. Hall, D. Luo, G. B. Sukhorukov, and A. F. Routh, “A fabrication method of gold coated colloidosomes and their application as targeted drug carriers,” *Soft Matter*, vol. 14, no. 14, pp. 2594–2603, 2018.

Candidate’s contribution is an extension of the work in this thesis but not included here.

Contents

List of Figures

List of Tables

Nomenclature

cm	centimetre
mm	millimetre
µm	micrometre
nm	nanometre
min	minute
g	gram
mg	milligram
µg	microgram
ng	nanogram
pg	picogram
s	second
ml	millilitre
µl	microlitre
mbar	millibar
RIU	refractive index unit
A.U.	arbitrary unit
M	molar concentration
SPR	surface plasmon resonance

RI	refractive index
Au	gold
ϵ	dielectric constant
λ	wavelength
c	speed of light in vacuum
n	refractive index
n_{ef}	effective refractive index
S	sensitivity
θ	incident angle
FWHM	full width at half maximum
LOD	limit of detection
Ab	antibody
SAM	self-assembly monolayer
IgG	immunoglobulin G
Fab	antibody-binding fragment
Fc	crystallizable fragment
LSP	localised surface polariton
SPP	surface propagating polariton
EM	electromagnetic
QD	quantum dot
OLED	organic light emitting diode
SERS	surface-enhanced Raman spectroscopy
SEM	scanning electron microscopy

EDX	energy-dispersive X-ray
DLS	dynamic light scattering
MS	mass spectroscopy
RIE	reactive ion etching
PECVD	plasma-enhanced chemical vapor deposition
ATR	attenuated total reflection
RPM	revolutions per minute
PBS	phosphate buffered saline
PDMS	polydimethylsiloxane
CMOS	complementary metal-oxide-semiconductor
Q	adsorbed amount
Q_{max}	maximum theoretical adsorbed amount
k_a	association rate
k_d	dissociation rate
k_{tr}	mass transfer rate
c_0	analyte concentration in bulk
c_s	analyte concentration on the adsorbent surface
ODE	ordinary differential equation
MGT	Maxwell-Garnett theory
EMT	effective medium theory
f	volume fraction
$\emptyset$	surface coverage
HPLC	high performance liquid chromatography

Hz	hertz
R	radius
ε	voidage
Re	Reynold's number
ρ	density
v	superficial velocity
d_p	particle diameter
μ	dynamic viscosity
k'_{tr}	reverse mass transfer rate

Chapter 1 Introduction

1.1 Biosensors – An Overview

1.1.1 Fundamentals of A Biosensor

A biosensor is a device which converts a biological event, for example, the binding between an analyte and a capture ligand, into a physiochemical signal such as colour change or electrochemical potential variation.

Biosensors as a concept were first introduced by Clark and Lyons in 1962 when they developed an amperometric enzyme-based electrode for the detection and measurement of glucose in any medium [1]. Since then, a tremendous amount of effort has been dedicated to this field and the area has expanded way beyond electrochemical glucose biosensors. Nonetheless, the fundamental principle that constitutes the terminology “biosensor” stays the same. A biosensor always has a bio-element and a sensor element. Researchers discover and innovate within the confinement of either domain or both. Figure 1.1 shows the generally employed bio-elements and sensor elements in biosensors. For example, a well-known glucose testing strip employs an enzyme as the bio-element and an electrochemical transducer as the sensor element. The final readout is an electrical signal.

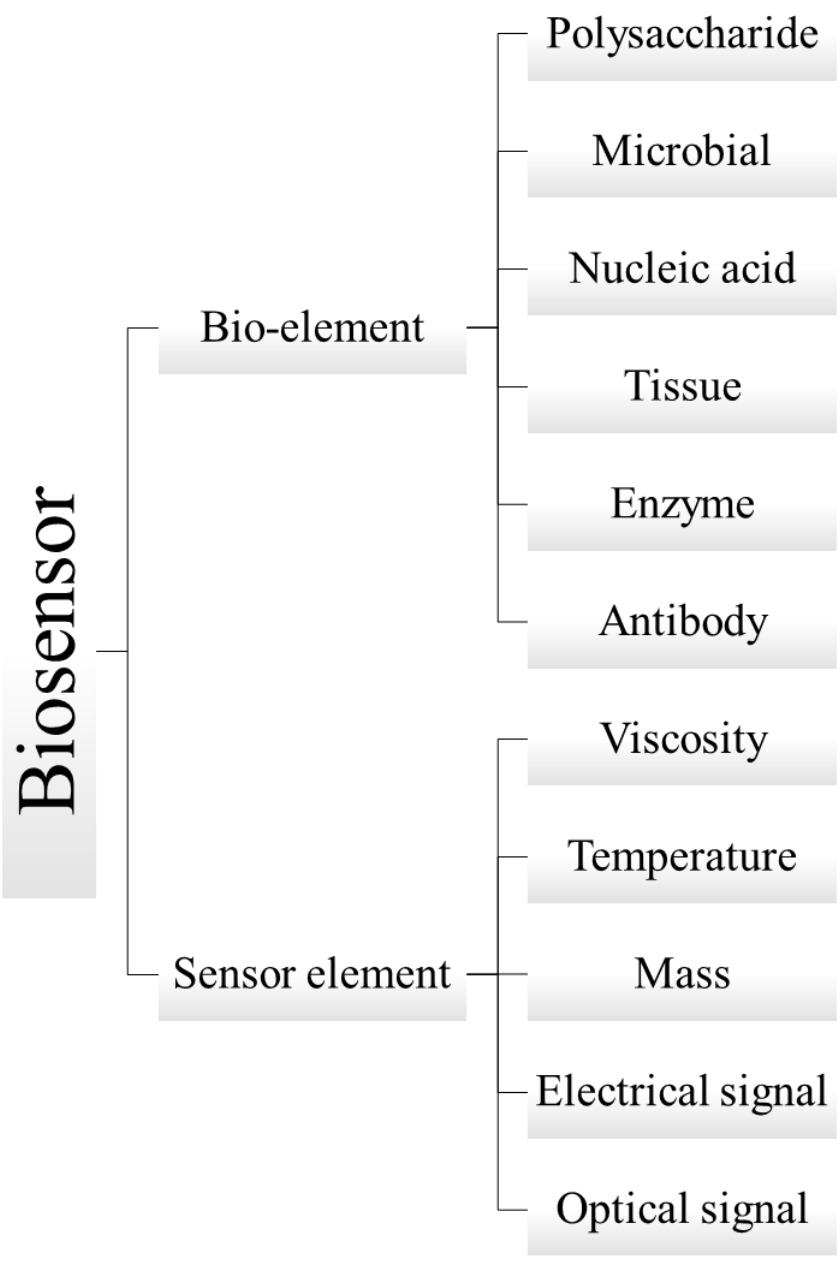

Figure 1.1 Generally employed bio-element and sensor element in biosensors.

For the biosensor to work, the bio-element and the sensor element must be coupled. There are generally four coupling methodologies that incorporate the bio-element into the sensor element: physical adsorption and entrapment, membrane immobilisation, covalent amalgamation and matrix entrapment. Physical adsorption involves the use of intermolecular forces such as hydrophilic/hydrophobic forces, Van Der Waals forces and

ionic forces for the bio-element to attach to the sensor element without a third medium [2]. Membrane immobilisation mainly uses a semi-permeable membrane that is directly on the sensor-element as a place for the bio-element to be embedded. The membrane acts as a different phase in this type of coupling [3]. Covalent amalgamation is similar to physical adsorption in the sense that there is no third medium involved but direct attachment. Instead of intermolecular forces employed in physical adsorption, covalent amalgamation takes advantage of covalent bonding [4]. Finally, matrix entrapment is the use of a porous substance such as sol or gel to restrict the bio-element, and the matrix encapsulation forms a direct link with the sensor element [5]. Figure 1.2 illustrates the four methodologies.

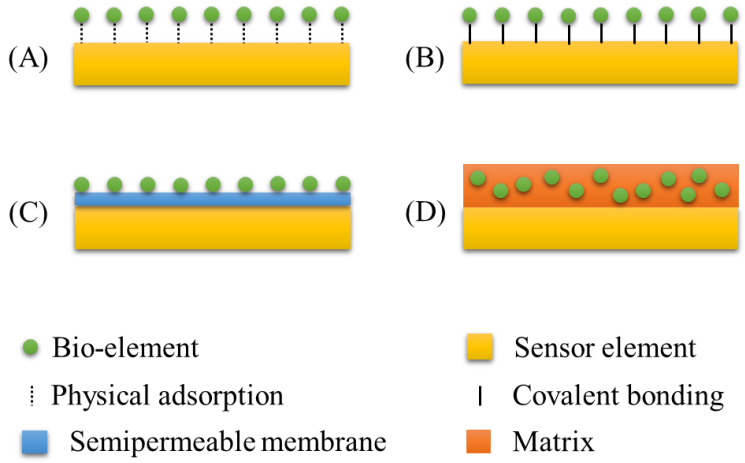

Figure 1.2 Coupling mechanisms between the bio-element and the sensor element. (A) Physical adsorption, (B) Covalent bonding, (C) Membrane encapsulation, and (D) Matrix entrapment.

1.1.2 Biosensor Applications

Through the development of half a century, biosensors have been researched extensively and have been applied in many aspects of our daily lives. A few of the representative impactful applications are summarised here with details on the bio-recognition elements and the transduction modalities.

Table 1.1 Applications of biosensors in disease prognosis.

Analyte	Bio-recognition element	Sample medium	Transduction modality	Reference
Prostate-specific antigen (PSA)	DNA aptamer	Buffer	Chemiluminescent	[6]
	DNA aptamer	Buffer	Electrochemical	[7]
Pancreatic cancer marker	Antibody	Buffer	SPR	[8]
Colorectal cancer marker carcinoembryonic antigen (CEA)	Antibody	Buffer	SPR & Electrochemical	[9]
	Antibody	Buffer	Electrochemical	[9, 10]
Epstein-Barr virus	Synthetic peptide	Buffer	SPR	[12]
	Antibody	Clinical serum	SPR	[13]
Hepatitis G virus	Synthetic peptide	Buffer	ELISA	[14]
Hepatitis B virus	Antibody	Serum	SPR	[15]
	Antibody	Buffer, blood serum and plasma	LSPR	[16]
Dengue virus	Antibody	Buffer	Electrochemical	[17]

	Synthetic peptide	Buffer	ELISA	[18]
	Synthetic peptide	Buffer	Electrochemical	[19]
Influenza virus	Antibody	Buffer	SPR	[20]
	Antibody	Saliva	SPR	[21]
	ssDNA	Buffer	Electrochemical	[22]

1.1.2.1 Biomedical Applications

Biosensors have been extensively applied to the biomedical field. One of the most impactful applications is electrochemical blood glucose sensing for the management of diabetes. The first mediated amperometric glucose sensor for home use by people with diabetes was launched to the market in 1987 [23]. Since then it has been expanded to a billion-dollar business. The global glucose biosensor market was estimated at 15.3 billion USD in 2015 and the outlook is that it will continue to grow to reach 31 billion by 2022 [24]. Another major application in the health monitoring field is pregnancy tests. The first home test kit for the detection of human chorionic gonadotropin (hCG) was invented in 1968 [25] and now the projected market size by 2022 is 489.3 million USD with an annual growth of 4.5% [26]. Some other applications in disease prognosis are listed in Table 1.1.

1.1.2.2 Food Quality Control

The food industry requires analytical methods for checking the safety and quality of foods. There are many well established methodologies and laboratory instrument techniques such as high-performance liquid chromatography (HPLC), gas chromatography (GC), etc. Biosensors represent a desirable alternative to identify any chemical and/or biological contaminants in foods as they are quick, portable, cheap and

easy to handle. Numerous biosensors have been developed to detect pathogens in food and some of them are listed in Table 1.2.

Table 1.2 Applications of biosensors in food quality control.

Analyte	**Bio-recognition element**	**Sample medium**	**Sensor type**	**Reference**
***Escherichia coli* (*E. coli*)**	Antibody	Culture	SPR	[26 – 28]
	Antibody	Culture	Electrochemical	[30]
	ssDNA	Culture	Electrochemical	[31]
Salmonella enteritidis	Antibody	Culture	SPR	[28, 31]
	Antibody	Liquid	SPR	[33]
	Antibody	Solid	Fluorescent	[33 – 35]
	Phage	Solid	Magnetoelastic	[37]
***Listeria monocytogenes* (*L. monocytogenes*)**	Antibody	Solid	Fluorescent	[34], [38]
	Antibody	Culture	Fluorescent	[39]
	Antibody	Culture	SPR	[28, 39]
	Antibody	Culture	Piezoelectric	[41]
	Antibody	Culture	Electrochemical	[42]
***Staphylococcus aureus* (*S. aureus*)**	Antibody	Culture	SPR	[43]
	Phage	Culture	SPR	[44]
	ssDNA	Culture	Fluorescent	[45]
	Aptamer	Solid	Electrochemical	[46]
Domoic acid	Antibody	Buffer	SPR	[46 – 48]
	Antibody	Buffer	Electrochemical	[50]
Aflatoxin B_1	Aptamer	Buffer	Fluorescent	[51]
	Antibody	Buffer	Piezoelectric	[52]

	Enzyme	Buffer	Electrochemical	[53]

1.1.2.3 Environment Monitoring

A growing number of initiatives and legislative actions for environmental pollutant control have taken place in recent years. The increasing social concern has sparked tremendous effort in scientific research. An ideal analytical tool for environmental monitoring needs to be portable, rapid, and cheap. Biosensors have proved to be a great option that check all the boxes if designed properly. Numerous biosensors that employ different detection schemes have been developed for a variety of pollutants. Some recent examples are listed in Table 1.3

Table 1.3 Applications of biosensors in environmental monitoring.

Analyte	**Bio-recognition element**	**Sensor type**	**Reference**
Atrazine	Enzyme	Electrochemical	[54, 55]
	Antibody	Piezoelectric	[56]
	Antibody	SPR	[57]
Dichlorodiphenyltrichloroethane (DDT)	Antibody	SPR	[58]
	Antibody	Nanomechanical	[59]
2,4-dichlorophenoxyacetic acid (2,4-D)	Antibody	Fluorescent	[60]
	Antibody	SPR	[61]
	Antibody	Piezoelectric	[62]
Cu^{2+}	ssDNA	Fluorescent	[63]
	Cell	Electrochemical	[64]
Cadmium	Enzyme	SPR	[65]
	Synthetic peptide	LSPR	[66]
	Protein	SPR	[67]
Chromium	Enzyme	Electrochemical	[68 – 70]
Lead	Enzyme	Electrochemical	[71]
	Aptamer	Fluorescent	[72]
Mercury	Cell	Luminescent	[73, 74]
2,4,6-trinitrotoluene (TNT)	Antibody	SPR	[75]
	Enzyme	Electrochemical	[76]

1.2 Surface Plasmon Resonance Biosensors

Surface plasmon resonance (SPR) has been a major modality in the development of biosensors. The versatility of an SPR biosensor allows it to be employed in many analytical fields if a suitable bio-affinity interaction exits for an analyte of interest. The physics behind the SPR phenomenon, various sensor configurations, some performance parameters and the advantages of SPR biosensors are reviewed in this section.

1.2.1 SPR Theory

Surface plasmon resonance or SPR is the phenomenon where a special mode of electromagnetic field propagates along the surface of a metal/dielectric interface due to collective vibrations of the electron cloud in the metal film excited by photons. The resonant electromagnetic field is called surface plasmon in this case [77]. The evanescent field of the electromagnetic wave is sensitive to the refractive index change in the dielectric medium. Figure 1.3 shows an illustration of surface plasmon propagation in different media.

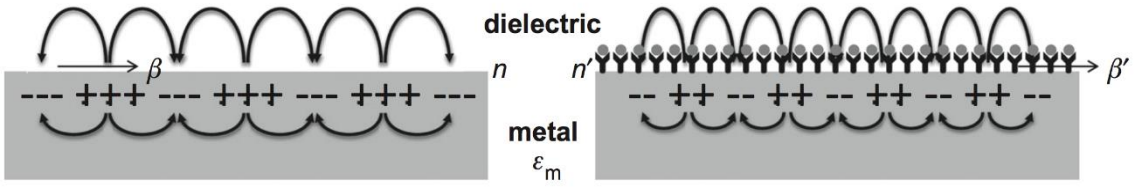

Figure 1.3 Illustration of surface plasmon propagation along the metal/dielectric interface before and after biomolecule immobilisation.

Quantitatively, the propagation constant of surface plasmon β propagating along a planar boundary between a semi-infinite metal with a complex permittivity constant $\varepsilon_m = \varepsilon_m' + i\varepsilon_m''$ and a semi-infinite dielectric with a refractive index n can be expressed as

$$\beta = \frac{2\pi}{c\lambda}\sqrt{\frac{n^2\varepsilon_m}{n^2+\varepsilon_m}} = \frac{2\pi}{c\lambda}\left(n_{ef} + i\gamma_i\right) \tag{1.1}$$

where λ is the wavelength of the excitation light and c is the speed of light in vacuum. The real and imaginary parts of the propagation constant can be expressed by means of the effective index n_{ef} and the attenuation coefficient γ_i of the plasmon [78].

Light waves can only couple to a surface plasmon at a metal-dielectric interface if the incident light's wavevector, which is parallel to the interface, matches the propagation constant of the surface plasmon. [79]. As a result, surface plasmons cannot be excited directly by light incident on a smooth metal surface. The main methods of optical excitation of surface plasmons include attenuated total reflection (prism coupling), diffraction on a metallic grating (grating coupling) and evanescent wave coupling between dielectric and plasmonic waveguides (waveguide coupling).

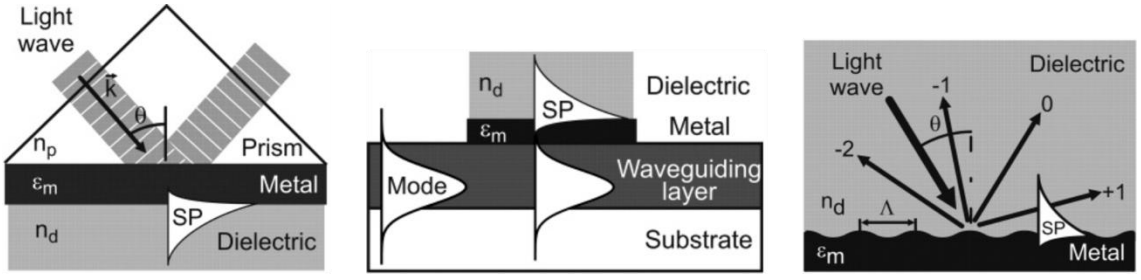

(A) (B) (C)

Figure 1.4 Coupling methods between incident light waves and surface polaritons. (A) Prism coupling, (B) waveguide coupling, and (C) grating coupling. Adapted from [79]

Prism coupling is the most suitable choice for fast prototyping since the prism is easy to assemble and the metal film is easy to fabricate. In this coupling mode, a coupling prism is interfaced with a thin metal film and the evanescent wave created by the attenuated total reflection of the light incident on the prism/metal interface couples with the surface plasmon if

$$n_p \sin\theta = n_{ef} \tag{1.2}$$

where θ is the incident angle and n_p is the refractive index of the prism [77].

The evanescent field penetration depth can be calculated through the following equation:

$$D_p = \frac{\lambda}{2\pi\sqrt{\sin^2\theta_1 - \left(\frac{n_0}{n_p}\right)^2}} \tag{1.3}$$

and the field strength E at a given depth z is given by:

$$E = E_0 e^{\left(-\frac{z}{d_p}\right)} \tag{1.4}$$

where E_0 is the evanescent field at the surface and n_0 is the refractive index of the dielectric media to be sensed [80].

Surface plasmon only propagates a distance of a fraction of the wavelength of excitation light. Since the intensity decreases exponentially with the distance from the surface, the most sensitive region is the medium closest to the metal/dielectric interface. This causes inefficiency in biosensor applications and is discussed in the next section.

1.2.2 Generic SPR Sensor Configuration

Since surface plasmon is sensitive to the refractive index change near the metal/dielectric interface, the resonance phenomenon can be engineered to detect local refractive index change caused by binding of target analyte onto the surface. An SPR biosensor can be characterised by its light coupling method, configuration, modulation and functionalisation strategy. The light coupling method has been mentioned previously in Section 1.2.1. Taking the most common prism coupling method as an example, there are two types of configurations used to couple surface plasmon polaritons to the sample medium as shown in Figure 1.5: that are termed the Kretschmann configuration [81] and the Otto configuration [82]. In general, the two configurations show similar efficiency in coupling with the surface plasmon polaritons while the Kretschmann scheme provides better flexibility regulating the sample media (chamber, channel or cell).

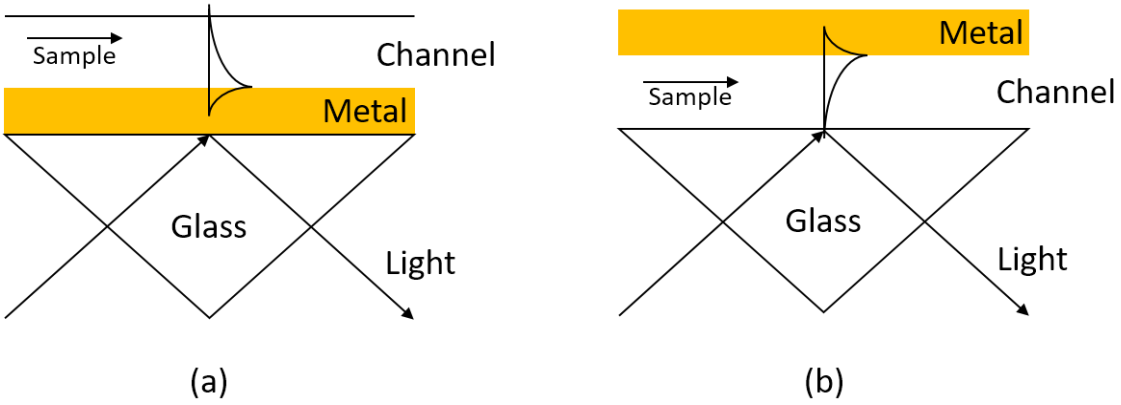

Figure 1.5 The Kretschmann (a) and Otto (b) configurations of surface plasmon polariton coupling.

In terms of modulation strategies, three are widely used in the literature: angular modulation, wavelength modulation and phase modulation. In an angular modulation set-up, a monochromatic laser with fixed wavelength is used as the light source and the sensor is fixed on a rotating stage which loops from a certain angle to another back and forth. The response is collected as the reflectance against the angle of incidence. In a wavelength modulation set-up, a white light (combination of light in different wavelengths) is used as the light source and the sensor is fixed at a certain angle. The

response is collected as the reflectance against the spectrum of the reflected light. In a phase modulation set-up, a monochromatic laser is used as the light source and the beam is split into a signal beam and a reference beam. The signal beam passes through the SPR sensor and the result is a relative phase shift when compared with the reference beam in the phase detector [83]. Among the three modulation techniques, phase modulation has the highest sensitivity but the most complexity. Literature suggests that the sensitivity of the wavelength modulation is comparable to that of the angular modulation [84]. Additionally, it is obvious that spectral SPR measurement has advantages over angular SPR measurement because of the lack of moving parts and fast readout. Some angular techniques are formatted to provide a measurement of angular shift relative to intensity at a fixed wavelength close to the resonance. While this does not allow the full angular spectrum to be recorded, it also avoids moving parts. Other ingenious ways to deliver the full angular spectrum have also been devised [85].

1.2.3 Performance Parameters

There are several parameters, namely the sensitivity, the figure of merit and the resolution, to characterise the performance of SPR sensors. Sensitivity is defined as the ratio of change in the optical output with respect to the change in refractive index. Depending on the modulation, the sensitivity S may be expressed in different forms:

$$S = \frac{\partial P}{\partial n} \tag{1.5}$$

where P represents the optical output in general. In a wavelength modulation, the output is the wavelength, λ, while in an angle modulation, the output is the incident angle, θ.

In an SPR biosensor, it is impractical to quantify the refractive index change. More commonly, the change of refractive index is substituted by the change in the measured quantity (e.g. concentration of analyte).

$$S = \frac{\partial P}{\partial c} \tag{1.6}$$

where c represents the concentration of the analyte.

The figure of merit (FoM) represents the quality of the resonance. For a clean and uniform metal surface at a certain thickness, the resonance peak is narrow and sharp. The FoM is expressed in terms of the sensitivity (S) and the line width of the resonance peak (the full width at half maximum, FWHM):

$$FoM = \frac{S}{FWHM} \tag{1.7}$$

In general, a sharper resonant peak translates to a smaller FWHM which results in a higher figure of merit.

The resolution represents the lowest change in the refractive index that can be detected. In many cases, it is also called the detection limit. The lowest magnitude of detection depends on the level of noise in the optical output expressed as the standard deviation σ of a static reference signal.

$$\delta n = \frac{\sigma_n}{S} \tag{1.8}$$

1.2.4 Advantages of an SPR Biosensor

A biosensor based on SPR has several advantages compared to those based on other principles [86]. First, it is a label-free detection mechanism that simplifies sample preparation. It can also be combined with other labelled detection methods to enhance sensitivity and selectivity. Secondly, it can be tailored to detect any analyte if it has a capture (or affinity) ligand that can be immobilised on the surface of the sensor. So far, many kinds of analyte have been successfully detected using SPR sensors, for instance, nucleic acids [87 – 89], antibodies [90 – 94], bacteria [95, 96], etc. Thirdly, SPR detection

is in real-time. It possesses great potential for instant diagnostic tests. Finally, the sensor can be configured to work in a continuous monitoring mode or a one-time analysis mode depending on the application. The continuous monitoring mode especially reveals information on the kinetics of binding which is important in many areas such as drug development [87, 97 – 100]. Resolving the dissociation and association reveals the entire picture of complex formation process. This information is especially critical when identifying the roles of specific functional groups both within a target and within a compound.

1.3 SPR Biosensor Developments

In 1982, Liedeberg and Nylander demonstrated the first biosensor utilising SPR as an optical biosensor [101]. Over the past three decades, this field of research has experienced considerable growth as shown in Figure 1.6. Recent progress can be categorised into four categories: immobilisation of the bio-recognition element on the sensor, surface modification of the sensor, miniaturisation of the SPR biosensor system and integration with other delivery system or sensing modalities.

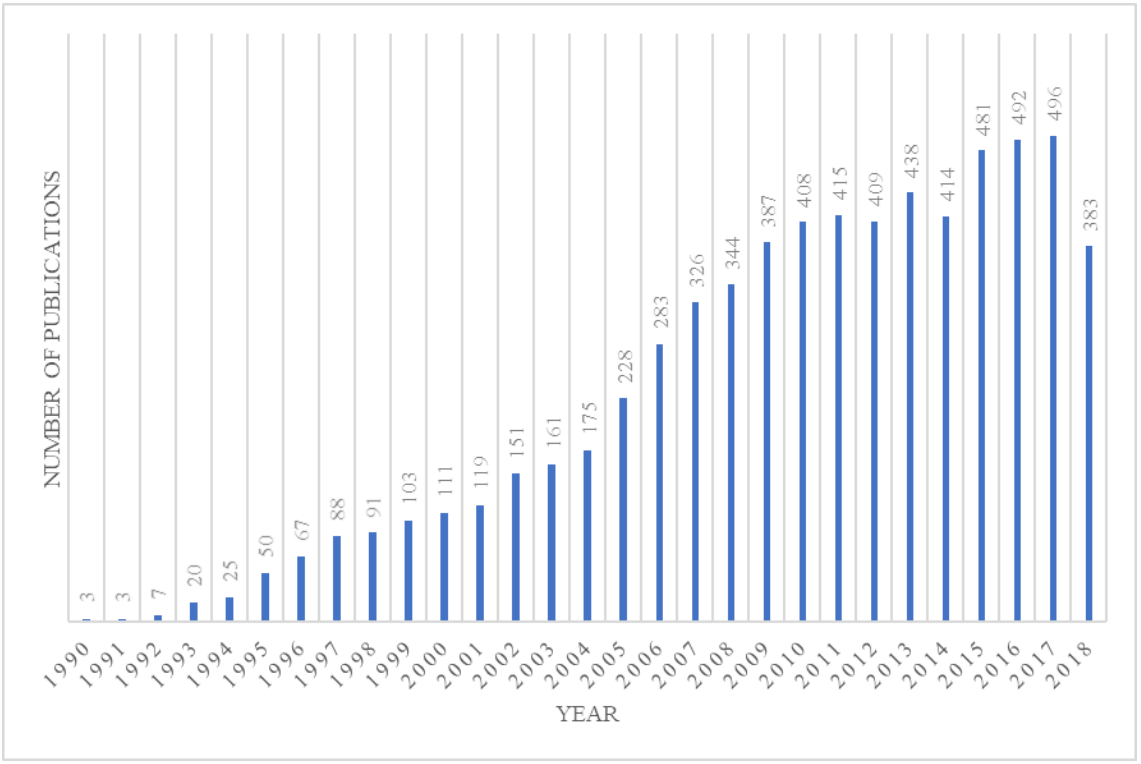

Figure 1.6 Number of publications each year with the key word "Surface Plasmon Resonance Biosensor" between 1990 to 2018. The data was retrieved in Sep 2018 from Web of Science.

1.3.1 Bioreceptor Immobilisation Strategies

SPR biosensors commonly use antibodies as the biorecognition elements. Although new bioreceptors have been developed, such as aptamers or imprinted polymers, antibodies [102] remain the most widely used biorecognition element due to their availability and

high affinity. The general direction of research on bioreceptor immobilisation on the surface has two branches: one is to increase the coverage of the bioreceptors so that the binding capacity is maximised; the other is to control the orientation of the bioreceptors such that they retain an optimal availability. Random orientation of the bioreceptors can be affected by steric hindrance and non-specific protein adsorption, resulting in inactivation and low binding capacity [103]. Oriented immobilisation normally provides a high sensitivity, but the immobilisation steps may get much more complicated and/or expensive. Some of the immobilisation strategies and their recent adoptions are reviewed below.

1.3.1.1 Physical Adsorption

Direct adsorption is the easiest and the most employed method of immobilisation. However, it is an uncontrolled and unspecific process that may result in inactivation and denaturation of the bioreceptors. Because of the direct contact between the metal surface and bioreceptors, the ligands may undergo conformational change. The suboptimal orientation of the bioreceptors also adversely affects binding. Some recent studies have compared the efficiency of physical adsorption with that of covalent coupling, specific adsorption via biotin orientation [104] and carbon nanotubes [105] and physical adsorption was proved to be the least effective immobilisation method.

1.3.1.2 Covalent Coupling by Self-Assembled Monolayer

Covalent attachment of the bioreceptors onto metal surfaces that are chemically modified has been the most widely used technique due to its relative simplicity and good performance. In particular, alkanethiolates are suitable for immobilising a variety of biomolecules onto gold surfaces. The method for functionalising the gold surface with alkanethiolates is simple and reproducible and the SAM formed on the gold surface provides a stable and ordered immobilisation foundation for bioreceptors and reduces non-specific adsorption [103]. The carboxylic acid at the other end of the alkanethiol is activated by N hydroxysuccinimide (NHS) and 1-ethyl-3(-3-dimethyl- aminopropyl) carbodiimide hydrochloride (EDC) and is capable to form a carbodiimide linkage with the

amine groups of the bioreceptors [106]. This immobilisation method has been employed, for example, in SPR biosensor detecting cancer biomarkers [107] and cell suspension [108].

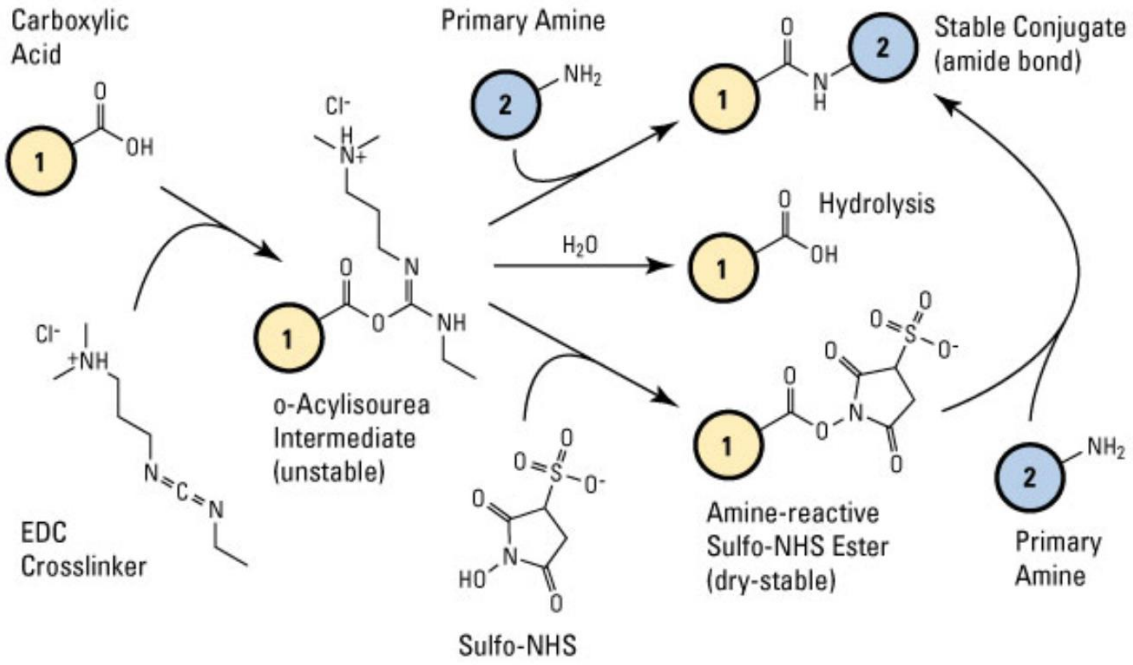

Figure 1.7 Illustration of carbodiimide coupling reaction pathway. Adapted from [106].

The technique of immobilisation using alkanethiolate SAM has also been expanded to using mixed layers of thiols. Tsai et al used a mixture of 16-Mercaptohexadecanoic acid (16-MHA), and 6-mercapto-1-hexanol (6-MCH) to form a SAM on the surface of an SPR biosensor and achieved higher sensitivity due to reduced non-specific binding and reduced steric hindrance.

1.3.1.3 Immobilisation by Antibody Binding Proteins

Proteins A and G are commonly used to immobilise antibodies on SPR biosensor surfaces. The immobilisation strategy requires the biosensor surface to be first immobilised with the antibody binding proteins often through covalent attachment. The immobilised antibody binding proteins then bind to the Fc region of the antibody bioreceptors leaving the Fab region which captures the analyte. Proteins A and G contain

4-5 and 2-3 IgG binding sites respectively, thus, the ligand antibodies can be properly oriented regardless of the protein orientation on the sensor surface. The resultant biosensor surface with the antibodies as bioreceptors are ready for the specific detection of the analyte [109, 110]. Furthermore, Protein G can be chemically or genetically modified to contain thiolates or cysteine residues so that they bind onto gold surfaces without an alkanethiolate layer [111 – 113]. Protein A conjugated with gold binding peptides (GBPs) [114, 115] and biotin tags [116] have also been reported to be immobilisation scaffolds on SPR biosensors.

1.3.1.4 Biotin-avidin Specific Adsorption

Another common choice to control the orientation of the bioreceptors during immobilisation is to use a biotin-avidin system. Biotin can be bound in a wide range of macromolecules (proteins, peptides, oligonucleotides and antibodies) while retaining its high binding affinity towards avidin or avidin-related molecules such as streptavidin, concanavalin and NeutrAvidin [117, 118]. One major disadvantage of this immobilisation strategy is the need to chemically modify the biotinylated antibodies which is time-consuming and costly. Biotin-avidin systems can also be combined with other immobilisation strategies to increase efficiency [116].

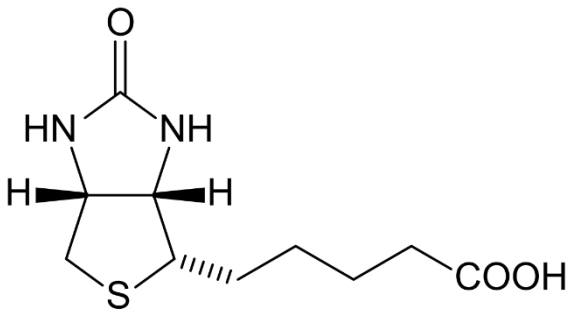

Figure 1.8 Structural formula of biotin.

1.3.1.5 Polymer Supports

A polymer immobilisation strategy provides a versatile and heterogeneous 3-dimensional matrix for the entrapment of bioreceptors through adsorption, diffusion and covalent coupling. One of the most well-known polymers is the dextran hydrogel used on the surface of CM5 SPR sensor chips in BIACORE systems. Dextran-hydrogel, typically about100 nm in thickness [119] has the advantage of providing many layers of binding sites for the bioreceptors compared to the single layer in a thiolated SAM. Thus, the ligand capacity on a dextran immobilised surface is higher resulting in a better sensitivity.

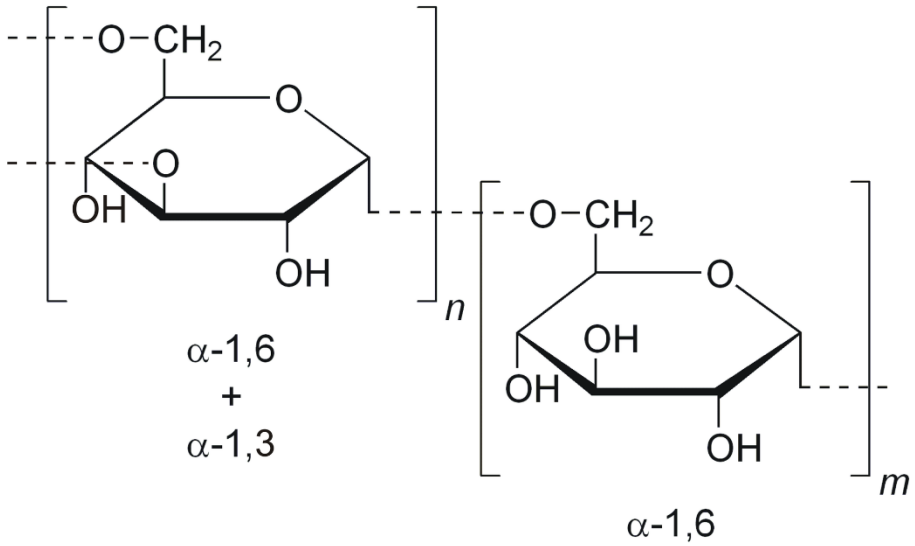

Figure 1.9 Structural formula of dextran.

A parylene coating, deposited by chemical vapor deposition, has also been demonstrated to improve the capture efficiency of antibodies by 20 fold when compared to 2-dimensional glass surfaces [120]. A parylene coating has also been combined with biotin-avidin coupling strategy to immobilise bioreceptors on SPR biosensors on an SPR biosensor and achieved a LOD of 1 pg/ml [121].

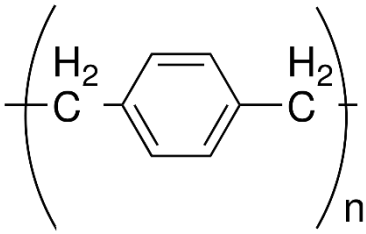

Figure 1.10 Structural formula of a parylene N repeat unit.

1.3.1.6 Fragmented Antibodies

Antibodies that are chemically fragmented or genetically engineered to have only the F(ab) fragment left which contains the antigen-binding domain are another great alternative for oriented immobilisation of antibodies (Figure 1.11). The smaller and more efficient fragments allow for better accessibility and higher ligand capacity [122]. The free sulfhydryl groups exposed after the antibody fragmentation by enzyme digestion or chemical reduction have the added benefit of direct immobilisation on gold surfaces [123]. Recombinant single domain antibodies (sdAbs) have also been reported as an immobilisation strategy for SPR biosensors [117].

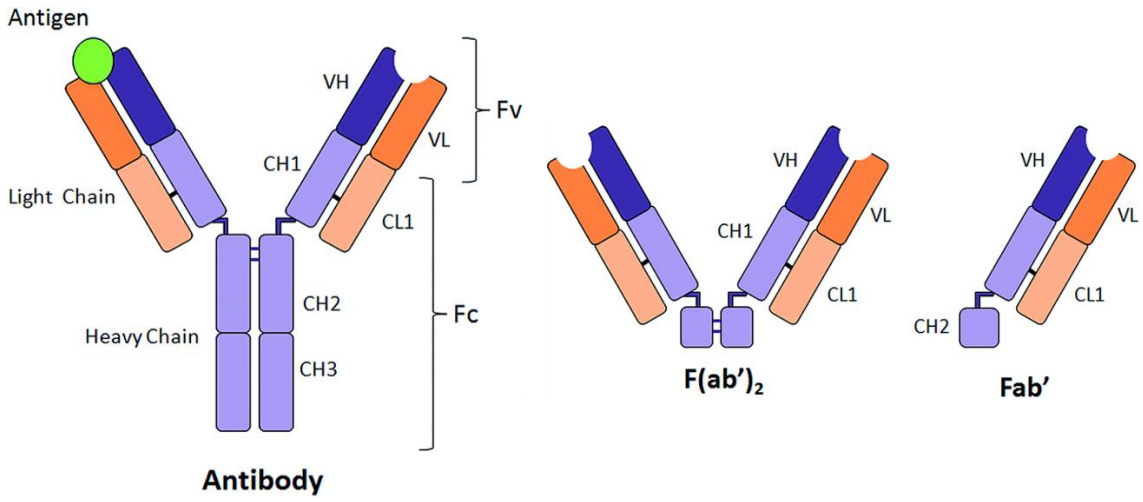

Figure 1.11 Illustration of the structures of an antibody whole molecule and its F(ab) fragments. Adapted from [124].

1.3.1.7 Surface Over-layers for Immobilisation

Strategies have also been considered to cover the gold surface to provide a different chemistry for immobilisation. For example, silicon dioxide-based materials such as glass are standard materials for biosensing. It is inexpensive and attachment schemes for biomolecules based on silane-coupling have been well developed. However, for SPR biosensors, silica coatings on gold surfaces need to be nanometre-thin to not affect the sensitivity of the gold film. The fabrication techniques have been extensively researched. SiO_x overlayers of 5-10 nm in thickness has been deposited on gold surfaces by plasma-enhanced chemical vapor deposition (PECVD) [125]. The sol-gel technique has been used to achieve a silica film in situ of 3-100 nm in thickness and ligands were immobilised on the silica with a biotin-avidin system [126]. Layer-by-layer deposition of poly(allylamine hydrochloride) and sodium silicate followed by calcination at high temperature has also been demonstrated to create silicate films of thickness 2 to 15 nm on gold surfaces [127]. Alternatively, a thin layer of silica has been created by modification of a layer of spin-coated polyhydroxymethylsiloxane using oxygen plasma and thermal treatment as reported by the Kasemo group [128, 129].

Carbon-based overcoatings on SPR biosensors have also been reported. Amorphous carbon up to 20 nm thick has been deposited on SPR biosensors but it was found that the presence of it decreases the sensitivity of the biosensor due to the complex dielectric function of the amorphous carbon [130, 131]. Graphene is a 2-dimensional carbon-based material that has shown great potential in many aspects of research [132]. A thin layer of graphene on top of a traditional SPR biosensor has been found to improve the sensitivity of the sensor through increase biomolecule adsorption onto the surface by π-π stacking [133]–[135].

Other films that have been tested on SPR biosensors are antimony-doped tin oxide (SnO_2:Sb) [125] and indium tin oxide (ITO) [136]. However, the complex dielectric constant of the tin oxide decreases the sensitivity of the biosensor.

1.3.1.8 Particle Immobilisation

Nanoparticles have long been used in SPR biosensors to enhance their sensitivity, but they are usually used as a label in a sandwich either to provide mass to the analyte or localised SPR coupling as discussed in detail in the next section. They are very rarely used as carriers or immobilisation supports for the bioreceptors on the SPR biosensor surface. Hua Zhang *et al*. reported an immobilisation method using a magnetic Au nanorod core-shell structure as the carrier [137]. The magnetic nanostructures were immobilised by magnetism and the bioreceptors were then immobilised on the nanostructures by alkanethiolates. The surface was easily regenerated by removing the magnetic field and flushing.

1.3.2 Surface Modification

Owing to advancements in nanotechnology, many nanostructures have been used to modify the surface of the traditional SPR sensor surface. These nanostructures improve the performance of the traditional SPR biosensor by either enhancing the evanescent field or the adsorption of analyte. Generally, the nanostructures can be categorised into three types: plasmonic nanoparticles that have localised SPR, non-plasmonic nanoparticles that facilitates the adsorption and finally nanostructure arrays that are fabricated directly onto the metal surface to enhance the SPR.

1.3.2.1 Plasmonic Nanoparticles

Gold and silver are known to have the best plasmonic properties and nanoparticles made of these materials are widely incorporated in conventional SPR biosensors to achieve ultra-high sensitivity. Theoretically, nanoparticles enhance the evanescent field by the coupling between localised surface polaritons (LSPs) and surface propagating polaritons (SPPs) [138]. Lévêque and Martin simulated the coupling between LSPs and SPPs and their result showed that it enhanced the electromagnetic (EM) field in the space between the nanoparticles and film by a factor up to 5000. [139, 140]. The EM field enhancement is shown to be usually the strongest in the gap between the nanoparticles and the film due

to near field coupling of the EM wave. Many ultra-sensitive SPR biosensors have been developed based on this coupling effect using spherical nanoparticles [141 – 145]. In those reports, Au nanoparticles have been utilised as a label to enhance the EM field around the analyte when the analyte is captured on the surface of the sensor film. Hong et al studied the enhancement by Au nanoparticles in detail and found that for 20 nm Au nanoparticles the dominant enhancement associated with the coupling between the LSPs and SPPs only occurs when the gap is smaller than approx. 8 nm. The enhancement beyond that distance is dominated by the mass of the Au nanoparticles [146]. Au nanorods have also been used together with an SPR biosensor to enhance its sensitivity and it offers tunability based on the orientation of the nanorods on the surface [143]. Kwon *et al.* compared the enhancement among three types of Au nanostructures (cubic cages, rods and quasi-spherical) and found that the greatest enhancement was observed for the quasi-spherical particles with the detection of thrombin concentrations as low as approx. 1 aM [147].

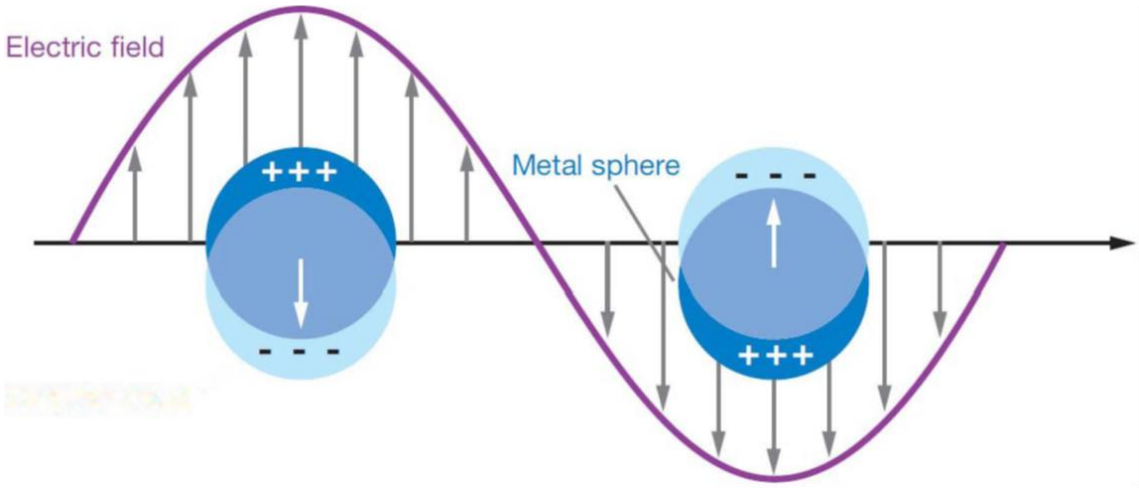

Figure 1.12 Illustration of plasmonic coupling. Adapted from [148]

1.3.2.2 Non-plasmonic Nanoparticles

Other nanoparticles have also been introduced to SPR biosensors, such as quantum dots (QDs), magnetic nanoparticles, hydrogel nanoparticles and silicon nanoparticles. They

improve the sensitivity of the SPR biosensor by either enhancing the signal output or improving the capture of the analyte.

QDs are semiconductor materials with size/composition-tuneable fluorescence and have been extensively utilised in sensing and imaging [149]. QD conjugated biomolecules have been detected at ultra-high sensitivity using SPR fluorescence microscopy in many reports [150 – 154]. Analogous to plasmonic nanoparticles, QDs are used as labels and need to be conjugated to the analyte for the sensitivity enhancement. The enhancement was attributed to the mass loading effect like the case with gold nanoparticles and/or a bidirectional coupling between the QDs and the SPPs where energy is transferred from SPPs to the excitons and the excited QDs prompt the generation of SPPs [155].

Magnetic nanoparticles have also been introduced into traditional SPR biosensors to enhance the sensitivity by enriching the analyte. 50 nm streptavidin-conjugated magnetic nanoparticles have been tested to amplify the signal on an SPR biosensor through a sandwich type immunoassay [137, 156 – 161]. It was also found that the magnetic nanoparticles not only enriched the analyte concentration, but also reduced the background noise by purification [162].

Apart from QDs and magnetic nanoparticles, other nanoparticles are not widely employed but are worth mentioning. Hydrogel nanoparticles have been used as carriers in single-particle SPR microscopy to monitor the bioactive peptide melittin uptake [163]. Silicon nanoparticles on a gold film have been studied to enhance the EM field due to their high refractive index [164]. Besides the use of a single type of particles, a combination of Au nanoparticles and QDs have also been conjugated to antibodies to have a signal enhancement of 50 fold in a sandwich assay [165].

1.3.2.3 Nanostructure Arrays

Plasmonic nanoparticles that are fabricated by colloidal synthesis are often used as labels since most of the enhancement takes place in the gap between the particles and the film. To finely control the separation among the nanoparticles/nanostructures, lithography methods such as electron beam lithography, interferometric lithography and colloidal

lithography are used to create nanostructures directly on a metal film [166 – 168]. In addition, the nanostructure arrays have the added benefit of direct excitation of the SPPs.

Among all nanostructures, nanohole arrays have received the most attention in research. Nanohole arrays support localised SPR in a manner analogous to that of nanoparticles. The incident light on the sensor surface excites LSPs that penetrate the holes and scatter on the other side of the film resulting in an enhanced transmission [169]. The increased surface area for reaction also captures more analyte. Nanohole arrays have been shown to increase the sensitivity three to four times when compared with smooth Au film SPR biosensors [170 – 173].

Other nanostructure arrays that have been fabricated and tested for enhancing SPR biosensor performances include nanocross arrays [174], nanodome arrays [175], nanocave arrays [176], nanodonut arrays [177]. All these nanostructures regardless of their shape enrich LSPs and therefore enhances the local evanescent EM field. Xiao *et al.* reported a large-scale and high throughput fabrication method of repetitive nanostructures on metal thin films [178]. They were able to have various designs imprinted, such as nanogratings, a nanobullseye and nanodots. Aristov et al. took the nanostructure design even further and created a 3-dimensional woodpile structure [179]. The final metastructure looked like layers of interlaced nanowires. The metastructure showed a delocalised plasmon mode and a large area for biomolecule immobilisation resulting in an extremely high spectral sensitivity of over 2600 nm/Refractive Index Unit.

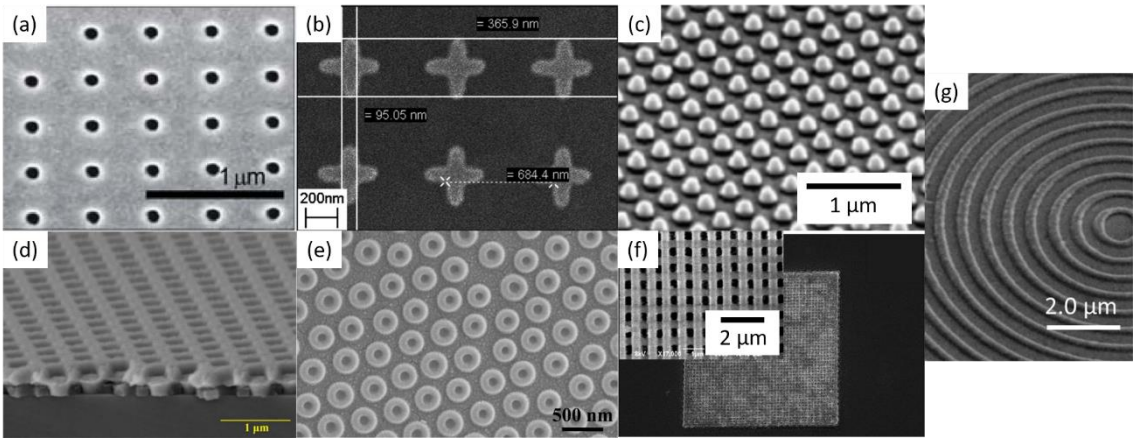

Figure 1.13 SEM images of (a) nanohole arrays [170], (b) nanocross arrays [174], (c) nanodome arrays [175], (d) nanocave arrays [176], (e) nanodonut arrays [177], (f) 3-D woodpile structure [179], and (g) nanobullseye [178].

1.3.3 Instrumental Design

The instrumentation design of an SPR biosensor system has always been heading towards miniaturisation. Thanks to the advancement in microelectronic and microfluidics, many of the integrated systems are small and self-contained enough to show good promises for point-of-care applications. In the literature, many of the SPR systems which the manufacturer claims to be portable are integrated boxes that resemble a bench top instrument, for instance the β-SPR sensor system from SENSIA Spain [58]. We only consider development towards the miniaturisation of SPR systems in this review.

1.3.3.1 Integrated Optical System

A widely used example of a portable SPR biosensor with an integrated optical system is the Spreeta 2000 platform [180]. The SPR integrated the light source, the prism, and the photodetector array in a closure comparable to the size of a coin. Pakorn Preechaburana used a PDMS based structure placed on the screen of a phone to complete a light path that uses the screen generated red light as a light source and the front-facing camera as the detector [181]. Briliant Adhi Prabowo simplified the conditioning of the light source by using OLED as a light source together with a brightness enhancement film and a

birefringent optical film [182]. But the entire system is far from being as portable as they claimed to be. Yong-beom Shin developed a portable SPR biosensor that integrated the optical path using a rotating mirror [183]. They commercialised their device and it was claimed to be the smallest SPR product.

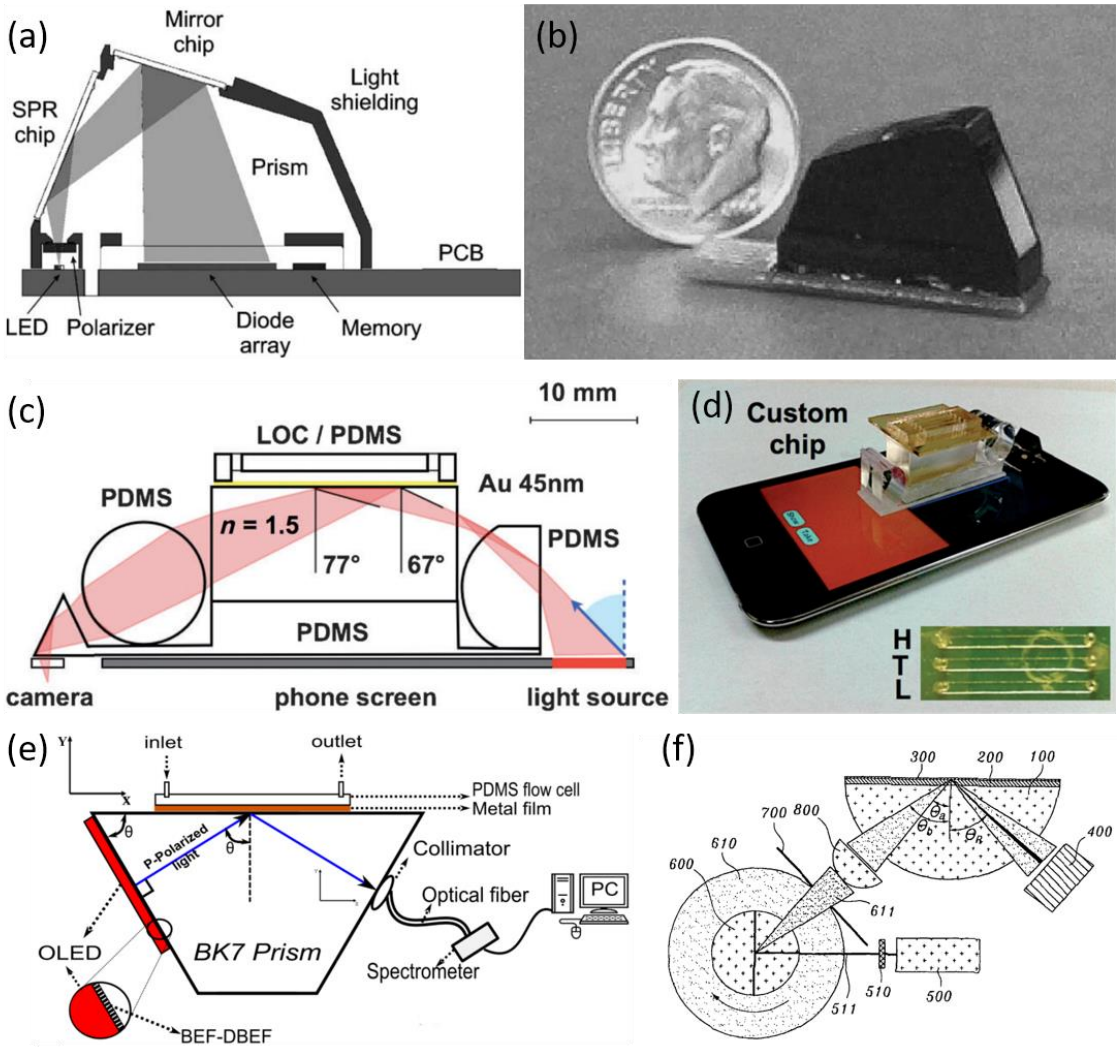

Figure 1.14 Surface plasmon resonance sensors with integrated optical paths. (a) Schematic design and (b) photo of the Spreeta 2000 [180]. (c) Schematic design and (d) photo of the on-cell-phone SPR sensor [181]. (e) Schematic design of the SPR sensor with integrated OLED light source [182]. (f) Schematic design of the SPR sensor with rotating mirror [183].

1.3.3.2 Integrated Micro-fluidics

Early development of portable SPR biosensors focused on miniaturising the fluidic system. Naimushin et al. reported a portable SPR system with a temperature control unit [184]. The flow cell was relatively small, but the Peltier and the pump added considerable bulk to the system. Sook Jin Kim et al reported a portable SPR system with an integrated 8-channel flow cell with Au film array on prism [61]. The sensor assembly has a dimension of 4.5 cm x 2.4 cm x 0.8 cm, but the SPR system without the computer for data analysis is still big enough to qualify only as an integrated benchtop apparatus. Similarly, a four micro-fluidic channel flow cell has been reported by Xiao-ling Zhang et al, but the rest of the system hardly qualifies as integrated or portable [185].

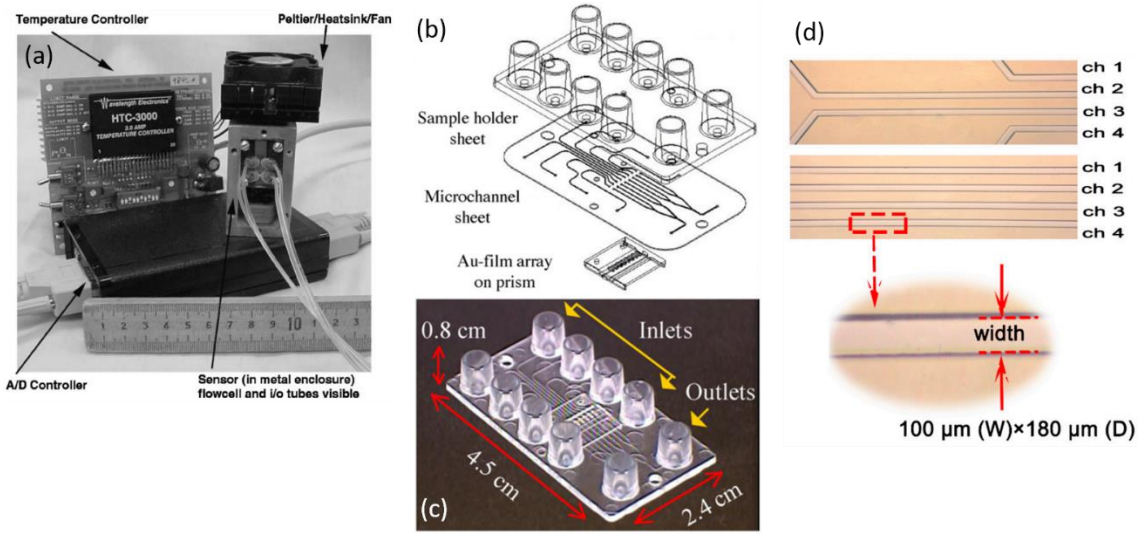

Figure 1.15 Microfluidic devices in SPR sensor systems. (a) SPR system photo in [184], (b) Schematic design and (c) photo of the SPR sensor in [61]. (c) Microfluidic channels in [185].

1.3.3.3 Integrated Data Analysis

Many of the portable systems reviewed above use a computer to analyse the sensor data. Although the SPR instrument may be portable enough to be employed in the field, a portable computer must be present as well for on-site data analysis. The rise of smart phones offers an opportunity for fast on-site data analysis. Hasan Guner reported a

smartphone based SPR biosensor that integrated a green LED light source, the collimation optical components and the sensor chip into a box that could be attached to the back of a smart phone. The back-facing camera on the phone captured images for the smart phone to record and analyse [186].

Among all the SPR systems that we have reviewed, Yun Liu et al. reported a system with the highest degree of integration [187]. They have constructed a two-channel SPR biosensor on a smart phone case which uses the flash light on the phone as the light source, the camera as to capture the signal and the processor of the phone to analyse the data. The majority of the parts that are necessary in an SPR biosensor system have been integrated and miniaturised except the pump.

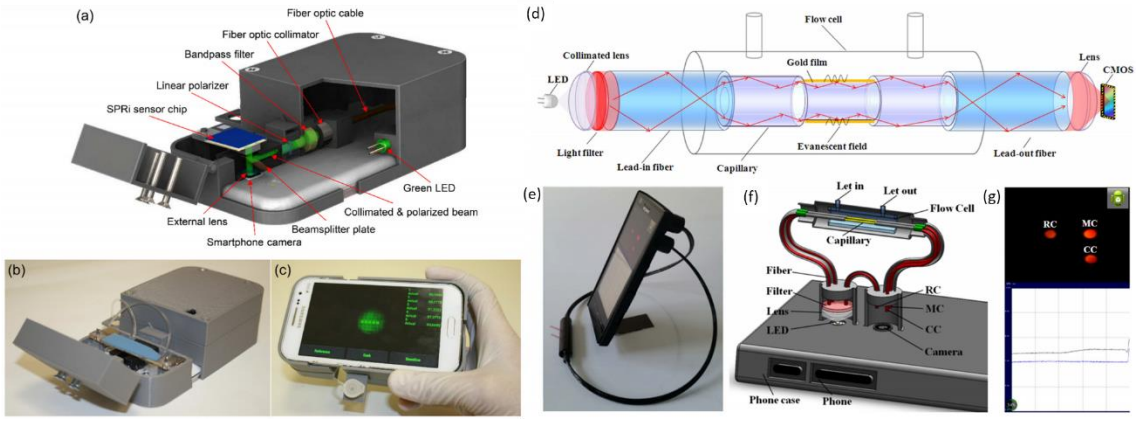

Figure 1.16 SPR sensor systems based on mobile phones for data analysis. (a), (b) and (c) Images of the system with external light source [186]. (d), (e), (f) and (g) Images of the fully integrated SPR system [187].

1.3.4 Combining SPR with Other Analytical Modalities

Besides the employment of SPR in a biosensor directly, SPR has been incorporated in other analytical modalities in recent years. The marriage between SPR and another analytical technique often falls into two research emphases: (1) utilising the physical phenomenon of SPR in another research modality to achieve a higher sensitivity and/or resolution; and (2) concatenating an SPR biosensor together with one or more biosensors using another modality to achieve extra functionalities.

SPR as a physical phenomenon has been most often combined with other spectroscopy techniques. One of the most popular examples is surface enhanced Raman spectroscopy (SERS). The technique pushes a phenomenal spectroscopic signal enhancement in the order of 10^6 for the detection of single molecules [188 – 190]. Similar to the SERS technique, surface-plasmon field enhance fluorescence spectroscopy enhances the sensitivity by several orders of magnitude thanks to the SPPs exciting the chromophore at a specific distance [150, 191, 192].

Concatenating a SPR biosensor with one or more different analytical instruments speeds up and complements the analysis procedure. SPR-mass spectrometry (MS) characterises the activity of a target molecule, which is then recovered for a subsequent MS analysis [193]. Scanning tunnelling microscopy (STM) and atomic force microscopy (AFM) have also been combined with a SPR biosensor to correlate the attachment and positioning of biomolecules [194, 195]. Other biosensing modalities that have been coupled with a SPR biosensors are electrochemical measurement [195 – 197], surface acoustic wave spectroscopy [198 – 201], and quartz micro balances [202].

Sample preparation and separation systems have also been integrated with SPR biosensors but the reports in the literature are limited. Micro-free flow electrophoresis (μ-FFE) has been added to an SPR biosensor on a single chip to streamline separation and detection [203]. Liquid chromatography has been coupled externally in both pre-column and post-column configurations to SPR for separation and detection [204, 205] and an immobilised enzyme reactor has been coupled to add a functionality of online protein digestion [206].

1.4 Silica Particles and SPR Biosensor Integration

In Section 1.3.1.7 the use of overlayers of silica on Au SPR devices was discussed. Due to the ease of synthesis and elaborate knowledge of silane chemistry, silica particles, as well as composite silica particles, have been proven to be an excellent substrate suitable for many surface immobilisation mechanisms. They are widely used in material science, electrochemical and biomedical research. They play a promising roll in drug delivery [207 – 210] and biolabeling [211 – 213] for miniaturisation of conventional bench-top assay systems when combined with microfluidics. Despite the reduced sensitivity reported in Section 1.3.1.7, the versatility of this material warrants further consideration.

Silica microspheres have been used by Xuan Dou et al. as a patterning template in the fabrication of nanodonut arrays on an Au surface [177]. The microspheres were first dispersed in ethoxylated trimethylolpropane triacrylate (ETPTA) and spin-coated on a silicon wafer. The ETPTA monomers were cured by ultraviolet (UV) light and the silica microspheres were fixed in place in the ETPTA. The matrix was then partially removed by an oxygen reactive ion etching (RIE) exposing the top half of the silica microspheres. The spheres were subsequently dissolved in hydrofluoric acid. The nanodonuts were created by sputtering gold on the ETPTA polymer template.

Enso et al used silica nanoparticles as a scaffold for forming a 3-dimensional gold film that was SPR active and used it as a biosensor to detect an antibody/antigen reaction [214] and nucleic acid and DNA hybridization [215]. They first had a layer of gold film evaporated on a glass slide. Silica particles were then immobilised on the gold film by carbodiimide coupling between 3-Aminopropyltriethoxysilane (γAPTES) on the silica surface and 4,4'-Dithiodibutyric acid (DDA) on the gold surface. The particle modified surface was coated with another layer of gold film and ready for use. Essentially, they batch produced a layer of pseudo core-shell particles on a glass slide and used the localised SPR effect for sensing.

To our best knowledge, these demonstrations of the use of silica in SPR devices has not yet been extended to the use of silica particles as carriers for the immobilisation of

biorecognition element in an SPR biosensor. Such a format could lead to the concatenation of SPR with chromatography.

1.5 Aims and Objectives

In this thesis, the integration of silica particles (as an immobilisation matrix) and an SPR biosensor is explored. IgG/anti-IgG interaction is used as a model immunoassay where the IgG acts as the receptor and the anti-IgG acts as the analyte to characterise the performance of the particle-modified sensor.

The thesis has the following objectives:

1. To investigate the direct immobilisation of sub-micron silica particles on a gold film SPR platform to examine:
    a. The particle immobilisation efficiency,
    b. Receptor IgG loading capacity, and
    c. IgG – anti-IgG binding kinetics.

    and thereby consider the impact of a particle system in the evanescent field on the SPR measured reaction between a particle immobilised biorecognition reagent and its analyte.
2. To investigate the use of a micro silica particle column in contact with a gold film SPR platform (Figure 1.17) to examine:
    a. Its capability as a biorecognition ligand carrier in comparison with (1),
    b. The IgG – anti-IgG binding kinetics as measured in the evanescent field by the column and SPR biosensor integration.
3. To explore the potential sensing capability and limitations of the particle-modified column SPR biosensor in an integrated SPR-chromatography platform.

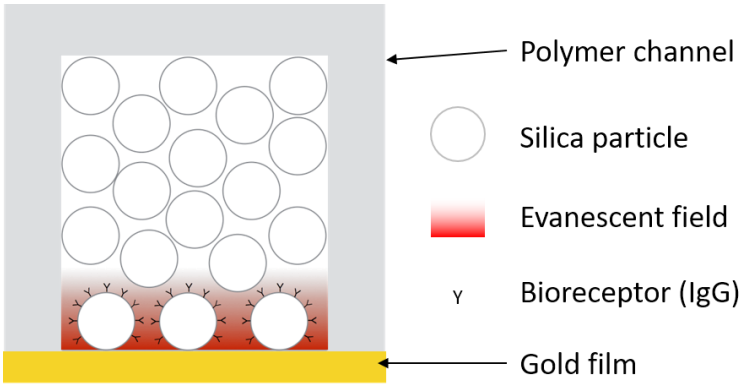

Figure 1.17 Schematic diagram of the particle-modified column SPR biosensor.

Chapter 2 Materials and Methods

2.1 Introduction

This chapter describes the materials and methods used in this project. It consists of six parts: sub-micron silica particle synthesis and characterisation, protein loading on particles, spectral SPR biosensor simulation and instrumentation, SPR imaging simulation and instrumentation, review of adsorption kinetic models and MATLAB data processing tools.

2.2 Sub-Micron Silica Particle Synthesis and Characterisation

2.2.1 Materials

Tetraethyl orthosilicate (TEOS) (98%), (3-Aminopropyl)triethoxysilane (γ-APTES) (> 98%), gold nanoparticles (20 nm), 4,4'-dithiodibutyric acid (DDA) (95%), N-hydroxysulfosuccinimide sodium salt (sulfo-NHS) (98%), N-(3-dimethylaminopropyl)-N'-ethylcarbodiimide hydrochloride (EDC) (98%), isopropanol (99.7%) and ammonia solution (2.0 M in isopropanol) were purchased from Sigma-Aldrich. Unless otherwise stated, water refers to ultra-high purity (UHP) water.

2.2.2 Particles Synthesis

Synthesis of silica nanoparticles is done by the well-established Stöber process [216] which is essentially the reaction between TEOS and water in low molecular weight alcohols catalysed by ammonia. In the Stöber process, two main types of reactions are involved

First, silanol groups are formed by hydrolysis:

$$Si-(OR)_4 + H_2O \leftrightharpoons Si-(OH)_4 + 4\,R-OH \tag{2.1}$$

Second, siloxane bridges are formed by a condensation polymerization reaction:

$$Si-(OH)_4 \rightarrow 2\,(Si-O-Si) + 4\,H_2O \tag{2.2}$$

The condensation rate, which depends on reaction conditions can be tuned to produce particles of sizes ranging from 50 nm to 2 μm [217]. The size of the particles produced by the Stöber synthesis can be controlled by the reaction conditions, including the choice of solvent, the relative concentrations of all the reactants, solvents and catalysts, and finally the duration of reaction. The kinetics have been well modelled and investigated elsewhere [218 – 220].

The sub-micron silica particles are synthesised with a protocol adapted from that used in the BiognostiX project [221]. Water and isopropanol (16.7% v/v) are mixed under constant stirring at 300 RPM in a 500ml conical flask. TEOS (0.5% v/v) is then added to the mixture. After sufficient mixing, ammonia (2% v/v) is added dropwise. After allowing all the reagents to react for 30min, further TEOS (1% v/v) is added drop by drop into the solution. After another 30min, the product is washed in isopropanol under 3 cycles of centrifugation (4300 RPM for 30 mins) and resuspension. Finally, the silica particles are desiccated overnight and ready to be used.

2.2.3 Particle Size Characterisation

2.2.3.1 Scanning Electron Microscopy

All the images in this thesis are obtained using the LEO GEMINI 1530VP FEG-SEM system housed at Nanoscience Centre, Cambridge. The system features a resolution of 1nm and acceleration voltage from 0.1 to 30kv.

The silica particles were first suspended in water (5 mg/ml) and drop-coated on a gold film. The particles were then air dried before use. All the gold films with nanoparticles immobilised on them were cut into suitable sizes and imaged using SEM. The seeming pattern in the dark background is caused by nanoscale roughness of the gold film. This phenomenon has been studied elsewhere [222] and it is not within the scope of this project.

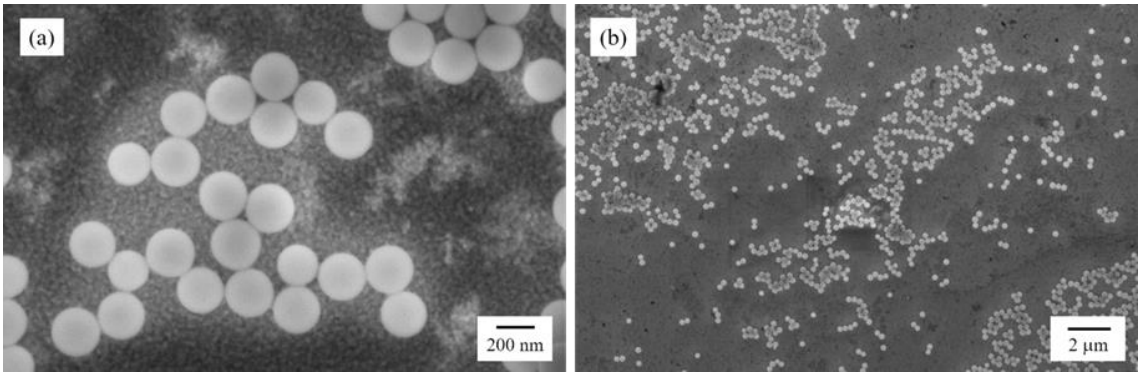

Figure 2.1 Particle characterisation using SEM. (A) A SEM image with high magnification showing the shape and size of the dry particle, (B) An image with lower magnification to show the distribution of the particles on a gold film.

The size of the nanoparticles as well as the percentage of the coverage is determined using image processing software, ImageJ. The particle diameter distribution is plotted in Figure 2.2. It shows that the sizes of the particles follow a log-normal distribution with a mean dry diameter of 245±49.0 nm.

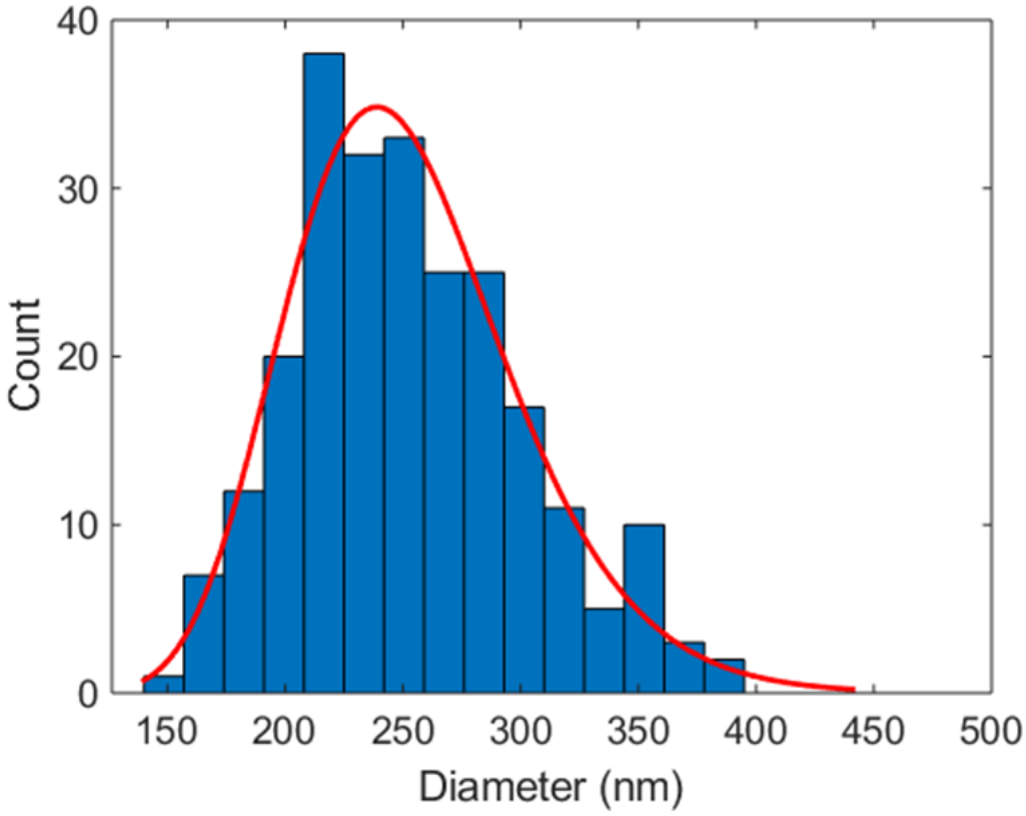

Figure 2.2 Particle size distribution and fitted to a log-normal distribution curve. The particles are sampled from several images taken at various locations and with various zoom.

2.2.3.2 Dynamic Light Scattering

The hydrodynamic size of the particles is characterised by BI-MAS Multi Angle Particle Sizing Option housed in BP Institute [223].

Before each measurement, the particle suspension is vortexed to ensure the particles are evenly suspended in water. The sizing result is shown in Figure 2.3. The DLS sizing option assumes the particle sizes follow a lognormal distribution. The mean hydrodynamic diameter measured is 500 nm. We can see that it differs from the dry size significantly. In the literature, this has been reported as due to the porous structure of the silica particles [224, 225]. As the particles absorb water, the surface of the particle

becomes a cloud-like material, therefore, increasing the apparent size calculated by Stokes-Einstein equation.

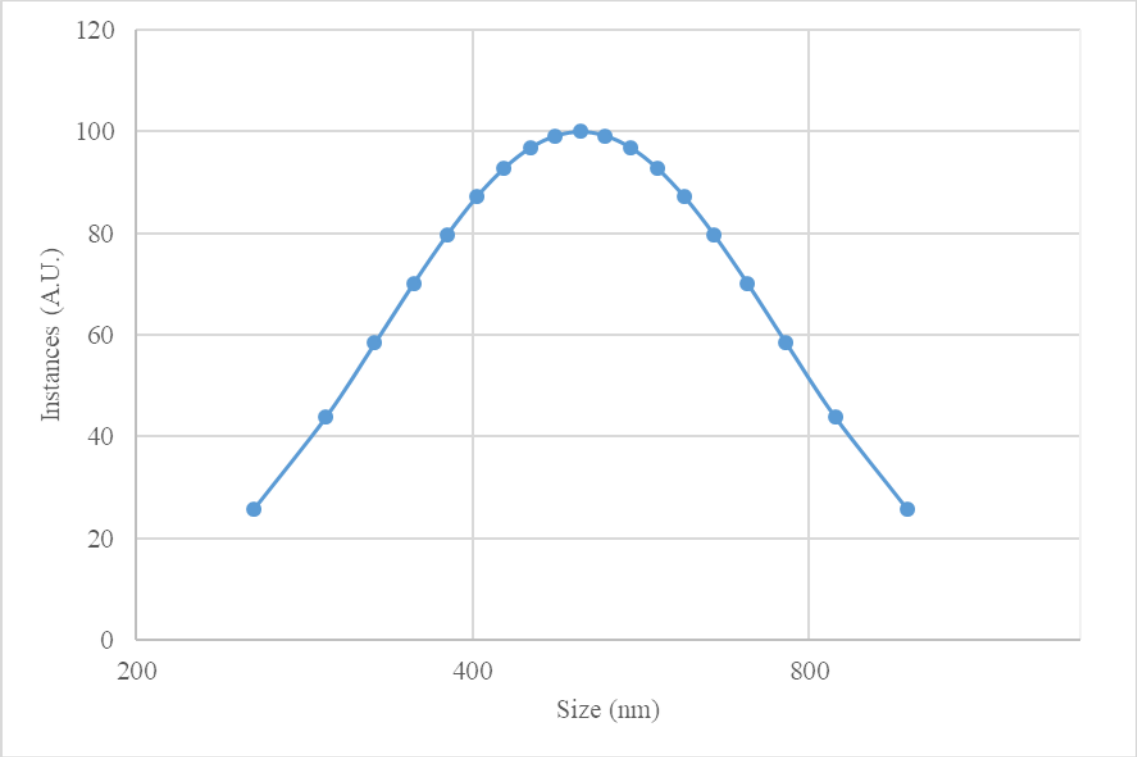

Figure 2.3 Sub-micron particle size distribution obtained from DLS sizing option. The average size is 500nm.

2.3 Protein Immobilisation on Particles and Gold Films

2.3.1 Materials

Silica gel 60 (particle size finer than 0.063mm) from Fluka, IgG from rabbit serum (≥95%) from Sigma-Aldrich, anti-rabbit IgG (whole molecule) antibody produced in goat from Sigma-Aldrich, anti-mouse IgG (whole molecule) antibody produced in goat from Sigma-Aldrich, StabilCoat® Immunoassay Stabiliser from Sigma-Aldrich, Sodium phosphate monobasic dehydrate (≥99.0%) from Sigma-Aldrich, Phosphate buffered saline (PBS) from Sigma-Aldrich, MES monohydrate (≥99.0%) from Sigma-Aldrich, 4,40-dithiodibutyric acid (DDA) (95%) from Sigma-Aldrich, Carboxyethylsilane triol (CEST) from Fluorochem, N-Hydrocysulfosuccinimide sodium salt (sulfo-NHS) (≥98%) from Sigma-Aldrich, N-(3-Dimethylaminopropyl)-N'-ethylcarbodiimide hydrochloride (EDC) from Sigma-Aldrich, Ultrahigh purity (UHP) water.

2.3.2 Immobilisation of IgG on Silica Particles

2.3.2.1 Adsorption

Synthesized silica particles were dispersed in PBS buffer to make 5 mg/ml suspension. A small volume of rabbit IgG (5 mg/ml in PBS) was added to each of the particle suspension at 4 °C to make 1 ml of rabbit IgG and particle mix at desired final concentrations ranging from 100 µg/ml to 1 mg/ml. The suspensions were then fixed on a rotational mixer under gentle speed and incubated for 1 hour at 4 °C. Finally, the suspensions were washed three times with PBS buffer and stored at 4 °C.

2.3.2.2 Covalent Attachment

For covalent attachment, the abundant free amine groups on the surface of IgG were targeted. IgG and anti IgG can be immobilised on a surface by strong carbodiimide links when the amine groups on the antibody condenses with the carboxylic acid groups on the other surface and form carbodiimide links [226]. Carboxyethylsilanetriol (CEST) was

used to functionalise the silica surface with carboxylic acid groups. An illustration of the covalent attachment is shown in Fig. 2.6.

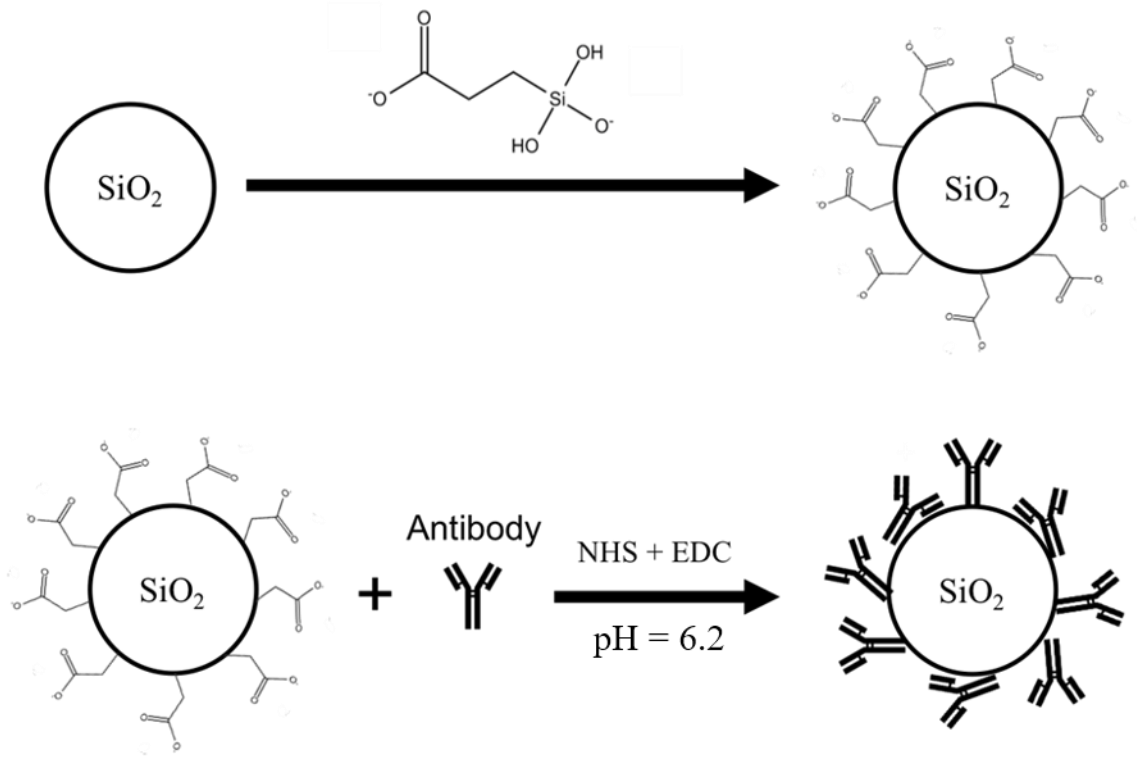

Figure 2.4 Illustration of the steps for immobilisation of antibodies on the surface of silica particles. The diagram is not drawn to scale.

Silica particles were dispersed in 1 ml of phosphate buffer solution (pH = 6.2) to make suspensions of a desired concentration. For synthesized sub-micron silica particles, the final concentration was 5 mg/ml and for the purchased silica gel particles, it was 50 mg/ml. 100 µl of CEST was added to 1 ml of the particle suspension and gently mixed on a rotational mixer overnight at 4 ºC. The next day, the suspension was washed with phosphate buffer solution three times using centrifugation (4300 RPM for 30min) and resuspension with sonication cycles. 10 µl of freshly prepared sulfo-NHS solution (230 mM, 50 mg/ml) was added into the suspension and mixed by a vortex mixer. Then 10 µl of freshly prepared EDC solution (260 mM, 50 mg/ml) was added into the suspension and mixed using a rotational mixer for 20 min at 4 ºC to activate the carboxyl groups on the surface of the particles. The activated particles were then washed with MES buffer

solution (pH = 5.0) three times using centrifugation (4300 RPM for 30min) and resuspension with sonication cycles. Concentrated IgG solution was added to the suspension to achieve a desired IgG concentration in the suspension and mixed on a rotational mixer for 2 hrs at 4 ºC. The IgG immobilised particles were washed three times with MES buffer solution (pH = 5.0) using centrifugation (4300 RPM for 30min) and resuspension with sonication cycles. The particles were then dispersed in 1 ml StabilCoat blocking mix (25%) and mixed on a rotational mixer for 2 hrs at 4 ºC to prevent unwanted unspecific binding. The blocked particles were washed three times with PBS buffer solution (pH = 7.4) using centrifugation (4300 RPM for 30min) and resuspension with sonication cycles. Finally, the particle suspension was stored at 4 ºC.

2.3.3 Immobilisation of IgG on Gold Films

To immobilise IgG proteins, the gold film was first treated with a 0.5% (w/w) 4,40-dithiodibutyric acid (DDA) ethanol solution for 48 hours at room temperature. The modified gold film was then washed 5 times using ultra-pure water. 100 µl of freshly prepared sulfo-NHS solution (50 mg/ml in UHP water) was dropped onto the gold film. Then 100 µl of freshly prepared EDC solution (50 mg/ml in UHP water) was added. The gold film was allowed to rest for 20 min at 4 ºC to activate the carboxyl groups on the surface of the film. The film was then washed with MES buffer solution (pH = 5.0) for 5 times. Concentrated IgG solution was dropped onto the activated film and rested for 2 hrs at 4 ºC. The film was washed 5 times with PBS buffer solution (pH = 7.4). Finally, the gold film was stored at 4 ºC.

2.4 Spectral SPR Refractive Index Sensing

2.4.1 Materials

Benzyl alcohol was purchased from Sigma-Aldrich. Gold powder (99.9994% purity) was purchased from Alfa Aesar. Chromium plated tungsten rods from Megatech. Glass microscope slides from VWR. Unless otherwise stated, water was MilliQ pure water.

2.4.2 Instrumentation

Tungsten halogen white light source from Ocean Optics, USA. Computed controlled rotation stage for optical components from Standa Ltd, Italy. USB4000 miniature fibre optical spectrometer from Ocean Optics, USA. Peristaltic pump (Model number 7521-35) from Cole-Parmer Instrument Co., USA. MATLAB software from MathWorks, USA.

2.4.3 Optical Set-up

A custom-made spectral SPR setup was used to perform all the measurements. The schematic illustration of the set-up is shown in Figure 2.5. The tungsten halogen white light source was implemented to generate a broad-band illumination. An optical fibre was used to collimate the light from the source into a beam (1 mm in diameter) and deliver it to other optical components. The collimated light passes through a polarizer and an iris then incident on the prism and then coupled to the gold film surface through benzyl alcohol and the glass substrate in the Kretschmann configuration. The prism and gold chip are held with a custom-made scaffold with a flow cell (1 cm in diameter, 1 mm in height) attached to the sensing side of the gold film. During the measurement, water is flowed continuously into and out of the flow cell by a peristaltic pump. The prism and flow cell assembly are fixed on the rotation stage with angle adjustment. The reflected light beam was collected by the spectrometer through an optical fibre. The spectral data is processed in real time by a custom-written control software on a computer. The reflection spectra are captured by a spectrometer 4 times every second and subsequently analysed by a computer to obtain the peak wavelength. The peak absorption wavelength in the reflected

spectrum was determined by a Lev-Mar non-linear curve fitting algorithm. All peak wavelengths together with their timestamps are recorded by the computer and stored in a text file ready for subsequent processing. MATLAB is used to process the raw data and plot it into a sensorgram. To reduce the noise of the raw signal, a moving average algorithm that uses a span of 1% of the total number of data points is employed.

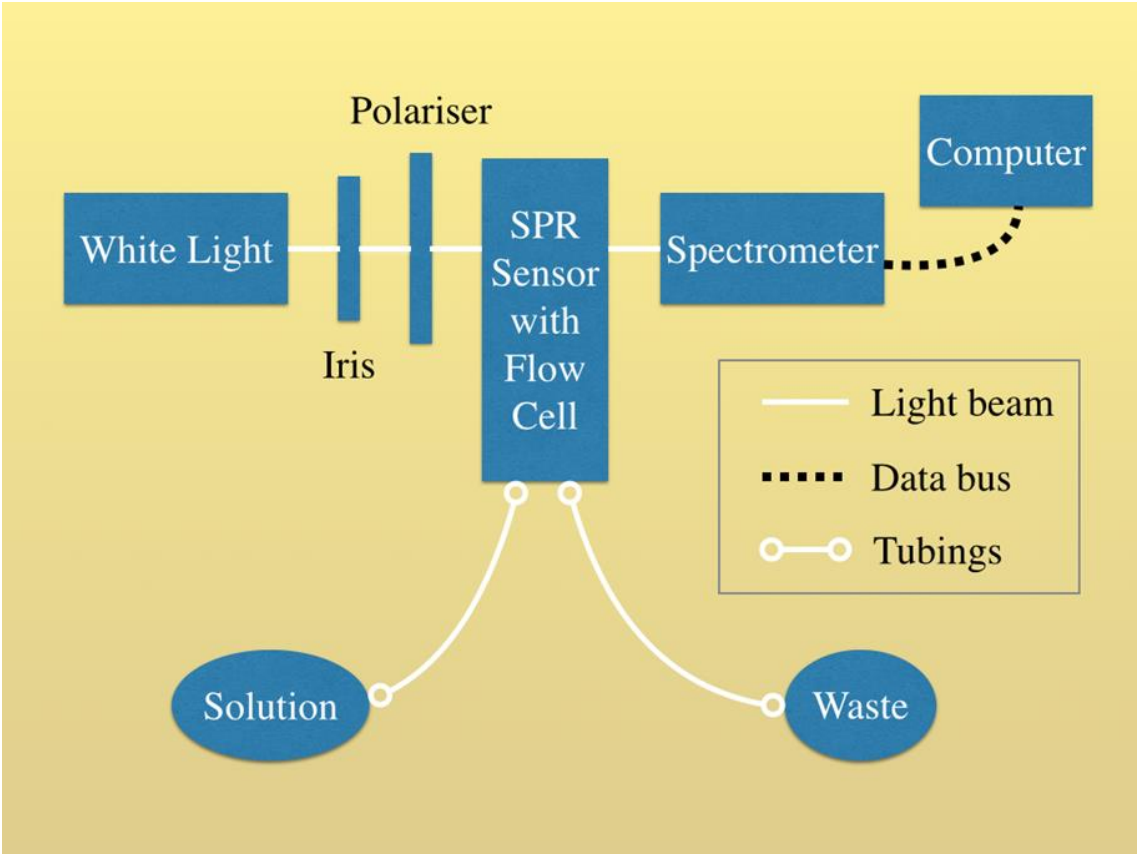

Figure 2.5 Schematic illustration of the custom-built SPR measurement system with a fluidic system. The diagram is not drawn to scale.

2.4.4 Spectral SPR Simulation and Optimisation

A one-dimensional three-phase stratified medium model consists of glass, gold and water is employed in the simulation. Figure 2.6 shows an illustration of the 3-layer model used for simulation, which is carried out using MATLAB.

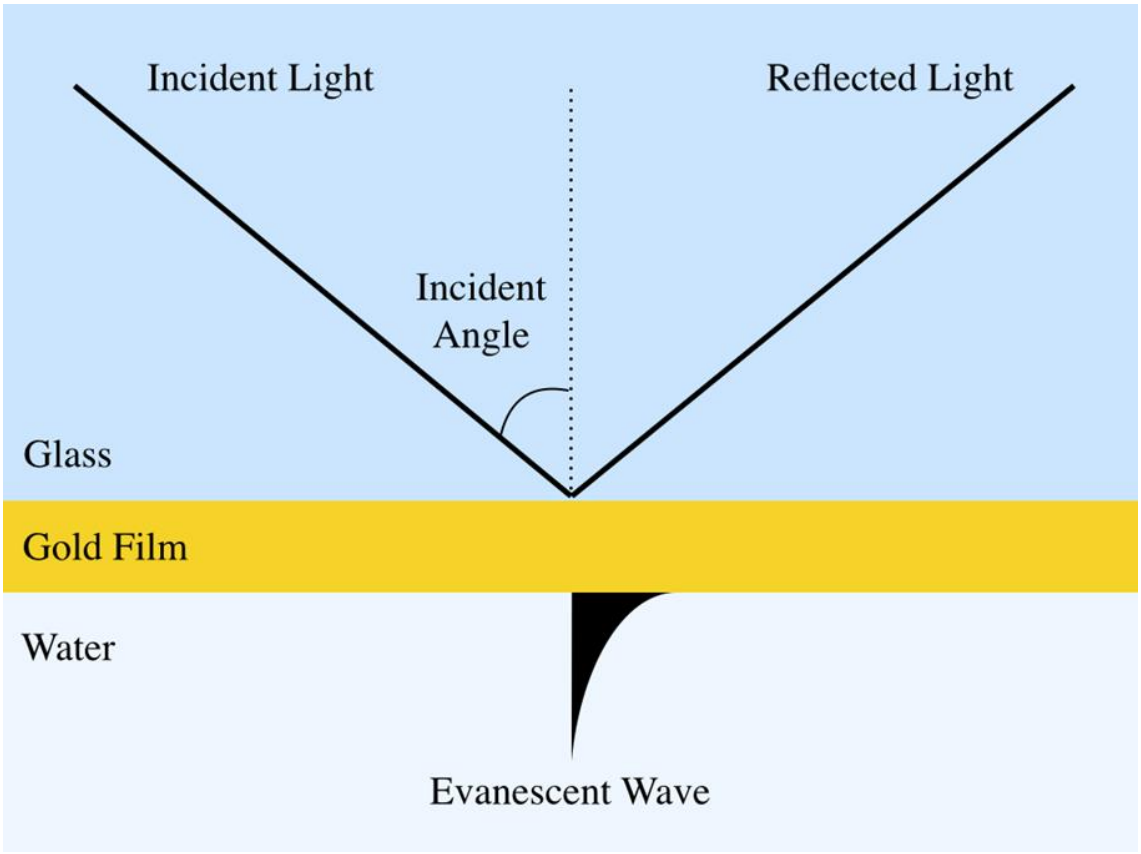

Figure 2.6 Schematic depiction of three-phase stratified medium model and incidence and reflection of a white light beam.

The wavelength-dependent refractive index of gold, glass and water used in the simulation is from the experiments of Rakić [227]. The thickness of the glass and water medium that sandwiches the gold film is assumed to be infinite. The partial transmission and reflection of a wave incident on any of the interfaces are calculated using the Fresnel equation. The reflectance for s-polarised light is

$$R_s = \left| \frac{n_1 \cos\theta_i - n_2 \cos\theta_t}{n_1 \cos\theta_i + n_2 \cos\theta_t} \right|^2 \tag{2.3}$$

where n refers to the refractive index and θ refers to the angle of incidence/reflection. The resultant reflectance is a fraction of power with respect to the incident light which has values between 0 and 1. The full 3-layer MATLAB script can be found in A.1.

The occurrence of the attenuated reflection depends on several parameters such as the incident angle, wavelength of the incident light, thickness of the stratified medium and the refractive index of each medium. For each of the SPR surfaces fabricated and used in sensing experiment in this project, the thickness of the gold film is fixed and determined by the deposition process. The refractive index of glass, gold and water are intrinsic properties of the material. The only two variables that affect the SPR response are the angle of incidence and the wavelength of the incident light. Here, a simulation on gold film of 55 nm is presented.

Figure 2.7 shows a simulated heat map detailing the reflectance with respect to the incident angle and the wavelength of incident light. Colder colours indicate attenuation in the reflectance which is caused by SPR. For a fixed thickness of gold film, 55nm in this case, discernible SPR occurs at angle and wavelength combination of 66% to 85% and 570 nm to 850 nm. The most significant SPR which is indicated by near black colour in the heat map occurs at angle and wavelength combination of 70% to 77% and 620 nm to 710 nm. For the surface polaritons to be sensitive to change of refractive index in the dielectric medium, two modulations are possible namely fixed wavelength of the incident light with variable incident angle and fixed incident angle with variable wavelength of the incident light.

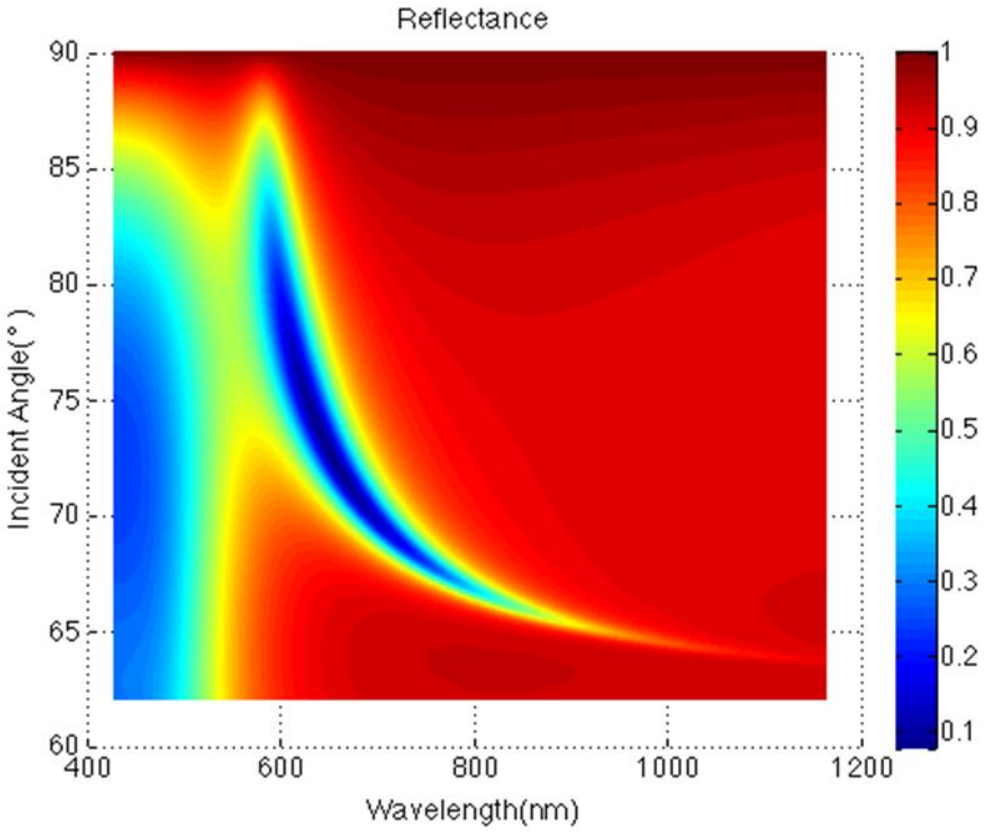

Figure 2.7 Simulated heat map showing reflectance with respect to incident angle and wavelength of the incident white light.

The wavelength modulation is chosen for all the spectral SPR experiments performed in this project, for its simplicity as mentioned in Section 1.2.2. Fast readout also allows for easier post processing in the kinetics study. In practice, the incident angle for all measurements was fixed at 72.99°. Standard white light that covers the visible light spectrum (400 nm to 700 nm) was utilised as the light source.

The thickness of the gold film layer was optimised by simulating the spectral SPR response at various gold film thickness and plotting it in the same graph for comparison. Figure 2.8A shows the reflectance spectra for a range of layer thicknesses of gold film. At different thickness, the SPR phenomenon is of different significance. At the thickness of approx. 45nm to 55nm, the reflectance attenuation has the lowest minimum. Therefore, the thickness of the gold film in all the experiments that follow is controlled within this range.

It is noteworthy to mention that the position of the peak attenuation is at different wavelengths although the dielectric medium is unchanged (Figure 2.8A). This is used to calibrate the thickness of the gold layer deposited in practice. To do that, the experimental reflectance spectrum is first obtained, a theoretical position of the attenuation peak is then aligned to the experimental data by altering the thickness parameter in the simulation.

Figure 2.8B shows the theoretical reflectance spectrum for a 55 nm thick gold film fitted to the experimental data. The peak wavelength here is at 645 nm. There are several other observations when comparing the theoretical and experimental curve.

Firstly, the reflectance spectrum is noisy at lower (< 550 nm) and higher (> 750 nm) wavelengths. This can be attributed to the imperfection of the white light source. Ideally, the power spectrum of the light source is a flat line across all visible wavelengths. However, in practice, attenuated power is observed at lower and higher wavelengths. Thus, when calculating the reflectance by normalising the collected power spectrum by the source power spectrum, noise due to the smaller denominator becomes more significant.

Secondly, the peak attenuation does not go down to a value as low as the theoretical expectation and the FWHM is wider than expected. This can probably be attributed to the surface roughness of the deposited gold layer as observed in Figure 2.1A. Since the surface is not perfectly smooth on the nanoscale, the resonance of the polaritons is affected slightly by scattering.

Thirdly, cracks of the gold surface also caused a small second dip at approx. 490 nm due to the resonant adsorption of gold films [228]. The dip position is independent of the crack sizes and dielectric indices of the surrounding media. The simulation was based on a smooth film; therefore, the second dip was not present in the simulated spectrum.

Nonetheless, these imperfections are acceptable in the measurements within the scope of this project where only the position of the large dip is of concern. The noise level is relatively low at resonance wavelength and the significance of the peak attenuation is good enough to be distinguished from the rest of the curve.

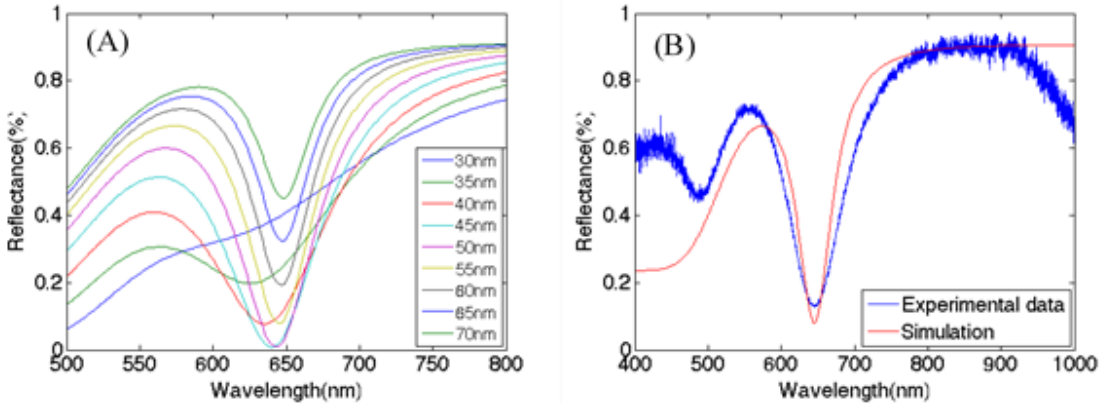

Figure 2.8 (A) Simulated ATR at various gold film thickness. (B) the comparison between theoretical and experimental reflection spectrum for 55 nm gold film. The experimental data is normalised with respect to halogen white light.

2.4.5 Gold Film Deposition

Gold films were fabricated using thermal evaporation, one of the most common physical vapour deposition methods. The system used in this thesis is an Edwards Auto 306 filament thermal evaporator. The gold film was prepared by thermally evaporating molten gold onto glass slides inside a high vacuum chamber. Three 25 mm by 75 mm glass slides were held inverted in the substrate holder. Before the evaporation of gold, 0.5 nm of chromium was first deposited on the glass to ensure film adhesion. Gold was evaporated subsequently into a vapour stream that traversed the chamber and hit the glass substrate, sticking to it as a film. During the deposition process, a film thickness monitor (FTM) measured the thickness of the film by calculating the mass of the material deposited on the sensor of a fixed surface area. One important thing to note is that the FTM is not necessarily on the same uniformity plane of the substrate (Figure 2.9). Therefore, the actual deposited thickness does not necessarily equal the thickness displayed, but is proportional to it. Various portions of the glass slides are not in the same uniformity plane as well, thus the thickness of the gold is slightly different at different positions on the glass substrate. This results in a different baseline in the ATR experiments.

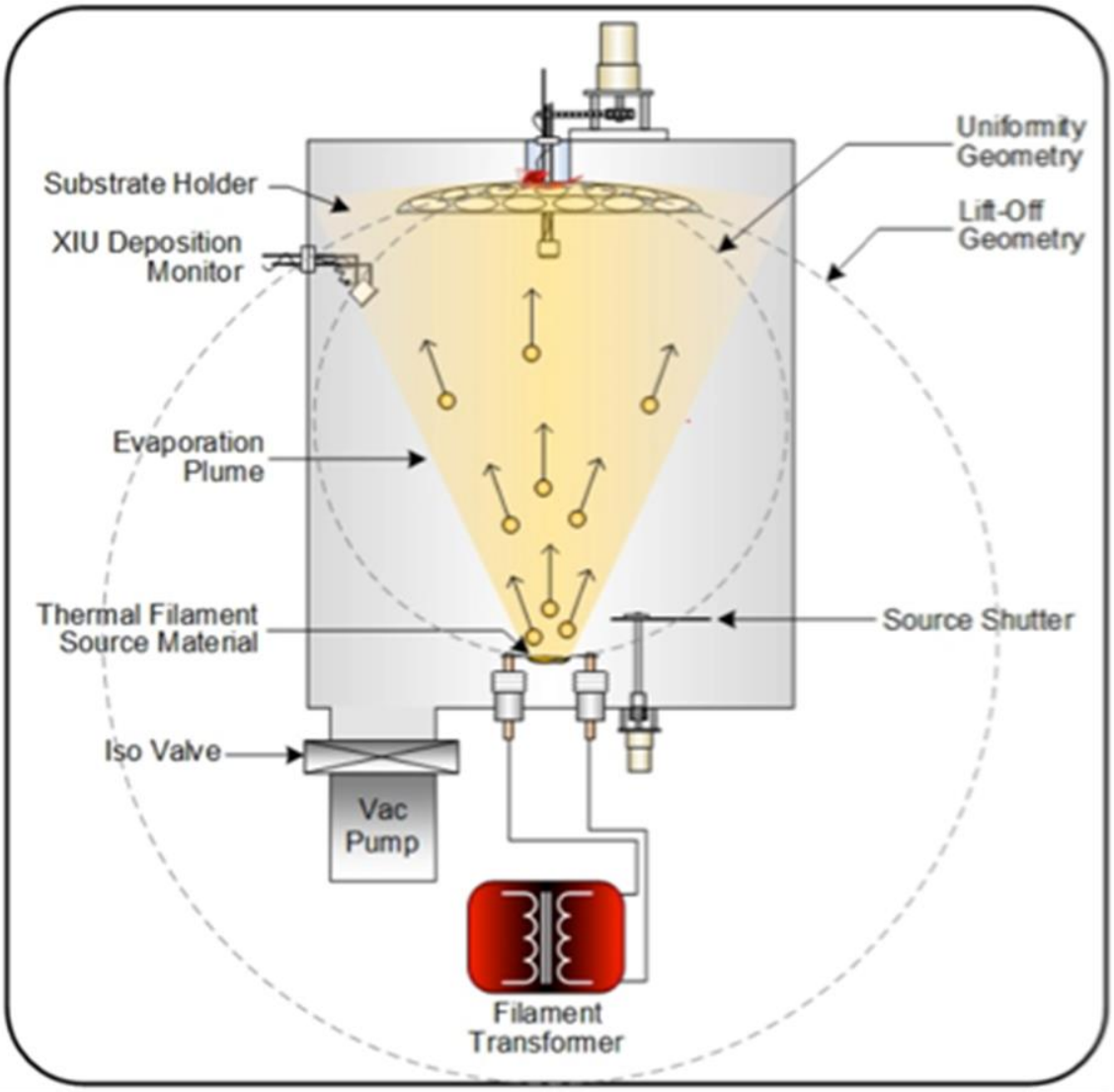

Figure 2.9 Schematic diagram of a thermal evaporator process. The diagram is not drawn to scale. Image reproduced from [229].

Glass microscope slides were cleaned with surfactant, water and ethanol in sequence in an ultrasound bath for 30 minutes each and dried in room temperature. They were kept in the oven at 120 °C overnight before use. 55 nm thick gold films were deposited onto glass substrates at a pressure of 2×10^{-6} mbar. To help gold adhere onto the glass substrate, 0.5 nm film of chromium was deposited before evaporation of gold. All gold films were rinsed with ethanol and dried with nitrogen gas at room temperature before use.

2.5 Column-modified SPR Sensor

2.5.1 Materials

Silica gel 60 (particle size finer than 0.063mm) from Fluka, IgG from rabbit serum (≥95%) from Sigma-Aldrich, Anti-Rabbit IgG (whole molecule) antibody produced in goat from Sigma-Aldrich, Anti-Mouse IgG (whole molecule) antibody produced in goat from Sigma-Aldrich, StabilCoat® Immunoassay Stabiliser from Sigma-Aldrich, Sodium phosphate monobasic dehydrate (≥99.0%) from Sigma-Aldrich, Phosphate buffered saline (PBS) from Sigma-Aldrich, MES monohydrate (≥99.0%) from Sigma-Aldrich, Carboxyethylsilane triol (CEST) from Fluorochem, N-Hydrocysulfosuccinimide sodium salt (sulfo-NHS) (≥98%) from Sigma-Aldrich, N-(3-Dimethylaminopropyl)-N'-ethylcarbodiimide hydrochloride (EDC) from Sigma-Aldrich, polydimethylsiloxane (PDMS) from Sigma-Aldrich, Ultrahigh purity (UHP) water.

2.5.2 PDMS Channel Fabrication

The channel was constructed from polydimethylsiloxane (PDMS) for its flexibility and ease of manufacture. The PDMS monomer was mixed thoroughly by stirring with the curing agent with a ratio of 10 to 1 by weight. The mixture was then poured into a small petri dish that contains the aluminium mould such that the mould was only just submerged in the mixture. The petri dish was then placed in a vacuum chamber to degas. In this process, all air bubbles that were introduced during the stirring escaped the mixture. The end of the process could be visually confirmed when the PDMS became clear with no bubbles in the mixture. Any foam on the surface was destroyed automatically when the vacuum is removed. The petri dish was then removed from the chamber and placed in an oven for at least 3 hours at 80 ºC. After that, the PDMS became a solid and it was taken out of the petri dish carefully. Any excess was trimmed off and a channel as shown in Figure 2.10 was obtained.

2.5.3 Assembly and Adjustment

A gold film on glass (25 mm x 25 mm) chip was rested on the PDMS channel scaffold with the gold side touching the PDMS. A droplet of 5 µl of benzyl alcohol was introduced on the centre of the bare side of the chip. Then the prism was pressed on the bare side of the chip so that the droplet of benzyl alcohol spread to fill the entire gap between the prism and the bare side of the chip. Figure 2.10 shows a picture of the completed assembly. The sensor and channel assembly were then fixed on the rotation stage. Water was pumped into the channel for calibration so that the resonance peak is at approx. 650 nm by adjusting the rotation stage and therefore the incident angle.

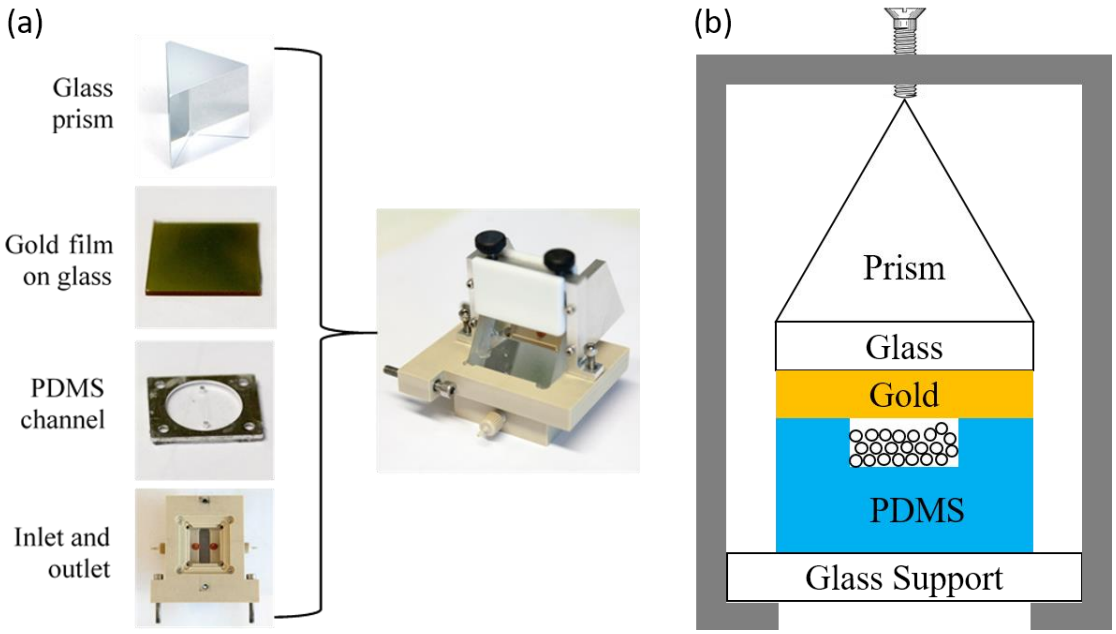

Figure 2.10 (a) Photos showing each component in the sensor assembly and the finished assembly. (b) Schematic side view of the SPR biosensor assembly.

2.5.4 Silica Gel Particle Packing

The slurry technique was used to achieve a packed particle bed in the channel. Before the assembly of the gold film and the PDMS channel, a filter with a pore size of 11 µm was fixed at the outlet of the channel to trap the silica gel particles of a mean size of 15 µm.

The suspension of silica gel particles immobilised with IgG beforehand (50 mg/ml) was vortexed to allow the particles to disperse before use. After assembly of the channel and sensor, 200 µl slurry was injected using a syringe into the channel under high pressure and high flow rate. 2 ml of PBS buffer solution was used to wash the channel under working flow rate and pressure to stabilise the particles and to wash away any free ligands in the particle bed. At the end of the buffer wash, the sensor was ready for affinity tests.

2.5.5 Immunoaffinity Column Test

Immunoaffinity column tests in this thesis were done under pressurised flow at constant flow rate using the peristaltic pump All solutions flow into the system without any air gap in between. Before the start, the packed particles in the channel were under constant flow of PBS buffer solution for stabilization. At the start of the experiment, 1ml of StabilCoat® (25% in PBS buffer solution) was flowed into the column. 3 ml of PBS buffer solution was then used to wash the column to get rid of any unbound molecules. 500 µl of sample with concentrations ranging from 50 µg/ml to 300 µg/ml was then flowed in the column before the column was washed with PBS buffer solution again.

2.6 One-dimensional SPR Imaging

2.6.1 Materials

Benzyl alcohol was purchased from Sigma-Aldrich. Gold powder (99.9994% purity) was purchased from Alfa Aesar. Water refers to MilliQ purity water.

2.6.2 Instrumentation

N-BK7 Bi-Convex Lens, Ø1", f = 150.0 mm, uncoated from THORLABS. 650 nm He-Ne laser pointer from Deli. USB 2.0 CMOS camera, 1280 x 1024, monochrome sensor from THORLABS. Laser Line Generating Lens, 30° Fan Angle, N-BK7 from THORLABS.

2.6.3 Optical Set-up

The custom-made laser line SPR imaging system illustrated in Figure 2.11 comprises four sections namely the optics, the fluidics assembly, the detector and the data analysis end. The optics include a low-cost laser pointer that emits a red beam at approx. 650 nm, a neutral density filter that decreased the intensity of the laser, a polariser, a laser line generator that scatters the beam horizontally to form a line of a span of 30°, a lens that collimates the spreading line beam to a parallel line beam and finally an iris that limits the line to a length suitable to the dimensions of the sensor assembly. The fluidics assembly is essentially the same as the one used in the spectral SPR sensor system. It has a prism, a channel made of PDMS, a gold film on glass and a plastic holder that secures all the components. The detector is a CMOS camera to capture the reflected line from the sensor assembly. It can capture single images and record a video continuously. The data analysis is done with a computer to analyse the intensity profile across the reflected line and to generate time plots.

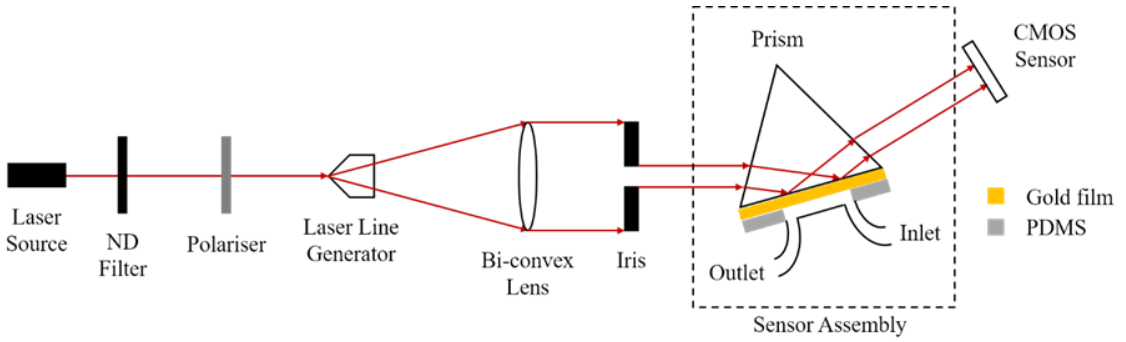

Figure 2.11 Schematic diagram of the one-dimensional SPR imaging platform. The diagram is not drawn to scale.

2.6.4 Laser Line Characterisation

The laser line generating lens ideally spreads the laser beam into a line of uniform intensity. However, the line has an intensity profile shown in Fig. 2.16. We can determine the intensity profile of the final line we get past the iris by calculating the perspective θ_{iris} of the line knowing length of the iris opening D_{iris}, the focal length of the convex lens and its distance from the laser generating lens f_{CL}.

$$\theta_{iris} = 2\tan^{-1}\left(\frac{D_{iris}}{2f_{CL}}\right) \tag{2.4}$$

The perspective is therefore calculated to be 1.91°. At this perspective and assuming the iris is at the centre of the line, the lowest normalised intensity is 0.735 and the highest is 0.765. The intensity variation is about 0.03 normalised intensity which is about 4% relative to the highest point on the line that passes the iris. The calculation has the assumption that the laser beam itself has uniform intensity ideally. However, the laser beam produced by the laser pointer has subjective speckles. Spatial filters can eliminate the speckles but add much more cost and complexity to the system. Besides the variation that can be attributed to the line generating lens, there are laser speckles on a microscopic level. That contributes to an intensity variation across the channel at a higher frequency shown in Fig. 2.17. This intensity fluctuation is fixed with position on the projection of the laser line. This means that the intensity at a position does not change much across

time. The intensity fluctuation across the line can be alleviated by taking the differential measurement along the temporal axis. Since the shift in the signal reflects the change of the refractive index, all the SPR imaging data shown in this thesis is processed as the difference from the baseline profile where the experiment starts.

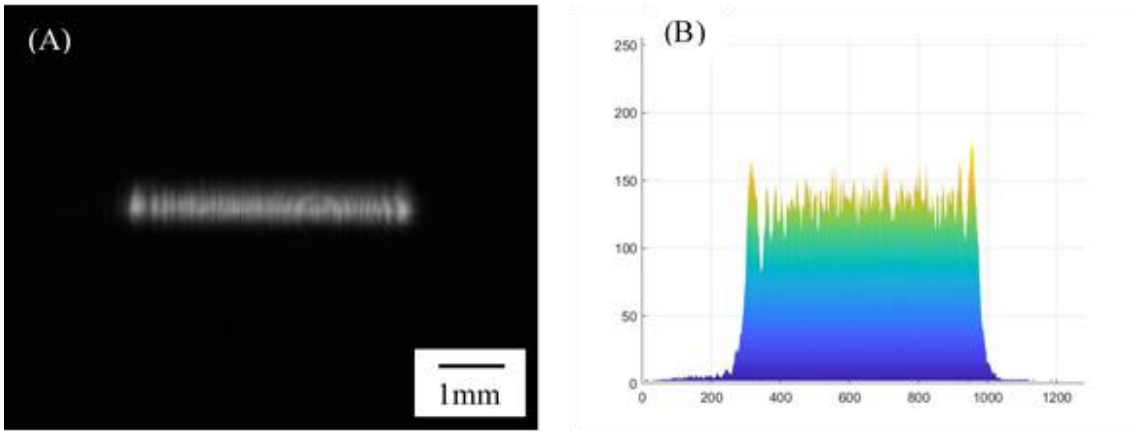

Figure 2.12 The intensity profile of a reflected laser line when the channel is filled with air (no attenuated reflected). (A) shows the image captured by the CMOS sensor. (B) shows the intensity plot of across the line.

2.6.5 Intensity Profile

Figure 2.13 shows the intensity profiles obtained as result of the one-dimensional SPR imaging system. The intensity profile is created by stacking all the intensity information along the laser line against time, resulting in a heat map. The differential intensity profile shows the change in intensity from the start. Due to possible fluctuations of the laser intensity from one experiment to another, the intensity data are normalised to the intensity without attenuation before cross comparison.

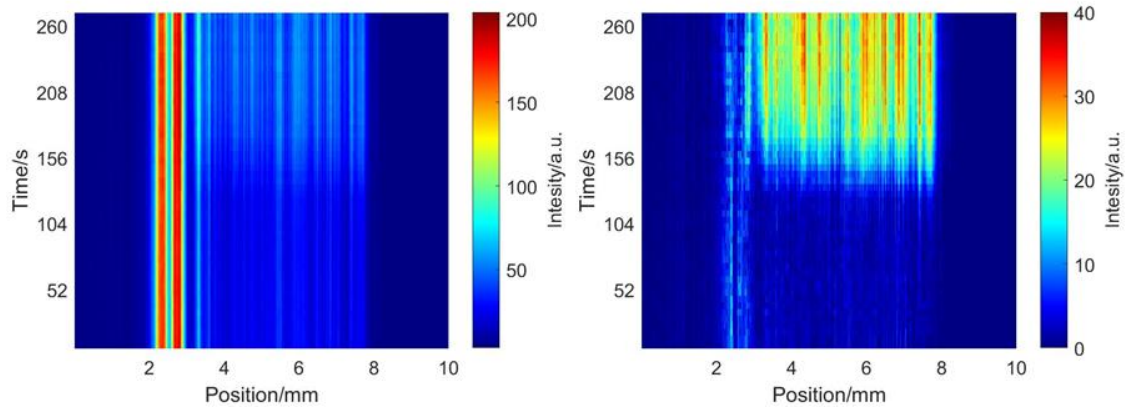

Figure 2.13 Intensity profiles showing the calibration using 5% glucose solution. (A) Raw intensity profile. (B) Differential intensity profile.

2.6.6 Bulk Sensitivity

The one-dimensional SPR imaging system was tested for its sensitivity towards refractive index change in the bulk using glucose solution of unknown concentration. The intensity change is found out to have a linear relationship with the concentration of the glucose. Using the refractive index for known concentrations of glucose solution as reported in [230], the sensor's sensitivity towards bulk medium is calculated to be 13.07 A.U./RIU.

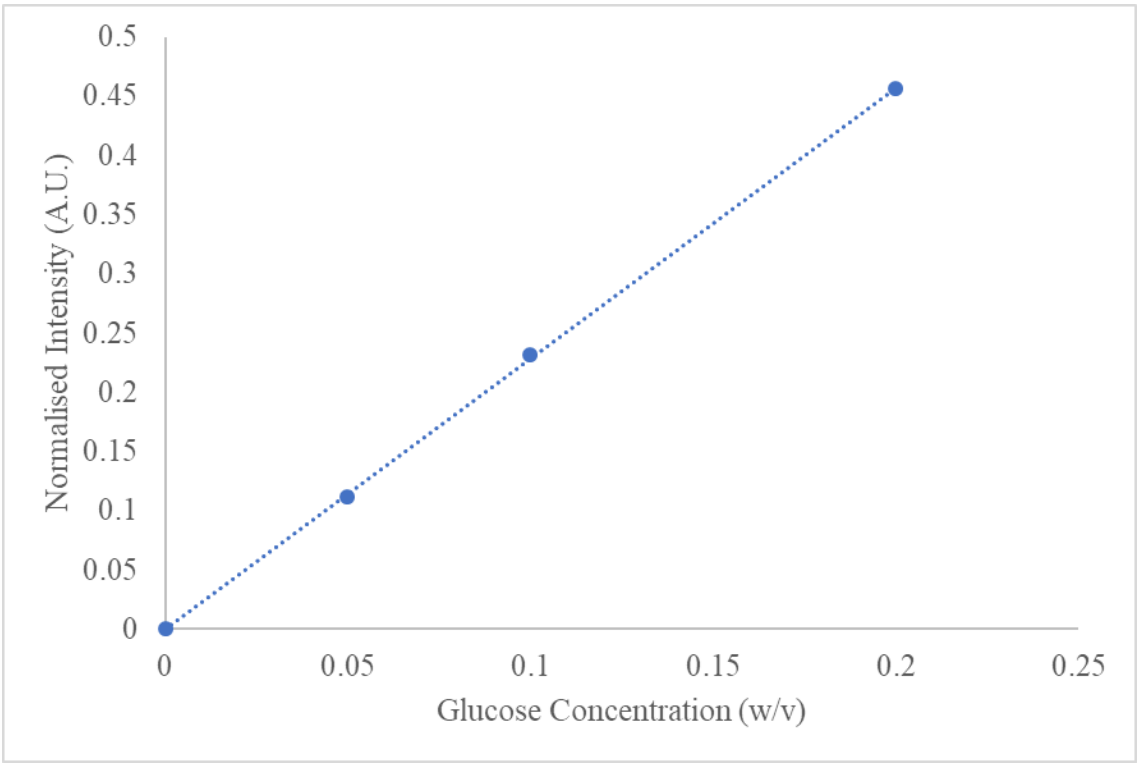

Figure 2.14 Bulk sensitivity towards various concentrations of glucose solution.

2.7 Adsorption Kinetic Models

2.7.1 Langmuir Model

The adsorption of IgG and anti IgG pairs near the surface of the particle-modified SPR sensor is extensively studied in this thesis. The Langmuir model is perhaps the most popular kinetic model for antigen and anti-body binding [231]. It is described by the following reversible model:

$$S + M \rightleftharpoons SM$$

The model has the following four assumptions:

1. The surface of the adsorbent is uniform, that is, all the adsorption sites are equivalent.
2. Adsorbed molecules do not interact.
3. All adsorption occurs through the same mechanism.
4. At the maximum adsorption, only a monolayer is formed: molecules of adsorbate do not deposit on other, already adsorbed, molecules of adsorbate, only on the free surface of the adsorbent.

The rate equation is:

$$\frac{dQ}{dt} = k_a c_0 (Q_{max} - Q) - k_d Q \tag{2.5}$$

The closed form is:

$$Q = Q_{max}\left(\frac{k_a c_0}{k_a c_0 + k_d}\right)\left(1 - e^{-(k_a c_0 + k_d)t}\right) \tag{2.6}$$

where Q is the quantity adsorbed on the adsorbent surface, Q_{max} is the maximum theoretical adsorbed quantity, k_a is the association rate, k_d is the dissociation rate and c_0 is the analyte concentration in bulk. This model assumes that after a brief transient, during

which the analyte is transported to the surface, no mass transport correction is needed, because the free analyte concentration remains uniform in space and constant in time, kept so by the continuous influx of new analyte. Thus, it is termed as the rapid mixing model [232].

2.7.2 Langmuir Model with Mass Transport

In the Langmuir model, the concentration of the adsorbate is assumed to be constant. However, binding of antigen and antibody often happens at a surface where the capture ligand is immobilised. In such a scenario, the rate of the binding and dissociation may be limited by the binding reaction itself or by mass transport to the surface (Figure 2.15) [233]. Adding the rate equation for the mass transfer to the surface we have a modified Langmuir model, also known as the two-compartment model, as follows [232]:

$$\frac{dQ}{dt} = k_a c_s (Q_{max} - Q) - k_d Q \tag{2.7}$$

$$\frac{dc_s}{dt} = k_{tr}(c_0 - c_s) - \frac{dQ}{dt} \tag{2.8}$$

where c_s is the concentration of the analyte at the surface of the adsorbent, k_{tr} is the mass transfer rate from the bulk medium to the surface. The initial conditions are $Q(t_0) = 0$, $c_s(t_0) = 0$.

The ordinary differential equation system does not have a closed form. It is solved and subsequently fitted to experimental data using MATLAB approximation algorithms.

A quasi-steady-state approximation can be made if we set $\frac{dc_s}{dt} = 0$. Eq. (2.8) then becomes

$$c_s = \frac{k_d Q + k_{tr} c_0}{k_a (Q_{max} - Q) + k_{tr}} \tag{2.9}$$

Substituting this expression for c_s into eq. (2.7), we obtain

$$\frac{dQ}{dt} = \frac{k_a c_0 (Q_{max} - Q) - k_d Q}{1 + \frac{k_a (Q_{max} - Q)}{k_{tr}}} \tag{2.10}$$

Eq. (2.10) has been widely used in the literature as a mass-transport-adjusted Langmuir adsorption model because it has the same form as the simple Langmuir and the true rate constants can be found by an easy transformation of the apparent ones. However, the justification of the quasi-steady-state approximation requires the assumption that when binding or dissociation is initiated, c_s changes rapidly over a short period of time and slowly thereafter.

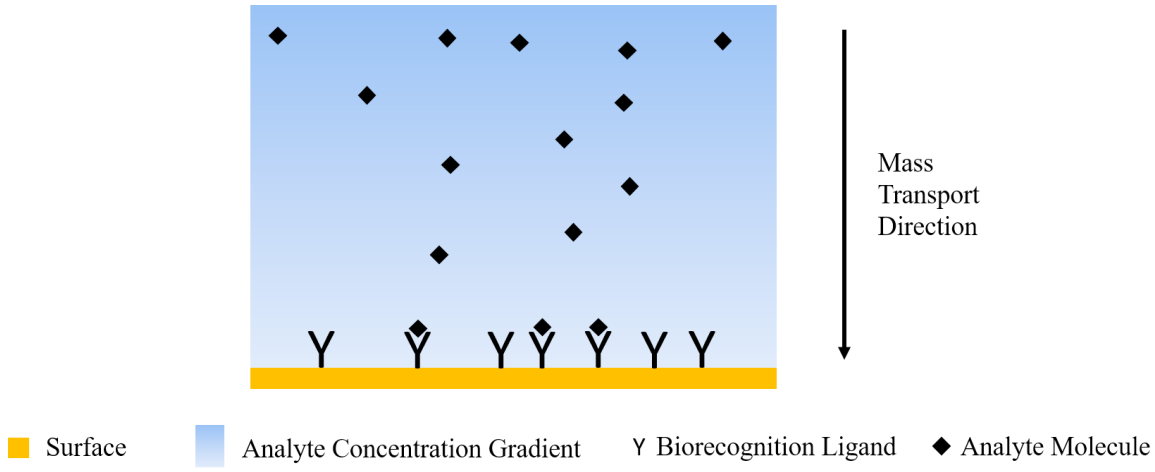

Figure 2.15 Illustration of a Langmuir adsorption model with mass transport considerations.

Chapter 3 Particle-modified Spectral SPR Biosensor

3.1 Introduction

The aim of this chapter is to investigate methods to modify the surface of a conventional SPR sensor with silica particles and further to investigate its functionality in SPR measurements. The common method for ligand immobilisation on conventional SPR biosensors centres around either covalent attachment or matrix entrapment as reviewed in Section 1.3.1. The SAM immobilisation method involves multiple steps of surface functionalisation to introduce the bio-recognition ligands that provide the surface selectivity. Matrix entrapment, although not requiring the user to functionalise the surface (except with the initial hydrogel), still requires the step of ligand immobilisation by flowing and washing of a ligand-containing solution and any required coupling chemicals. To explore an alternative approach to the preparation of the sensor, two strategies of attaching ligands on silica particles first and then immobilising the particles on the sensor surface are proposed namely thiol silane coupling and physical adsorption aided by mechanical pressure. The potential advantages of this approach are:

- 'off-chip' bio-functionalisation.
- Compatibility with a chromatography format, which could lead to further development of SPR.

However, the potential loss in sensitivity is a counter issue that must also be investigated.

The surface coverage of the particles on the gold surface after particle modification was characterised. To establish the effect of the particles on sensing, the gold surface with

overlaying particles was assessed for its sensitivity towards refractive index changes in a bulk medium. Additionally, the modified surface was studied for its potential capability of sensing an antigen and antibody binding interaction. Finally, the binding kinetics was studied under both stop flow and continuous flow configurations.

3.1.1 Particle Immobilisation Strategies

3.1.1.1 Chemical Coupling by Thiol Silane

Particle modification will leave inter-particle spaces at the gold surface within the evanescent field. Since the biorecognition ligand will be on the particle and not on the gold, it is expected that the surface coverage of particles will be paramount to the model. The initial approach to particle decoration of the gold surface was through thiol silane functionalisation of the gold. The thiol end of the 3-mercaptopropyltrimethoxysilane (MPTMS) molecules was chemisorbed on gold by a strong thiolate-Au bond (40-50 kcal mol^{-1}) leaving the alkyl backbone packed away from the gold surface [234]. The silica particles were immobilised on the MPTMS functionalised gold surface through the formation of Si-O-Si bonds between hydrolysed organosilane MPTMS molecules and the free silanol groups of the silica particles [235]. The process is illustrated in Figure 3.1

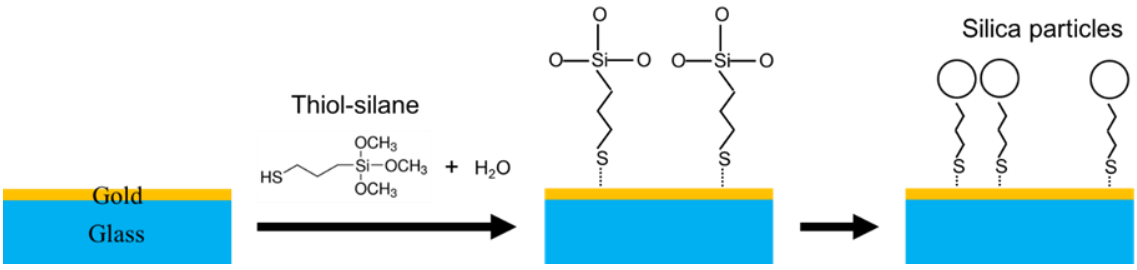

Figure 3.1 Illustration of the functionalisation of gold surface using 3-Mercaptopropyltrimethoxysilane (MPTMS) and the subsequent immobilisation of the silica particles. The diagram is not drawn to scale.

3.1.1.2 Physical Adsorption Aided by Mechanical Pressure

Particles unlike other immobilisation matrices are large enough and free to move, therefore, they can be manipulated easily. The linker layer might not be necessary if we can bring the ligand molecules onto or near the surface without it being washed away. We propose a mechanical technique of particle immobilisation here. With a flexible channel support that can be filled with particles, a particle bed can be simply pressed onto the Au surface.

Although a rigid flow chamber/channel assembly commonly used in SPR biosensors could also be used to contain a particle bed, the intimate contact with the sensor surface, needed for interaction with the SPR evanescent field becomes a feature of the packing of the column. On the other hand, a compressible channel also offers the functionality of mechanically pressing a particle bed on the sensor. A new design employing a channel made with flexible PDMS is illustrated in Figure 3.2. Submicron silica particles were first packed in the PDMS channel following the procedures in Section 2.5.4. The particles were immobilised by pressing the Au film through the prism onto the PDMS channel. When compressed, the height of the channel is expected to shrink therefore pressing the particle bed on the gold film. An illustration of the immobilisation process is given in Figure 3.3. Ingeneral, this method of particle immobilisation has the advantage of eliminating the step that involves the use of a chemical and therefore the corresponding steps of activation and washing, therefore achieving reagentless on-chip immobilisation of the particles. The disadvantge is that the immobilisation might be less well defined.

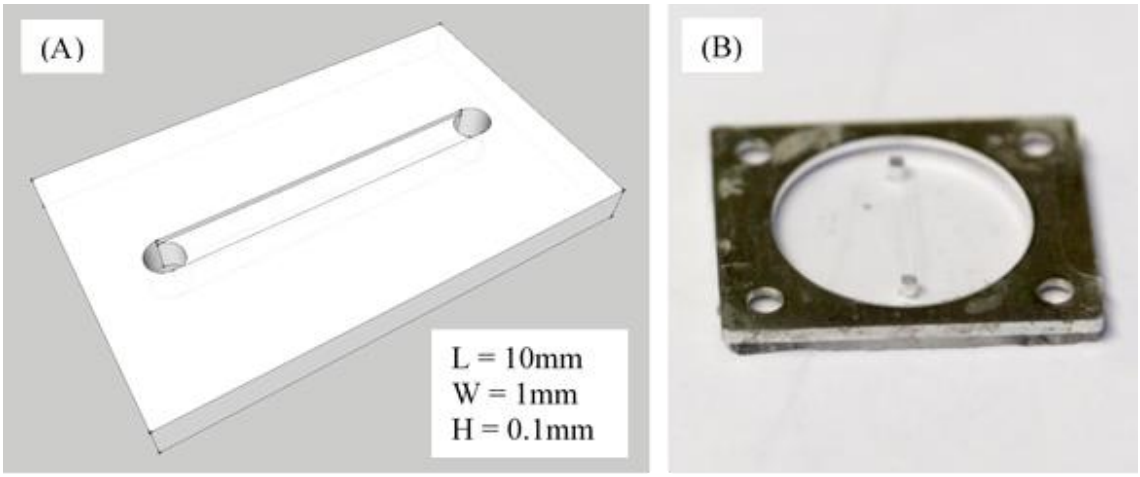

Figure 3.2 (A) 3D model of the PDMS channel with dimensions: 10 mm x 1 mm x 0.1 mm. (B) A photo of the PDMS channel on a slab. The aluminium support was removed in the experiments.

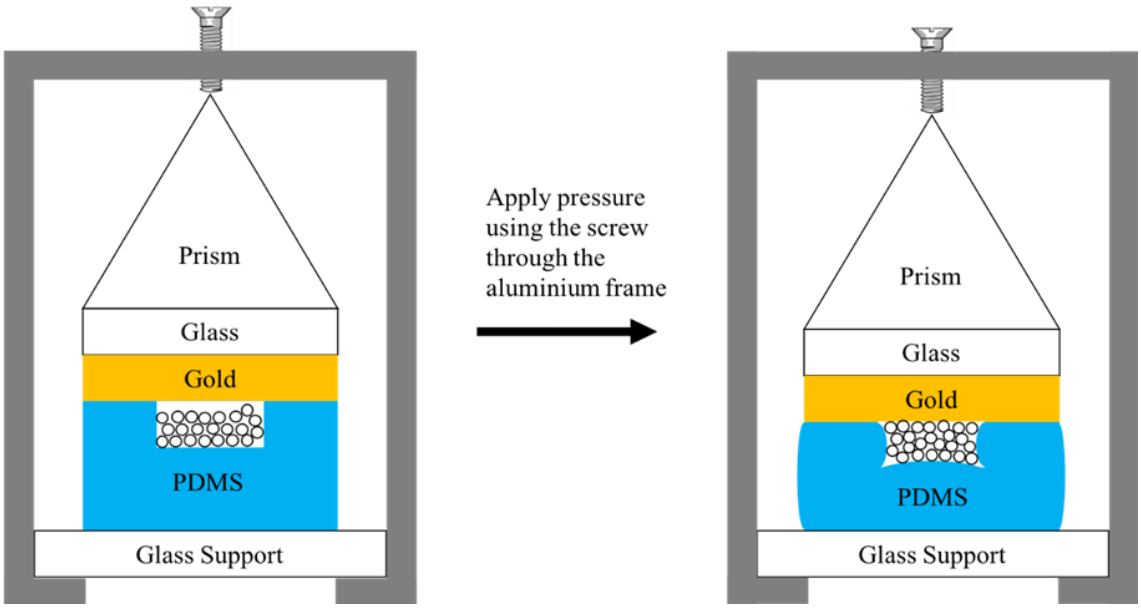

Figure 3.3 Illustration of the particle immobilisation strategy by the compression of the channel. This pressure is not released during the experiment. The diagram is not drawn to scale.

3.2 Results and Discussion

3.2.1 Protein Loading on the Silica Particles

To pursue the silica particle bed formation for an SPR platform, the particles must first be derivatised with the desired biorecognition ligand. As an exemplar test system, rabbit IgG was used as a capture molecule. To assess the loading efficiency of IgG loaded on the silica surface, the concentration of the supernatant after the ligand immobilisation process (Section 2.3) was measured and subtracted. Figure 3.4 shows the result for loading a particle suspension of 5 mg/ml silica particles with various amounts of Rabbit IgG as described in Section 2.3. Results shows that for both non-specific physical adsorption and covalent immobilisation techniques, there is a trend towards higher loading at higher mass of ligand molecules added to the silica suspension, but total uptake from the supernatant is not obtained for the amount of silica employed. The loading of Rabbit IgG via carbodiimide coupling is higher than by non-specific adsorption. Therefore, in all the subsequent tests, only carbodiimide linking of ligands on silica particles was used for its higher efficiency. For 200 µg of antibody loaded on 5 mg of silica particles, the loading was 40 µg/mg.

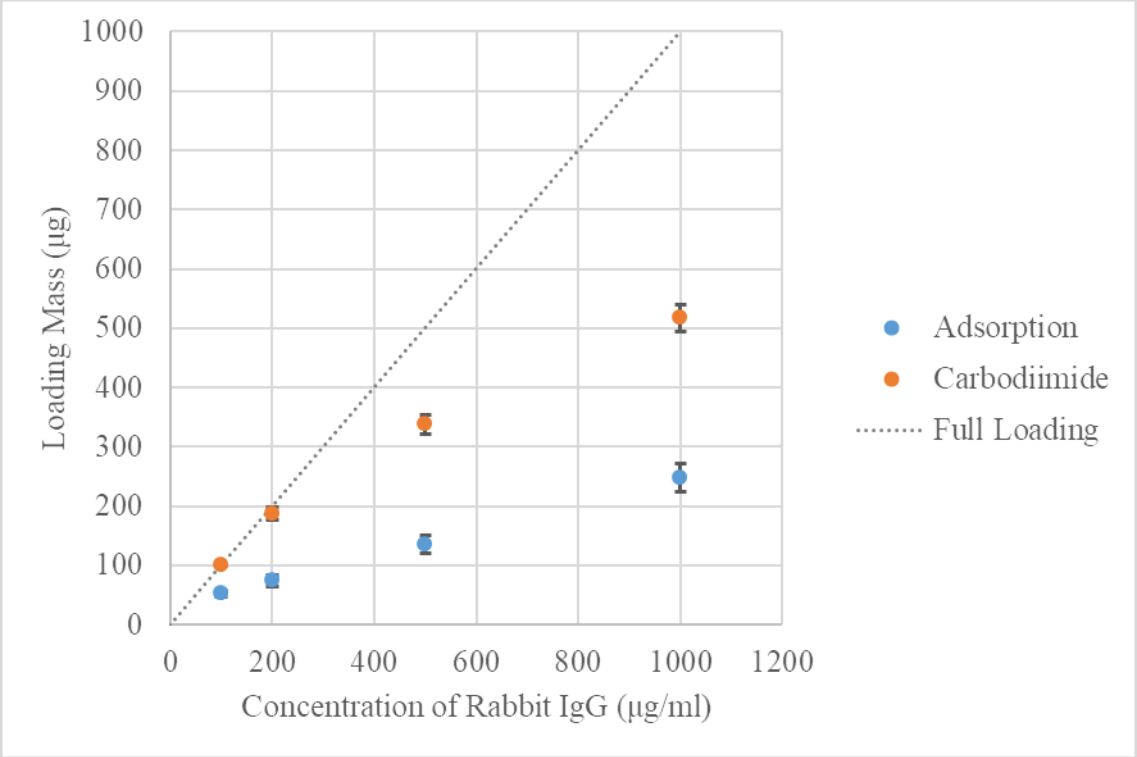

Figure 3.4 Loading efficiency of Rabbit IgG on 5 mg sub-micron silica particles in 1 ml PBS buffer solution.

3.2.2 Particle Loading on the SPR Surface

3.2.2.1 Particle Coverage Using Thiol Silane

Following attachment of the silica particles to the gold surface, as described in Section 3.1.1.1, the particle coverage was examined by SEM as shown in Figure 3.5. The particles largely formed islands in single- or double-layer structure on the surface. This may be attributed to the coagulation of particles due to the inter-particle disulphuric bond formation.

The area that the particles cover was estimated by manual identification and calculation using ImageJ and the result is tabulated in Table 3.1. On average, the particles covered 38.3 ± 3.1% of the surface. In an attempt to improve the coverage, higher concentrations

of particles were used. However, it did not improve the coverage, which may be due to the underlying thiol modification efficiency.

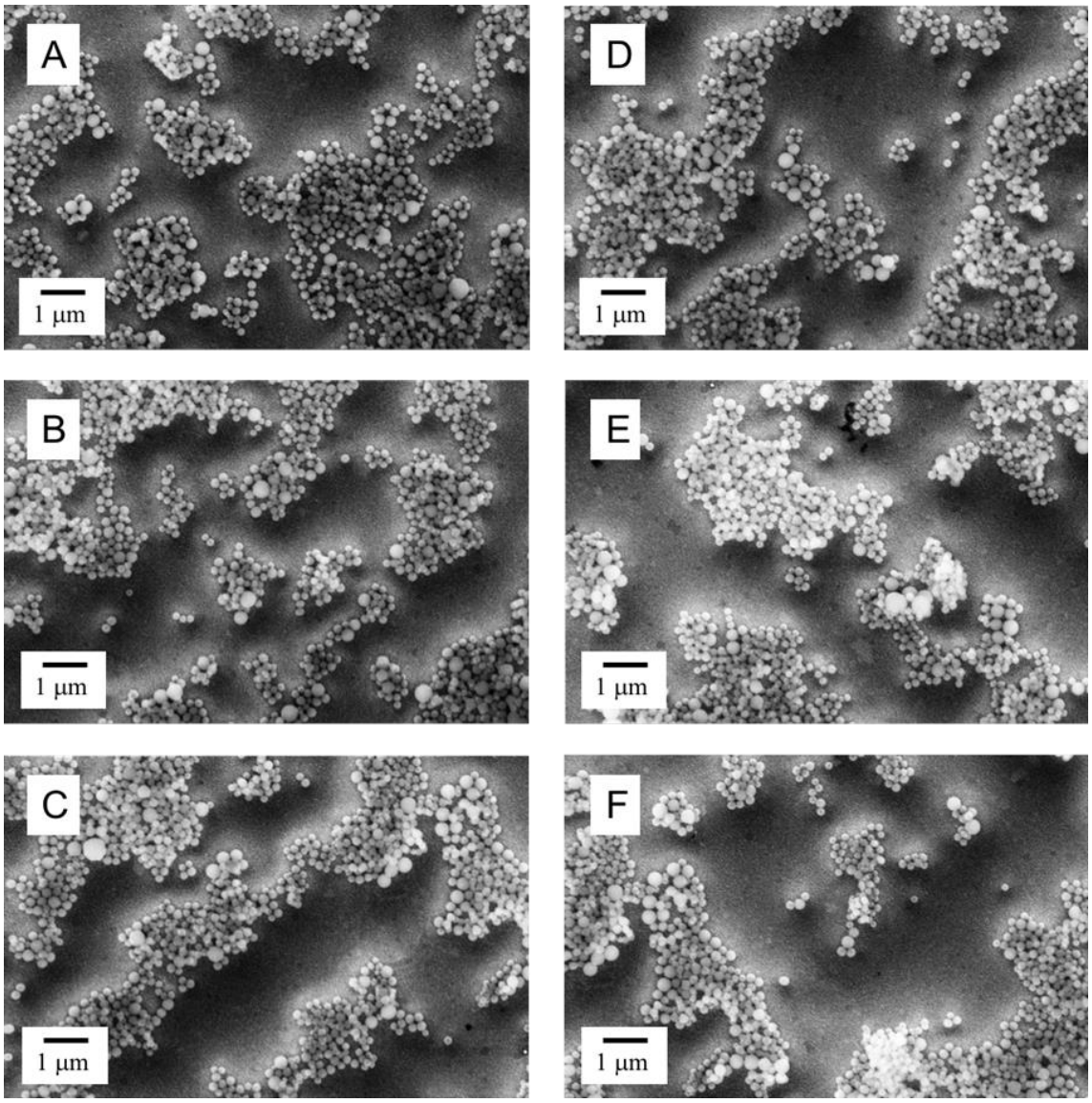

Figure 3.5 SEM images showing the coverage of silica particles on gold film at various places.

Table 3.1 Coverage percentages of silica particles on the Au surface for each image in Figure 3.5.

Sample	A	B	C	D	E	F	Mean	Standard Deviation
Coverage (%)	43.08	40.85	34.90	32.22	38.38	32.22	38.3	3.1

To confirm the function of the thiol silane linker, sub-micron silica particles were directly drop casted on bare gold film as a control. Figure 3.6A shows the distribution of the particles on the gold film after a suspension of them was air dried. The right half of the field of view was dominated by enormous clumps of particles forming a multilayer cloud-like structure (potentially at the site where the particles were dropped). The left half, however, only had individual particles scattered around. This distribution pattern was different in the case with the thiol silane linker where the particles formed relatively small, near monolayer clusters. After washing the surface with water, a clear majority of the particles were washed away without the thiol silane modification, as shown in Figure 3.6B. The lack of stability of the particles was undesirable where the particles are constantly in a system with the sample flowing over them. Thus, thiol silane could play a useful role in keeping the silica particles in place in the particle immobilisation strategy.

Also of note is that the assembly of particles on the thiol-silane-modified surface does not show any regular assembly pattern, as usually seen in opal like self-assembly of silica particles; this may also be associated with the particle attachment being determined more by the silane ligand density than by opal-like inter-particle forces (the inhomogeneity of the particle sizes (Section 2.2.3) is also evident from the SEMs which may also influence packing forces).

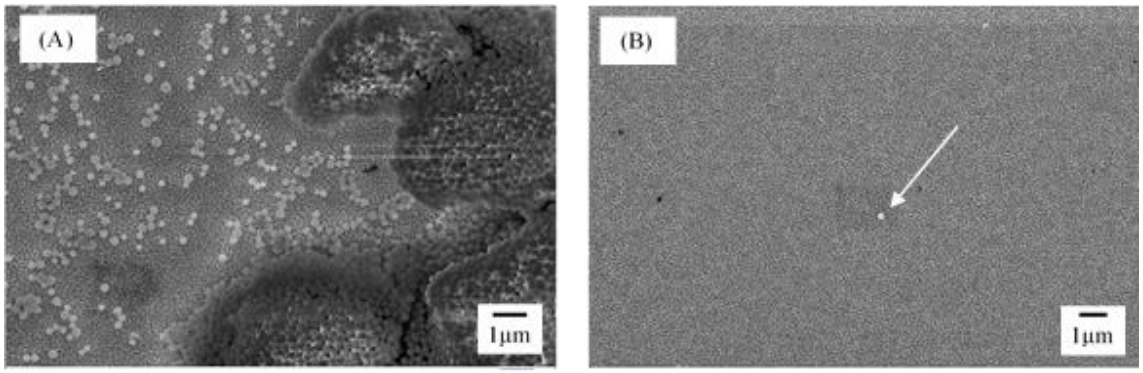

Figure 3.6 SEM images of sub-micron drop-casted particles on bare gold film. (A) Gold surface with air dried particles. (B) Gold surface washed with water.

Even with thiol silane as a linker, the particles did not cover the entirety of the sensor surface. To check if this result was attributed to the lack of functionalisation efficiency of the thiol silane, areas of the Au film that were not covered by the particles were analysed by EDX spectroscopy. Figure 3.7A shows the spectrum confirming the presence of sulphur alongside Au, Si, O and C as expected. Figure 3.7B shows the distribution of the detected sulphur element. It can be seen that thiol silane was present and distributed on the area that was not covered by the particles. The imperfect coverage of the particles was therefore not associated with the coverage of thiol silane but could be associated with the hydrolysis of the headgroup, causing inter-headgroup coupling instead of headgroup-particle coupling (Figure 3.8).

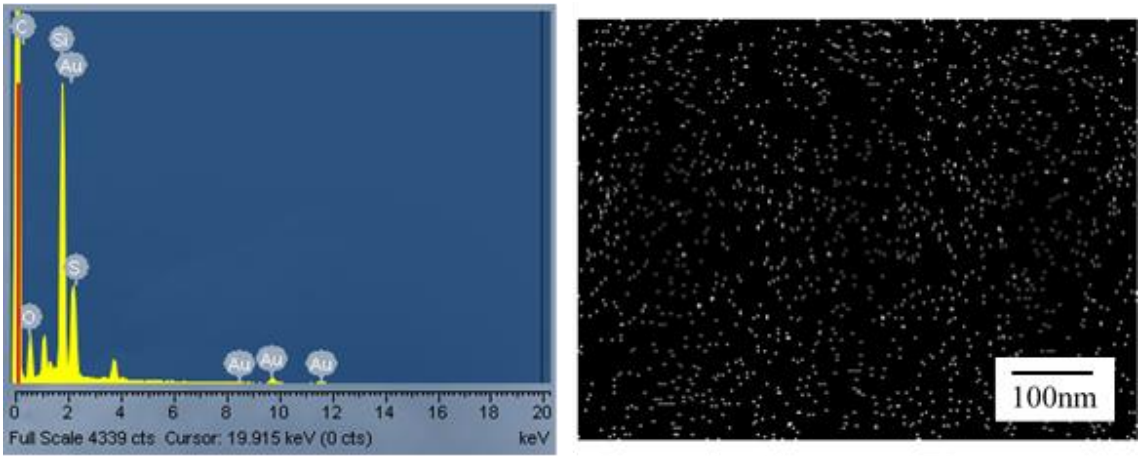

Figure 3.7 (A) EDX spectrum of the thiol silane-functionalised Au surface. (B) Element distribution map of sulphur. The white dots indicate the location of sulphur. The mapping was done on an uncovered area of the particle modified Au surface.

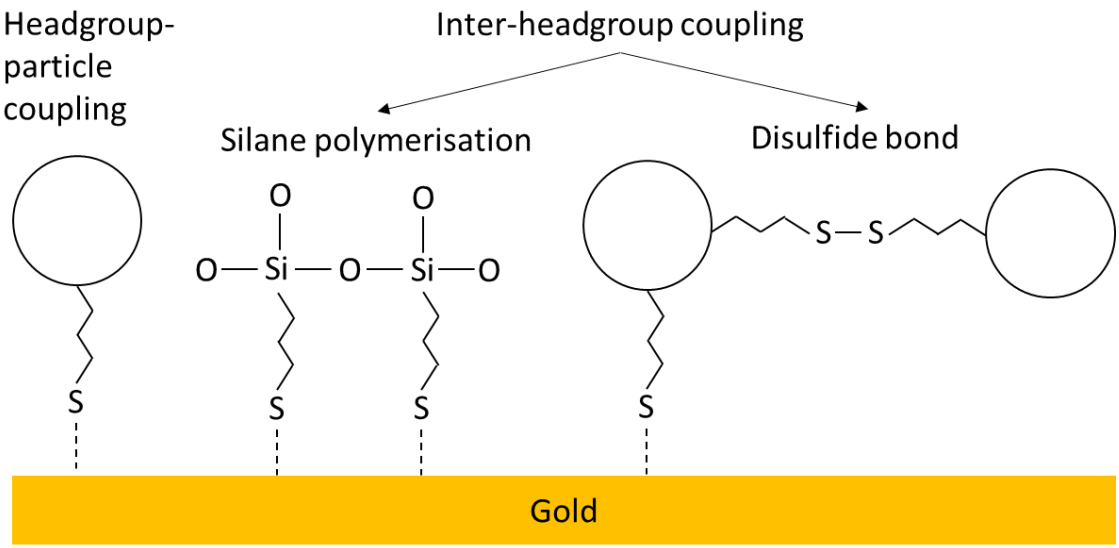

Figure 3.8 Illustration of the headgroup-particle coupling and the inter-headgroup coupling.

3.2.2.2 Particle Coverage Using Physical Adsorption Aided by Mechanical Pressure

Figure 3.9A shows a microscopic image of the submicron silica particles on the left side and the PDMS channel wall in the middle and the PDMS bank on the right. The bank and

the particle bed were in a separate plane of focus indicating that the particles did not completely fill the channel. This was to prevent overflow of the particles on the PDMS bank resulting in an imperfect seal when the gold film was placed on the PDMS. Once the gold film and the PDMS channel were assembled, it became difficult to assess the particle association with the gold film by visual means. After the experiment, the sensor was disassembled, and the gold surface was washed with water a few times to get rid of unbound particles. Figure 3.9B shows an SEM image of the particles on the film. In contrast to the drop-casted particles in Figure 3.6 (Section 3.2.2.1), many particles remain stuck to the surface with this mechanical pressure technique, even after five washing steps. The particles appear in single-layer clusters resembling the coverage achieved using thiol silane coupling. This was surprising, and the adsorption forces were not identified, but may be a result of the IgG molecules on the particles' surface also adsorbing on the gold film.

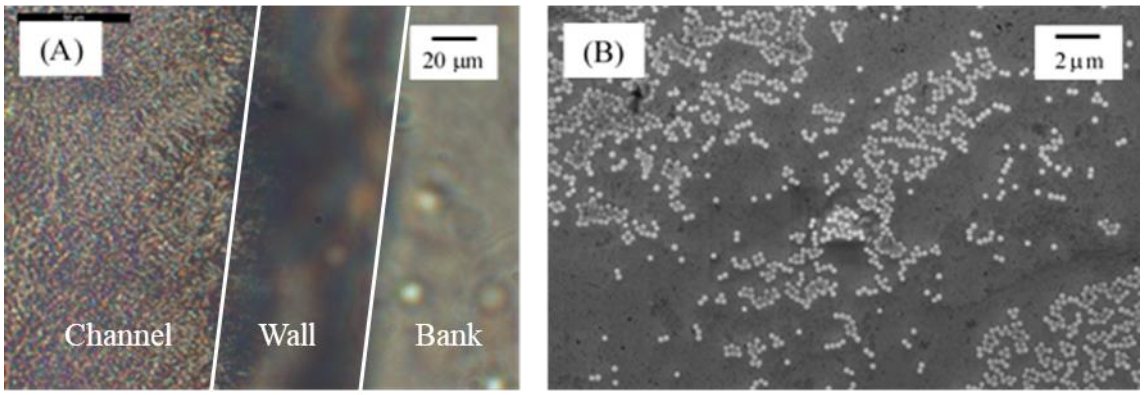

Figure 3.9 (A) Optical microscope image of the submicron silica particles packed in the PDMS channel. The particles are in the channel. (B) SEM image of the submicron particles stuck on the gold surface after the experiments. The film was washed with water to get rid of any unbound particles.

It is also clear that the SEM image in the previous case is no longer appropriate here. The SEM image only shows the particles that are stuck on the gold surface after the experiment and after washing. It does not show the number of particles that are close enough to the gold film for the ligands to be in the evanescent field, but still too far to adsorb on the gold surface as illustrated in Figure 3.10. The method for calculating surface coverage using the SEM image in the previous case is therefore no longer

appropriate. However, from the optical microscope image (Figure 3.9A), it can be seen that there is a good packing density in the channel. Thus, the density in the evanescent field (i.e. the first layer) when the particles (245±49.0 nm) are pressed onto the surface is expected to be higher than the apparent coverage in Figure 3.9B (which is 16±3.2%).

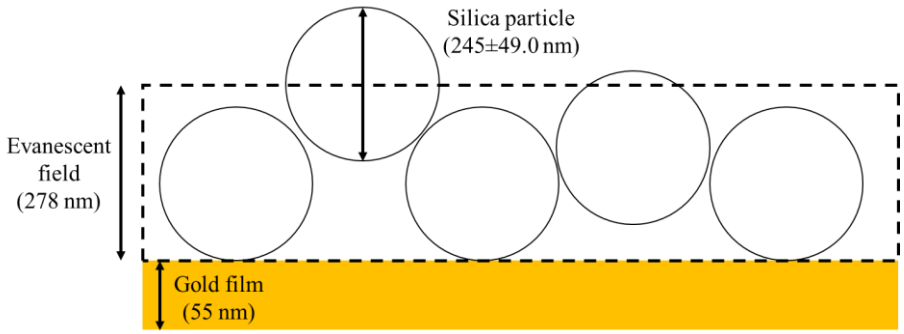

Figure 3.10 Illustration of a packed particle bed on the gold film with indication of the evanescent filed depth.

3.2.3 Equivalent Local Refractive Index within the Evanescent Field on a Silica-particle-modified Au Film

The penetration depth of the evanescent field of the resonant surface plasmon polaritons is 278 nm as calculated from eq. (1.3), assuming the resonant peak wavelength is 650 nm. Considering that depth together with the sizes of the submicron silica particles (245±49.0 nm as in Section 2.2.3), it can be concluded that the first layer of particles when immobilised on the film are completely immersed within the evanescent field, possibly with some influence from a second layer for the particle bed model. As seen in Figure 3.5, the addition of the particles increased the local refractive index in the evanescent field resulting in a red shift. For better understanding of the particle layer and predicting its behaviour, the particulate system can be approximated as a sub monolayer with an equivalent RI of its own using the Maxwell-Garnett theory (MGT). A cartoon showing the approximation is shown in Figure 3.11

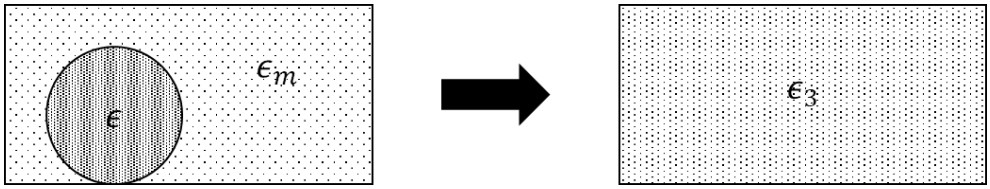

Figure 3.11 Illustration of the equivalent RI approximation of a particulate system.

The MGT model is a theory that is accurate for small particle concentrations. For spherical particles of dielectric function ϵ, the equivalent dielectric constant ϵ_3 is given in the following form [236]:

$$\epsilon_3 = \epsilon_m \left(1 + \frac{3f\beta}{1 - f\beta}\right)$$
$$\beta = \frac{\epsilon - \epsilon_m}{\epsilon + 2\epsilon_m} \tag{3.1}$$

where ϵ is the dielectric constant of the particles, ϵ_m is the dielectric constant of the medium, ϵ_3 is the equivalent average dielectric constant of the layer, and f is the volume fraction.

For a particulate sub monolayer, the volume fraction is:

$$f = \frac{\frac{4}{3}\pi r^3 \emptyset}{(2r)^3} = \frac{\emptyset\pi}{6} \tag{3.2}$$

where $\emptyset$ is the percentage coverage by area.

The estimated equivalent dielectric constants within the evanescent field for the particle modification systems are tabulated in Table 3.2.

Table 3.2 Equivalent refractive indices within the evanescent field.

System	∅	ϵ	ϵ_m	ϵ_3
Thiol silane coupled sub-monolayer in water	38	2.1228	1.7769	1.8428
Thiol silane coupled sub-monolayer in PBS solution	38	2.1228	1.7822	1.8466
Pressed sub-monolayer in water	16	2.1228	1.7769	1.8042
Pressed sub-monolayer in PBS solution	16	2.1228	1.7822	1.8092

Another popular theory estimating the dielectric constant of mixtures is the effective medium theory (EMT) proposed by Landauer [237]. According to EMT, the dielectric constant of the composite system ϵ_3 in the case where the two grains are of spherical shape is given by the relation:

$$f\frac{\epsilon_1-\epsilon_3}{\epsilon_1+2\epsilon_3}+(1-f)\frac{\epsilon_2-\epsilon_3}{\epsilon_2+2\epsilon_3}=0 \tag{3.3}$$

where ϵ_1 and ϵ_2 are the dielectric constants of the grains and f is the volume fraction.

Substituting the dielectric constants for water and silica in the formula yields $n_3 = 1.4321$. Upon closer inspection of the EMT, it can be seen that the two components are treated in an equivalent manner. The two grains are assumed to be embedded in an effective medium whose dielectric constant is ϵ_3, the same as that of the composite material. However, in the MGT, the grain is assumed to be embedded in the matrix of the other component that forms the composite. The MGT apparently describes the situation in this experiment better since the silica particles are embedded in the sample solution resulting in a non-symmetric system. Thus, the approximation of an equivalent RI by the MGT is more plausible. All subsequent analysis is based on this approximation.

Figure 3.12 shows the reflectance spectra of the gold surfaces with and without particle-modification when sensing in pure water. The experimental peak position aligns well with

the theoretical predictions. The slightly worse figure of merit in Figure 3.12A is consistent with a difference in surface roughness. The Au film was assumed to be perfectly smooth in the simulation, but SEM images of the Au film suggested otherwise as shown in Figure 2.1. It is well known in the literature that an inhomogeneous metallic surface results in a worse FWHM [238]. However, the larger FWHM in Figure 3.12B compared to the simulation can be caused by the absorption or scattering by the overlaying particles. The particles absorb or scatter light, which consequently changes the conditions for exciting the surface polaritons [239]. A simulation of the effect using the imaginary RI component *k* is shown in Figure 3.13. A higher value of *k* translates to a higher absorption or scattering of energy by the silica particles and, therefore, the FWHM increases. The ATR spectrum of the particle-modified surface was refitted to the absorption and scattering model and the result is shown in Figure 3.13A.

The noise and deviations at extremely low and high wavelengths are due to normalisation to the low intensity of the white light at those wavelengths. The normalised value got noisy and unpredictable when the reflected light was divided by the low intensities.

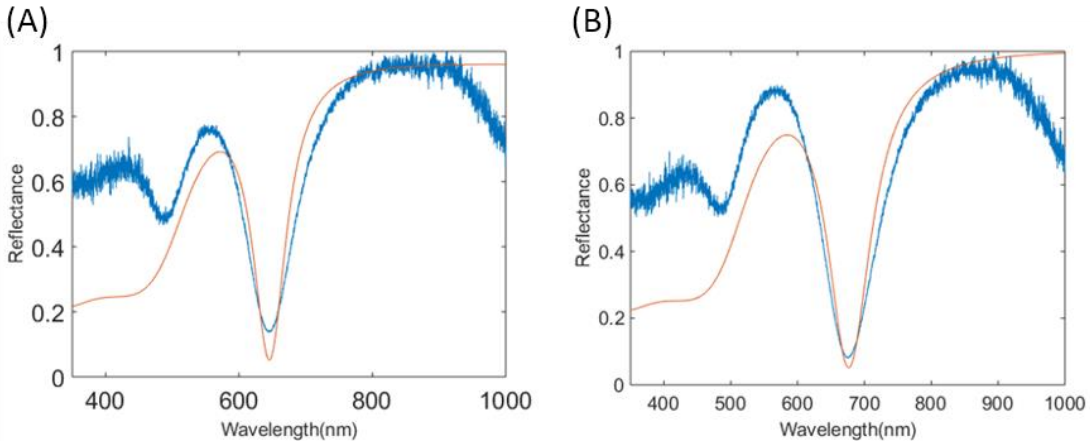

Figure 3.12 The reflected spectra of the SPR sensor with water in the chamber obtained with (A) an unmodified gold surface and (B) a particle-modified gold surface. The angle of incidence was set as 73.7°. The blue curve is the experimental data and the red one is the predicted value.

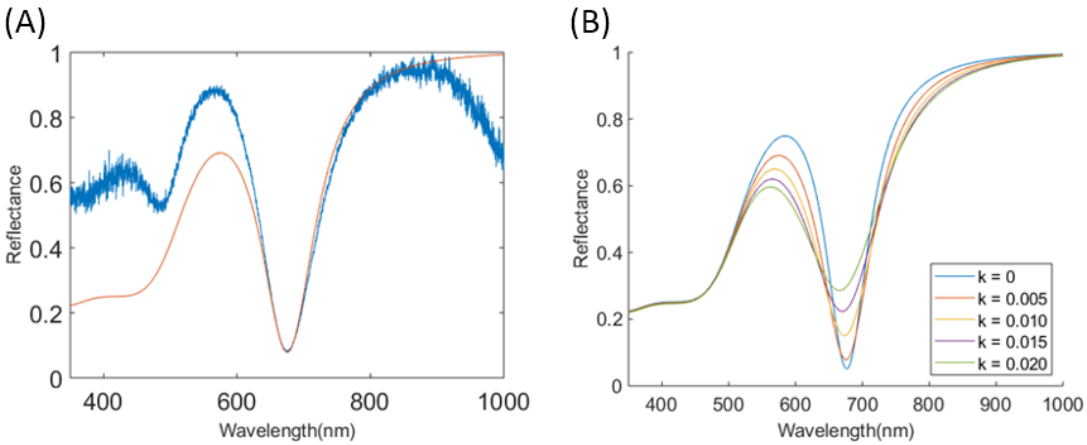

Figure 3.13 (A) The experimental ATR spectrum (blue) and the simulated one (red) after adding an imaginary component (k = 0.005) in the RI of the silica particles to account for the absorption or scattering. (B) Simulations showing the effect of k on the ATR spectra for a particle-modified Au surface. The real part of the refractive index was fixed at 1.3573 as predicted by the MGT.

3.2.4 Sensitivity towards Bulk Medium

For the particle-modified gold film to work as an SPR sensor, it needs to respond to refractive index changes in the evanescent field. The bulk sensitivity of the particle-modified SPR sensor was measured using 10% (w/w) glucose solution with a RI of 1.348 [230]. The sensorgram is shown in Figure 3.14A. Initially, when there was only water ($RI = 1.330$) [240] flowing in the chamber, the peak wavelength was recorded at approx. 668.5 nm. The injection of glucose solution caused a red shift of approx. 37 nm. The peak position returned to approx. 669 nm upon flushing with water.

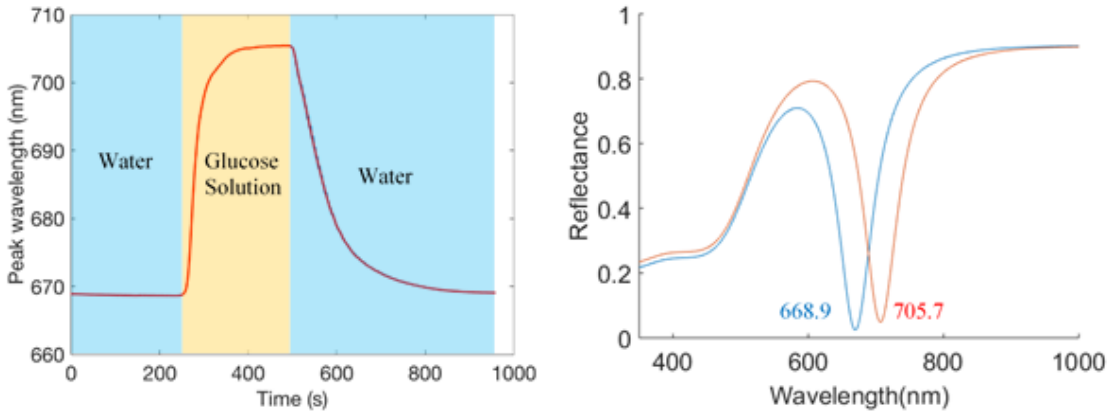

Figure 3.14 (A) The sensorgram showing the peak attenuation wavelength against time as 10% (w/w) glucose solution was injected in the chamber. The glucose solution was flowed into the chamber at 250 s and was flushed by water at 500 s. (B) The predicted spectra showing the peak positions when water (blue curve) and 10% glucose solution (red curve) are in the chamber respectively. The incident angle was set as 75.1° to align the baseline peak position to 668.9 nm as obtained in the experiment.

To model the result, the equivalent RI of the particle layer was calculated to be 1.3573 in water (Section 3.2.3). When 10% glucose solution replaced water, the equivalent RI of the particle layer changed to 1.3692 because glucose solution fills the void. The predicted peak shift is 36.6 nm (Figure 3.14B) which is close to the experimental result (Figure 3.14A).

Figure 3.15 shows the results comparing the sensitivity of a bare gold film and a particle-modified gold film. The results show that after particle modification, the signal towards bulk media stayed the same as the unmodified gold film. Using the refractive index of 10% glucose solution reported in [230], the modified sensor is found to have a sensitivity of 2.034 μm/RIU.

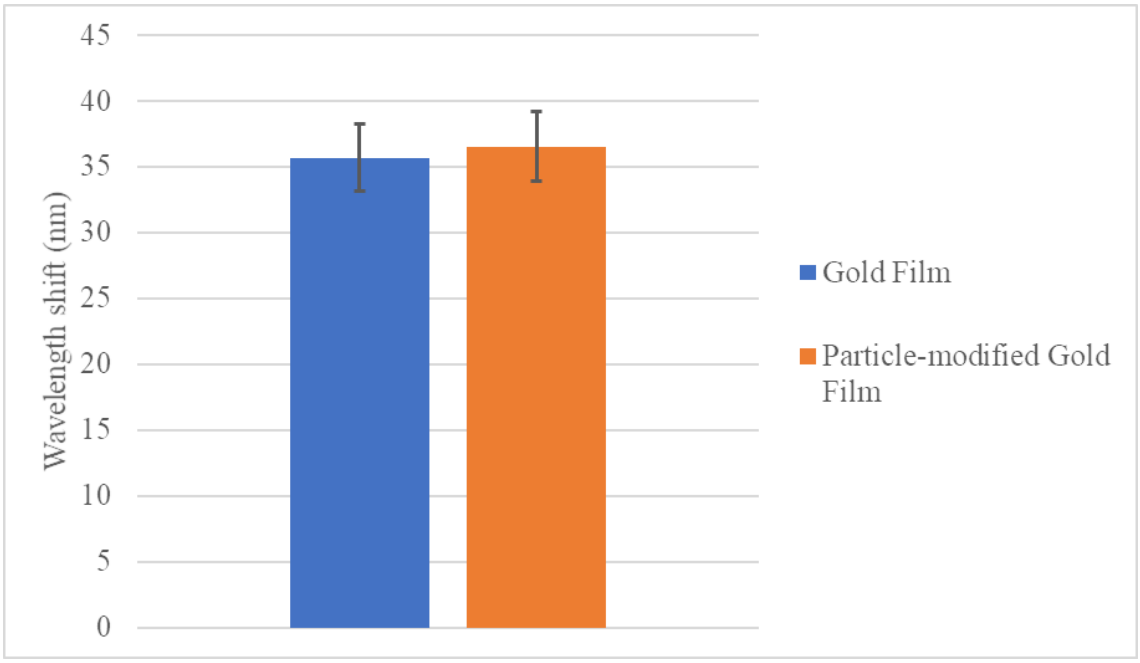

Figure 3.15 Frequency shifts when 10% (w/w) glucose solution flushes water on bare Au film and on particle modified Au films. Three tests were done on each type of surface.

3.2.5 Sensitivity Towards Antigen/Antibody Interaction

The RI test performed in the previous section shows equivalent sensitivity for RI changes on the gold film with and without particles. However, the RI change is occurring in the voids between the particles, whereas SPR has typically become a tool of choice for studying binding between a surface immobilised biorecognition ligand and its binding complement. Such unlabelled SPR sensing is usually considered to be best used for sensing large biomolecules. This is because in a one-to-one interaction with a biorecognition ligand at the surface of a gold film, large biomolecules are more optically dense than small ones at the same binding density. Small molecules can be detected easily only when they are labelled with a large molecule or a heavy nanoparticle [241]. In order to compare this scenario for the particle modified SPR surface, IgG and anti-IgG pairs were selected as the capture ligand and the analyte to test the sensitivity of the particle immobilisation model because of their large size and availability.

3.2.5.1 SPR Biosensor Modified by Particles using Thiol Silane

Figure 3.6A shows a sensorgram obtained for the detection of 200 µg/ml anti-Rabbit IgG. There was a 6.0 nm red shift following injection of the analyte. The response time in this figure due to the anti-IgG/IgG binding was much slower than the step change in the signal due to the bulk medium in Figure 3.14A.

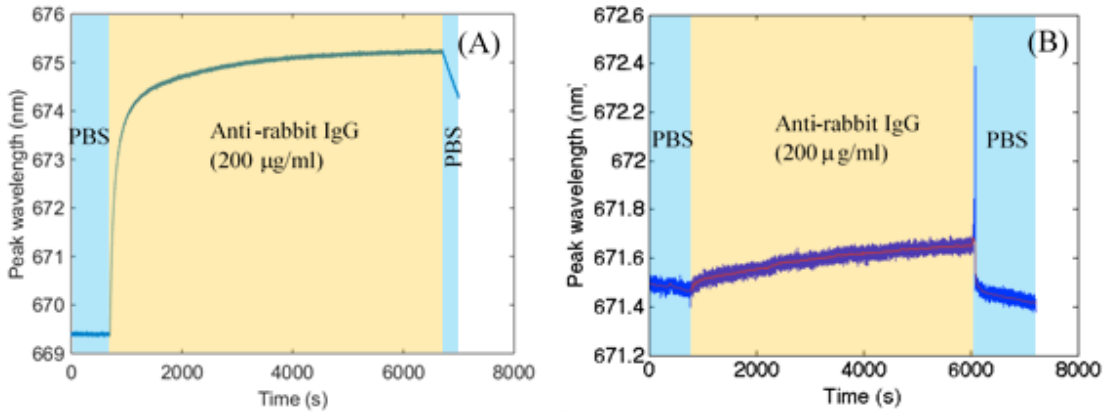

Figure 3.16 (A) The sensorgram showing the signal when anti-Rabbit IgG bound to the Rabbit IgG on the particles. (B) The sensorgram showing the signal where the particles were blocked by StabilCoat. The experiment was done in a stop-flow fashion. The coloured blocks indicate the solution in the chamber at that moment.

The result of a control experiment where the particle-modified sensor surface was treated with StabilCoat instead of the capture ligand is shown in Figure 3.16B. The StabilCoat immunoassay blocker ensured there was no non-specific binding of the analyte on the blocked surface. The signal of approx. 0.2 nm shift was recorded which can be considered as the blank reference measurement. The difference between the positive signal and the blank one was the response to the anti-IgG. It is calculated to be 5.8 nm for 200 µg/mL anti-Rabbit IgG in this case.

A series of concentrations of anti-Rabbit IgG were tested and the result is shown in Figure 3.17. The sensitivity towards anti-Rabbit IgG is found to be 0.0328 nm/(µg/ml) or 4.36×10^{6} nm/M.

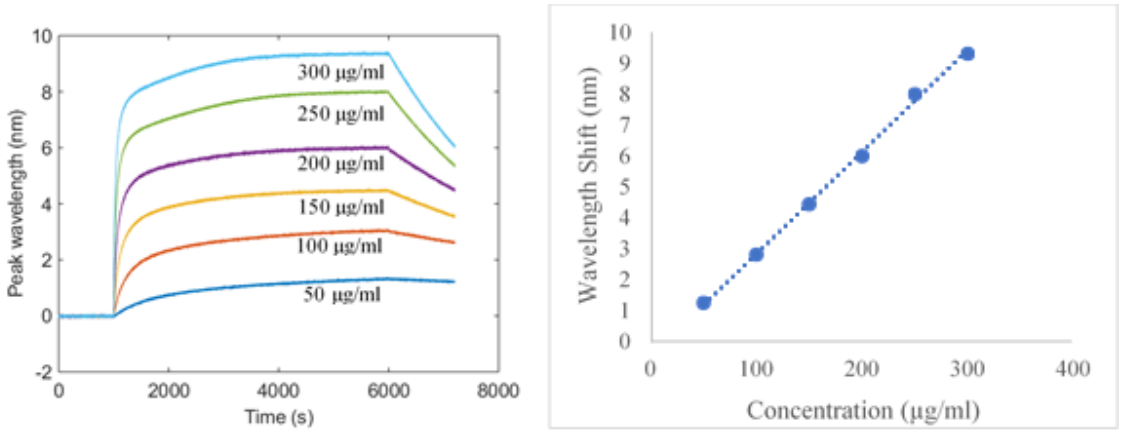

Figure 3.17 The particle-modified sensor response towards analyte concentrations from 50 to 300 µg/ml. (A) The respective sensorgrams at various concentrations. (B) The wavelength shifts plotted against the analyte concentrations.

To compare the performance of the particle-modified sensor with a conventional gold film biosensor with SAM immobilisation, gold surfaces were functionalised with DDA first and the capture ligands were immobilised as described in Section 2.3.3. The results for the detection of 100 µg/ml are shown in Figure 3.18. From this bar graph we can see that the classical SPR biosensor with SAM immobilisation is much more sensitive. The difference in the sensitivity will be discussed in Section 3.2.6.5.

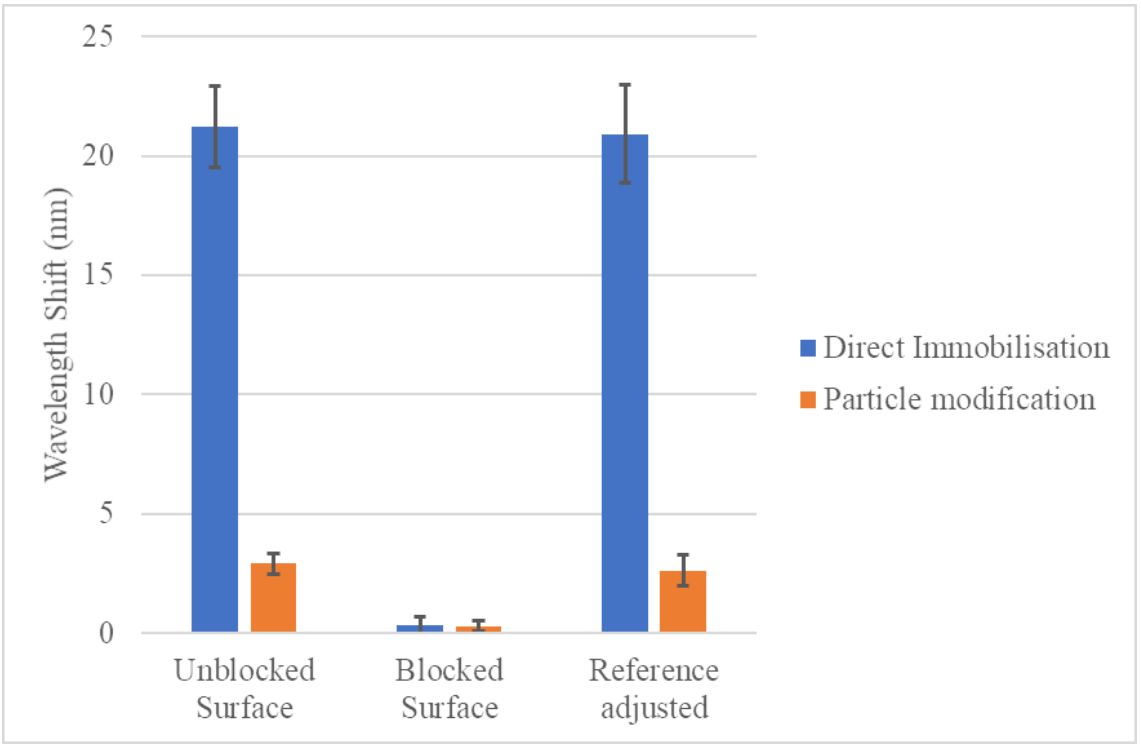

Figure 3.18 Frequency shifts at equilibrium on the gold film with alkanethiolate SAM and on particle modified gold films when sensing 100 µg/ml of anti-Rabbit IgG.

3.2.5.2 SPR Biosensor Modified by Particles Using Mechanical-pressure-aided Adsorption

The sensorgram for the detection of 200 µg/ml of anti-Rabbit IgG is shown in Figure 3.19. When StabilCoat blocking mix was in the channel to prevent non-specific binding, the refractive index increased initially to a saturation plateau. When it was washed away by PBS buffer solution, the sensorgram quickly returned to a lower level and stabilised. The increase attributed to the StabilCoat was due to the bulk increase of the refractive index. This is supported by the fast increase during the flow phase and the sharp decrease during the wash phase. Subsequently when the sample was flowed into the system and washed away, the sensorgram demonstrated an association and dissociation profile respectively which was governed by the kinetics on the antigen/antibody interaction.

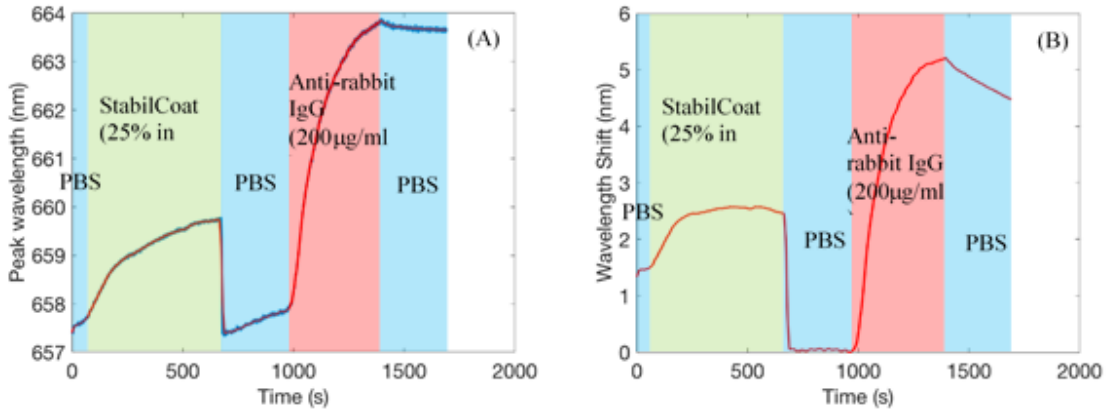

Figure 3.19 (A) The sensorgram showing the signal when StabilCoat and 200 µg/ml anti-Rabbit IgG were flowed into the channel with intermediate PBS buffer washes. The experiment was done in a continuous flow. The blue curve is the raw data and the red one is smoothed. (B) The same sensorgram was adjusted for the baseline drift. The difference between time zero and the first wash phase may be attributed to the loss of particles.

The apparent shift caused by the binding is 5.2 nm. This result is close to the 5.8 nm shift obtained in Section 3.2.5.1 where the particles were immobilised on the sensor surface using thiol silane coupling.

3.2.6 Equivalent RI Analysis within the Evanescent Field

The equivalent RI approximation has been a powerful tool for understanding the behaviour of the particle-modified surface towards a bulk medium as shown in Section 3.2.3. It can also be used to shed some light on the binding behaviour between IgG and anti-IgG in the particle-modified SPR biosensor.

3.2.6.1 Equivalent RI of Particles with Immobilised IgG.

In a heterogeneous system such as the particle suspension discussed here, the refraction at each interface is often difficult to model individually. Instead, the particulate system can be simplified to a homogenous medium with an equivalent refractive index. A particle with immobilised IgG in the buffer solution can be modelled as a particle immersed in a hypothetical layer of IgG solution with a thickness same as the size of the protein. The

MGT can then be used to approximate the equivalent RI of the IgG immobilised particle using the dielectric constants of the solution layer and silica particles.

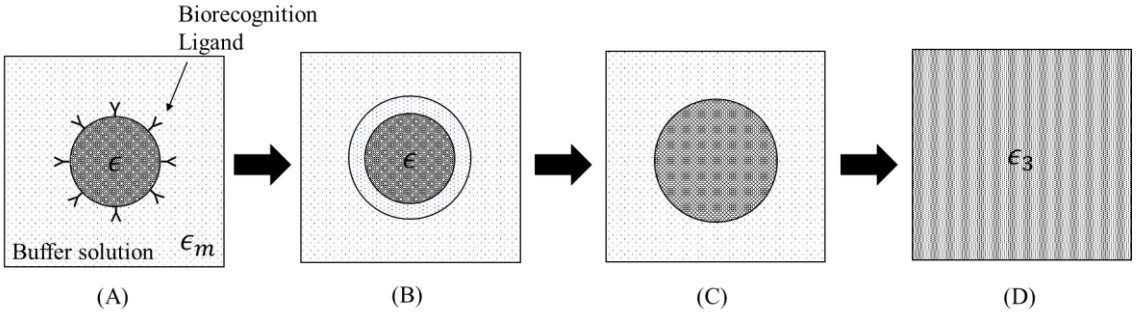

Figure 3.20 Illustration of the equivalent RI approximation process. (A) The particle with immobilised ligands in the buffer solution. (B) The ligands together with the surrounding buffer solution are approximated by a liquid shell. (C) The particle and the liquid shell system can be modelled using MGT. (D) The particulate system can be then modelled using MGT.

The refractive index of the IgG solution layer n_m can be obtained by

$$n_m = c_m \Delta n + n_0 = \frac{m_{Ab}}{V_m}\Delta n + n_0 = \frac{\emptyset m_p}{V_p' - V_p}\Delta n + n_0 = \frac{\emptyset \rho_p V_p}{V_p' - V_p}\Delta n + n_0$$
$$= \frac{\emptyset \rho_p (\frac{d_p}{2})^3}{(\frac{d_p}{2} + d_{Ab})^3 - (\frac{d_p}{2})^3}\Delta n + n_0 \quad (3.4)$$

where c_m is the concentration of IgG on the particle surface, Δn is the refractive index increment per concentration of protein in solution, n_0 is the RI of the buffer solution, m_{Ab} is the mass of the IgG on the particle surface, V_m is the volume of the hypothetical ligand layer, $\emptyset$ is the average load (weight ratio) of IgG on the particles, m_p is the mass of the particle, V_p' is the volume of the IgG immobilised particle, V_p is the volume of unmodified particle, ρ_p is the density of the particle, d_p is the average diameter of the particles and d_{Ab} is the size of the IgG molecule.

Table 3.3 Parameters used in the MGT approximation of equivalent RI of a particle immobilised with IgG.

Parameter Name	Nomenclature	Value and unit	Reference
Refractive Index Increment	Δn	0.19 RIU/(g/ml)	[242 – 244]
Buffer solution RI	n_0	1.335	Sigma-Aldrich
Ligand loading	$\emptyset$	40 µg/mg	Section 3.2.1
Silica particle density	ρ_p	1.9 g/cm^3	[245]
Silica particle diameter	d_p	245 nm	Section 2.2.3.1
IgG molecule size	d_{Ab}	14.5 nm	[246]

Substituting all the values in Table 3.3 into eq. (3.4), we have the following estimations. The concentration of IgG in the layer on the particle surface is 190.5 mg/ml. Note the magnitude difference from the concentration in the bulk. The equivalent RI of the IgG layer, n_m, is 1.3712 and the dielectric constant ϵ_m is 1.8802. Substituting ϵ_m and the dielectric constant of silica (ϵ =2.1228) into the MGT as in eq. (3.1), we have an equivalent RI of an IgG-immobilised particle of 1.4323.

3.2.6.2 Modelling of the Biosensor Response with Blocked Particles

For the SPR biosensor surface with overlaying blocked particles (i.e. particles that do not have Rabbit IgG ligands and are blocked by StabilCoat to prevent unspecific binding), the particles are essentially in a solution of 100 ug/ml anti-Rabbit IgG with no interactions. An equivalent RI of the particle layer in the evanescent field can be calculated by MGT. The blocked particles are assumed to have the same amount of blocking protein as discussed in Section 3.2.6.1 and the equivalent RI is therefore 1.4323. The RI of the buffer solution with 100 µg/ml of anti-Rabbit IgG is estimated to have a RI of 1.3350.

Therefore, the equivalent RI of the particle layer within the evanescent field is 1.3541 in buffer solution and 1.3542 in the anti-Rabbit IgG sample.

Figure 3.21 shows the simulated spectra corresponding to the experimental results shown in Section 3.2.5. The resolution of the simulated spectra does not allow for the peak position to be determined to the precision of 0.1 nm, but an estimation of 0.2 nm shift agrees well with the experimental data.

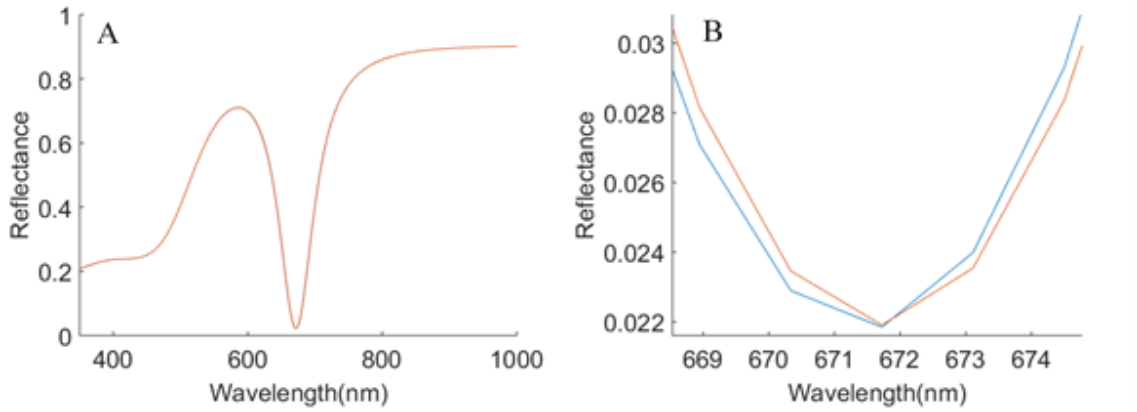

Figure 3.21 Simulated spectra for an SPR biosensor modified with blocked particles in response to PBS buffer solution and the anti-IgG sample. (A) Full Spectra. (B) Spectra magnified to the attenuation peaks. The blue spectrum is the result in the buffer solution and the red is in the anti-IgG sample.

3.2.6.3 Modelling of the Biosensor Response with Thiol Silane Coupled IgG Immobilised Particles

The anti-Rabbit IgG molecules when bound to the Rabbit IgG ligands on the particles are expected to result in a higher local concentration. The bound anti-Rabbit IgG can be modelled as a denser layer of protein solution on the particle system modelled in Section 3.2.6.1. The experimental result obtained in Section 3.2.5.1 can be used to trace back the local density of the captured anti-Rabbit IgG. Figure 3.22 shows the simulated spectra before the experiment and at equilibrium, showing a shift of 2.8 nm. The equivalent RI of the particle layer within the evanescent field was found to be 1.3554 after the binding reached an equilibrium. The corresponding equivalent RI of the particle and immobilised proteins was 1.4384. This translated to an equivalent RI of 1.3920 in the protein layer and

a concentration of 299.9 mg/ml in the layer on the particle surface. The concentration of the captured anti-Rabbit IgG, therefore, is 109.4 mg/ml after subtracting the concentration of the IgG ligands estimated in 3.2.6.1.

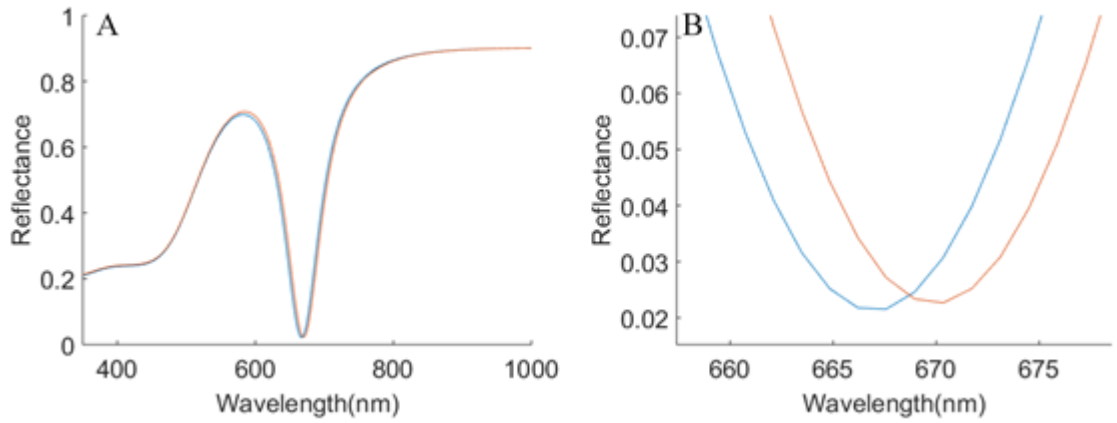

Figure 3.22 Simulated spectra for a particle-modified SPR biosensor in response to the PBS buffer solution and the anti IgG sample. (A) Full Spectra. (B) Spectra magnified to the attenuation peaks. The blue spectrum is the result in the buffer solution and the red is in the sample.

Table 3.4 Simulated refractive indices and local concentrations at various analyte concentrations.

Analyte Concentration (µg/ml)	**Peak wavelength shift (nm)**	**Evanescent field RI after binding**	**Particle RI after binding**	**Anti-IgG local concentration (mg/ml)**
50	1.3	1.3547	1.4353	61.60
100	2.8	1.3554	1.4384	109.4
150	4.4	1.3561	1.4421	177.9
200	5.8	1.3567	1.4456	241.1
250	8.0	1.3578	1.4509	338.4
300	9.3	1.3584	1.4540	395.8

The analyte local concentrations can be estimated using the MGT model system for all the bulk concentrations tested in Section 3.2.5.1. The results are shown in Table 3.4 and Figure 3.23. The estimated local concentrations follow a linear relationship with the bulk analyte concentrations.

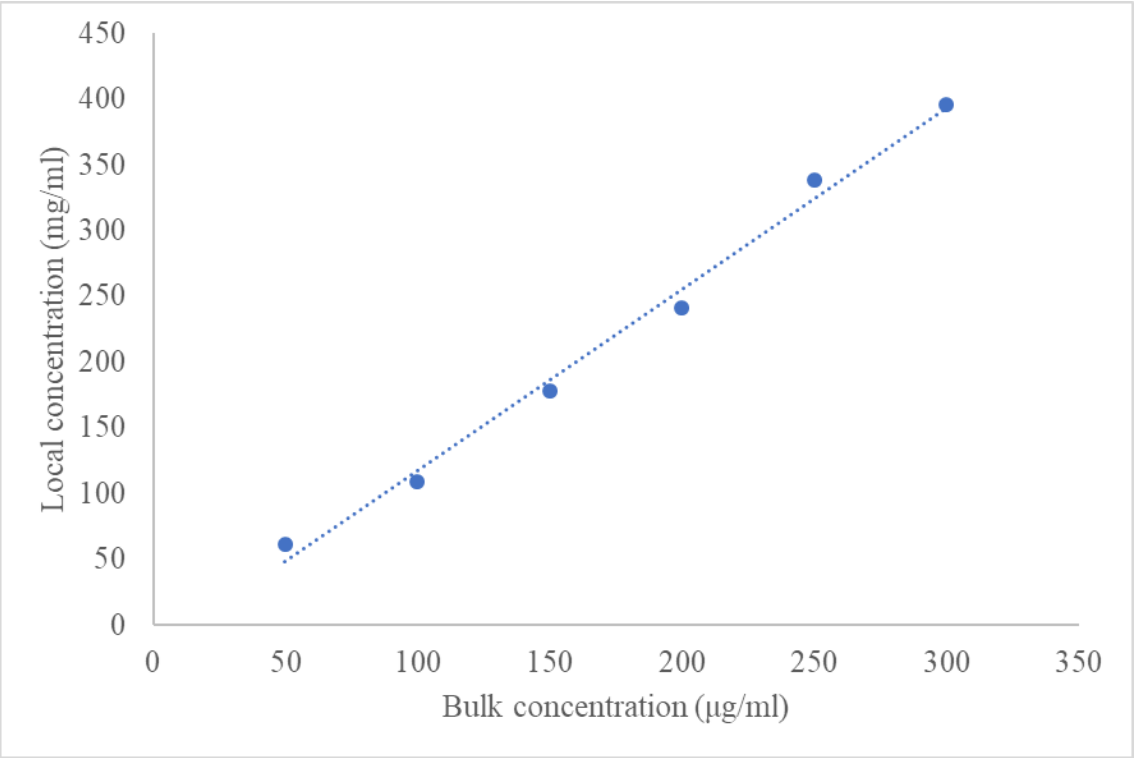

Figure 3.23 Estimated local analyte concentration around the particle surface versus the bull concentration.

3.2.6.4 Modelling of the Biosensor Response with Mechanically Pressed IgG Immobilised Particles

As discussed in Section 0, the actual surface coverage of the mechanically pressed particles could not be determined by SEM images of the surface after the experiment. It may be estimated by modelling the biosensor's sensitivity towards anti-IgG/IgG binding obtained in Section 3.2.5.2. Assuming the same local analyte concentrations on the particles as in the thiol silane coupled particle-modified SPR biosensor, the peak wavelength shifts when sensing 200 µg/ml anti-IgG for various surface coverage of

particles were simulated and the results are tabulated in Table 3.5. As expected, the surface coverage of the mechanically pressed particles is higher than the apparent value obtained from the SEM image in Section 0. Figure 3.9B only shows the particles that were stuck on the surface after washing. Particles that did not stick but were in the evanescent field during the experiment contributed to the sensitivity and the surface coverage was estimated to be 33 %. It is also evident that the sensitivity is highly reliant on the packing density of the particles in the evanescent field.

Table 3.5 Simulated sensitivities for various surface coverage.

Surface coverage (%)	**Evanescent filed RI (before binding)**	**Evanescent field RI (after binding)**	**Peak wavelength shift (nm)**
16 [1]	1.3431	1.3441	2.27
20	1.3451	1.3464	2.96
33 [2]	1.3516	1.3539	5.2 [3]
38 [4]	1.3541	1.3567	5.91 [5]
60	1.3653	1.3694	8.87
90.7 [6]	1.3809	1.3871	14.1

[1] Actual coverage calculated from the SEM image post experiment after washing.

[2] Estimated coverage based on the particle-modified biosensor's sensitivity.

[3] Actual peak wavelength shift measured by the SPR biosensor with mechanically pressed particles.

[4] Actual surface coverage on the SPR biosensor with thiol silane coupled particles.

[5] Actual peak wavelength shift measured by the SPR biosensor with thiol silane coupled particles.

[6] Maximum theoretical coverage for a monodisperse particle layer.

3.2.6.5 Sensitivity Comparison Between Particle Modification and SAM Immobilisation

To compare the sensitivity between the SAM immobilisation system and the particle immobilisation system, we first assume the ligand density is the same on the SAM modified gold surface and the particle-modified gold surface. In other words, the concentration of Rabbit IgG on the alkanethiolate SAM modified gold surface is also 190.5 mg/ml (Section 3.2.6.1), and the ligands capture 109.4 mg/ml of anti-Rabbit IgG (Section 3.2.6.3)out of the sample solution (100 µg/ml). The equivalent RI of the protein layer is 1.3712 before binding (Section 3.2.6.1) and 1.3920 after binding (Section 3.2.6.3). Substituting these values into the 3-layer model in Section 2.4.4, we have the spectra before and after binding as shown in Figure 3.24. The shift is 5.6 nm.

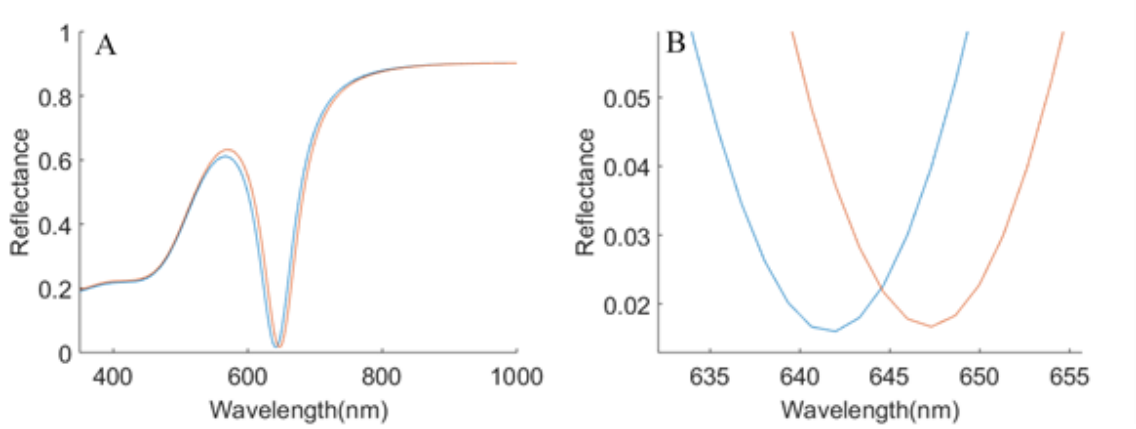

Figure 3.24 Simulated spectra for SPR sensor with SAM immobilised IgG ligands in response to PBS buffer and anti-Rabbit IgG sample assuming full coverage of same ligand density as on the particles. (A) Full Spectra. (B) Spectra magnified to the attenuation peaks. The blue spectrum is the result in the buffer solution and the red is in the anti-IgG sample.

If we reduce the estimate of the coverage and assume only 38% of the gold surface has ligands on it, the equivalent RI within the binding layer is 1.3488 before binding and 1.3567 after. The shift in the attenuation peak becomes 2.3 nm as shown in Figure 3.25.

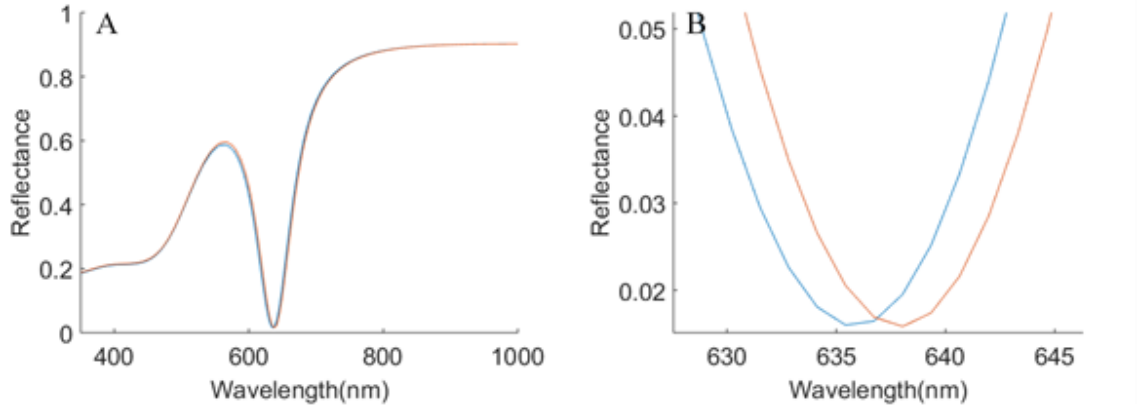

Figure 3.25 Simulated spectra for SPR sensor with SAM immobilised IgG ligands in response to PBS buffer and anti-Rabbit IgG sample assuming 38% coverage of same ligand density as on the particles. (A) Full Spectra. (B) Spectra magnified to the attenuation peaks. The blue spectrum is the result in the buffer solution and the red is in the anti-IgG sample.

The first simulation overestimated the coverage of the ligands as the particles only had a coverage of 38% while the second simulation underestimated it as it ignored the curvature of the particles providing a larger surface area. It is difficult to estimate an equivalent ligand density due to the 3-dimensional distribution of the ligands on the particle, but the actual ligand density must fall between those two estimations. Therefore, if the estimated ligand density matches that in the particle-modified SPR biosensor, the traditional SPR biosensor should have a response between 2.3 nm and 5.6 nm. This range of values does not deviate far from the response of 2.8 nm obtained in the particle-modified SPR biosensor as discovered in Section 3.2.5

Although the sensitivity of the particle-modified SPR biosensor is in the same ballpark of the traditional SPR biosensor, the location of the analyte does influence the sensitivity of the biosensor. To assess the effect of the binding location towards the sensitivity, the binding analyte concentration obtained from Section 3.2.6.3 was simulated at various distances from the sensor surface. Figure 3.26 shows a depiction of the distribution of the biorecognition molecules and the analyte molecules at the surface of each type of biosensor. Because of the particles' presence, the ligand and analyte molecules are immobilised at different distances away from the sensor surface. And almost all of them are further away than if they were covalently attached to an alkanethiolate SAM. The

theory in Section 1.2.1 states that the evanescent field strength decreases exponentially with the penetration depth according to eq. (1.4). A simulation of the wavelength shifts due to analytes at different distances is shown in Figure 3.27. For the same local concentration of analyte, the exponentially decreasing sensitivity can be seen clearly. As a combined effect, the particle-modified biosensor generally has a lower sensitivity than a traditional biosensor if the binding density is similar.

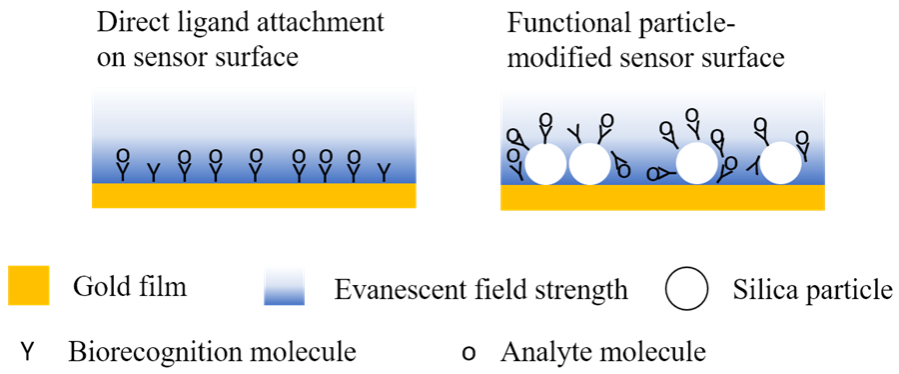

Figure 3.26 Illustration of the different positions of the captured analyte molecules on a sensor surface with ligands attached directly and a surface with particle modification. The diagram is not drawn to scale.

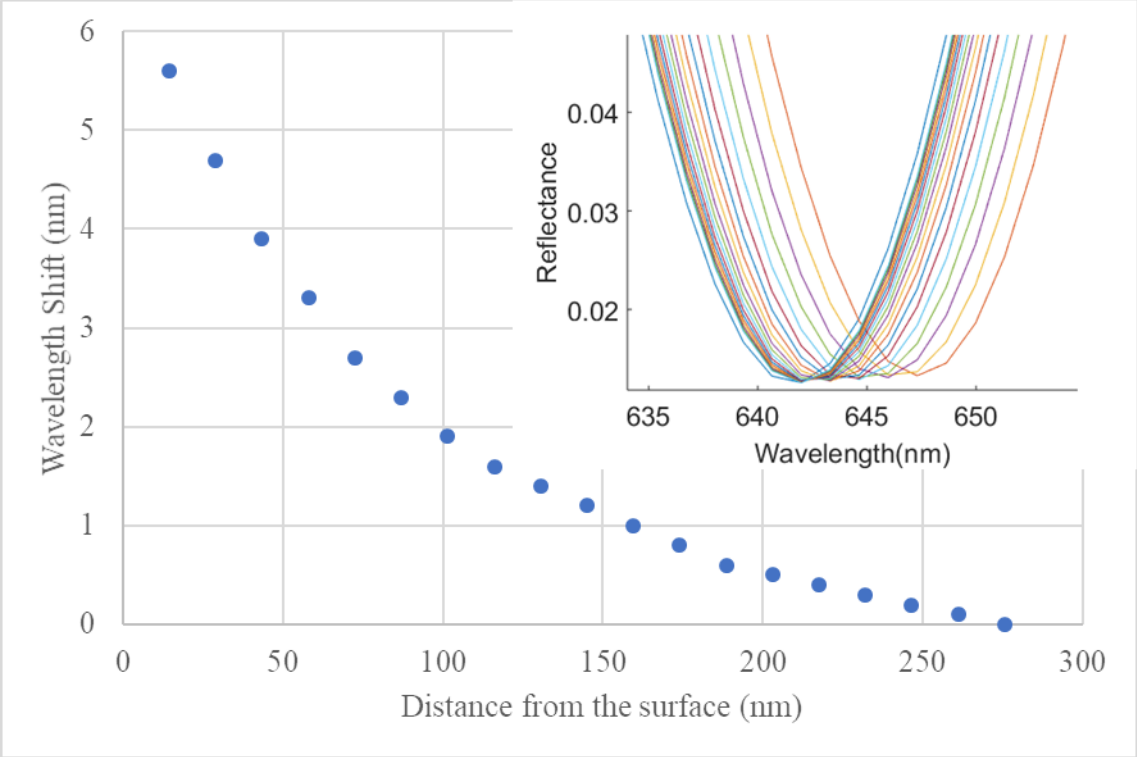

Figure 3.27 Relationship between the sensor response and the analyte's distance from the surface. The local concentration of the analyte is assumed to be 109.4 mg/ml. The simulation is done in a discrete fashion where a layer of 14.5 nm of IgG solution is situated at various distances from the sensor surface.

All the simulations above assumed matching ligand density on the biosensors and the simulated response of a traditional sensor is much smaller than the experimental response (over 20 nm) obtained in Section 3.2.5.1. This is probably due to the surface having a higher ligand density in practice on the surface using the alkanethiolate SAM immobilisation method. An SPR biosensor surface with a higher ligand density captures more analyte from the same concentration of sample, therefore, has a higher apparent sensitivity.

3.2.7 Kinetic Model of the Binding Interaction

3.2.7.1 Particle-modified SPR Biosensor under Stop-flow Condition

The reference-adjusted sensorgram in response to 100 µg/ml anti-Rabbit IgG (first 30 mins of binding) is fitted to the Langmuir model described in 2.7.1 (Figure 3.28B). The fit is bad as the modelled curve reaches an equilibrium earlier than the experimental data.

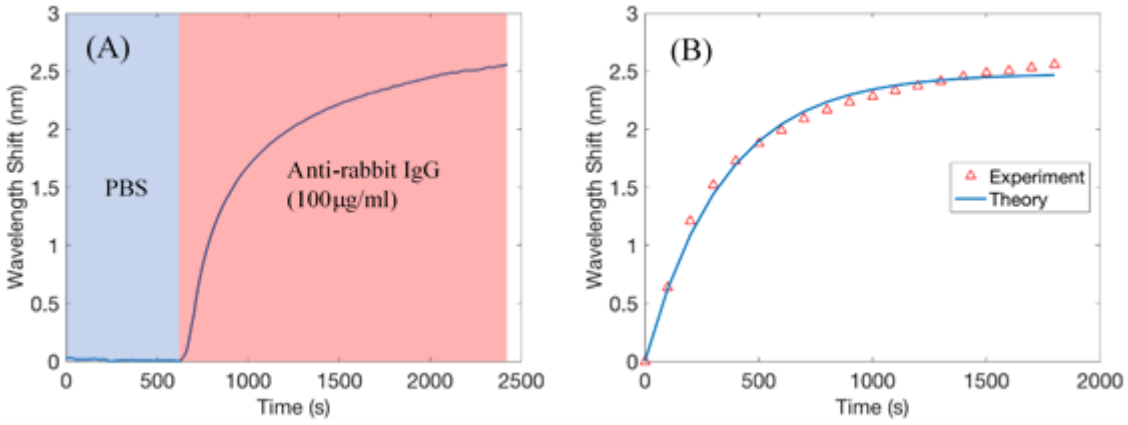

Figure 3.28 (A) Reference-adjusted sensorgram showing the detection of 100 µg/ml anti-Rabbit IgG for the first 30 minutes after injection. The vertical axis shows the wavelength shift from the baseline for PBS buffer solution. (B) Data points from the sensorgram and the fitted Langmuir kinetic binding model.

Two considerations were made to improve the fit of the Langmuir model. Firstly, at the start of the injection, the sample took a while to enter the chamber resulting in a slow initial response. To account for this transition period, the sensorgram was extrapolated backwards in time, resulting in a virtual time zero (Figure 3.29A). Figure 3.29B is obtained by fitting the Langmuir model to the adjusted data. The residue value is 0.1006 and the fit has not improved visually. The simulated sensorgram still reaches equilibrium faster than the experimental data.

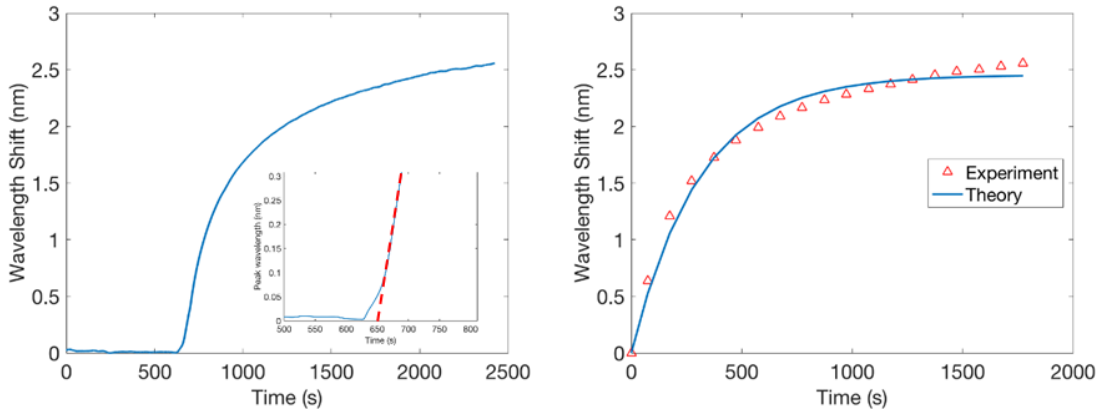

Figure 3.29 (A) Reference-adjusted sensorgram showing the detection of 100 µg/ml anti-Rabbit IgG for the first 30 minutes after injection with an extrapolated time zero. The insert shows the magnified curve between 500s and 800s. The virtual time zero starts at 650 s. (B) The corrected data and the fitted Langmuir binding model.

Secondly, the mass transfer effect may be prominent because the experiment was done in a stop-flow configuration. In the Langmuir model, the concentration of the adsorbate is assumed to be constant. However, the antigen/antibody binding often happens on a surface where the capture ligand is immobilised. In such a scenario, the rate of the binding and dissociation may be limited by the binding reaction itself and/or by mass transport to the surface [233].

The Langmuir model accounting for the mass transfer effect (as described in Section 2.7.2 eq. (2.7) and eq. (2.8)) fits well in Figure 3.30. This suggests that the IgG/anti-IgG binding on the particles is limited by the mass transfer of analyte from the bulk solution to the sensor surface.

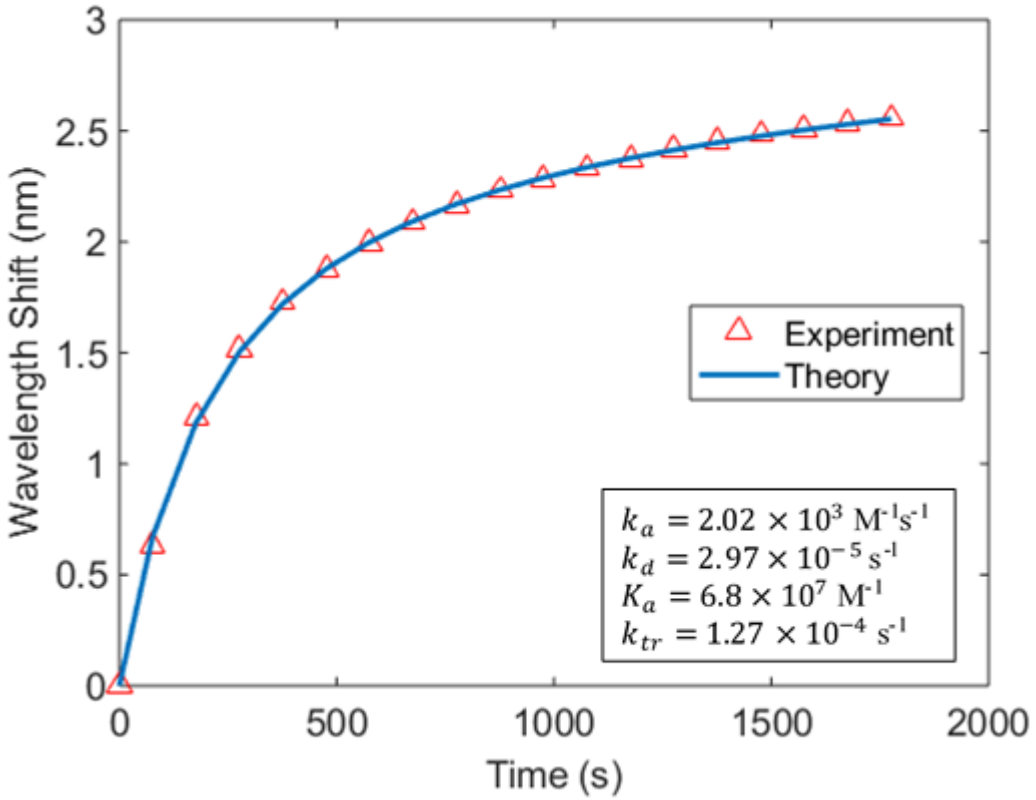

Figure 3.30 Sensorgram data points of the particle-modified biosensor fitted to the Langmuir model with mass transfer consideration. The data was obtained sensing 100 µg/ml anti-Rabbit IgG under a stop-flow configuration.

The Langmuir model with mass transfer consideration fits well to the sensor data for various analyte concentrations and the resultant parameters are shown in Table 3.6. The association rate constant and the dissociation rate constant increase as the concentration increases indicating that both the association and dissociation are analyte-concentration-dependent to approximately the same level. The affinity constant stays relatively constant. The mass transfer rate constant stays relatively constant too.

Table 3.6 The parameters of the Langmuir model with mass transfer consideration fitted to sensorgram data for various analyte concentrations on the particle-modified gold surfaces under stop-flow.

Analyte Concentration c_0 (µg/ml)	**Association Rate Constant k_a ($\times 10^3$ $M^{-1}s^{-1}$)**	**Dissociation Rate Constant k_d ($\times 10^{-5}$ s^{-1})**	**Mass transfer Rate Constant k_{tr} ($\times 10^{-4}$ $M^{-1}s^{-1}$)**	**Affinity Constant K_a ($\times 10^7$ s^{-1})**
50	1.12	1.63	1.15	6.87
100	2.02	2.97	1.27	6.80
150	3.16	4.76	1.30	6.64
200	4.06	5.83	1.12	6.96
250	5.13	8.23	1.23	6.23
300	6.10	9.10	1.25	6.70

3.2.7.2 Traditional SPR Biosensor under Stop-flow Condition

To compare the binding kinetics of antibody/antigen interaction on traditional SPR biosensors, the sensorgram data obtained on a surface with an alkanethiolate SAM immobilisation was also fitted to the Langmuir model. Results with and without a virtual zero are shown in Figure 3.31. As expected, the simple Langmuir model does not fit the experimental data well even though the slow start was accounted for.

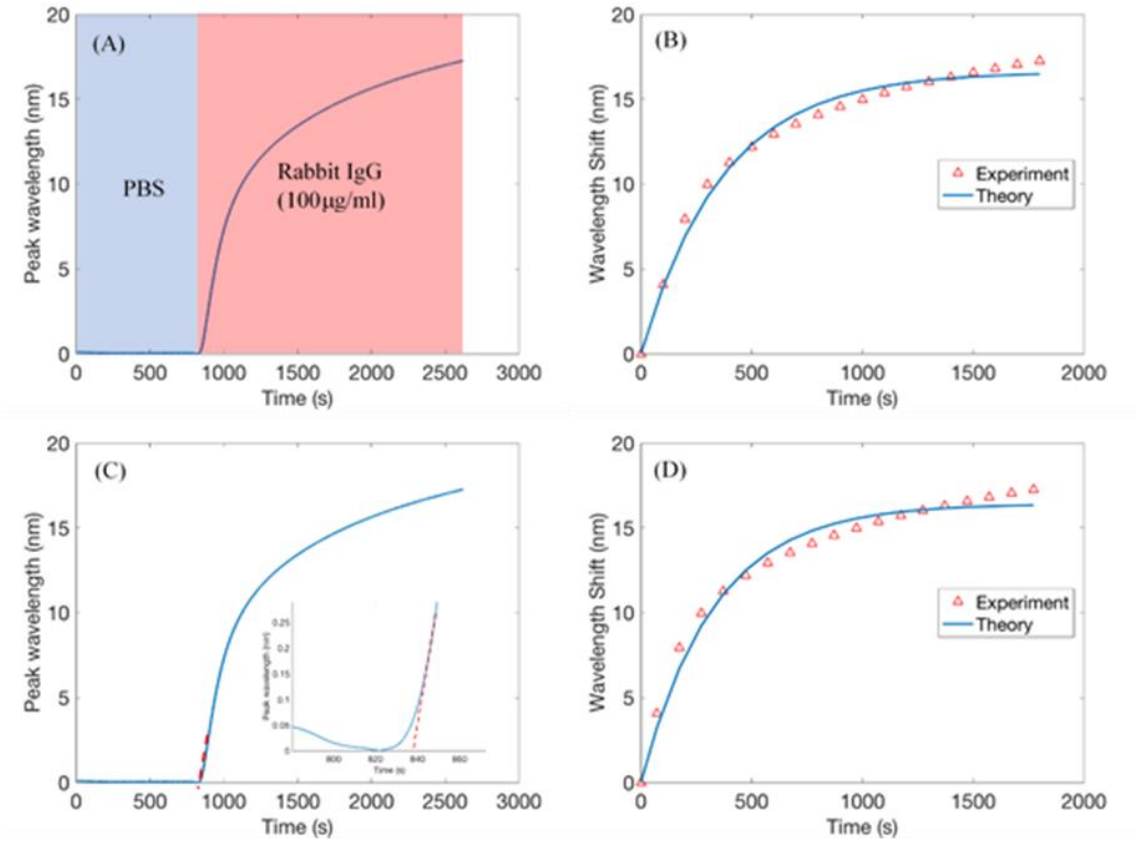

Figure 3.31 (A) Reference-adjusted sensorgram showing the detection of 100 µg/ml anti-Rabbit IgG on a gold surface with alkanethiol SAM for the first 30 minutes after injection. The vertical axis shows the wavelength shift from the baseline for PBS buffer solution. (B) Data points from the sensorgram fitted to the simple Langmuir kinetic model. (C) Sensorgram with an extrapolated virtual time zero. The insert shows a magnified view from 780s to 860s. (D) Data points from the zero-adjusted sensorgram fitted to the simple Langmuir kinetic model.

After the mass transfer to the surface is accounted for in the model, it fits well as shown in Figure 3.32. The fitted parameters when compared with that of the particle-modified surface show similarities in the binding kinetics but deviations in the mass transfer. The similar association and dissociation rate constant suggest that the overlaying particles have little effect on the binding mechanism between the IgG and anti-IgG molecules. The mass transfer rate constant on the flat gold film almost doubles that on the particle-modified gold film and indicates a faster mass transfer of the analyte to the sensor surface. More tests with various concentrations of anti-Rabbit IgG on flat gold films confirmed this and the fitted parameters are tabulated in Table 3.7 (concentrations higher than 150

µg/ml could not be tested due to the large shift causing the theoretical peak to fall out of the max wavelength on the halogen white light spectrum).

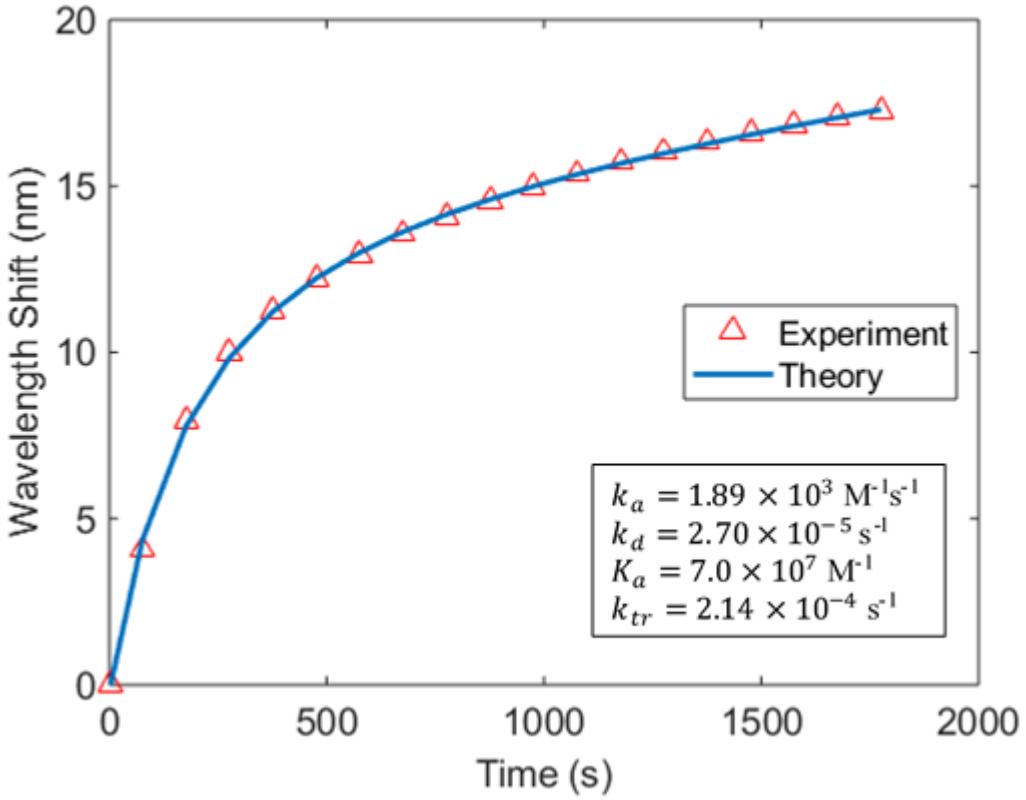

Figure 3.32 Sensorgram data points obtained on a gold surface with alkanethiolate SAM immobilisation fitted to the Langmuir model with mass transfer consideration. The data was obtained sensing 100 µg/ml anti-Rabbit IgG in a stop-flow configuration.

Table 3.7 The parameters of the Langmuir model with mass transfer consideration fitted to the sensorgram data points for the detection of various analyte concentrations under a stop-flow configuration.

Analyte Concentration c_0 (µg/ml)	**Association Rate Constant k_a ($\times 10^3$ $M^{-1}s^{-1}$)**	**Dissociation Rate Constant k_d ($\times 10^{-5}$ s^{-1})**	**Mass transfer Rate Constant k_{tr} ($\times 10^{-4}$ $M^{-1}s^{-1}$)**	**Affinity Constant K_a ($\times 10^7$ s^{-1})**
50	0.95	1.39	2.36	6.83
100	1.89	2.68	2.85	7.05
150	2.76	3.91	2.23	7.06

Mass transfer coefficients depend on many parameters including the physical properties of the fluid, the geometry of the interface along with its dimensions, and the average velocity [233]. In a series of experiments, the property of the fluid stayed unchanged as the same sample and buffer solution were used. The average velocity was zero in the stop-flow configuration. The discrepancy in the resultant mass transport rate, therefore, is largely because of the geometry of the interface, in this case, the topography of the surface. On the particle-modified sensor, there is an extra phase between the bulk and the surface as shown in Figure 3.33. The addition of this extra phase changed the mass transfer rate.

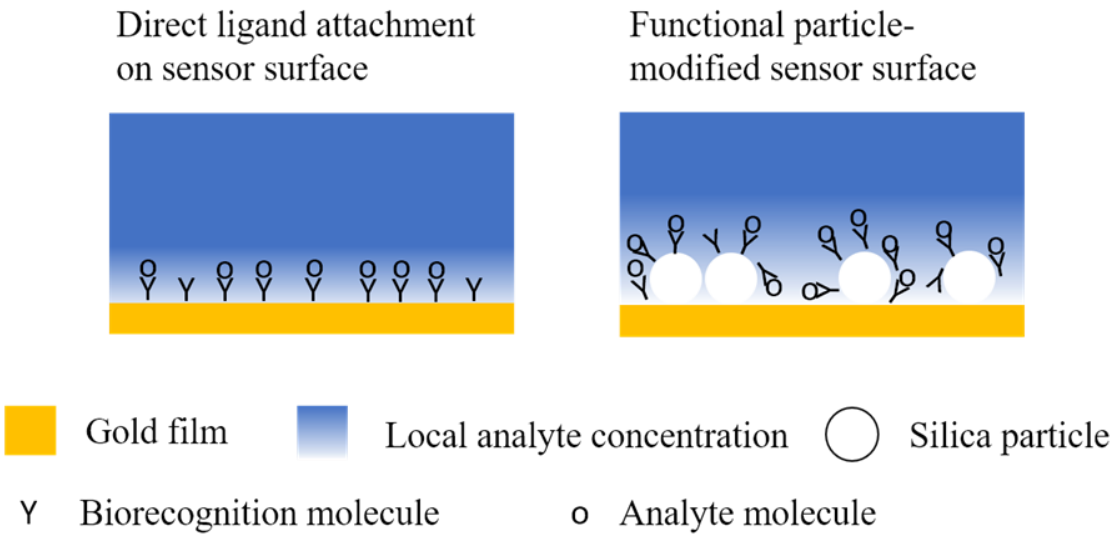

Figure 3.33 Illustration of the different mass transfer behaviour on flat gold surfaces and on particle-modified gold surfaces. A stop-flow configuration is assumed for both surfaces. The diagram is not drawn to scale.

In summary, the binding between rabbit IgG and anti-Rabbit IgG exhibited similar association and dissociation rates on the particle-modified SPR biosensor and on the gold surface with alkanethiolate SAM. In a stop-flow configuration, the binding on both surfaces is largely limited by the mass transfer of the analyte to the biorecognition sites. And the complex 3-dimensional particle-modified surface results in a slower mass transfer rate than on a flat gold surface in a stop-flow configuration.

3.2.7.3 Particle-modified SPR Biosensor under Continuous Flow Condition

To study the binding kinetics on the immobilised submicron silica particles by physical adsorption aided by mechanical pressure, the sensorgram data discussed in Section 3.2.5.2 was fitted to the Langmuir model. Figure 3.34 shows the raw data points fitted to the model without any modification. The model fits well, and the apparent association coefficient is 5.09×10^3 $M^{-1}s^{-1}$, and the dissociation coefficient is 1.68×10^{-5} s^{-1}.

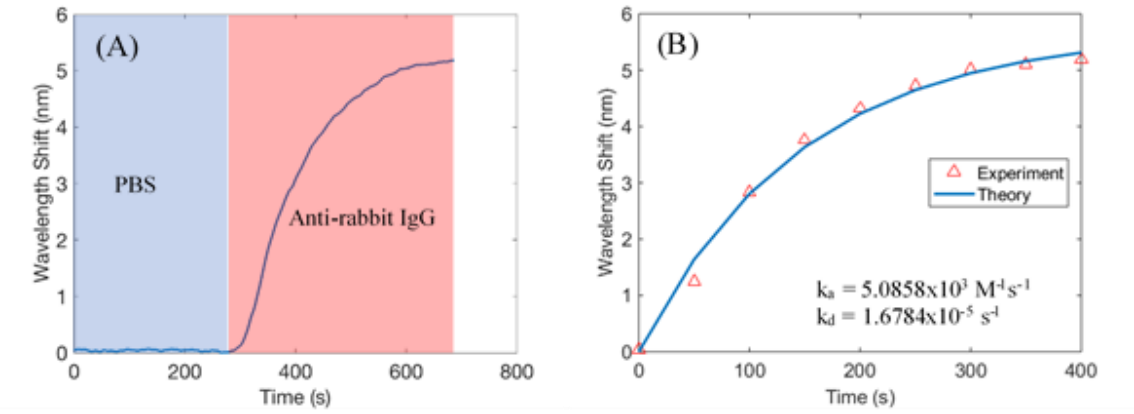

Figure 3.34 (A) Sensorgram showing the detection of 200 µg/ml anti-rabbit IgG for the first 6.5 minutes after the injection. The vertical axis shows the wavelength shift from the baseline for the PBS buffer solution. (B) Data points from the sensorgram fitted to the simple Langmuir adsorption model.

Once again, a slower process can be seen at the start of the injection where the sample entered the channel and the anti-IgG started to bind to the IgG. The sensorgram was adjusted for this phenomenon with a pseudo time zero, as before, and a more informative kinetic curve was obtained in Figure 3.35. The adjusted sensorgram fits to the Langmuir model better than the raw data. The corresponding association coefficient and dissociation coefficient are $6.91 \times 10^3\ M^{-1}s^{-1}$ and $3.37 \times 10^{-5}\ s^{-1}$.

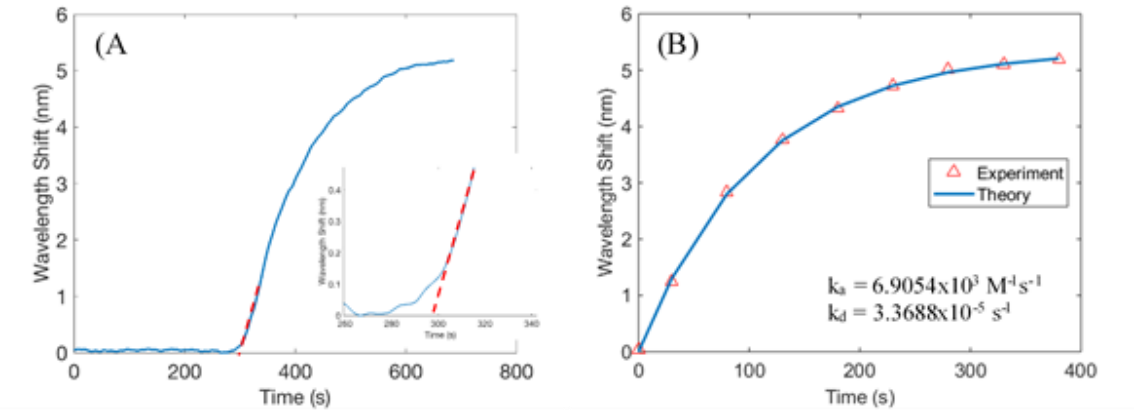

Figure 3.35 Sensorgram showing the detection of 200 µg/ml rabbit IgG for the first 6.5 minutes after the injection with an extrapolated time zero for binding event. The insert shows the magnified curve between 250 s and 340 s. The virtual time zero starts at 298 s. (B) The adjusted data fitted to the simple Langmuir adsorption model.

The kinetic behaviour differs greatly from the case where the submicron silica particles were immobilised by thiol silane. This may be attributed to how the sample flows. In the case of thiolsilane immobilisation, the particles were only on the surface of the gold film and were analysed under stop-flow. However, in the case of mechanical immobilisation, the sensor was used under a continuous flow configuration. This was because the particles loosely filled the entire channel and were affected by the flow motion, thereby influencing the signal recorded when the flow stopped. In the continuous flow process, the mass transfer was from a replenishing sample to the binding sites, without a depletion zone. The adsorbate concentration at the adsorbent surface remained close to the analyte concentration in the bulk sample as predicted by the rapid mixing model. Therefore, the system reduced to a simple Langmuir kinetic model.

The experimental data was also fitted to the Langmuir model with mass transport considerations and the result is shown in Figure 3.36. The model fits well as expected. The affinity constant is unchanged from the one in Section 3.2.7.1, but the mass transport rate is 3 orders of magnitude higher than the stop-flow configuration. This supports the suggestion made above that the mass transport to the surface is much faster in the continuous flow configuration than in the stop-flow configuration. The binding kinetics was not mass transport limited therefore can be approximated to the basic Langmuir model.

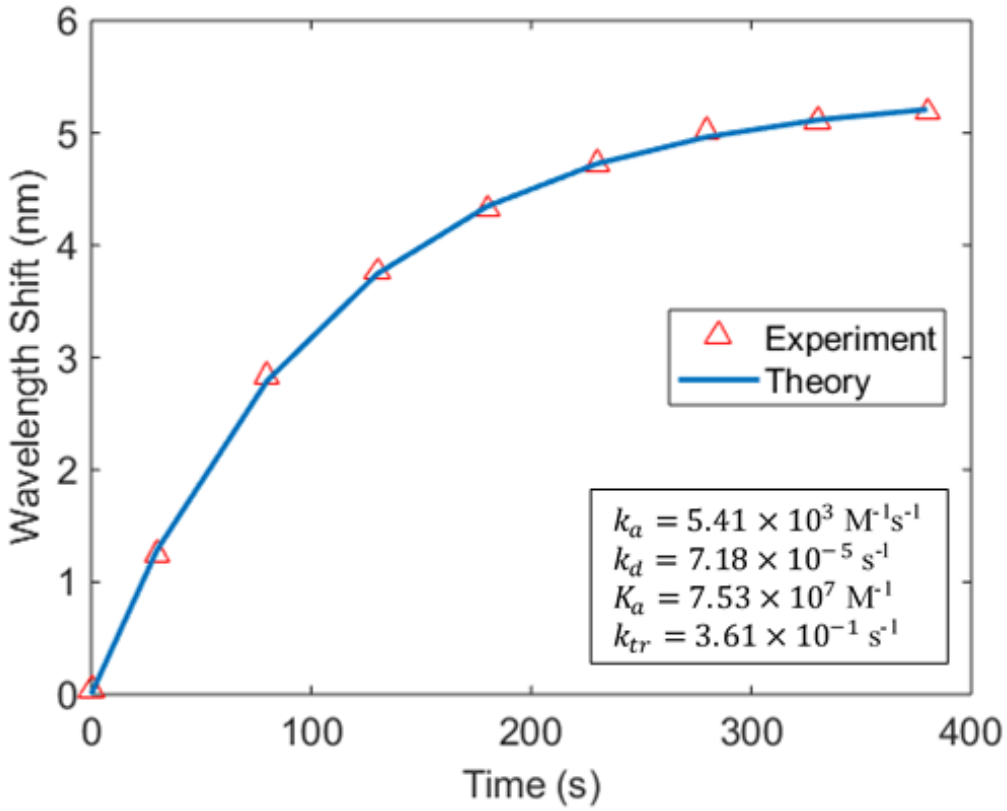

Figure 3.36 Sensorgram data points obtained on a sensor with particles immobilised by pressure-aided physical adsorption fitted to the Langmuir model with mass transfer considerations. The data was obtained when sensing 200 µg/ml anti-Rabbit IgG in a continuous flow configuration.

Experimental data points for detecting various sample concentrations were fitted to the mass-transport-limited Langmuir model and the parameters are tabulated in Table 3.8. The affinity constant is relatively unchanged, and the rates of mass transport are high in all models.

Table 3.8 The fitted parameters of the Langmuir model with mass transfer at various analyte concentration on the sensor modified with particles using aided adsorption under continuous flow.

Analyte Concentration c_0 (µg/ml)	**Association Rate Constant k_a ($\times 10^3$ $M^{-1}s^{-1}$)**	**Dissociation Rate Constant k_d ($\times 10^{-5}$ s^{-1})**	**Mass transfer Rate Constant k_{tr} ($\times 10^{-1}$ $M^{-1}s^{-1}$)**	**Affinity Constant K_a ($\times 10^7$ s^{-1})**
100	2.36	3.28	3.19	7.20
200	5.41	7.18	3.61	7.53
300	7.95	9.93	3.25	8.01

3.3 Summary

In this chapter, the particle immobilisation strategy on an SPR biosensor was explored. Two techniques employing silica particles as ligand carriers were proposed.

The first technique used thiolsilane coupling to fixate the silica particles on a gold surface. The coverage by such method was found to be roughly 38%. The sensitivity of the particle-modified surface towards a bulk medium was found to be unchanged from an unmodified surface while the sensitivity towards an antibody antigen interaction is found to be lower than if the capture ligands were directly immobilised by an alkanethiolate SAM on the surface. Theoretical simulation revealed that although the distance of the binding interaction to the surface affected the sensitivity, the said difference was mainly due to the discrepancy in the ligand density by the different immobilisation strategies.

The second technique used mechanical pressure to immobilise the particles on a gold surface using a flexible PDMS channel. The channel deformed and pressed the particle bed close to the sensor surface. The subsequent antigen-antibody binding experiment showed a slightly lower sensitivity to the thiol treated surface, due to a lower particle density in the evanescent field. The particle packing near the Au film was estimated to be 33%.

As expected, the binding kinetics between IgG and anti-IgG were found to be unchanged for the two particle modification systems, with similar association and dissociation rate constants for the same analyte concentration. The difference in mass transport was associated with the flow procedure. In the continuous flow set up, the binding followed the simple Langmuir kinetics model. In the stop-flow experiment, the kinetic behaviour was greatly affected by the mass transport of the analyte to the sensor surface.

Overall, we demonstrated an SPR biosensor with the gold surface modified by sub-micron silica particles. These particles acted as carriers of the biorecognition ligands. The particle-modified sensor was sensitive towards the RI change for both bulk medium and the IgG/anti-IgG interaction on the surface of the particles.

Although the viability of a particle-modified SPR sensor was shown, the gold surface modification with particles is below 50 %, further development of the particle fixation technique is required. This with be explored in the next chapter.

Chapter 4 Column-modified Spectral SPR Biosensor

4.1 Introduction

The previous chapter explored SPR biosensors with the particles as an overlaying layer at the surface. The continuous flow experimental results showed that the kinetics did not differ from a traditional sensor with a SAM immobilisation layer. The particles could be considered as a new surface immobilisation matrix and its behaviour resembled traditional SPR biosensors with other immobilisation layers or matrices.

To further simplify the preparation step and in the hope of improving the sensitivity by improving the particle coverage on the sensor surface, the particle packing technique is further optimised in this chapter. As the chamber is filled with the IgG-immobilised particles, its entirety can be considered as the immobilisation and binding matrix. This greatly affects the mass transport kinetics of the analyte and the sensor shows responses, which to the best of our knowledge, have never been reported.

This chapter introduces the sensor configuration first. The results section reports on the IgG loading on the silica gel particles and the sensor's sensitivity towards IgG/anti-IgG binding. It then explores the sensorgrams' pulsation due to fluid pumping and presents an algorithmic solution to data smoothing. Finally, the chapter studies the kinetics behaviour of the column-modified biosensor and proposes a bi-directional mass transport model to explain the phenomena.

4.1.1 Silica Column Assembly

In a traditional chromatography column, a cylindrical tube filled with particles/beads is used. In the configuration of the column-modified SPR sensor, we have a channel with

four flat walls. Figure 4.1 shows a cartoon of the column with the particles packed in the channel. By adding a filter plug at the outlet end, the particles get trapped in the channel and can pack behind the plug (although probably not in the regular pattern of the cartoon). The channel depth is also increased to 1 mm from 0.1 mm in the model in Section 3.1.1.2. as the mechanical deformation of the PDMS channel to compress the particles on the Au surface is no longer necessary and a deeper channel allows the plug to be relatively large at 1 mm x 1 mm x 1 mm and therefore easier to manipulate.

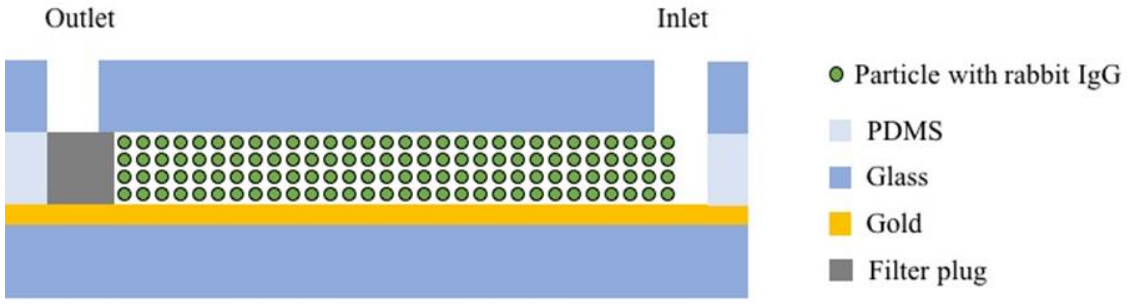

Figure 4.1 Illustration of a particle modified SPR sensor using the injection method. The diagram is not drawn to scale.

Due to the increase in the channel volume, submicron particles are no longer economically the size of choice as the yield is low and the fabrication cost is high. Instead, commercial silica gel that is commonly used in chromatography is explored as a cheap and readily available alternative. The particles have a size range of 15±10 μm. The details of the materials and method can be found in Section 2.5.

4.2 Results and Discussion

4.2.1 Antibody Loading on Silica Gel Particles

Various concentrations of rabbit IgG were immobilised on the particle surface following the steps introduced in Section 2.3.2.2. The loading efficiency is plotted in Figure 4.2. Carbodiimide coupling again offers higher efficiencies at all concentrations. Therefore, it was the choice for all subsequent experiments. At low concentrations, the loading efficiency is around 100%. However, after taking the concentration of the particles (50 mg/ml) into account, 200 µg/ml of rabbit IgG only has a ligand-to-particle ratio of 4 µg/mg. This value is lower than the ratio of IgG to submicron silica particles in the previous chapter. To achieve a higher loading mass, the IgG concentration of 1000 µg/ml was used, and the loading ratio was 14 µg/mg. The lower efficiency might be attributed to the smaller surface-to-volume ratio of the larger silica gel particles and therefore a lower loading capacity per mass of the particles.

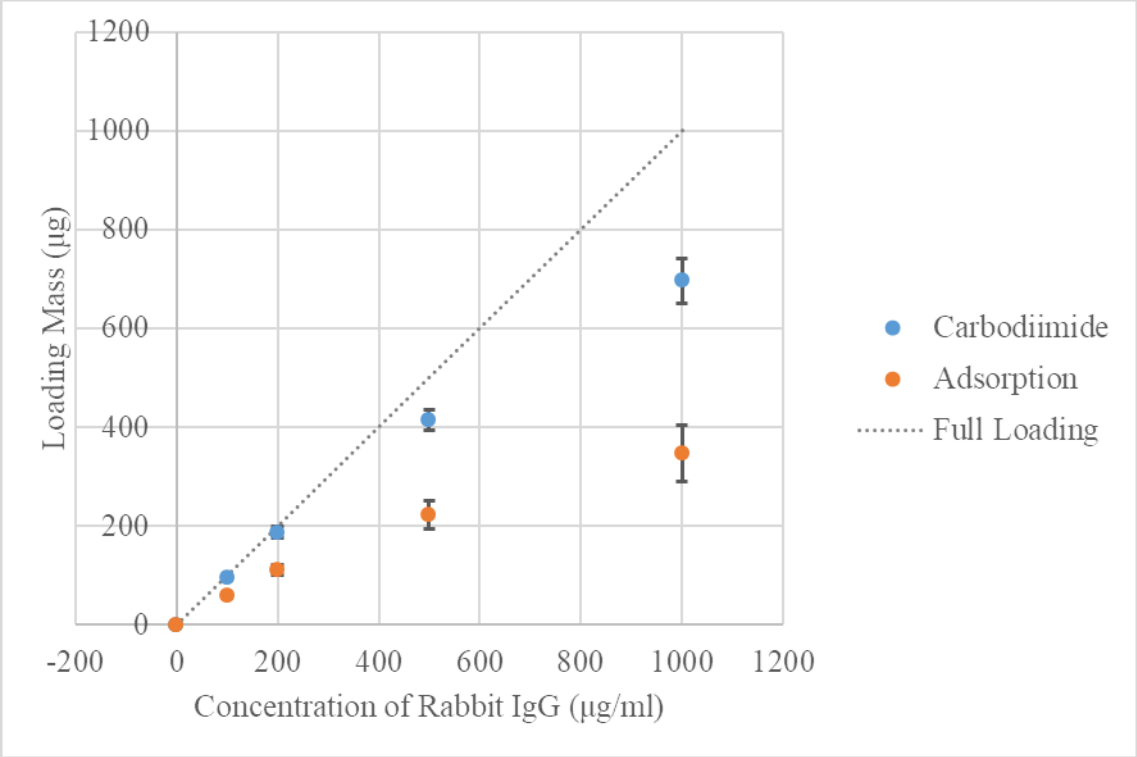

Figure 4.2 Loading efficiency of Rabbit IgG on 50mg silica gel particles (15 µm mean diameter) in 1 ml PBS buffer solution.

4.2.2 Filtering of Periodic Noise on the Sensorgrams

Figure 4.3 shows the sensorgram of the column-modified SPR biosensor detecting a sample containing 200 µg/ml of anti-Rabbit IgG. The sensorgram has much more noise than those obtained in the previous sections. Unlike the noise encountered before which is random, the noise here appears to be periodical. This is attributed to the pressure fluctuation when the peristaltic pump delivered the solution to the channel. In a traditional or particle-layer-modified SPR biosensor, there was no filter plug blocking the exit of the channel. The pressure of the liquid in the channel was equalised to the atmospheric pressure at all time despite the pulsation of the pump. When the filter plug was in place, the pressure inside the channel was no longer equalised immediately. Thus, the pulsation of the pump was reflected in the signal on the sensorgram as a fluctuating noise. To prove

this hypothesis, various flow speeds were tested, and the resulting frequencies of the noise are recorded in Table 4.1.

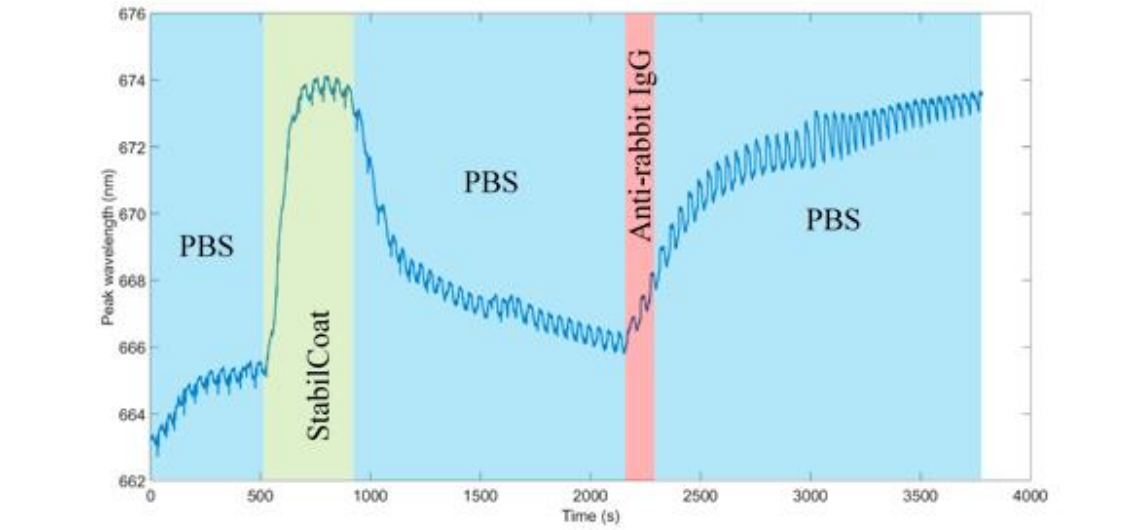

Figure 4.3 Sensorgram showing the raw data of the column-like SPR sensor detecting anti-Rabbit IgG binding to the Rabbit IgG on the surface of the particles in a continuous flow configuration.

Table 4.1 Observed noise frequencies and the corresponding flow rates.

Pump speed setting	**Observed average flow rate (ml/min)**	**Noise frequency (Hz)**
0.66	0.095	0.019
0.68	0.109	0.024
0.70	0.126	0.038

To correct for this pulsation noise, a band-stop filter algorithm was used. The filtered sensorgram is shown in Figure 4.4. The algorithm successfully eliminated periodic noise in the signal while retaining the information of the refractive index change. All subsequent wavelength shift calculations and the kinetic analysis are extracted from the filtered signal instead of the raw data.

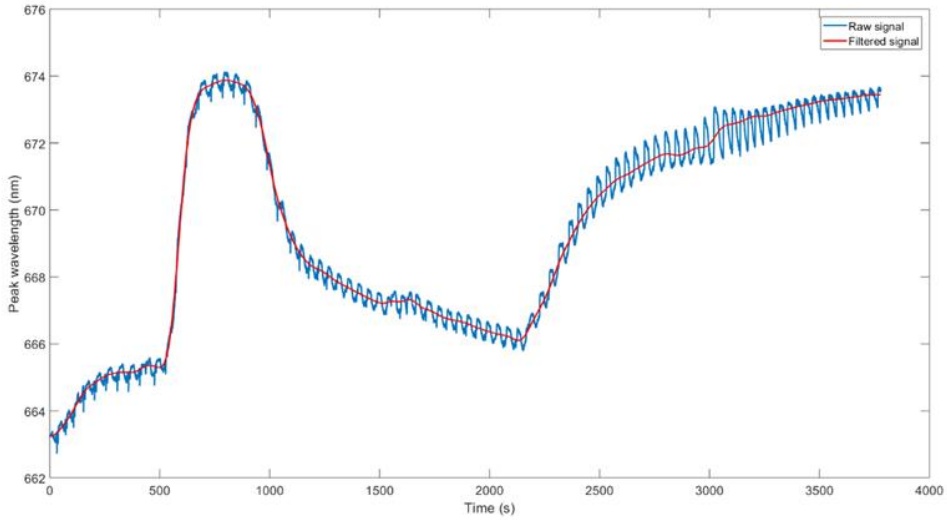

Figure 4.4 Sensorgram showing the raw signal (blue) of the column-like SPR sensor detecting the Rabbit IgG/anti-Rabbit IgG binding in a continuous flow configuration and the filtered signal (red). A band-stop Butterworth filter was applied to eliminate frequencies around 0.024Hz using MATLAB.

The idea of using band-stop filters to eliminate the periodic noise arising from the pulsation has a much wider implication. In most commercial high-performance liquid chromatography (HPLC) systems equipped with reciprocating pumps, dampening devices are used to reduce the flow pulsations. The dampening device increases the complexity of the fluid delivery system and adds cost to the setup. A simple algorithmic approach as shown here, is perhaps better if the detection period is much longer than the cycle period of the pulsations. It is especially favourable when the system has constraints on budget, complexity and space, for instance, in a point-of-care setting. In the scope of this thesis, the band-stop filter has a designed extinction frequency at 0.024 Hz and it works for all the flow rates used in the project. For a wider application, an extra algorithm can be employed to determine the frequency of the pulsation before having a filter designed accordingly.

4.2.3 Sensitivity Towards IgG/anti-IgG Interaction

Figure 4.5 shows the filtered sensorgram by itself when detecting a 500 µl sample containing 200 µg/ml of anti-Rabbit IgG. At the start of the experiment, PBS buffer

solution was flowed in the column to stabilise it. During the washing phase after the StabilCoat blocking step, the signal does not drop sharply as in the experiments discussed in Section 3.2.5.2. After approx. 2200 s it gradually drops to approx. 10% of its peak value. When the sample was flowed in the column, the signal started to increase, but it did not stop or decrease even after the next flushing phase. This behaviour also differs from traditional SPR biosensors or the particle-layer-modified ones. The kinetics of the binding event is studied in detail later in Section 4.2.4.

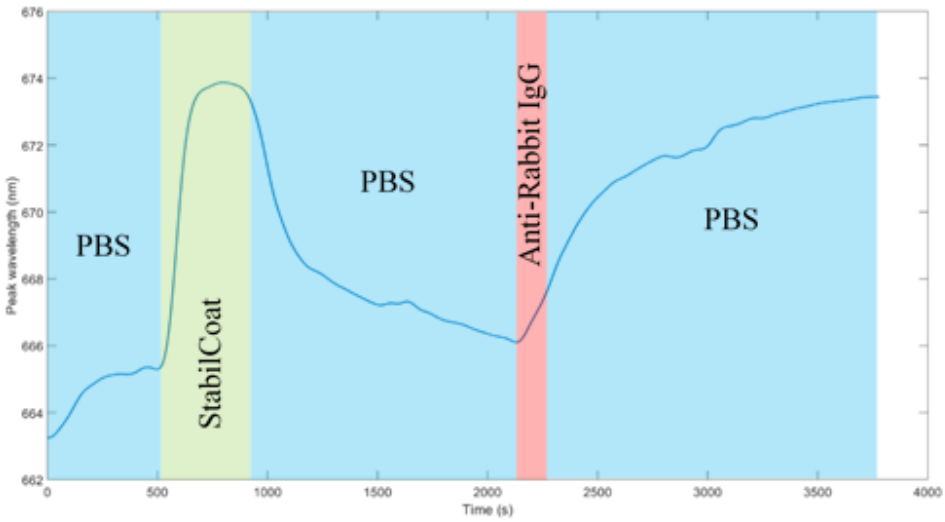

Figure 4.5 Filtered sensorgram showing the SPR sensor detecting anti-rabbit IgG binding to the particles in a continuous flow fashion in an affinity chromatography. The coloured block indicates the duration that a certain type of solution that is flowing in the column.

To our best knowledge, this is the first time an unlabelled analyte's behaviour is observed in a particle column using an integrated SPR biosensor. It is possible to label the analyte molecule with a reporter molecule (e.g. a chromophore) to visualise its behaviour within the column but the presence of this agent may alter the nature of the analyte-ligand interaction [247] and also its mass transport within the column. A few researchers reported experiments done using an SPR biosensor and a liquid chromatography system together [204, 205, 248], but all of them had the sensor and the LC system in series. The

integration was, as they call it, post-column. The column-modified SPR biosensor is the first integration that has the sensor online with the column.

The difference between the peak extinction wavelengths before the flow of the sample and at the end of the experiment was recorded as the signal for a specific analyte concentration. In the experiment shown in Figure 4.5, the shift of wavelength is 7.4 nm for 200 μg/ml of anti-rabbit IgG. Fig. 4.13 shows a graph of the results of a series of experiments with various analyte concentrations. The maximum wavelength shift is proportional to the analyte concentration in the region between 50 to 300 μg/ml as expected.

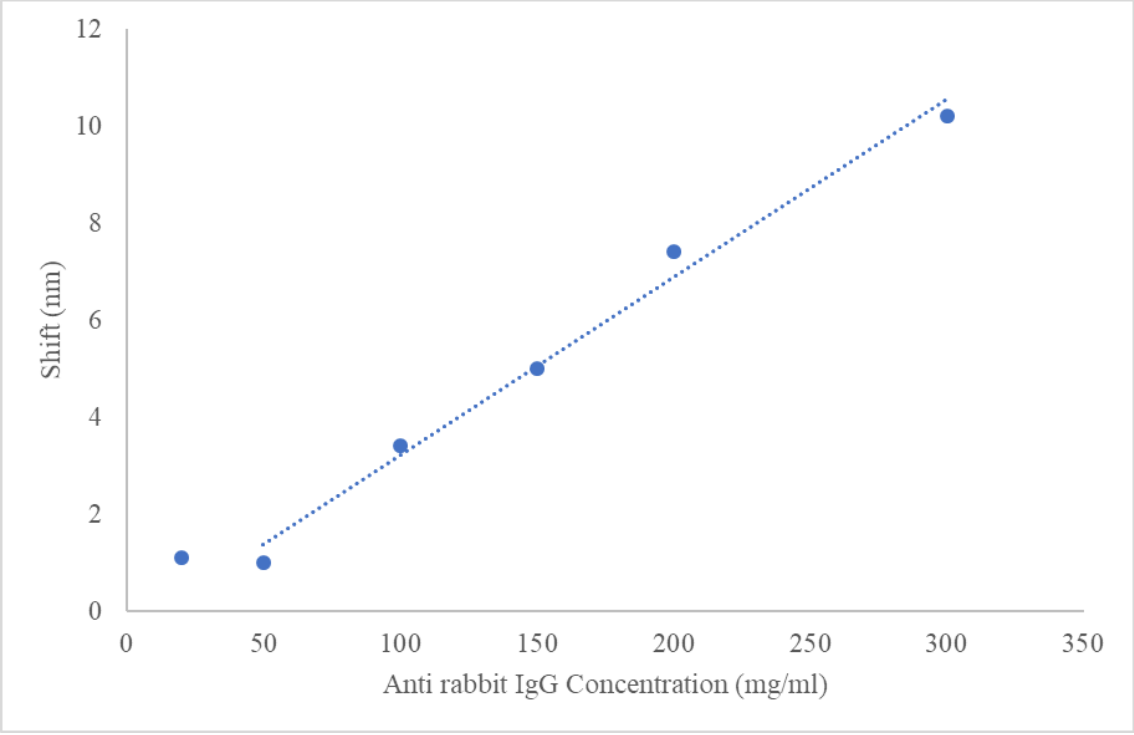

Figure 4.6 Plot of the maximum wavelength shifts when detecting various concentrations of anti-Rabbit IgG.

The sensitivities of the column-modified SPR biosensor, the two types of particle-layer-modified SPR biosensors and a traditional one with a SAM immobilisation layer are tabulated in Table 4.2. The sensitivity is slightly higher for the column configuration. However, it is still much lower than the SAM configuration.

The commercial silica gel particles are polydisperse according to the manufacturer. The particle sizes range from 5 μm to 25 μm. Polydisperse particles when packed provide a higher packing density according to the studies in the literature [249 – 251]. A higher packing density results in a higher ligand density, and therefore, potentially a higher sensitivity towards IgG/anti-IgG interaction within the evanescent field as simulated in Section 3.2.6.4. Therefore, among all the particle modification techniques, the packed polydisperse silica gel particles provide the highest sensitivity. The large difference between SAM immobilisation and particle immobilisation strategies are due to the difference in the ligand capacity as studied before.

Table 4.2 Sensitivity comparison among SPR biosensors with various immobilisation strategies.

Method of Immobilisation	**Sensitivity (mm/M)**	**Sensitivity (RIU/M)**
Alkanethiolate SAM	31.8	15630
Particle layer bound by thiolsilane coupling	4.36	2144
Particle layer bound by mechanical pressure	3.90	1917
Particle bed in a column	5.55	2729

Nonetheless, the particle column configuration has potential. It simplifies the sensor preparation procedure when compared to the multiple chemical derivatisation steps in a traditional SPR biosensor experiment and is suitable for many affinity ligands. The column could also be extended to separation science as intended with chromatography with the benefit of an online refractive index detector.

The particle column was also tested for its sensitivity towards nonspecific binding. In this test, an anti-Rabbit IgG sample was injected after an anti-Mouse IgG sample of the same concentration. Each of the washing steps was shortened with 2 ml of PBS buffer solution to maintain similar experiment duration in total. The resultant sensorgram is shown in

Figure 4.7. It is seen that the anti-Mouse IgG sample did not give a binding signal like the anti-Rabbit IgG sample because the former does not bind specifically to the Rabbit IgG on the particles. The signal increased slightly with the anti-Mouse IgG sample in the column due to the increase in the average refractive index in bulk from PBS buffer solution. This increase was similar to the increase attributed to the StabilCoat mix and was not caused by binding as the sensorgram went back down when the column was flushed with PBS buffer solution in the next phase. The anti-Rabbit IgG sample, however, behaved similarly as discussed in Section 4.2.3 resulting in a continual signal both in the injection and flushing phases.

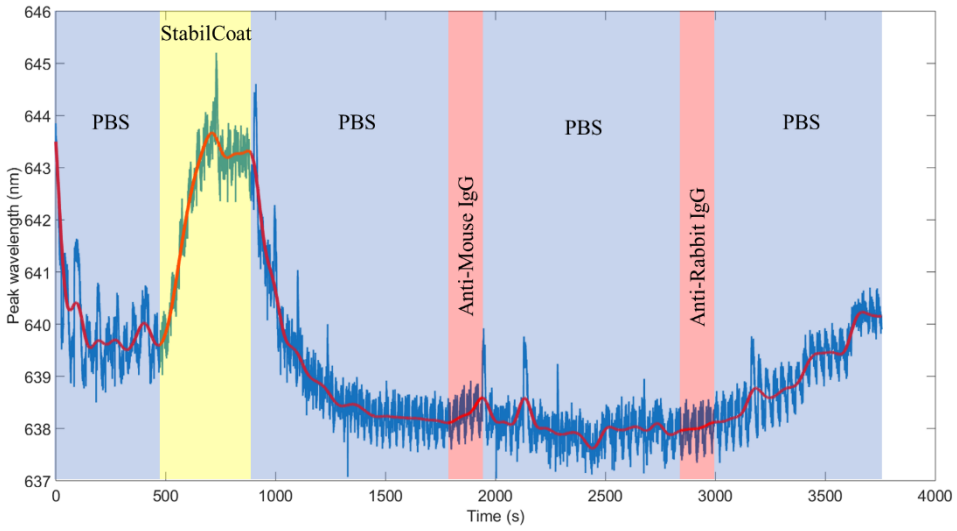

Figure 4.7 Sensorgram showing the detection of anti-Mouse IgG and anti-Rabbit IgG in series on a biosensor with a Rabbit IgG immobilised column.

4.2.4 Kinetic Model of a Column-modified SPR Biosensor

4.2.4.1 Adsorption Model on a Particle Column

In the previous modelling, the particulate surface was treated as a flat surface as the size of the particles (245 nm) was negligible when compared with the dimension of the channel (100 µm). However, this approximation is no longer valid as the particles fill the entire channel in the column modification. The non-porous particle adsorption model

(NPPAM) [252] is therefore applicable. The NPPAM is true for all the particles in a column if we further assume:

1. The effect of axial diffusion is negligible.
2. The fluid velocity is uniform over the cross section of the column.
3. The transport of adsorbate from the bulk fluid to the surface of the particle can be described by a film resistance mechanism.
4. The interaction between the adsorbate and the immobilised ligand at the particle surface is described by a Langmuir type model.
5. The mass transfer and surface interaction steps are considered to occur in series.

The rate of mass transfer in the liquid film at the particle surface is described by

$$\frac{\partial c_s}{\partial t} = \frac{3}{R}\frac{1-\varepsilon}{\varepsilon} k_{tr}(c - c_s) \tag{4.1}$$

where R is the radius of the particle, k_{tr} is the liquid film mass transfer coefficient, and c_s is the intermediate concentration of the adsorbate in the liquid phase at the surface of the particles. The term $\frac{3}{R}\frac{1-\varepsilon}{\varepsilon}$ is the interface area per unit interstitial void volume of the packed bed.

The surface adsorption rate is described by the Langmuir reversible reaction

$$\frac{\partial Q}{\partial t} = k_a c_s (Q_{max} - Q) - k_d Q \tag{4.2}$$

where k_a is the association rate, Q_{max} is the theoretical maximum amount of the adsorbate on the adsorbent, k_d is the dissociation rate constant.

As the film mass transfer and the surface interaction steps are considered to occur in series, the mass balance between the liquid concentration at the particle surface and the solid concentration can be written as

$$\varepsilon \frac{\partial c_s}{\partial t} = (1-\varepsilon)\frac{\partial Q}{\partial t} \tag{4.3}$$

Eliminating c_s and its derivative from the three equations above, we have the adsorption rate equation simplified as

$$\frac{\partial Q}{\partial t} = \frac{A[k_a c(Q_{max} - Q) - k_d Q]}{A + k_a(Q_{max} - Q)} \tag{4.4}$$

where $A = \frac{3}{R} k_{tr}$.

In a continuous flow experiment where the mass transfer between the mobile phase and the particle surface is fast, the adsorption becomes binding kinetic limited. As a result, $A \gg k_a(Q_{max} - Q)$, the adsorption rate equation becomes

$$\frac{\partial Q}{\partial t} = k_a c(Q_{max} - Q) - k_d Q \tag{4.5}$$

Note that it reduces to the basic Langmuir adsorption model employed in Section 4.2 and it is independent of the particle size.

4.2.4.2 Proposed Adsorption Model with Bi-directional Diffusion

In a simple open tube, the velocity of the solute in a mobile phase follows a parabolic flow profile, also known as laminar flow, as depicted in Figure 4.8 [232, 253]. The velocity at any location on the cross section of the tube varies according to its relative distance from the centre. Theoretically, molecules at the walls do not move and those at the centre of the column move at twice the average velocity of all the molecules. The flow profile creates a concentration gradient in the direction of the radius of the column, so the solute molecules diffuse from the centre to the walls (Figure 4.9). After the solute plug during the washing phase, the solute concentration is higher near the walls and zero in the centre of the column. The solute molecules diffuse in the reverse direction from the walls to the centre.

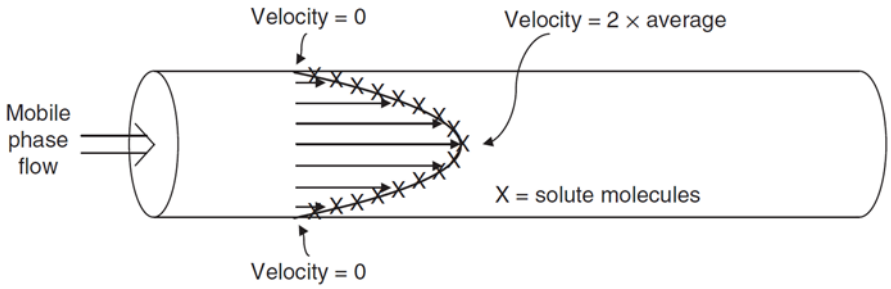

Figure 4.8 Depiction of the parabolic flow profile assuming at this point that there is no mechanism for combating the spread of molecules). Adapted from [253].

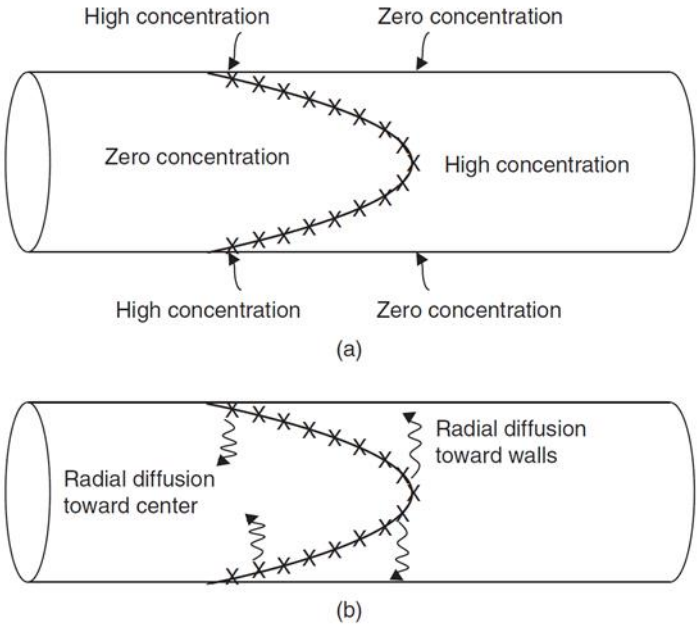

Figure 4.9 Depiction of radial diffusion in response to concentration gradients caused by parabolic flow. X = solute molecules. Note that in (a), on the far-right side, the solute concentration is high in the centre of the column and zero at the walls. Conversely, on the far-left side, the solute concentration is high near the walls and zero in the centre of the column. In both cases, a radial concentration gradient exists. In (b), radial diffusion acts to decrease these concentration gradients. Adapted from [253]

In a column with a packed bed of particles, the flow profile is more complicated due to the presence of the particles. The mobile phase travels faster in some paths and slower in

the others in a turbulent flow depending on the packing density of the particles at various regions. The solutes undergo eddy diffusion under such circumstances. Details are discussed elsewhere [253].

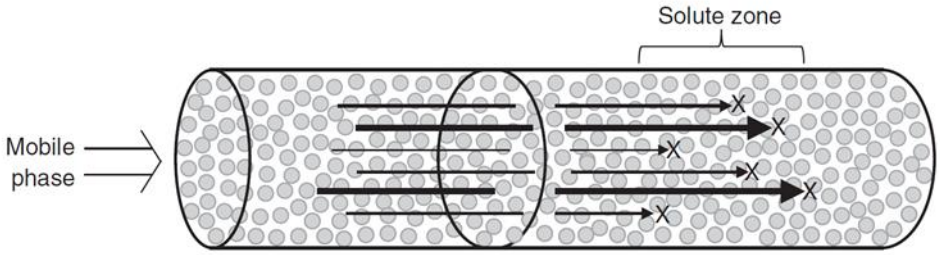

Figure 4.10 Velocities of the mobile phase vary in different regions in a column packed with particles (grey dots). The different thicknesses of the arrows represent the differing velocities. The size of the particles is greatly exaggerated. Adapted from [253]

Reynold's number can be used to characterise the type of flow in any column with a packed bed and it is given by three forms [254]:

$$Re = \frac{\rho v d_p}{\mu} \tag{4.6}$$

$$Re = \frac{\rho v d_p}{\mu \varepsilon} \tag{4.7}$$

$$Re = \frac{\rho v d_p}{\mu(1-\varepsilon)} \tag{4.8}$$

where ρ is the density of the mobile phase, v is the superficial velocity of the mobile phase, d_p is the diameter of the particles, ε is the voidage and μ is the dynamic viscosity of the mobile phase. Fully laminar flow has a Re up to 10 and fully turbulent flow's onset is $Re = 2000$, and any number between those thresholds indicates that the system has a combination of laminar and turbulent flow [255]. The choice of formula has not been totally consistent in the literature, but eq. (4.7) is generally associated with fixed beds and eq. (4.8) with fluidised beds. Eq. (4.6) has been used for either type [254]. Reynold's

numbers based on all three formulas have been calculated and tabulated in Table 4.3 together with all the parameters used in the calculation.

Table 4.3 Parameters used in the calculation of Reynold's number.

Parameter	**Nomenclature**	**Value and unit**	**Reference**
PBS buffer solution density	ρ	1.006 g/ml	Sigma-Aldrich
Superficial velocity	v	2.2 mm/s	Section 4.2.2
Particle diameter	d_p	15 μm	Fluka
Dynamic viscosity	μ	1.02 mPa·s	[256]
Voidage	ε	0.40	[249]
Reynold's number	Re	0.03	Eq. (4.6)
Reynold's number	Re	0.08	Eq. (4.7)
Reynold's number	Re	0.05	Eq. (4.8)

The Reynold's number is below 10 regardless of the method of calculation. The column is therefore in a laminar flow profile. A laminar flow profile means the velocity at the walls of the column (the sensor surface) is close to zero. Although the column is in continuous flow mode, the surface of the sensor is close to a stopped state. The surface scenario resembles a stop flow configuration and the kinetics should follow the mass-transport-corrected Langmuir adsorption model.

When the sample flows in the column, the mass transfer rate from the centre of the column to the particle at the sensor surface can be approximated by the same two-compartment model given by eq. (2.8), When the column is being flushed by PBS buffer solution, the concentration of analyte in bulk tends to zero. Substituting $c_0 = 0$ into eq. (2.8), the mass transport becomes:

$$\frac{dc_s}{dt} = k_{tr}(0 - c_s) - \frac{dQ}{dt} = -k_{tr}c_s - \frac{dQ}{dt} \tag{4.9}$$

$$\frac{dc_s}{dt} = k'_{tr}c_s - \frac{dQ}{dt} \tag{4.10}$$

where k'_{tr} is the mass transfer rate constant from the surface of the sensor to the centre of the column during the wash phase. The mass transfer is reversed.

Peter Schuck et al. predicted this retention effect, but it was under the consideration of only the SPR biosensor surface [257]. The retention effect typically caused a small deviation from the rapid mixing model, but never so prominent such that it caused continual analyte binding in a particle bed modified setting.

4.2.4.3 Kinetic Behaviour of Non-adsorbing Species

For unbound molecules, the mass transport rate during the washing step is reduced to:

$$\frac{dc_s}{dt} = k'_{tr}c_s \tag{4.11}$$

Solving for c_s using the initial condition $c_s = \frac{\Delta P}{S}$ when $t = 0$, we have

$$c_s = \frac{\Delta P}{S} e^{-k'_{tr}t} \tag{4.12}$$

where ΔP is the change in the optical output and S is the sensitivity. The exponential decay in the concentration of the unbound molecules is reflected as an exponential decrease in the sensorgram instead of a sharp drop typically observed in a traditional SPR biosensor. The bi-directional diffusion model correctly predicts the lingering phenomenon of the StabilCoat blocking discovered in Section 4.2.1.

4.2.4.4 Kinetic Behaviour of Adsorbing Species

An adsorbing species has a more complicated kinetic behaviour. Figure 4.11 shows the sensorgram in Figure 4.5 fitted with the Langmuir model with bi-directional mass transport using MATLAB. During the time when the sample was flowing in the column, the mass transport was in the direction from the centre of the column to the sensor surface. While in the wash phase, the mass transport was in the reverse direction from the sensor surface to the centre.

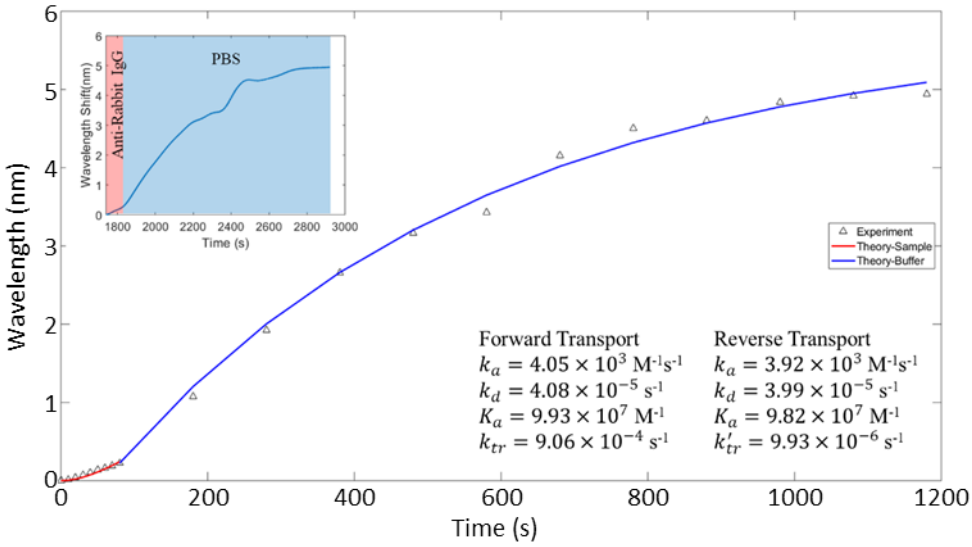

Figure 4.11 Sensorgram showing the detection of 200 µg/ml anti-Rabbit IgG in a column fitted with the bi-directional mass transport model. The insert is the filtered sensorgram during the injection of the sample and the subsequent washing phase.

The binding between the Rabbit IgG and anti-Rabbit IgG during the flow of the sample shows comparable association rate constant, dissociation rate constant and affinity constant with the results obtained in Section 3.2.7.1. The outward rate of mass transfer k_{tr} from the centre, however, is an order of magnitude higher than that obtained in a stop-flow experiment. The higher rate of mass transport is expected as this is not a true stop-flow configuration and any flow will result in a higher rate of mass transport.

When PBS buffer solution flowed in the column, the fitted association rate and dissociation rates do not change much from the previous binding phase. However, the rate of mass transfer was slower. This phenomenon will be discussed in Section 4.2.4.5.

Selected fitted parameters for the binding data of analyte concentrations ranging from 50 µg/ml to 300 µg/ml are tabulated in Table 4.4. The affinity constants obtained are of the same order but slightly higher than those obtained in Section 3.2.7. The outward mass transfer rates are relatively stable while the inward rates decrease with an increase of the analyte concentration.

Table 4.4 Fitted parameters using the Langmuir adsorption model with bi-directional mass transport for various analyte concentrations.

Analyte Concentration c_0 (µg/ml)	**Affinity Constant K_a ($\times 10^7$ s^{-1})**	**Outward Mass transfer Rate Constant k_{tr} ($\times 10^{-4}$ $M^{-1}s^{-1}$)**	**Inward Mass transfer Rate Constant k'_{tr} ($\times 10^{-5}$ $M^{-1}s^{-1}$)**
50	9.84	9.73	20.1
100	9.13	9.46	8.43
150	9.74	9.51	2.07
200	9.93	9.06	0.993
300	10.1	9.54	0.423

4.2.4.5 Asymmetric Mass Transport Mechanism

The reason for the discrepancy between the inward and outward diffusion must be considered under the context that the outward radial diffusion happened after the affinity column has been in contact with the analyte. During the time when the sample was in the column, binding started and by the time that the column was flushed with the PBS buffer solution, some of the biorecognition sites on the particles all over the column had

captured analyte molecules. Comparing the same section of the column during the outward and inward diffusion processes in a model as depicted in Figure 4.12, we can see that the paths are more crowded by all those captured analyte molecules in the washing phase. The packed silica gel particles can be considered as a porous bed. As the biorecognition sites capture the analyte molecules, the physical presence of the analyte molecules results in an equivalent decrease of the pore size. Since diffusion is restricted with the decrease of pore size [219], the rate of inward radial diffusion is smaller than the outward rate. The analyte molecules therefore were observed to linger around in the washing phase resulting in continual binding to the biorecognition sites on the sensor surface.

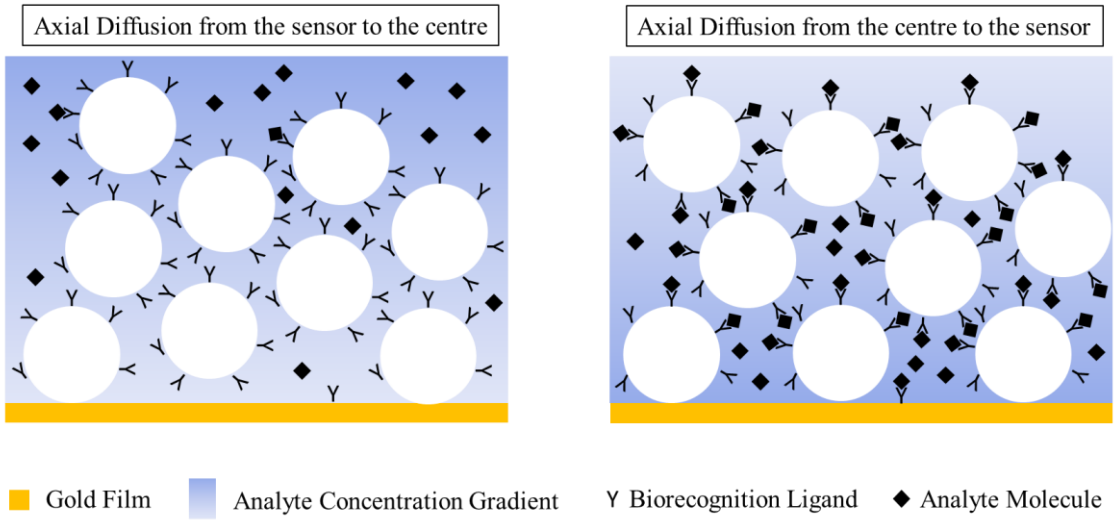

Figure 4.12 Depiction of the particles and biorecognition sites before and after analyte binding.

Since the inward mass transfer rate depends on the amount of captured analyte, we see that it negatively correlates to the analyte concentrations in the sample. The outward rate, on the other hand, depends only on the packing of the particles and the geometry of the column. Therefore, it stays relatively unchanged for any analyte concentration.

4.3 Summary

In this chapter, particle modification of an SPR biosensor was extended to an affinity chromatography column with an integrated SPR biosensor. Silica gel particles were immobilised with biorecognition ligands using carbodiimide coupling. A loading capacity of 14 μg/mg on the silica gel particles was achieved.

The column-modified SPR biosensor was used to detect IgG and anti-IgG interaction. The new configuration exhibited slightly higher sensitivity than the two particle-modified SPR biosensor discussed in Chapter 3 probably due to the packing of the silica gel particles having a better coverage of the sensor surface.

Despite the similarity in the sensitivity, the column-modified SPR sensorgram revealed several differences. Firstly, the sensorgram exhibited a periodical noise that could be reduced in post processing employing a band-stop filter tuned to the characteristic frequency. Secondly, unbound StabilCoat proteins were not immediately washed away but followed an exponential decay. Thirdly, flushing by the PBS buffer solution did not induce an apparent dissociation of the analyte as expected. Instead, the signal kept increasing during the washing phase. A Langmuir adsorption model with bi-directional radial diffusion was proposed to explain the latter two observations. As the flow in the column was largely laminar, the surface of the sensor experienced a near stop-flow environment. Both transport to and from the sensor surface were diffusion limited resulting in a lingering effect of the free molecules in the column. The outward radial diffusion rate was higher than that in a true stop flow configuration. And the inward radial diffusion was found to be two orders of magnitudes slower due to the asymmetric particle bed environment before and after binding.

Overall, a particle column with an integrated spectral SPR biosensor was studied for its sensitivity towards an antigen and antibody interaction and the binding kinetic behaviour within the column. A bi-directional mass transport model was proposed to explain the newly discovered sensing behaviour. This has implications in terms of development of an ‘on-ship’ SPR chromatography system, which would be an obvious extension of the

particle column SPR. In the next Chapter, the sensor assembly is configured to have SPR imaging capability and the sensing capability is investigated with an extra dimension along the length of the channel revealing how these mass transport effects complicate multicomponent affinity adsorption.

Chapter 5 Column-modified SPR Imaging Biosensor

5.1 Introduction

The spectral SPR spectroscopy in the previous chapters provides binding information upon the assumption that the surface within the interrogation zone can be averaged to approximate a homogenous surface, i.e. the binding density is the same at different places in the interrogation zone. In traditional SPR biosensing, that assumption is mostly valid since the sensor surface is treated indiscriminately in both the ligand immobilisation step and the analyte binding step. However, spatial variations must be considered in the column-modified biosensors and it was clear from the modelling of the column in the previous chapter that the 'average' in the evanescent field was made up of particles very close to the gold surface and particles at different distances but still having a part in the evanescent field. Furthermore, the particles are polydisperse, so the packing may not be uniform. The analyte in the packed particle bed may form a band in the column if the amount is limited as typically seen in affinity chromatography, but as seen in the previous chapter, the SPR mainly interrogates the stagnant layer at the surface of the gold film and not the core; this does not include the band front. The complexity of the fluid dynamics in this measurement system and possibly lack of lateral resolution in the spectroscopy technique may lead to measurement errors. According to Section 2.4.3, the lateral interrogation area is approximately 1 mm^2. That is massive when compared to the diameters of the particles and the sizes of the biomolecules. The spectroscopy technique averages all the binding information across the entire area thus neglecting information on a spatial scale. To obtain a lateral resolution on the column, 1-dimentional SPR imaging was used to explore the limitations of using SPR to follow binding in affinity chromatography (Figure 5.1).

In principle, the lateral resolution enabled by the SPR imaging technique allows the possibility for detecting multiple analytes along the same channel, but the complexity of the fluid dynamics and inhomogeneous particle packing and distance from the gold surface along the column are likely to limit the resolution of the technique. This chapter explores the idea by placing particles with different affinities within the column and evaluates the effectiveness of multiplexing in such configuration.

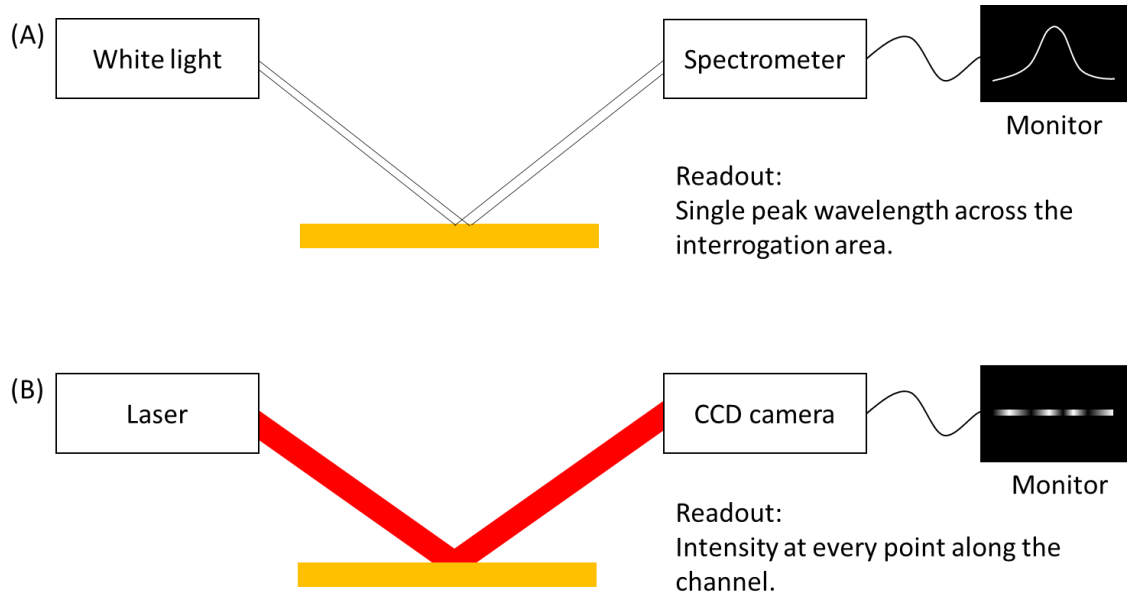

Figure 5.1 Schematic diagram of (A) spectral SPR and (B) 1-D SPR imaging showing the different data readout.

5.2 Results and Discussion

5.2.1 Spectroscopy-equivalent Analysis for Samples in Excess

5.2.1.1 Response at the Area Equivalent to the Interrogation Zone in Spectroscopy

To provide lateral resolution to the results in Chapter 4, the experiments were repeated using 1-D SPR imaging under the same conditions. Figure 5.2A shows the intensity profile for the detection of 500 µl of Rabbit IgG (100 µg/ml) in an area equivalent to the interrogation zone (1 mm at the centre of the column) in the SPR spectroscopy. The intensity profile shows a noticeable increase at the start of the experiment when StabilCoat was in the column. This is attributed to the higher refractive index of the StabilCoat than the buffer solution which was previously in the column. The simultaneous onset of the increase across the entire column suggests that the StabilCoat reached the end of the particle bed quickly in the direction of the flow. Once the column was flushed with PBS buffer solution, the intensity dropped. It increased again when the analyte in the sample bound to the ligands in the evanescent filed of the biosensor.

Figure 5.2B and Figure 5.2C show the fluctuation of the intensity across the area at the binding equilibrium and the StabilCoat saturation respectively. The fluctuations in the intensity plots are possibly attributable to the laser speckles discussed in Section 2.6.5 and the particle packing profile in the evanescent filed discussed in Section 0. If the absolute laser intensity at a spot is lower, the relative change due to refractive index change in the medium must also be lower. This phenomenon is supported by the several simultaneous dips in both the intensity plots. Despite the laser speckles, the intensity profile confirms the detection of the anti-IgG in the area equivalent to the interrogation zone.

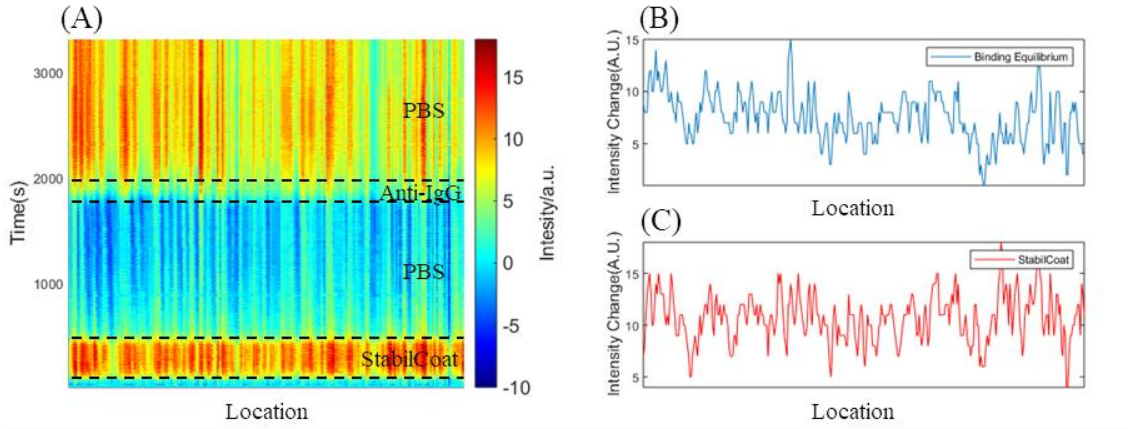

Figure 5.2 (A) Intensity profile at the area equivalent to the interrogation zone in the SPR spectroscopy. (B) Intensity plot across the zone at the binding equilibrium (3305 s). (C) Intensity plot across the zone at the StabilCoat saturation (290 s).

5.2.1.2 Sensitivity and Binding Kinetics

The sensorgram extracted and averaged from an area equivalent to the interrogation zone in the SPR spectroscopy is shown in Figure 5.3A and the binding data points are extracted and fitted to the bi-directional mass transfer model in Figure 5.3B. Similar traits to the previous spectroscopic sensorgrams can be observed here including: 1) the exponential decay due to StabilCoat escaping from the column in the first washing phase as the kinetics was governed by inward radial diffusion, 2) the immediate binding/mass transport of the analyte molecules when the sample was flowing in the column and 3) the continual analyte binding when the column is washed with PBS buffer solution again and the kinetics follow the model well.

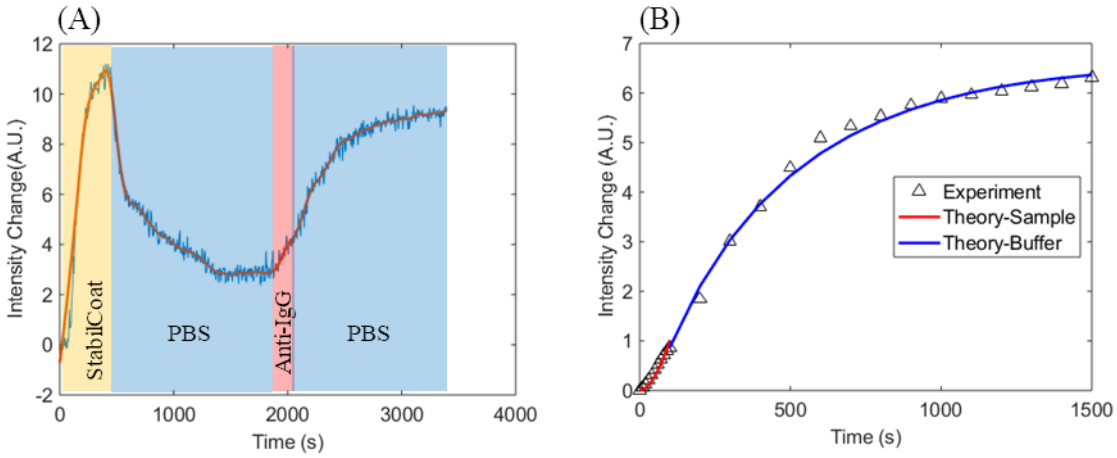

Figure 5.3 (A) Sensorgram averaging at the area equivalent to interrogation zone in the SPR spectroscopy. (B) Data points during the IgG/anti-IgG binding fitted to the bi-directional mass transfer model.

Figure 5.4 shows all the normalised intensities at equilibrium for the detection of 500 µl samples containing various concentrations of Rabbit IgG. The sensitivity is 3.67×10^4 A.U./M. Using the bulk sensitivity from Section 2.6.6, the sensitivity can be translated to 2.81×10^3 RIU/M. This is close to the result (2.73×10^3 RIU/M) obtained using the spectroscopy technique in Section 4.2.3.

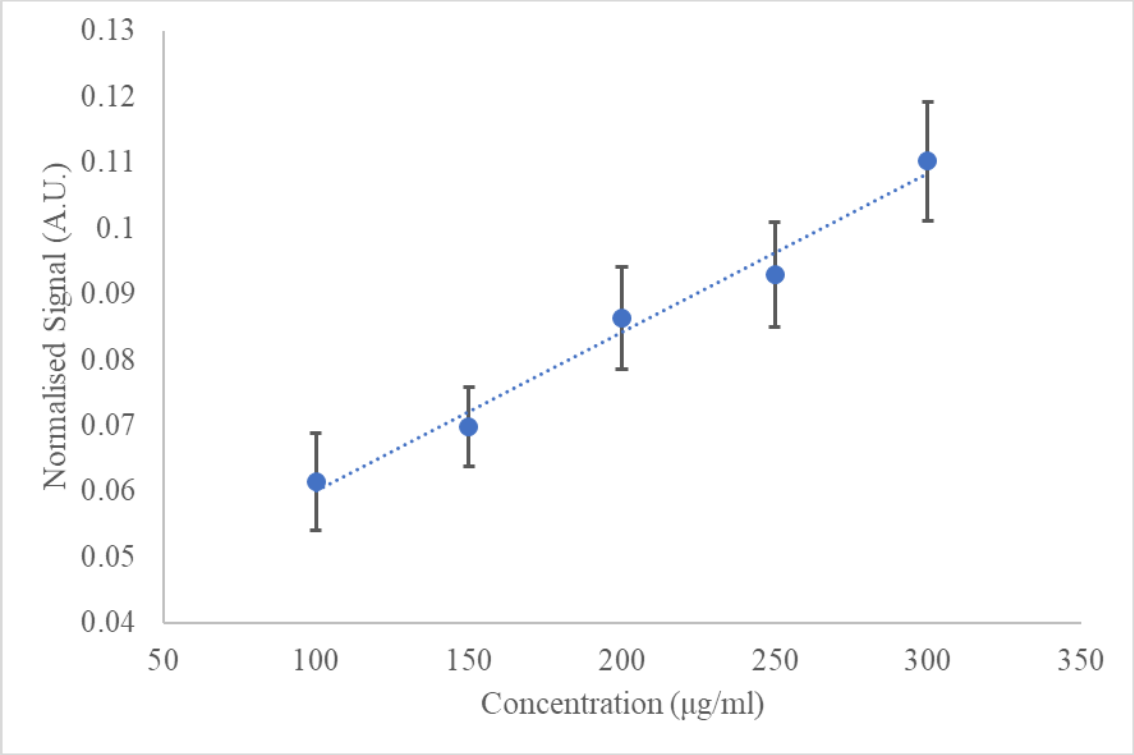

Figure 5.4 Normalised signal against the analyte concentration for the detection of 500 µl samples.

Table 5.1 shows the average parameters used to fit the binding data points to the bi-directional diffusion model at various concentrations. The parameters are close to those obtained using spectroscopy in Section 4.2.4.4.

Table 5.1 Fitted parameters using the Langmuir adsorption model with bi-directional mass transport for various analyte concentrations.

Analyte Concentration c_0 (µg/ml)	**Affinity Constant K_a ($\times 10^7$ s^{-1})**	**Outward Mass transfer Rate Constant k_{tr} ($\times 10^{-4}$ $M^{-1}s^{-1}$)**	**Inward Mass transfer Rate Constant k'_{tr} ($\times 10^{-5}$ $M^{-1}s^{-1}$)**
100	9.08	10.2	9.24
150	9.78	9.72	2.53
200	9.38	9.96	1.24
250	9.62	10.3	0.768
300	10.1	9.44	0.389

5.2.2 Band Analysis for Limited Amount of Sample

5.2.2.1 Appearance of the Signal Band

When the amount of sample is limited, the SPR imaging technique reveals the band formation as predicted. Figure 5.5A shows the intensity profile obtained when detecting 200 µl anti-Rabbit IgG sample at a concentration of 100 µg/ml. The band appeared near the upstream of the column after the injection of the sample and it continued to increase in intensity in the flushing phase. Figure 5.5B and Figure 5.5C show the intensity plots taken at the binding equilibrium and the StabilCoat saturation respectively. Besides the fluctuations caused by the laser speckles and particle profile in the evanescent field that appear in both plots, the intensity increase due to the IgG/anti-IgG binding at the band area is clearly visible on the right-hand side of Figure 5.5B. This differs from the previous results where the signal appeared across the entire column when the sample was in excess. The limited quantity of analyte when captured by the ligands on the particles were only

able to saturate a small length on the column. As a result, a signal band appeared in the intensity profile.

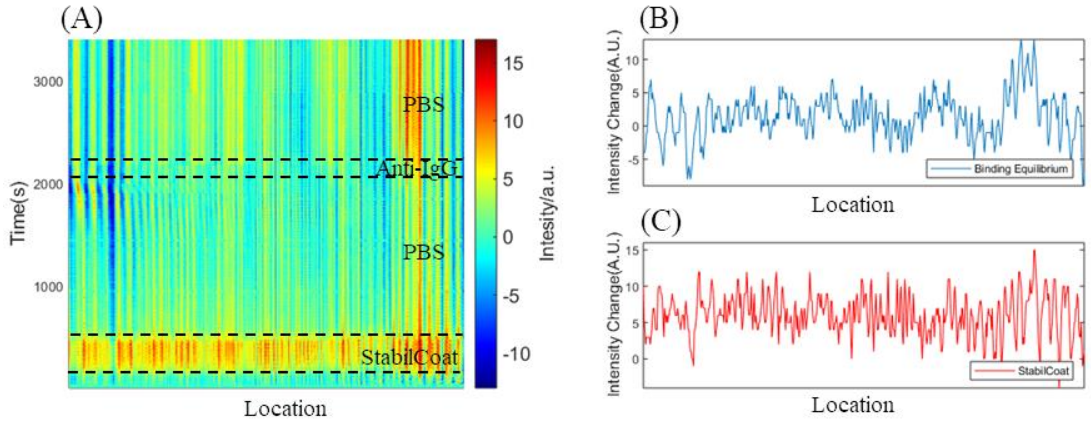

Figure 5.5 (A) Intensity profile against time (zoomed in to the length of the column. (B) Intensity plot cut across the column at the binding equilibrium (3400 s). (C) Intensity plot cut across the column at the StabilCoat saturation (350 s).

If this experiment was hypothetically observed using the spectroscopy where the interrogation area was only at the centre of the column downstream of the binding band, it would give a sensorgram analogous to Figure 5.6A, where the anti-IgG that is washed out of the initial binding with PBS is able to bind in downstream IgG sites. However, the initial binding signal appeared at the band area on the right in Figure 5.5A, and Figure 5.6B shows the sensorgram at this area. Comparing the two sensorgrams, it can be seen that both give similar response for the blocking phase but only the sensorgram at the band gives the full initial signal due to binding. The signal obtained from the centre of the column shows a lower signal due to the analyte that has been eluted downstream with the PBS and is captured by further IgG sites on the particles.

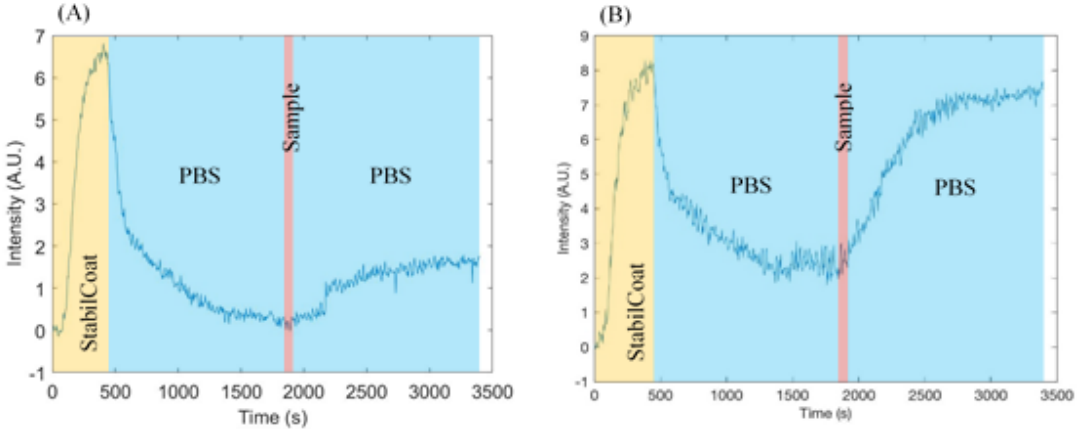

Figure 5.6 Sensorgrams obtained by averaging the intensity at (A) the area equivalent to the interrogation zone in the spectroscopy, and (B) the band.

At first sight, this seems to be quite a powerful analysis, which allows the elution and rebinding to be studied as well as the initial binding challenge. However, the location that the initial band appeared in each experiment was very inconsistent. Figure 5.7 shows 3 repeat experiments detecting 100 μg/ml anti-Rabbit IgG samples. The band appeared in at a different location each time. One possible explanation is the non-uniform packing density across the length of the column. Since the particles are polydisperse and the column is in constant flow, the packing density was not uniform across the entire column especially at the surface of the sensor. Only the area with the highest packing density close to the gold surface is detected when it captures the majority of the analyte due to a combined effect of higher ligand density and smaller voidage in the evanescent field. Besides the band, the other parts of the particle bed only capture the eluted analyte which gives different information resulting in a much lower signal.

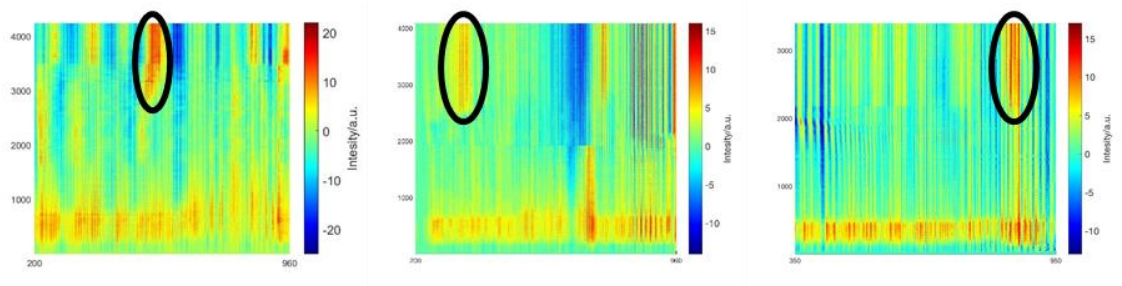

Figure 5.7 Intensity profiles showing three experiments detecting 200 µl samples containing 100 µg/ml anti-Rabbit IgG.

5.2.2.2 Sensitivity and Binding Kinetics

Anti-Rabbit IgG samples of various volume and concentrations were tested and the responses at the band were recorded and plotted.

Figure 5.8 shows the relationship between the analyte concentration in the sample and the intensity change. There is a positive correlation between the analyte concentration and the intensity change, but the linearity is visibly worse than the calibration curve obtained in Section 5.2.1.2 where the samples were in excess. The apparent sensitivity is 1.86×10^4 A.U./M. Using the bulk sensitivity from Section 2.6.6, the sensitivity can be translated to 1.42×10^3 RIU/M. This is about half of the sensitivity measured in Section 5.2.1.2 and in the previous chapters. This could be attributed to the bands not capturing all the analyte in each experiment.

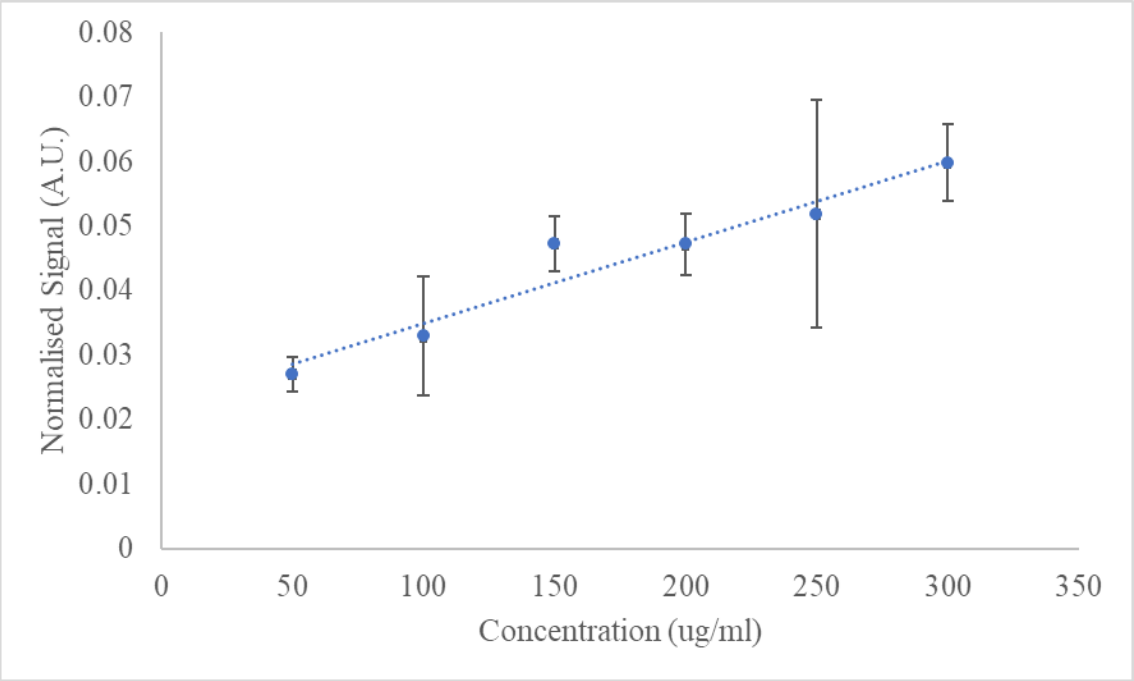

Figure 5.8 Normalised intensity change at the binding equilibrium when 200 µl anti-Rabbit IgG samples of various concentrations were injected in the column.

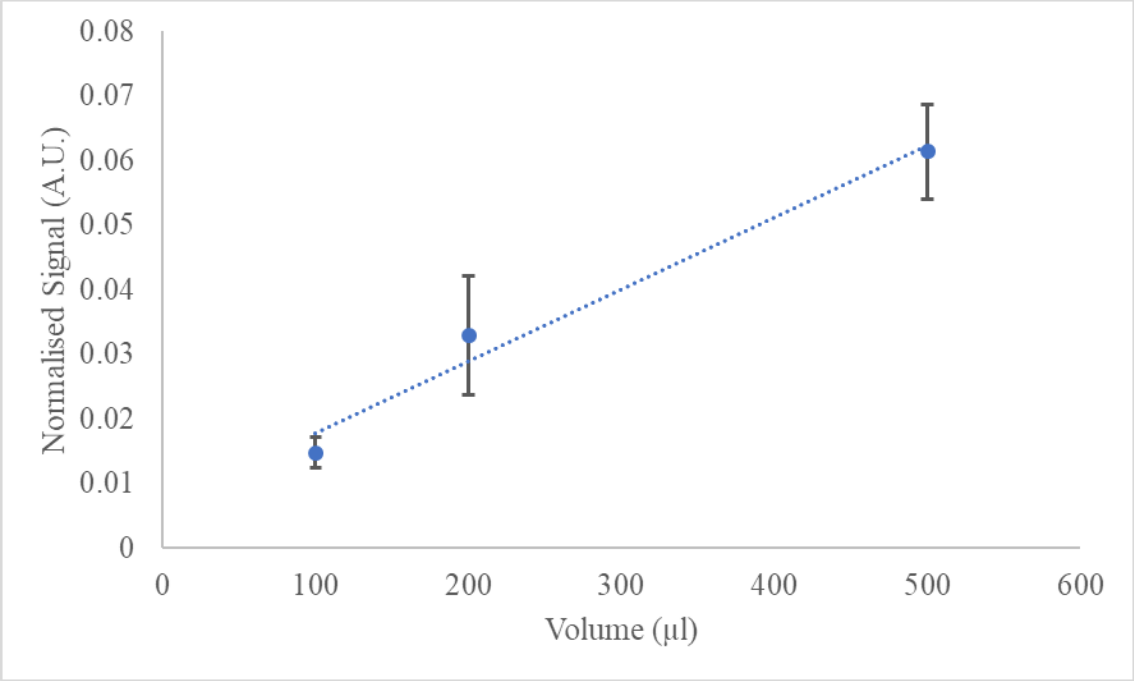

Figure 5.9 Normalised intensity change at the binding equilibrium when various volume of anti-Rabbit IgG samples of the same concentration (100µg/ml) were injected in the column.

Figure 5.9 shows the relationship between the analyte volume and the intensity change at the band. Since the column concentrated the analyte at the band, higher sample volume contained more analyte at the same concentration thereby causing a higher intensity change. Figure 5.10 shows a combined graph correlating the amount of the analyte and the intensity change at the band. The intensity change follows a positive correlation with the amount of the analyte in general. In a traditional SPR biosensor, only the surface of the sensor can capture the analyte molecules. The sensor usually does not deplete all the analyte molecules in the sample when a sample passes over the sensor surface. Therefore, the response correlates to the concentration only. Higher sample volume means more analyte eluted and wasted. In a column-modified sensor, however, the vast number of ligands on the particle bed means a high capacity of analyte molecules. A small sample volume otherwise sufficient will result in a signal band.

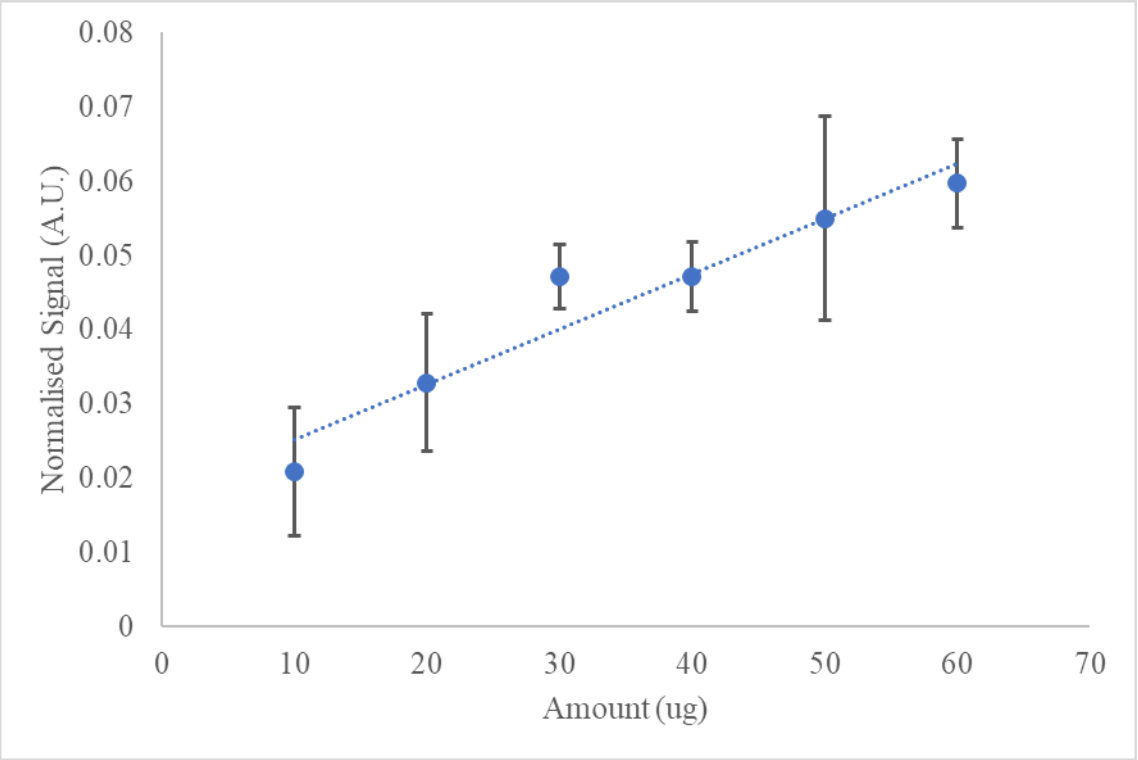

Figure 5.10 Normalised intensity change against the amount of anti-Rabbit IgG injected in the column.

Although the signal band does not reflect the analyte concentration reliably, it has value in elucidating the binding kinetic behaviour. Figure 5.11 shows the sensorgram at the band discussed in Section 5.2.2.1 fitted with the bi-directional mass transport model proposed in Section 4.2.4.

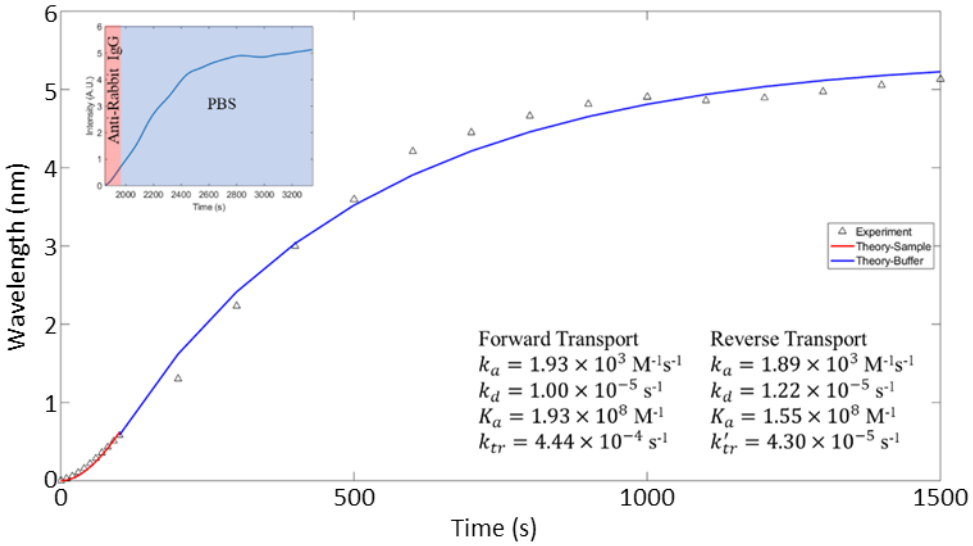

Figure 5.11 Sensorgram extracted from the band showing the detection of 200 µl anti-Rabbit IgG (100 µg/ml) in a column fitted with the bi-directional mass transport model. The insert is the filtered sensorgram during the flow of the sample and the subsequent washing phase.

The model fits reasonably well with expected association rate constant for both the outward and the inward radial mass transport duration, comparable to those obtained in the previous sections. The affinity constant, however, is approximately twice of that obtained in Section 4.2.4.4 due to the smaller dissociation rate constant. The mass transfer rate in both directions are about half the value obtained in Section 4.2.4.4. Some selected fitting parameters of the binding data for analyte concentrations ranging from 50 µg/ml to 300 µg/ml in samples of 200 µl are tabulated in Table 5.2.

The area where the band occurs should have a better particle packing density than the rest of the column as speculated in Section 5.2.2.1. This leads to the higher apparent affinity constant when compared to the previous results where the interrogation zone was fixed at the centre of the column. A higher packing density is also equivalent to having smaller pores therefore allowing a lower rate of mass transfer in both the outward and inward directions.

Table 5.2 Fitted parameters using Langmuir adsorption model with bi-directional mass transport for various analyte concentrations.

Analyte Concentration c_0 (µg/ml)	**Affinity Constant K_a ($\times 10^8$ s^{-1})**	**Outward Mass transfer Rate Constant k_{tr} ($\times 10^{-4}$ $M^{-1}s^{-1}$)**	**Inward Mass transfer Rate Constant k'_{tr} ($\times 10^{-5}$ $M^{-1}s^{-1}$)**
50	2.03	6.26	8.22
100	1.93	4.44	4.30
150	2.14	3.87	1.53
200	1.84	4.21	0.416
250	2.89	5.78	0.321
300	1.98	4.23	0.192

5.2.3 Qualitative Differential Sensing

Multiplexing on a SPR biosensor is highly sought after in the literature. Many of them employs parallel channels and spectroscopy [29, 258 – 260], or patterned gold film grid with SPR imaging [261 – 263]. The former methodology has a simpler immobilisation method as each channel only needs to be functionalised with one biorecognition element. It is analogous to doing multiple traditional single channel SPR biosensing at the same time. However, it often requires a more sophisticated design of the fluidics and the optical detection system. The latter method where one channel/flow cell is used is comparatively simple in the fluidics and the optics design, but the immobilisation of the biorecognition on each patterned element is more complicated. Different biorecognition elements or various concentrations of the same biorecognition element need to be precisely immobilised at the designated areas. This often involves repetition of multiple steps of pipetting and washing that requires expensive expertise.

Particle-modified SPR biosensors as discussed in this thesis could have an advantage over traditional method in that the immobilisation of the biorecognition procedure is drastically simplified to a one-step injection of particles with a desired ligand. On the other hand, as has been established in previous sections, the interrogation is confined to the evanescent field where the signal is susceptible to the particle density and profile in the field and not fully representative of the core of the column. To explore the limitations of multiplexing on a column-like SPR biosensor, a two-part model was tested. Particles with Rabbit-IgG immobilised was first packed in the channel followed by the particles with Mouse-IgG immobilised. With the two distinct biorecognition elements at different locations in the channel, the SPR sensor were separated into two zones sensitive towards two monoclonal antibodies respectively as illustrated in Figure 5.12.

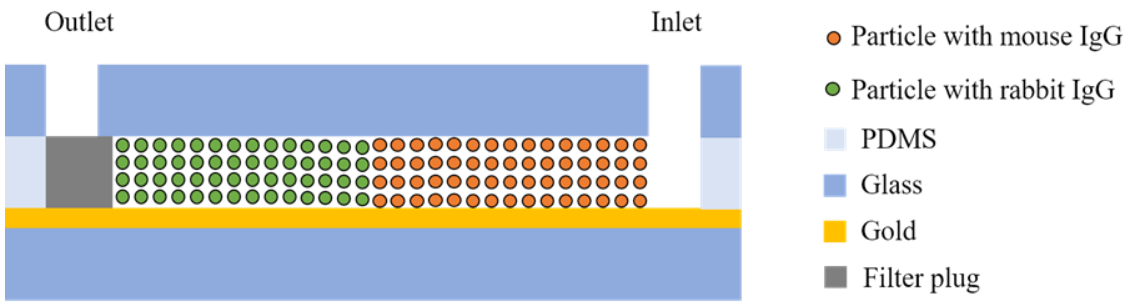

Figure 5.12 Illustration of two particle zones in the column. The red particles are sensitive to anti-Mouse IgG and the green ones are sensitive to anti-Rabbit IgG. The diagram is not drawn to scale.

The intensity profile is shown in Figure 5.13 when the samples containing the corresponding analytes were injected in the same order as the particles. Upon visual inspection, the separation between the zones is clearly seen here as the zone that is sensitive to anti-rabbit IgG showed a signal first and the other that is sensitive to anti-Mouse IgG showed a visible signal after.

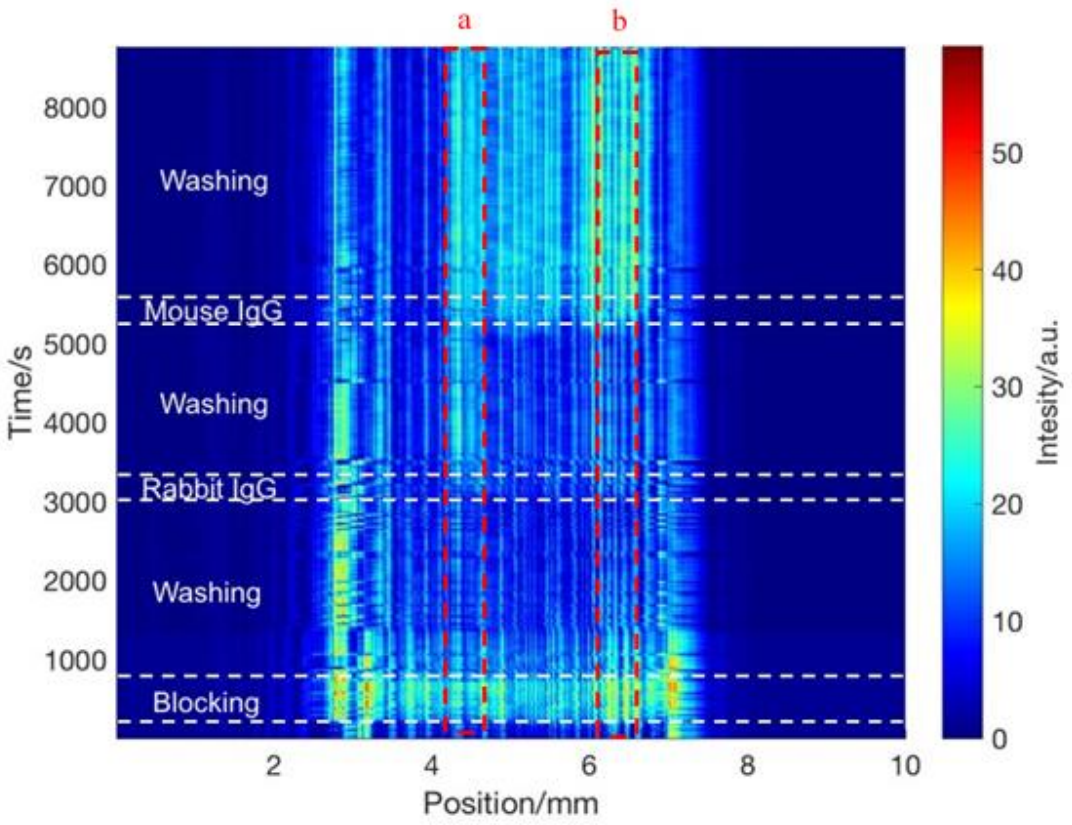

Figure 5.13 Intensity profile for samples injected in the same order as the corresponding particles. 1 ml of StabilCoat blocking mix was injected shortly after the start of the recording. 200 µl of anti-Rabbit IgG (200 µg/ml) was injected at approx. 3000s and 200 µl of anti-Mouse IgG (200µg/ml) was injected at approx. 5000s. PBS buffer solution was used to wash away any unbound molecules in between those injections.

Figure 5.14 shows the sensorgram at the bands in the two zones respectively (locations indicated by the red dash lines). We can see the difference in the behaviour of the two analytes in the two zones. Some cross reactivity might be anticipated and indeed, both zones showed a small sensitivity towards the other analyte. The reason for this cross sensitivity is a combined result of the following two processes: (i) cross reactivity between the different anti-IgG – IgG pairs or (ii) the serial particle packing process.

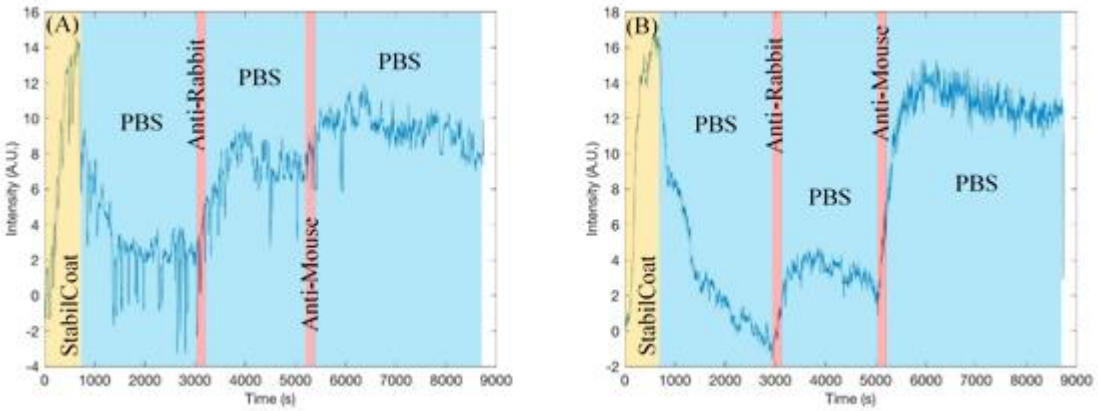

Figure 5.14 Sensorgrams taken at the (A) Rabbit-IgG particle zone, and (B) Mouse-IgG zone for samples injected in the same order as the particles.

In the process of packing the Rabbit-IgG immobilised particles first, some of these Rabbit IgG particles could stick to the upstream of the column where the other zone should be. The number of these stray particles may be small but as seen in previous sections, IgG modified silica has an affinity for gold. This process renders the part of sensor that would be only sensitive to anti-Mouse IgG slightly sensitive to anti-Rabbit IgG as well. On the other hand, in the process of packing the particles with Mouse-IgG immobilised, the dilute slurry method allows the particles to be retained in place. Any excess supernatant solution is pushed out of the column.

Table 5.3 Normalised maximum signal at time of equilibrium for similar injection sequence.

	Rabbit IgG	**Mouse IgG**	**Ratio**
Anti-Rabbit IgG	0.0571	0.0418	1.37
Anti-Mouse IgG	0.0214	0.0959	0.223

The intensity change at each zone for each analyte is tabulated in Table 5.3. We can see that regardless of the order of injection, the additional cross sensitivity at each zone is

smaller than the direct specific pair sensitivity. For example, the signal for sensing anti-Rabbit IgG at the zone with Rabbit IgG as biorecognition ligands is greater than that at the zone with Mouse IgG. The ratio between the zones is greater than 1 for anti-Rabbit IgG. On the other hand, when anti-Mouse IgG is detected the ration is smaller than 1. By taking the ratio between the responses, the double-zone column-like SPR biosensor is able to distinguish between anti-Rabbit IgG and anti-Mouse IgG.

Figure 5.15 shows the intensity profile of the test for a column where the order of the zones was reversed. The samples were injected in the same order as before. The sensorgrams (Figure 5.16) taken at the bands in the left and right zones respectively show similar behaviour of cross-sensitivity.

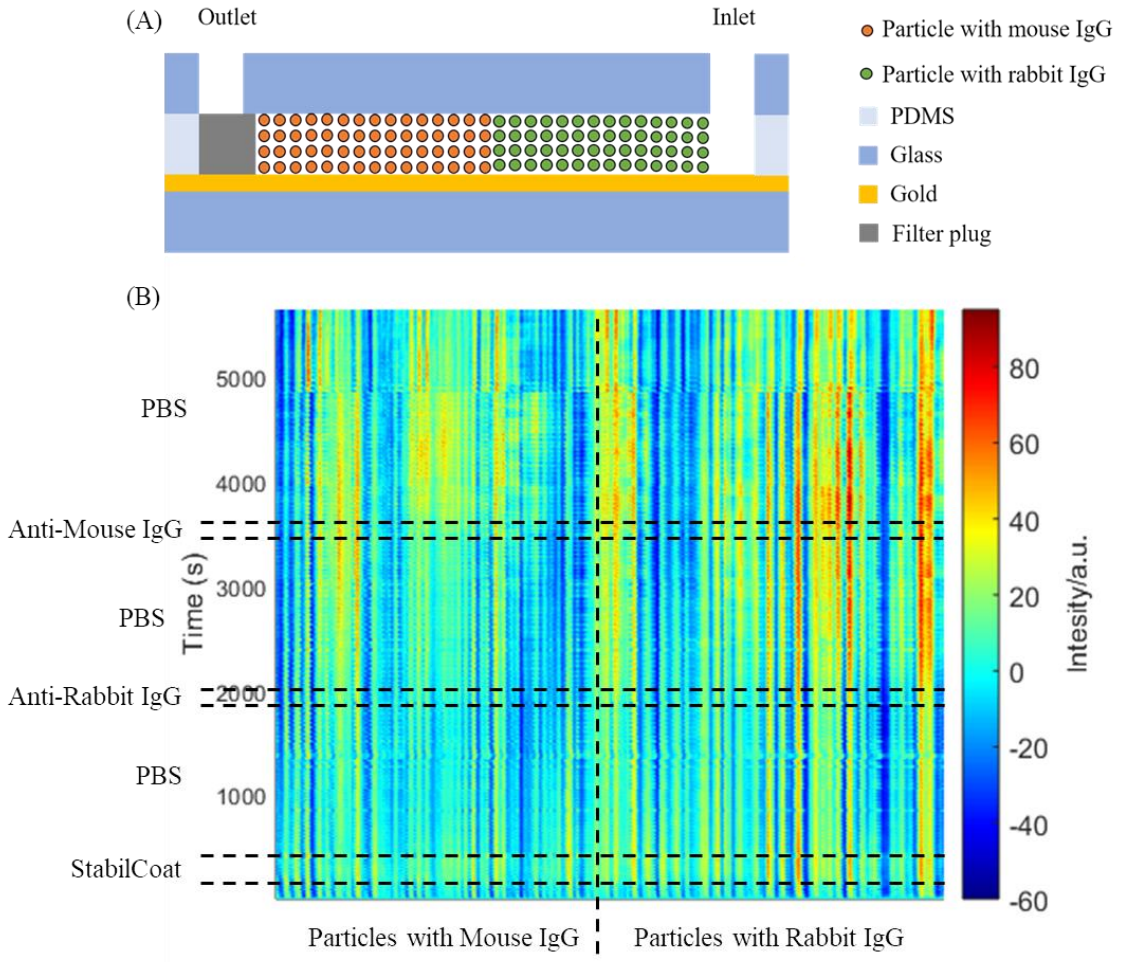

Figure 5.15 (A) Illustration of the particle configuration. Diagram not drawn to scale. (B) Differential intensity profile of the column.

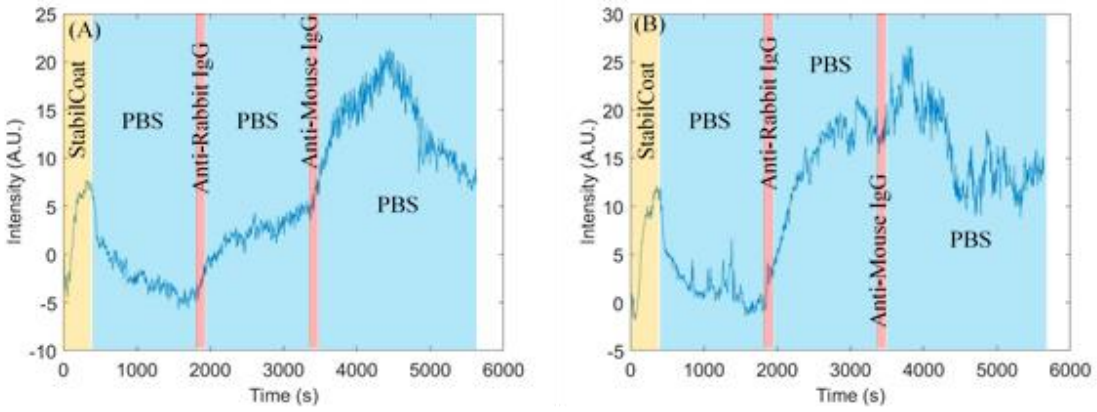

Figure 5.16 Sensorgrams taken at the (A) Mouse-IgG particle zone, and (B) Rabbit-IgG zone for samples injected in the reverse order as the particles. Visible disruption happened at approx. 4700s where the image was shifted due to impact.

Blocking of the entire sensor surface prior to the injection of the particle slurry was attempted to reduce the cross sensitivity, but the column-like sensor did not show any sensitivity towards any analyte at any zone.

The intensity change at each zone for each analyte is tabulated in Table 5.4. The intended sensitivity is higher than the cross sensitivity as expected. Therefore, the sensitivity ratio can qualitatively distinguish the analyte species regardless of the injection order.

Table 5.4 Normalised maximum signal at time of equilibrium for reverse injection sequence.

	Rabbit IgG	**Mouse IgG**	**Ratio**
Anti-Rabbit IgG	0.0640	0.0240	2.67
Anto-Mouse IgG	0.0400	0.0720	0.556

5.3 Summary

This chapter further investigated the column-like SPR biosensor using the 1-dimensional laser line SPR imaging technique.

When the sample was in excess, the analyte saturated the entire column. The intensity of the reflected laser increased across the entire column showing the irregular particle profile in the evanescent field overlaid with noises due to the laser speckles. Sensorgrams taken at the centre of the column where the interrogation zone was in the spectroscopy technique showed similar bio-sensitivity and binding kinetics to the previous results in Chapter 4.

When the quantity of sample added to the column was unable to saturate the column, a band would be identifiable showing the sample response. However, signal bands were formed in the intensity profiles at seemingly random locations. The sensitivity data obtained from the signal bands showed positive correlation with the analyte concentration, but the linearity was worse than previous results obtained with excess samples. The signal correlated with the amount of the analyte rather than the concentration alone, probably because the particle bed depletes the sample when its quantity was limited and so the column does not reach overall equilibrium with the sample. The binding kinetics extracted from the data at the bands did not fit the model developed in Chapter 4 as well but suggested a higher affinity and a lower mass transport possibly as a result of the sample depletion from the carrier solution. Some future work is needed to further develop the model for these limited analyte volume cases.

The lateral resolution enabled by the SPR imaging technique was also employed to identify the analyte species qualitatively. Two zones of particles with different affinity were studied as a model system. Each zone had some cross sensitivity towards the other analyte (as might be expected), which may have been increase due to the method of serial packing. However, the cross sensitivity is smaller than the true complementary-pair-sensitivity regardless of the order of the packing procedure. A ratiometric analysis on the sensitivities was able to distinguish the species of the analyte.

Overall however, this multicomponent, limited sample volume experiment pushes the SPR detection in the evanescent field to the limit. Issues with particle packing inhomogeneities on the nanometre scale, which are unimportant in a classical SPR system that interrogates an area of circa 1 mm^2, cause significant irreproducibility in the signal intensity and spatial resolution. More work is required to further develop the kinetic model of analyte binding kinetics with mass transport effects for this scenario, but the question also has to be asked whether the resolution and evanescent field information obtained from a chromatography platform is sufficiently robust and informative for further work.

Chapter 6 Conclusions and Recommended Future Work

6.1 Summary of Findings

6.1.1 IgG Loading on Silica Particles

Rabbit-IgG molecules were immobilised on both sub-micron silica particles made in-house and commercial silica gel particles using carbodiimide covalent coupling. The immobilisation efficiency of covalent attachment was found to be generally better than physical adsorption. Best efficiency was achieved up to 200 μg/ml IgG concentration in the mix. The loading of IgG was determined to be 40 μg/mg on the sub-micron particles and 14 μg/mg on the silica gel particles. The particles with the immobilised IgG were used as the immobilisation matrix in the particle-modified SPR biosensor.

6.1.2 Particle Coverage on A Gold Film

Three methods of sensor surface modification were investigated in this thesis. The first two namely, thiol silane coupling and pressure-aided physical adsorption, were employed to form a sub-monolayer on the sensor surface. The thiol silane coupling approach covered approx. 38% of the sensor surface while the mechanically pressed approach covered approx. 33%. The third method namely, particle packing via slurry injection, was used to create a particle bed on the sensor. The system was essentially transformed to a chromatography column with an *in situ* SPR sensor. It was impractical to determine the surface coverage visually for this modification approach, but the polydispersity of the gel

particles was speculated to improve the packing density and resulted in a higher bio-sensitivity.

6.1.3 Bio-sensitivity of Particle-modified SPR Biosensor

All the three types of particle-modified SPR biosensors exhibited sensitivity towards anti-IgG with the column modification being the most sensitive. As the analyte bound to the ligands on the particles, it increased the average refractive index within the evanescent field of the sensor resulting in a red-shift of the attenuation peak in the ATR spectrum. Simulations showed that the sensitivity of the binding interaction decreased exponentially with the increase of the distance between the location where the interactions took place and the gold surface. The bio-sensitivity of the particle-modified sensor was lower when compared to that of traditional SPR biosensors using alkanethiolate SAM ligand immobilisation strategy. Equivalent refractive index analysis revealed that this was not a result of the sub-monolayer coverage of the particles. It was most likely to be due to the ligand density difference on the particles and on the SAM functionalised gold surface.

6.1.4 Binding Kinetics in Particle-modified SPR Biosensor

The two particle layer modification strategies resembled conventional matrix immobilisation strategy when considering the binding kinetics. Both strategies had the ligand molecules spaced out in a matrix of considerable thickness in the evanescent field between the sensor and the bulk sample. In a continuous flow configuration where the flow rate was high, the binding was found to be governed by the simple Langmuir adsorption model. In a stop flow configuration, however, the binding was heavily limited by the mass transport of the analyte from the bulk to the immobilisation matrix. The kinetic model must be modified with a two-compartment model that considered the mass transport.

In the column-modified sensor, the mass transport limitation was most prominent. The particle bed and the laminar flow together caused retention of the biomolecules. Non-binding biomolecules exhibited an exponential escape and binding biomolecules showed

continual binding at the surface of the sensor. The mass transport limitation had never been so significant in other SPR biosensor immobilisation strategies and this retention effect had never been reported to our best knowledge to cause continual binding at the sensor surface. A bi-directional diffusion model was proposed to describe the continual binding. The inward radial diffusion during the flushing phase was found to be smaller than the outward radial diffusion during the injection of the sample. This was likely to be explained by the molecular hindrance exerted by the bound analyte molecules.

6.1.5 Importance of Lateral Resolution

Unlike most of the SPR biosensors reported in the literature, the response on a column-modified SPR biosensor was found to be ununiform unless the analyte saturated the column. When the quantity of the sample was limited, the 1-dimensional imaging result along the column showed a binding band. The refractive index changes at the band area due to binding correlated with the amount of the analyte. The position of the band was inconsistent and was likely due to the ununiform packing and the polydispersity of the particles.

The lateral resolution along the column was also used to detect multiple analyte in the same assay. A ratiometric analysis at the two distinctive zones was able to reveal the species of the sample analyte qualitatively.

6.2 Limitations and Future Work

6.2.1 Penetration Depth of the SPR Biosensor

The simulation in Section 3.2.6 revealed that the sensitivity of the particle-modified SPR biosensor largely depends on the loading density of the ligand molecules on the particle carriers. Large dose of ligand molecules in the immobilisation could improve the density but the efficiency suffered as shown in Section 3.2.1 and Section 4.2.1. One of the prospective approaches to further improve the sensitivity involves extending the evanescent fiend further into the particle bed using long-range surface plasmons (LRSP). Various LRSP-based SPR biosensors have been reported to have a 2- to 5-fold improvement in sensitivity when sensing large bio-elements such as *E.coli*. [264 – 267]. The field of long-range surface plasmons extends much further from the sensing surface than that of conventional surface plasmons, this improvement can be fully harnessed by the packed particle bed in a column-modified SPR biosensor.

6.2.2 Noise Reduction and the SPR Imaging Instrumentation

Although the 1-dimensional SPR imaging technique enabled the possibility of providing lateral resolution on the column, the noise due to the laser speckles was large. It reduced the available sensitive area on a column that was already short. Spatial filter systems can be employed to alleviate the noise problem. In these systems, the laser beam is first transformed into a central gaussian spot and side fringes. The spot passes a pinhole and then transforms again to a parallel beam by another collimating lens. A spatial filter system adds considerable complexity and cost to the optical set-up and it defeats the purpose of developing towards cheap and portable SPR operation. Nonetheless, if the particle-modified SPR sensor is used in a chromatography setting that requires unlabelled visualisation of the bands, a clean signal is paramount, and the extra cost of the spatial filter may be justifiable.

6.2.3 Plasmonic and Other Functional Particles

A silica particle bed is only the beginning in the development of particle-modified SPR biosensors. In this thesis, we only reported using silica particles as carriers for the ligands. Plasmonic materials and structures including Au-silica core-shell submicron particles, submicron silica particles with decorated Au nanoparticles, silica gel and Au nano-urchin particle mix and Au colloidosomes have been attempted with minimal success. In the attempts of the first three materials, the amount of the plasmonic materials in the gel particle bed were little compared to the silica and they were too thinly spread to couple the evanescent field further into the channel. In the last attempt, the amount of the Au colloidosomes were not enough to be packed into a bed in the column despite my collaborators best effort of producing them and they were too large to be immobilised as a layer on the gold surface in a vertical sensor configuration. Nonetheless, when large amount of plasmonic materials can be produced cheaply or the sensor is further miniaturised, particle-modified SPR biosensors have a promising potential.

6.3 Conclusion

In this thesis, silica particle modification as a ligand immobilisation strategy was studied. The sensing and kinetic behaviour of the particle-modified SPR biosensors were investigated.

IgG molecules were successfully immobilised on sub-micron silica particles. The silica particles were immobilised on a gold surface using chemical and physical means and formed a sub-monolayer structure. The particle-modified SPR sensor had similar sensitivity towards refractive index change in bulk when compared with an unmodified gold surface. The SPR biosensor with the IgG-functionalised silica particles were sensitive to anti-IgG samples but the sensitivity was lower than traditional biosensors with ligands immobilised by alkanethiolate SAMs. Simulations showed the difference was probably due to the ligand density difference on the silica particles and on the SAM. The binding kinetics followed the Langmuir adsorption model in the continuous flow configuration. In the stop-flow configuration, the binding was mass transport limited and followed the Langmuir model modified with two-compartment mass transport.

The investigation was extended to a particle column modification. The ligand immobilisation step in the SPR biosensing operation was simplified to the packing of the IgG-functionalised silica gel into a column. The column-modified SPR biosensor exhibited similar bio-sensitivity as the previous two types but distinctive binding kinetics. Because of the retention of the biomolecules in the particle bed, the SPR biosensor limited the mass transport to an extent that it retained the analyte even after the sensor was flushed by a buffer solution. This retention enabled continual binding of the analyte in the flushing phase.

The column-modified SPR biosensor was later investigated for its lateral resolution using a 1-dimensional SPR imaging system. When the sample saturated the column, the affinity results were comparable to the spectroscopy results in terms of both the bio-sensitivity and the kinetics. When the sample quantity was limited, signal bands appeared in the column. Therefore, spectroscopy result taken only at the centre of the column was no

longer reliably. The binding information extracted from the bands in the SPR imaging revealed that the sensor response correlated to the amount of the analyte. And the kinetics generally followed the Langmuir model with bi-directional mass transport with a higher apparent affinity constant but some tweaks to the model to reflect the sample volume limitation are needed in future work. The lateral resolution was also demonstrated to provide qualitative multiplexing if more than one type of functional silica gel particles were packed in the column.

Overall, we demonstrated a novel ligand immobilisation strategy using silica particles and achieved a one-step, reagentless preparation of the SPR biosensor that has great potential in the simplification of SPR biosensing experiments by immobilising biorecognition elements ‘off-chip’. The column-modified SPR also has great potential in multiplexed sensing and chromatography techniques.

References

[1] L. C. Clark and C. Lyons, “Electrode systems for continuous monitoring in cardiovascular surgery,” *Ann. N. Y. Acad. Sci.*, vol. 102, no. 1, pp. 29–45, 1962.

[2] J. Wang, M. Musameh, and Y. Lin, “Solubilization of carbon nanotubes by Nafion toward the preparation of amperometric biosensors,” *J. Am. Chem. Soc.*, vol. 125, no. 9, pp. 2408–2409, 2003.

[3] L. Doretti, D. Ferrara, S. Lora, F. Schiavon, and F. M. Veronese, “Acetylcholine biosensor involving entrapment of acetylcholinesterase and poly(ethylene glycol)-modified choline oxidase in a poly(vinyl alcohol) cryogel membrane,” *Enzyme Microb. Technol.*, vol. 27, no. 3–5, pp. 279–285, Aug. 2000.

[4] Rajesh, V. Bisht, W. Takashima, and K. Kaneto, “An amperometric urea biosensor based on covalent immobilization of urease onto an electrochemically prepared copolymer poly (N-3-aminopropyl pyrrole-co-pyrrole) film,” *Biomaterials*, vol. 26, no. 17, pp. 3683–3690, Jun. 2005.

[5] R. Gupta and N. K. Chaudhury, “Entrapment of biomolecules in sol-gel matrix for applications in biosensors: Problems and future prospects,” *Biosensors and Bioelectronics*, vol. 22, no. 11. Elsevier, pp. 2387–2399, 15-May-2007.

[6] P. Jolly *et al.*, “DNA aptamer-based sandwich microfluidic assays for dual quantification and multi-glycan profiling of cancer biomarkers,” *Biosens. Bioelectron.*, vol. 79, pp. 313–319, May 2016.

[7] N. Formisano *et al.*, “Optimisation of an electrochemical impedance spectroscopy aptasensor by exploiting quartz crystal microbalance with dissipation signals,” *Sensors Actuators B Chem.*, vol. 220, pp. 369–375, Dec. 2015.

[8] J. W. Chung, R. Bernhardt, and J. C. Pyun, “Additive assay of cancer marker CA 19-9 by SPR biosensor,” *Sensors Actuators B Chem.*, vol. 118, no. 1–2, pp. 28–32, Oct. 2006.

[9] D.-P. Tang, R. Yuan, and Y.-Q. Chai, “Novel immunoassay for carcinoembryonic antigen based on protein A-conjugated immunosensor chip by surface plasmon resonance and cyclic voltammetry,” *Bioprocess Biosyst. Eng.*, vol. 28, no. 5, pp. 315–321, May 2006.

[10] P. Norouzi, V. K. Gupta, F. Faridbod, M. Pirali-Hamedani, B. Larijani, and M. R. Ganjali, “Carcinoembryonic Antigen Admittance Biosensor Based on Au and ZnO Nanoparticles Using FFT Admittance Voltammetry,” *Anal. Chem.*, vol. 83, no. 5, pp. 1564–1570, Mar. 2011.

[11] H. Shu, W. Wen, H. Xiong, X. Zhang, and S. Wang, “Novel electrochemical aptamer biosensor based on gold nanoparticles signal amplification for the detection of carcinoembryonic antigen,” *Electrochem. commun.*, vol. 37, pp. 15–19, Dec. 2013.

[12] H. Vaisocherová, K. Mrkvová, M. Piliarik, P. Jinoch, M. Šteinbachová, and J. Homola, “Surface plasmon resonance biosensor for direct detection of antibody against Epstein-Barr virus,” *Biosens. Bioelectron.*, vol. 22, no. 6, pp. 1020–1026, Jan. 2007.

[13] T. Riedel *et al.*, “Diagnosis of Epstein–Barr virus infection in clinical serum samples by an SPR biosensor assay,” *Biosens. Bioelectron.*, vol. 55, pp. 278–284, May 2014.

[14] N. Rojo, G. Ercilla, and I. Haro, “GB Virus C (GBV-C) / Hepatitis G Virus (HGV): Towards the Design of Synthetic Peptides-based Biosensors for Immunodiagnosis of GBV-C / HGV Infection,” *Curr. Protein Pept. Sci.*, vol. 4, no. 4, pp. 291–298, Aug. 2003.

[15] J. W. Chung, S. D. Kim, R. Bernhardt, and J. C. Pyun, “Application of SPR

biosensor for medical diagnostics of human hepatitis B virus (hHBV)," *Sensors Actuators B Chem.*, vol. 111–112, pp. 416–422, Nov. 2005.

[16] X. Wang *et al.*, "Gold nanorod-based localized surface plasmon resonance biosensor for sensitive detection of hepatitis B virus in buffer, blood serum and plasma," *Biosens. Bioelectron.*, vol. 26, no. 2, pp. 404–410, Oct. 2010.

[17] B. T. T. Nguyen *et al.*, "Electrochemical impedance spectroscopy characterization of nanoporous alumina dengue virus biosensor," *Bioelectrochemistry*, vol. 88, pp. 15–21, Dec. 2012.

[18] N. V. Zaytseva, R. A. Montagna, and A. J. Baeumner, "Microfluidic biosensor for the serotype-specific detection of dengue virus RNA," *Anal. Chem.*, vol. 77, no. 23, pp. 7520–7527, 2005.

[19] G.-J. Zhang *et al.*, "Silicon nanowire biosensor for highly sensitive and rapid detection of Dengue virus," *Sensors Actuators B Chem.*, vol. 146, no. 1, pp. 138–144, Apr. 2010.

[20] J. Xu, D. Suarez, and D. S. Gottfried, "Detection of avian influenza virus using an interferometric biosensor," *Anal. Bioanal. Chem.*, vol. 389, no. 4, pp. 1193–1199, Sep. 2007.

[21] T. Endo, S. Ozawa, N. Okuda, Y. Yanagida, S. Tanaka, and T. Hatsuzawa, "Reflectometric detection of influenza virus in human saliva using nanoimprint lithography-based flexible two-dimensional photonic crystal biosensor," *Sensors Actuators, B Chem.*, vol. 148, no. 1, pp. 269–276, Jun. 2010.

[22] D.-J. Chung, K.-C. Kim, and S.-H. Choi, "Electrochemical DNA biosensor based on avidin–biotin conjugation for influenza virus (type A) detection," *Appl. Surf. Sci.*, vol. 257, no. 22, pp. 9390–9396, Sep. 2011.

[23] A. E. G. Cass *et al.*, "Ferrocene-mediated enzyme electrode for amperometric determination of glucose," *Anal. Chem.*, vol. 56, no. 4, pp. 667–671, 1984.

[24] R. Manuel, “Glucose Biosensor Market To Reach $31.0 Billion By 2022,” *Million Insights*, 2018. [Online]. Available: https://www.prnewswire.com/news-releases/glucose-biosensor-market-size-to-reach-31-billion-by-2022--million-insights-681600061.html. [Accessed: 06-Aug-2018].

[25] M. M. Crane, “Diagnostic test device,” 1971.

[26] Prescient & Strategic (P&S) Intelligence, “Global Female Fertility and Pregnancy Rapid Test Market Size, Share, Development, Growth and Demand Forecast to 2022 – Industry Insights by Type of Test (LH, FSH and HCG) and by Products (Strips/Dipsticks, Cards/Cassettes and Midstreams),” 2016. [Online]. Available: https://www.psmarketresearch.com/market-analysis/fertility-and-pregnancy-rapid-test-market. [Accessed: 06-Aug-2018].

[27] P. M. Fratamico, T. P. Strobaugh, M. B. Medina, and A. G. Gehring, “Detection of Escherichia coli 0157:H7 using a surface plasmon resonance biosensor,” *Biotechnol. Tech.*, vol. 12, no. 7, pp. 571–576, 1998.

[28] J. Waswa, J. Irudayaraj, and C. DebRoy, “Direct detection of E. Coli O157:H7 in selected food systems by a surface plasmon resonance biosensor,” *LWT - Food Sci. Technol.*, vol. 40, no. 2, pp. 187–192, Mar. 2007.

[29] A. D. Taylor, J. Ladd, Q. Yu, S. Chen, J. Homola, and S. Jiang, “Quantitative and simultaneous detection of four foodborne bacterial pathogens with a multi-channel SPR sensor,” *Biosens. Bioelectron.*, vol. 22, no. 5, pp. 752–758, Dec. 2006.

[30] Y. Luo *et al.*, “Surface functionalization of electrospun nanofibers for detecting E. coli O157:H7 and BVDV cells in a direct-charge transfer biosensor,” *Biosens. Bioelectron.*, vol. 26, no. 4, pp. 1612–1617, Dec. 2010.

[31] J.-J. Gau, E. H. Lan, B. Dunn, C.-M. Ho, and J. C. . Woo, “A MEMS based amperometric detector for E. Coli bacteria using self-assembled monolayers,” *Biosens. Bioelectron.*, vol. 16, no. 9–12, pp. 745–755, Dec. 2001.

[32] G. C. A. M. Bokken, R. J. Corbee, F. Knapen, and A. A. Bergwerff,

"Immunochemical detection of *Salmonella* group B, D and E using an optical surface plasmon resonance biosensor," *FEMS Microbiol. Lett.*, vol. 222, no. 1, pp. 75–82, May 2003.

[33] S. D. Mazumdar, M. Hartmann, P. Kämpfer, and M. Keusgen, "Rapid method for detection of Salmonella in milk by surface plasmon resonance (SPR)," *Biosens. Bioelectron.*, vol. 22, no. 9–10, pp. 2040–2046, Apr. 2007.

[34] S.-H. Ohk and A. K. Bhunia, "Multiplex fiber optic biosensor for detection of Listeria monocytogenes, Escherichia coli O157:H7 and Salmonella enterica from ready-to-eat meat samples," *Food Microbiol.*, vol. 33, no. 2, pp. 166–171, Apr. 2013.

[35] C. Zhou, P. Pivarnik, A. G. Rand, and S. V. Letcher, "Acoustic standing-wave enhancement of a fiber-optic Salmonella biosensor," *Biosens. Bioelectron.*, vol. 13, no. 5, pp. 495–500, Mar. 1998.

[36] S. Ko and S. A. Grant, "A novel FRET-based optical fiber biosensor for rapid detection of Salmonella typhimurium," *Biosens. Bioelectron.*, vol. 21, no. 7, pp. 1283–1290, Jan. 2006.

[37] S. Li *et al.*, "Direct detection of Salmonella typhimurium on fresh produce using phage-based magnetoelastic biosensors," *Biosens. Bioelectron.*, vol. 26, no. 4, pp. 1313–1319, Dec. 2010.

[38] S. H. Ohk, O. K. Koo, T. Sen, C. M. Yamamoto, and A. K. Bhunia, "Antibody-aptamer functionalized fibre-optic biosensor for specific detection of Listeria monocytogenes from food," *J. Appl. Microbiol.*, vol. 109, no. 3, pp. 808–817, Sep. 2010.

[39] W. Hong, L. Yanbin, and M. Slavik, "Rapid detection of listeria monocytogenes using quantum dots and nanobeads-based optical biosensor," in *Journal of Rapid Methods and Automation in Microbiology*, 2007, vol. 15, no. 1, pp. 67–76.

[40] V. Nanduri, A. K. Bhunia, S.-I. Tu, G. C. Paoli, and J. D. Brewster, "SPR

biosensor for the detection of L. monocytogenes using phage-displayed antibody," *Biosens. Bioelectron.*, vol. 23, no. 2, pp. 248–252, Sep. 2007.

[41] R. . Vaughan, C. . O'Sullivan, and G. . Guilbault, "Development of a quartz crystal microbalance (QCM) immunosensor for the detection of Listeria monocytogenes," *Enzyme Microb. Technol.*, vol. 29, no. 10, pp. 635–638, Dec. 2001.

[42] D. Davis, X. Guo, L. Musavi, C.-S. Lin, S.-H. Chen, and V. C. H. Wu, "Gold Nanoparticle-Modified Carbon Electrode Biosensor for the Detection of *Listeria monocytogenes*," *Ind. Biotechnol.*, vol. 9, no. 1, pp. 31–36, Feb. 2013.

[43] A. Subramanian, J. Irudayaraj, and T. Ryan, "Mono and dithiol surfaces on surface plasmon resonance biosensors for detection of Staphylococcus aureus," *Sensors Actuators B Chem.*, vol. 114, no. 1, pp. 192–198, Mar. 2006.

[44] S. Balasubramanian, I. B. Sorokulova, V. J. Vodyanoy, and A. L. Simonian, "Lytic phage as a specific and selective probe for detection of Staphylococcus aureus—A surface plasmon resonance spectroscopic study," *Biosens. Bioelectron.*, vol. 22, no. 6, pp. 948–955, Jan. 2007.

[45] J. Shi *et al.*, "A fluorescence resonance energy transfer (FRET) biosensor based on graphene quantum dots (GQDs) and gold nanoparticles (AuNPs) for the detection of mecA gene sequence of Staphylococcus aureus," *Biosens. Bioelectron.*, vol. 67, pp. 595–600, May 2015.

[46] G. A. Zelada-Guillén, J. L. Sebastián-Avila, P. Blondeau, J. Riu, and F. X. Rius, "Label-free detection of Staphylococcus aureus in skin using real-time potentiometric biosensors based on carbon nanotubes and aptamers," *Biosens. Bioelectron.*, vol. 31, no. 1, pp. 226–232, Jan. 2012.

[47] Q. Yu, S. Chen, A. D. Taylor, J. Homola, B. Hock, and S. Jiang, "Detection of low-molecular-weight domoic acid using surface plasmon resonance sensor," *Sensors Actuators B Chem.*, vol. 107, no. 1, pp. 193–201, May 2005.

[48] M. Lotierzo *et al.*, "Surface plasmon resonance sensor for domoic acid based on

grafted imprinted polymer," *Biosens. Bioelectron.*, vol. 20, no. 2, pp. 145–152, Sep. 2004.

[49] R. C. Stevens *et al.*, "Detection of the toxin domoic acid from clam extracts using a portable surface plasmon resonance biosensor," *Harmful Algae*, vol. 6, no. 2, pp. 166–174, Feb. 2007.

[50] L. Micheli *et al.*, "Disposable immunosensor for the determination of domoic acid in shellfish," *Biosens. Bioelectron.*, vol. 20, no. 2, pp. 190–196, Sep. 2004.

[51] F. S. Sabet, M. Hosseini, H. Khabbaz, M. Dadmehr, and M. R. Ganjali, "FRET-based aptamer biosensor for selective and sensitive detection of aflatoxin B1 in peanut and rice," *Food Chem.*, vol. 220, pp. 527–532, Apr. 2017.

[52] X. Jin, X. Jin, L. Chen, J. Jiang, G. Shen, and R. Yu, "Piezoelectric immunosensor with gold nanoparticles enhanced competitive immunoreaction technique for quantification of aflatoxin B1," *Biosens. Bioelectron.*, vol. 24, no. 8, pp. 2580–2585, Apr. 2009.

[53] S. chuan Li, J. hua Chen, H. Cao, D. sheng Yao, and D. ling Liu, "Amperometric biosensor for aflatoxin B1 based on aflatoxin-oxidase immobilized on multiwalled carbon nanotubes," *Food Control*, vol. 22, no. 1, pp. 43–49, Jan. 2011.

[54] T. M. Anh, S. V. Dzyadevych, M. C. Van, N. J. Renault, C. N. Duc, and J.-M. Chovelon, "Conductometric tyrosinase biosensor for the detection of diuron, atrazine and its main metabolites," *Talanta*, vol. 63, no. 2, pp. 365–370, May 2004.

[55] Z. Yu, G. Zhao, M. Liu, Y. Lei, and M. Li, "Fabrication of a Novel Atrazine Biosensor and Its Subpart-per-Trillion Levels Sensitive Performance," *Environ. Sci. Technol.*, vol. 44, no. 20, pp. 7878–7883, Oct. 2010.

[56] C. Steegborn and P. Skládal, "Construction and characterization of the direct piezoelectric immunosensor for atrazine operating in solution," *Biosens. Bioelectron.*, vol. 12, no. 1, pp. 19–27, Jan. 1997.

[57] M. Farré *et al.*, “Part per trillion determination of atrazine in natural water samples by a surface plasmon resonance immunosensor,” *Anal. Bioanal. Chem.*, vol. 388, no. 1, pp. 207–214, Mar. 2007.

[58] E. Mauriz *et al.*, “Optical immunosensor for fast and sensitive detection of DDT and related compounds in river water samples,” *Biosens. Bioelectron.*, vol. 22, no. 7, pp. 1410–1418, Feb. 2007.

[59] M. Alvarez, A. Calle, J. Tamayo, L. M. Lechuga, A. Abad, and A. Montoya, “Development of nanomechanical biosensors for detection of the pesticide DDT,” *Biosens. Bioelectron.*, vol. 18, no. 5–6, pp. 649–653, May 2003.

[60] A. C. Vinayaka, S. Basheer, and M. S. Thakur, “Bioconjugation of CdTe quantum dot for the detection of 2,4-dichlorophenoxyacetic acid by competitive fluoroimmunoassay based biosensor,” *Biosens. Bioelectron.*, vol. 24, no. 6, pp. 1615–1620, Feb. 2009.

[61] S. J. Kim, K. V. Gobi, H. Iwasaka, H. Tanaka, and N. Miura, “Novel miniature SPR immunosensor equipped with all-in-one multi-microchannel sensor chip for detecting low-molecular-weight analytes,” *Biosens. Bioelectron.*, vol. 23, no. 5, pp. 701–707, 2007.

[62] J. Horáček and P. Skládal, “Improved direct piezoelectric biosensors operating in liquid solution for the competitive label-free immunoassay of 2,4-dichlorophenoxyacetic acid,” *Anal. Chim. Acta*, vol. 347, no. 1–2, pp. 43–50, Jul. 1997.

[63] J. Huang, Q. Zheng, J.-K. Kim, and Z. Li, “A molecular beacon and graphene oxide-based fluorescent biosensor for Cu2+ detection,” *Biosens. Bioelectron.*, vol. 43, pp. 379–383, May 2013.

[64] K. Tag, K. Riedel, H.-J. Bauer, G. Hanke, K. H. R. Baronian, and G. Kunze, “Amperometric detection of Cu2+ by yeast biosensors using flow injection analysis (FIA),” *Sensors Actuators B Chem.*, vol. 122, no. 2, pp. 403–409, Mar. 2007.

[65] L. May May and D. A. Russell, “Novel determination of cadmium ions using an enzyme self-assembled monolayer with surface plasmon resonance,” *Anal. Chim. Acta*, vol. 500, no. 1–2, pp. 119–125, Dec. 2003.

[66] T.-J. Lin and M.-F. Chung, “Detection of cadmium by a fiber-optic biosensor based on localized surface plasmon resonance,” *Biosens. Bioelectron.*, vol. 24, no. 5, pp. 1213–1218, Jan. 2009.

[67] C.-M. Wu and L.-Y. Lin, “Immobilization of metallothionein as a sensitive biosensor chip for the detection of metal ions by surface plasmon resonance,” *Biosens. Bioelectron.*, vol. 20, no. 4, pp. 864–871, Nov. 2004.

[68] A. Attar, M. Emilia Ghica, A. Amine, and C. M. A. Brett, “Poly(neutral red) based hydrogen peroxide biosensor for chromium determination by inhibition measurements,” *J. Hazard. Mater.*, vol. 279, pp. 348–355, Aug. 2014.

[69] O. Domínguez Renedo, M. A. Alonso Lomillo, and M. J. Arcos Martinez, “Optimisation procedure for the inhibitive determination of chromium(III) using an amperometric tyrosinase biosensor,” *Anal. Chim. Acta*, vol. 521, no. 2, pp. 215–221, Sep. 2004.

[70] G.-M. Zeng, L. Tang, G.-L. Shen, G.-H. Huang, and C.-G. Niu, “Determination of trace chromium(VI) by an inhibition-based enzyme biosensor incorporating an electropolymerized aniline membrane and ferrocene as electron transfer mediator,” *Int. J. Environ. Anal. Chem.*, vol. 84, no. 10, pp. 761–774, Aug. 2004.

[71] † Yi Xiao, ‡ and Aaron A. Rowe, and ‡,§ Kevin W. Plaxco*, “Electrochemical Detection of Parts-Per-Billion Lead via an Electrode-Bound DNAzyme Assembly,” 2006.

[72] M. Li, X. Zhou, S. Guo, and N. Wu, “Detection of lead (II) with a ‘turn-on’ fluorescent biosensor based on energy transfer from CdSe/ZnS quantum dots to graphene oxide,” *Biosens. Bioelectron.*, vol. 43, pp. 69–74, May 2013.

[73] T. Omura, M. Kiyono, and H. Pan-Hou, “Development of a Specific and Sensitive

Bacteria Sensor for Detection of Mercury at Picomolar Levels in Environment," *J. Heal. Sci.*, vol. 50, no. 4, pp. 379–383, 2004.

[74] O. K. Lyngberg, D. J. Stemke, J. L. Schottel, and M. C. Flickinger, "A single-use luciferase-based mercury biosensor using Escherichia coli HB101 immobilized in a latex copolymer film," *J. Ind. Microbiol. Biotechnol.*, vol. 23, no. 1, pp. 668–676, Jul. 1999.

[75] D. R. Shankaran, K. Matsumoto, K. Toko, and N. Miura, "Development and comparison of two immunoassays for the detection of 2,4,6-trinitrotoluene (TNT) based on surface plasmon resonance," *Sensors Actuators B Chem.*, vol. 114, no. 1, pp. 71–79, Mar. 2006.

[76] Z. Naal, J. H. Park, S. Bernhard, J. P. Shapleigh, C. a Batt, and H. D. Abruña, "Amperometric TNT biosensor based on the oriented immobilization of a nitroreductase maltose binding protein fusion.," *Anal. Chem.*, vol. 74, no. 1, pp. 140–8, 2002.

[77] M. Piliarik and J. Homola, "Surface plasmon resonance (SPR) sensors: approaching their limits?," *Opt. Express*, vol. 17, no. 19, p. 16505, 2009.

[78] H. Raether, "Surface plasmons on smooth surfaces," in *Surface Plasmons on Smooth and Rough Surfaces and on Gratings*, Berlin, Heidelberg: Springer Berlin Heidelberg, 1988, pp. 4–39.

[79] J. Homola, "Surface plasmon resonance sensors for detection of chemical and biological species," *Chem. Rev.*, vol. 108, no. 2, pp. 462–493, 2008.

[80] N. J. Harrick and F. K. du Pré, "Effective Thickness of Bulk Materials and of Thin Films for Internal Reflection Spectroscopy," *Appl. Opt.*, vol. 5, no. 11, p. 1739, 1966.

[81] E. Kretschmann and H. Raether, "Radiative decay of non-radiative surface plasmons excited by light," *Z. Naturforsch.*, vol. 23, no. November 1968, pp. 2135–2136, 1968.

[82] A. Otto, “Excitation of nonradiative surface plasma waves in silver by the method of frustrated total reflection,” *Zeitschrift für Phys.*, vol. 216, no. 4, pp. 398–410, 1968.

[83] S. . Nelson, K. . Johnston, and S. . Yee, “High sensitivity surface plasmon resonace sensor based on phase detection,” *Sensors Actuators B Chem.*, vol. 35, no. 1–3, pp. 187–191, 1996.

[84] T. Akimoto, S. Sasaki, K. Ikebukuro, and I. Karube, “Effect of incident angle of light on sensitivity and detection limit for layers of antibody with surface plasmon resonance spectroscopy.,” *Biosens. Bioelectron.*, vol. 15, no. 7–8, pp. 355–62, 2000.

[85] J. M. Rooney and E. A. H. Hall, “Surface plasmon resonance: Theoretical evolutionary design optimization for a model analyte sensitive absorbing-layer system,” *Anal. Chem.*, vol. 76, no. 23, pp. 6861–6870, 2005.

[86] E.-P. Li and H.-S. Chu, *Plasmonic nanoelectronics and sensing*. Cambridge University Press, 2014.

[87] R. Georgiadis, K. P. Peterlinz, and A. W. Peterson, “Quantitative measurements and modeling of kinetics in nucleic acid monolayer films using SPR spectroscopy,” *J. Am. Chem. Soc.*, vol. 122, no. 13, pp. 3166–3173, 2000.

[88] R. J. Heaton, A. W. Peterson, and R. M. Georgiadis, “Electrostatic surface plasmon resonance: direct electric field-induced hybridization and denaturation in monolayer nucleic acid films and label-free discrimination of base mismatches.,” *Proc. Natl. Acad. Sci. U. S. A.*, vol. 98, no. 7, pp. 3701–4, Mar. 2001.

[89] Y. Sato, K. Fujimoto, and H. Kawaguchi, “Detection of a K-ras point mutation employing peptide nucleic acid at the surface of a SPR biosensor,” *Colloids Surfaces B Biointerfaces*, vol. 27, no. 1, pp. 23–31, Jan. 2003.

[90] H. V. Hsieh, B. Stewart, P. Hauer, P. Haaland, and R. Campbell, “Measurement of Clostridium perfringens β-toxin production by surface plasmon resonance

immunoassay," *Vaccine*, vol. 16, no. 9–10, pp. 997–1003, May 1998.

[91] C. Hu, N. Gan, Y. Chen, L. Bi, X. Zhang, and L. Song, "Detection of microcystins in environmental samples using surface plasmon resonance biosensor," *Talanta*, vol. 80, no. 1, pp. 407–410, Nov. 2009.

[92] H. E. Indyk and E. L. Filonzi, "Determination of immunoglobulin G in bovine colostrum and milk by direct biosensor SPR-immunoassay.," *J. AOAC Int.*, vol. 86, no. 2, pp. 386–93.

[93] M. Miyashita, T. Shimada, H. Miyagawa, and M. Akamatsu, "Surface plasmon resonance-based immunoassay for 17?-estradiol and its application to the measurement of estrogen receptor-binding activity," *Anal. Bioanal. Chem.*, vol. 381, no. 3, pp. 667–673, Feb. 2005.

[94] J. Treviño, A. Calle, J. M. Rodríguez-Frade, M. Mellado, and L. M. Lechuga, "Determination of human growth hormone in human serum samples by surface plasmon resonance immunoassay," *Talanta*, vol. 78, no. 3, pp. 1011–1016, May 2009.

[95] H. Baccar, M. B. Mejri, I. Hafaiedh, T. Ktari, M. Aouni, and A. Abdelghani, "Surface plasmon resonance immunosensor for bacteria detection," *Talanta*, vol. 82, no. 2, pp. 810–814, Jul. 2010.

[96] F. C. Dudak and I. H. Boyacı, "Rapid and label-free bacteria detection by surface plasmon resonance (SPR) biosensors," *Biotechnol. J.*, vol. 4, no. 7, pp. 1003–1011, Jul. 2009.

[97] K. A. Peterlinz and R. Georgiadis, "In Situ Kinetics of Self-Assembly by Surface Plasmon Resonance Spectroscopy," *Langmuir*, vol. 12, no. 20, pp. 4731–4740, 1996.

[98] V. Silin, H. Weetall, and D. J. Vanderah, "SPR Studies of the Nonspecific Adsorption Kinetics of Human IgG and BSA on Gold Surfaces Modified by Self-Assembled Monolayers (SAMs)," *J. Colloid Interface Sci.*, vol. 185, no. 1, pp. 94–

103, Jan. 1997.

[99] J. Wang, F. Wang, H. Chen, X. Liu, and S. Dong, “Electrochemical surface plasmon resonance detection of enzymatic reaction in bilayer lipid membranes,” *Talanta*, vol. 75, no. 3, pp. 666–670, May 2008.

[100] L. K. Wolf, D. E. Fullenkamp, and R. M. Georgiadis, “Quantitative Angle-Resolved SPR Imaging of DNA−DNA and DNA−Drug Kinetics,” *J. Am. Chem. Soc.*, vol. 127, no. 49, pp. 17453–17459, Dec. 2005.

[101] B. Liedberg, C. Nylander, and I. Lundstr6m, “Biosensing with surface plasmon resonance-how it all started,” 1995.

[102] A. Henseleit *et al.*, “A compact and rapid aptasensor platform based on surface plasmon resonance,” *Eng. Life Sci.*, vol. 11, no. 6, pp. 573–579, Dec. 2011.

[103] D. R. Shankaran, K. V. Gobi, and N. Miura, “Recent advancements in surface plasmon resonance immunosensors for detection of small molecules of biomedical, food and environmental interest,” *Sensors Actuators, B Chem.*, vol. 121, no. 1, pp. 158–177, 2007.

[104] Ö. Torun, İ. Hakkı Boyacı, E. Temür, and U. Tamer, “Comparison of sensing strategies in SPR biosensor for rapid and sensitive enumeration of bacteria,” *Biosens. Bioelectron.*, vol. 37, no. 1, pp. 53–60, Aug. 2012.

[105] W. Hu, Z. Lu, Y. Liu, and C. M. Li, “In Situ Surface Plasmon Resonance Investigation of the Assembly Process of Multiwalled Carbon Nanotubes on an Alkanethiol Self-Assembled Monolayer for Efficient Protein Immobilization and Detection,” *Langmuir*, vol. 26, no. 11, pp. 8386–8391, Jun. 2010.

[106] G. T. Hermanson, *Bioconjugate techniques*. Academic press, 2013.

[107] Z. Altintas, Y. Uludag, Y. Gurbuz, and I. E. Tothill, “Surface plasmon resonance based immunosensor for the detection of the cancer biomarker carcinoembryonic antigen,” *Talanta*, vol. 86, pp. 377–383, Oct. 2011.

[108] E. Mauriz *et al.*, "On-line surface plasmon resonance biosensing of vascular endothelial growth factor signaling in intact-human hepatoma cell lines," *Analyst*, vol. 139, no. 6, p. 1426, Feb. 2014.

[109] M. Akram, M. C. Stuart, and D. K. . Wong, "Direct application strategy to immobilise a thioctic acid self-assembled monolayer on a gold electrode," *Anal. Chim. Acta*, vol. 504, no. 2, pp. 243–251, Feb. 2004.

[110] H. Y. Song, X. Zhou, J. Hobley, and X. Su, "Comparative Study of Random and Oriented Antibody Immobilization as Measured by Dual Polarization Interferometry and Surface Plasmon Resonance Spectroscopy," *Langmuir*, vol. 28, no. 1, pp. 997–1004, Jan. 2012.

[111] J. M. Fowler, M. C. Stuart, and D. K. Y. Wong, "Self-assembled layer of thiolated protein G as an immunosensor scaffold," *Anal. Chem.*, vol. 79, no. 1, pp. 350–354, 2007.

[112] Jeong Min Lee, Hyun Kyu Park, Yongwon Jung, Jin Kyeong Kim, and Sun Ok Jung, and B. H. Chung*, "Direct Immobilization of Protein G Variants with Various Numbers of Cysteine Residues on a Gold Surface," 2007.

[113] Y. Jung, M. L. Jeong, H. Jung, and H. C. Bong, "Self-directed and self-oriented immobilization of antibody by protein G-DNA conjugate," *Anal. Chem.*, vol. 79, no. 17, pp. 6534–6541, 2007.

[114] S. Ko, T. J. Park, H. S. Kim, J. H. Kim, and Y. J. Cho, "Directed self-assembly of gold binding polypeptide-protein A fusion proteins for development of gold nanoparticle-based SPR immunosensors," *Biosens. Bioelectron.*, vol. 24, no. 8, pp. 2592–2597, 2009.

[115] E. de Juan-Franco, A. Caruz, J. R. Pedrajas, and L. M. Lechuga, "Site-directed antibody immobilization using a protein A–gold binding domain fusion protein for enhanced SPR immunosensing," *Analyst*, vol. 138, no. 7, p. 2023, Mar. 2013.

[116] M. J. W. Ludden *et al.*, "Assembly of bionanostructures onto β-cyclodextrin

molecular printboards for antibody recognition and lymphocyte cell counting," *J. Am. Chem. Soc.*, vol. 130, no. 22, pp. 6964–6973, Jun. 2008.

[117] S. A. Walper, P. A. Brozozog Lee, E. R. Goldman, and G. P. Anderson, "Comparison of single domain antibody immobilization strategies evaluated by surface plasmon resonance," *J. Immunol. Methods*, vol. 388, no. 1–2, pp. 68–77, Feb. 2013.

[118] E. de Juan-Franco, J. M. Rodríguez-Frade, M. Mellado, and L. M. Lechuga, "Implementation of a SPR immunosensor for the simultaneous detection of the 22K and 20K hGH isoforms in human serum samples," *Talanta*, vol. 114, pp. 268–275, Sep. 2013.

[119] J. S. Mitchell, "Spin-coated methacrylic acid copolymer thin films for covalent immobilization of small molecules on surface plasmon resonance substrates," *Eur. Polym. J.*, vol. 47, no. 1, pp. 16–23, Jan. 2011.

[120] P. T. Charles, E. R. Goldman, J. G. Rangasammy, C. L. Schauer, M.-S. Chen, and C. R. Taitt, "Fabrication and characterization of 3D hydrogel microarrays to measure antigenicity and antibody functionality for biosensor applications," *Biosens. Bioelectron.*, vol. 20, no. 4, pp. 753–764, Nov. 2004.

[121] H. Q. A. Lê, H. Sauriat-Dorizon, and H. Korri-Youssoufi, "Investigation of SPR and electrochemical detection of antigen with polypyrrole functionalized by biotinylated single-chain antibody: A review," *Anal. Chim. Acta*, vol. 674, no. 1, pp. 1–8, Jul. 2010.

[122] J. Baniukevic, J. Kirlyte, A. Ramanavicius, and A. Ramanaviciene, "Application of oriented and random antibody immobilization methods in immunosensor design," *Sensors Actuators B Chem.*, vol. 189, pp. 217–223, Dec. 2013.

[123] M. Wąsowicz, M. Milner, D. Radecka, K. Grzelak, and H. Radecka, "Immunosensor Incorporating Anti-His (C-term) IgG F(ab') Fragments Attached to Gold Nanorods for Detection of His-Tagged Proteins in Culture Medium," *Sensors*,

vol. 10, no. 6, pp. 5409–5424, Jun. 2010.

[124] V. L. Stefanelli and T. H. Barker, “The evolution of fibrin-specific targeting strategies,” *J. Mater. Chem. B*, vol. 3, no. 7, pp. 1177–1186, Feb. 2015.

[125] M. Manesse, R. Sanjines, V. Stambouli, R. Boukherroub, and S. Szunerits, “Preparation and characterization of antimony-doped SnO2 thin films on gold and silver substrates for electrochemical and surface plasmon resonance studies,” *Electrochem. commun.*, vol. 10, no. 7, pp. 1041–1043, Jul. 2008.

[126] D. K. Kambhampati, T. A. M. Jakob, J. W. Robertson, M. Cai, J. E. Pemberton, and W. Knoll, “Novel silicon dioxide sol-gel films for potential sensor applications: a surface plasmon resonance study,” *Langmuir*, vol. 17, no. 4, pp. 1169–1175, 2001.

[127] K. Scott Phillips, Jong-Ho Han, Marilyn Martinez, Zhuangzhi Wang, and David Carter, and Q. Cheng*, “Nanoscale Glassification of Gold Substrates for Surface Plasmon Resonance Analysis of Protein Toxins with Supported Lipid Membranes,” 2005.

[128] C. Satriano, G. Marletta, and B. Kasemo, “Oxygen plasma-induced conversion of polysiloxane into hydrophilic and smooth SiOx surfaces,” *Surf. Interface Anal.*, vol. 40, no. 3–4, pp. 649–656, Mar. 2008.

[129] C. Satriano, M. Edvardsson, G. Ohlsson, G. Wang, S. Svedhem, and B. Kasemo, “Plasma Oxidized Polyhydroxymethylsiloxane—A New Smooth Surface for Supported Lipid Bilayer Formation,” *Langmuir*, vol. 26, no. 8, pp. 5715–5725, Apr. 2010.

[130] H. Akasaka, N. Gawazawa, T. Suzuki, M. Nakano, S. Ohshio, and H. Saitoh, “Evaluation of protein adsorption on hydrogenated amorphous carbon films by surface plasmon resonance phenomenon,” *Diam. Relat. Mater.*, vol. 19, no. 10, pp. 1235–1239, Oct. 2010.

[131] Bin Sun *et al.*, “Covalent Photochemical Functionalization of Amorphous Carbon

Thin Films for Integrated Real-Time Biosensing," 2006.

[132] W. Choi, I. Lahiri, R. Seelaboyina, and Y. S. Kang, "Synthesis of Graphene and Its Applications: A Review," *Crit. Rev. Solid State Mater. Sci.*, vol. 35, no. 1, pp. 52–71, Feb. 2010.

[133] L. Wang, C. Zhu, L. Han, L. Jin, M. Zhou, and S. Dong, "Label-free, regenerative and sensitive surface plasmon resonance and electrochemical aptasensors based on graphene," *Chem. Commun.*, vol. 47, no. 27, p. 7794, Jun. 2011.

[134] P. Subramanian *et al.*, "Lysozyme detection on aptamer functionalized graphene-coated SPR interfaces," *Biosens. Bioelectron.*, vol. 50, pp. 239–243, Dec. 2013.

[135] S. Zeng *et al.*, "Graphene-Gold Metasurface Architectures for Ultrasensitive Plasmonic Biosensing," *Adv. Mater.*, vol. 27, no. 40, pp. 6163–6169, Oct. 2015.

[136] S. Szunerits, X. Castel, and R. Boukherroub, "Surface Plasmon Resonance Investigation of Silver and Gold Films Coated with Thin Indium Tin Oxide Layers: Influence on Stability and Sensitivity," *J. Phys. Chem. C*, vol. 112, no. 40, pp. 15813–15817, Oct. 2008.

[137] H. Zhang *et al.*, "Preparation and application of novel nanocomposites of magnetic-Au nanorod in SPR biosensor," *Biosens. Bioelectron.*, vol. 34, no. 1, pp. 137–143, Apr. 2012.

[138] T. Maurer, P.-M. Adam, and G. Lévêque, "Coupling between plasmonic films and nanostructures: from basics to applications," *Nanophotonics*, vol. 4, pp. 363–382, 2015.

[139] G. Lévêque and O. J. F. Martin, "Tunable composite nanoparticle for plasmonics," *Opt. Lett.*, vol. 31, no. 18, p. 2750, Sep. 2006.

[140] G. Lévêque and O. J. F. Martin, "Optical interactions in a plasmonic particle coupled to a metallic film," *Opt. Express*, vol. 14, no. 21, p. 9971, Oct. 2006.

[141] L. Andrew Lyon, and Michael D. Musick, and M. J. Natan*, "Colloidal Au-

Enhanced Surface Plasmon Resonance Immunosensing," 1998.

[142] A. García-Marín, J. M. Abad, E. Ruiz, E. Lorenzo, J. Piqueras, and J. L. Pau, "Glutathione Immunosensing Platform Based on Total Internal Reflection Ellipsometry Enhanced by Functionalized Gold Nanoparticles," *Anal. Chem.*, vol. 86, no. 10, pp. 4969–4976, May 2014.

[143] W.-C. Law, K.-T. Yong, A. Baev, and P. N. Prasad, "Sensitivity Improved Surface Plasmon Resonance Biosensor for Cancer Biomarker Detection Based on Plasmonic Enhancement," *ACS Nano*, vol. 5, no. 6, pp. 4858–4864, Jun. 2011.

[144] Shiping Fang, Hye Jin Lee, and Alastair W. Wark, and R. M. Corn*, "Attomole Microarray Detection of MicroRNAs by Nanoparticle-Amplified SPR Imaging Measurements of Surface Polyadenylation Reactions," 2006.

[145] A. R. Halpern, J. B. Wood, Y. Wang, and R. M. Corn, "Single-Nanoparticle Near-Infrared Surface Plasmon Resonance Microscopy for Real-Time Measurements of DNA Hybridization Adsorption," *ACS Nano*, vol. 8, no. 1, pp. 1022–1030, Jan. 2014.

[146] X. Hong and E. A. H. Hall, "Contribution of gold nanoparticles to the signal amplification in surface plasmon resonance," *Analyst*, vol. 137, no. 20, p. 4712, 2012.

[147] M. J. Kwon, J. Lee, A. W. Wark, and H. J. Lee, "Nanoparticle-Enhanced Surface Plasmon Resonance Detection of Proteins at Attomolar Concentrations: Comparing Different Nanoparticle Shapes and Sizes," *Anal. Chem.*, vol. 84, no. 3, pp. 1702–1707, Feb. 2012.

[148] D. Mortazavi, A. Z. Kouzani, Y. Mafinejad, and M. K. Hosain, "Plasmon eignevalues as a function of nano-spheroids size and elongation," in *2012 ICME International Conference on Complex Medical Engineering (CME)*, 2012, pp. 495–499.

[149] J. Zhou, Y. Yang, and C. Zhang, "Toward Biocompatible Semiconductor Quantum

Dots: From Biosynthesis and Bioconjugation to Biomedical Application," *Chem. Rev.*, vol. 115, no. 21, pp. 11669–11717, Nov. 2015.

[150] R. Robelek, L. Niu, E. L. Schmid, and W. Knoll, "Multiplexed hybridization detection of quantum dot-conjugated DNA sequence using surface plasmon enhanced fluorescence microscopy and spectrometry," *Anal. Chem.*, vol. 76, no. 20, pp. 6160–6165, 2004.

[151] L. Malic, M. G. Sandros, and M. Tabrizian, "Designed Biointerface Using Near-Infrared Quantum Dots for Ultrasensitive Surface Plasmon Resonance Imaging Biosensors," *Anal. Chem.*, vol. 83, no. 13, pp. 5222–5229, Jul. 2011.

[152] G. P. Anderson *et al.*, "Single domain antibody–quantum dot conjugates for ricin detection by both fluoroimmunoassay and surface plasmon resonance," *Anal. Chim. Acta*, vol. 786, pp. 132–138, Jul. 2013.

[153] A. M. Foudeh, J. T. Daoud, S. P. Faucher, T. Veres, and M. Tabrizian, "Sub-femtomole detection of 16s rRNA from Legionella pneumophila using surface plasmon resonance imaging," *Biosens. Bioelectron.*, vol. 52, pp. 129–135, Feb. 2014.

[154] S. A. Vance and M. G. Sandros, "Zeptomole Detection of C-Reactive Protein in Serum by a Nanoparticle Amplified Surface Plasmon Resonance Imaging Aptasensor," *Sci. Rep.*, vol. 4, no. 1, p. 5129, May 2015.

[155] H. Wei, D. Ratchford, X. (Elaine) Li, H. Xu, and C.-K. Shih, "Propagating Surface Plasmon Induced Photon Emission from Quantum Dots," *Nano Lett.*, vol. 9, no. 12, pp. 4168–4171, Dec. 2009.

[156] Y. Teramura, Y. Arima, and H. Iwata, "Surface plasmon resonance-based highly sensitive immunosensing for brain natriuretic peptide using nanobeads for signal amplification," *Anal. Biochem.*, vol. 357, no. 2, pp. 208–215, Oct. 2006.

[157] Y. Wang, J. Dostalek, and W. Knoll, "Magnetic Nanoparticle-Enhanced Biosensor Based on Grating-Coupled Surface Plasmon Resonance," *Anal. Chem.*, vol. 83, no.

16, pp. 6202–6207, Aug. 2011.

[158] R.-P. Liang, G.-H. Yao, L.-X. Fan, and J.-D. Qiu, “Magnetic Fe3O4@Au composite-enhanced surface plasmon resonance for ultrasensitive detection of magnetic nanoparticle-enriched α-fetoprotein,” *Anal. Chim. Acta*, vol. 737, pp. 22–28, Aug. 2012.

[159] J. Wang, Z. Zhu, A. Munir, and H. S. Zhou, “Fe3O4 nanoparticles-enhanced SPR sensing for ultrasensitive sandwich bio-assay,” *Talanta*, vol. 84, no. 3, pp. 783–788, May 2011.

[160] J. Wang *et al.*, “Studies of Fe3O4/Ag/Au composites for immunoassay based on surface plasmon resonance biosensor,” *Colloids Surfaces B Biointerfaces*, vol. 102, pp. 165–170, Feb. 2013.

[161] L. Wang *et al.*, “Preparation of surface plasmon resonance biosensor based on magnetic core/shell Fe3O4/SiO2 and Fe3O4/Ag/SiO2 nanoparticles,” *Colloids Surfaces B Biointerfaces*, vol. 84, no. 2, pp. 484–490, Jun. 2011.

[162] S. D. Soelberg, R. C. Stevens, A. P. Limaye, and C. E. Furlong, “Surface Plasmon Resonance Detection Using Antibody-Linked Magnetic Nanoparticles for Analyte Capture, Purification, Concentration, and Signal Amplification,” *Anal. Chem.*, vol. 81, no. 6, pp. 2357–2363, Mar. 2009.

[163] K. Cho, J. B. Fasoli, K. Yoshimatsu, K. J. Shea, and R. M. Corn, “Measuring Melittin Uptake into Hydrogel Nanoparticles with Near-Infrared Single Nanoparticle Surface Plasmon Resonance Microscopy,” *Anal. Chem.*, vol. 87, no. 9, pp. 4973–4979, May 2015.

[164] Y.-L. Kuo, S.-Y. Chuang, S.-Y. Chen, and K.-P. Chen, “Enhancing the Interaction between High-Refractive Index Nanoparticles and Gold Film Substrates Based on Oblique Incidence Excitation,” *ACS Omega*, vol. 1, no. 4, pp. 613–619, Oct. 2016.

[165] H. Wang, X. Wang, J. Wang, W. Fu, and C. Yao, “A SPR biosensor based on signal amplification using antibody-QD conjugates for quantitative determination

of multiple tumor markers," *Sci. Rep.*, vol. 6, no. 1, p. 33140, Dec. 2016.

[166] Y. Chen, "Nanofabrication by electron beam lithography and its applications: A review," *Microelectron. Eng.*, vol. 135, pp. 57–72, Mar. 2015.

[167] D. Xia, Z. Ku, S. C. Lee, and S. R. J. Brueck, "Nanostructures and Functional Materials Fabricated by Interferometric Lithography," *Adv. Mater.*, vol. 23, no. 2, pp. 147–179, Jan. 2011.

[168] X. Ye and L. Qi, "Two-dimensionally patterned nanostructures based on monolayer colloidal crystals: Controllable fabrication, assembly, and applications," *Nano Today*, vol. 6, no. 6, pp. 608–631, Dec. 2011.

[169] D. Sinton, R. Gordon, and A. G. Brolo, "Nanohole arrays in metal films as optofluidic elements: progress and potential," *Microfluid. Nanofluidics*, vol. 4, no. 1–2, pp. 107–116, Jan. 2008.

[170] J. C. Sharpe, J. S. Mitchell, L. Lin, N. Sedoglavich, and R. J. Blaikie, "Gold nanohole array substrates as immunobiosensors," *Anal. Chem.*, vol. 80, no. 6, pp. 2244–2249, 2008.

[171] S. A. Kim *et al.*, "Surface-enhanced localized surface plasmon resonance biosensing of avian influenza DNA hybridization using subwavelength metallic nanoarrays," *Nanotechnology*, vol. 21, no. 35, p. 355503, Sep. 2010.

[172] A. G. Brolo, R. Gordon, B. Leathem, and K. L. Kavanagh, "Surface plasmon sensor based on the enhanced light transmission through arrays of nanoholes in gold films," *Langmuir*, vol. 20, no. 12, pp. 4813–4815, 2004.

[173] A. De Leebeeck, L. K. S. Kumar, V. De Lange, D. Sinton, R. Gordon, and A. G. Brolo, "On-chip surface-based detection with nanohole arrays," *Anal. Chem.*, vol. 79, no. 11, pp. 4094–4100, 2007.

[174] F. J. Rodríguez-Fortuo *et al.*, "Highly-sensitive chemical detection in the infrared regime using plasmonic gold nanocrosses," *Appl. Phys. Lett.*, vol. 98, no. 13, p.

133118, Mar. 2011.

[175] J. McPhillips *et al.*, “Plasmonic sensing using nanodome arrays fabricated by soft nanoimprint lithography,” *J. Phys. Chem. C*, vol. 115, no. 31, pp. 15234–15239, Aug. 2011.

[176] J. Zhu *et al.*, “Large-Scale Uniform Silver Nanocave Array for Visible Light Refractive Index Sensing Using Soft UV Nanoimprint,” *IEEE Photonics J.*, vol. 8, no. 4, pp. 1–7, Aug. 2016.

[177] X. Dou, Y. C. Lin, B. Choi, K. Wu, and P. Jiang, “Sensitive surface plasmon resonance enabled by templated periodic arrays of gold nanodonuts,” *Nanotechnology*, vol. 27, no. 19, p. 195601, May 2016.

[178] B. Xiao, S. K. Pradhan, K. C. Santiago, G. N. Rutherford, and A. K. Pradhan, “Topographically Engineered Large Scale Nanostructures for Plasmonic Biosensing,” *Sci. Rep.*, vol. 6, 2016.

[179] A. I. Aristov *et al.*, “3D plasmonic crystal metamaterials for ultra-sensitive biosensing,” *Sci. Rep.*, vol. 6, no. 1, p. 25380, Jul. 2016.

[180] T. . Chinowsky, J. . Quinn, D. . Bartholomew, R. Kaiser, and J. . Elkind, “Performance of the Spreeta 2000 integrated surface plasmon resonance affinity sensor,” *Sensors Actuators B Chem.*, vol. 91, no. 1–3, pp. 266–274, Jun. 2003.

[181] P. Preechaburana, M. C. Gonzalez, A. Suska, and D. Filippini, “Surface Plasmon Resonance Chemical Sensing on Cell Phones,” *Angew. Chemie*, vol. 124, no. 46, pp. 11753–11756, Nov. 2012.

[182] B. A. Prabowo *et al.*, “Application of an OLED integrated with BEF and giant birefringent optical (GBO) film in a SPR biosensor,” *Sensors Actuators B Chem.*, vol. 198, pp. 424–430, Jul. 2014.

[183] B.-H. Chung and Y. Shin, “Surface plasmon resonance sensor using rotating mirror.” Google Patents, 2011.

[184] A. N. Naimushin, S. D. Soelberg, D. U. Bartholomew, J. L. Elkind, and C. E. Furlong, “A portable surface plasmon resonance (SPR) sensor system with temperature regulation,” *Sensors Actuators, B Chem.*, vol. 96, no. 1–2, pp. 253–260, 2003.

[185] X. ling Zhang *et al.*, “Design and performance of a portable and multichannel SPR device,” *Sensors (Switzerland)*, vol. 17, no. 6, pp. 1–7, Jun. 2017.

[186] H. Guner *et al.*, “A smartphone based surface plasmon resonance imaging (SPRi) platform for on-site biodetection,” *Sensors Actuators, B Chem.*, vol. 239, pp. 571–577, Feb. 2017.

[187] Y. Liu, Q. Liu, S. Chen, F. Cheng, H. Wang, and W. Peng, “Surface plasmon resonance biosensor based on smart phone platforms,” *Sci. Rep.*, vol. 5, pp. 1–9, 2015.

[188] S. Nie and S. R. Emory, “Probing Single Molecules and Single Nanoparticles by Surface-Enhanced Raman Scattering Probing Single Molecules and Single Nanoparticles by Surface-Enhanced Raman Scattering,” vol. 1102, no. 1997, 2009.

[189] L.-J. Xu, Z.-C. Lei, J. Li, C. Zong, C. J. Yang, and B. Ren, “Label-Free Surface-Enhanced Raman Spectroscopy Detection of DNA with Single-Base Sensitivity,” *J. Am. Chem. Soc.*, vol. 137, no. 15, pp. 5149–5154, Apr. 2015.

[190] S.-Y. Ding *et al.*, “Nanostructure-based plasmon-enhanced Raman spectroscopy for surface analysis of materials,” *Nat. Rev. Mater.*, vol. 1, no. 6, p. 16021, Jun. 2016.

[191] T. Liebermann and W. Knoll, “Surface-plasmon field-enhanced fluorescence spectroscopy,” *Colloids Surfaces A Physicochem. Eng. Asp.*, vol. 171, no. 1–3, pp. 115–130, Oct. 2000.

[192] C.-J. Huang, J. Dostalek, A. Sessitsch, and W. Knoll, “Long-Range Surface Plasmon-Enhanced Fluorescence Spectroscopy Biosensor for Ultrasensitive Detection of *E. coli* O157:H7,” *Anal. Chem.*, vol. 83, no. 3, pp. 674–677, Feb.

2011.

[193] R. W. Nelson, J. R. Krone, and O. Jansson, “Surface Plasmon Resonance Biomolecular Interaction Analysis Mass Spectrometry. 1. Chip-Based Analysis,” *Anal. Chem.*, vol. 69, no. 21, pp. 4363–4368, 1997.

[194] J. Davies *et al.*, “Use of Scanning Probe Microscopy and Surface Plasmon Resonance as Analytical Tools in the Study of Antibody-Coated Microtiter Wells,” 2654.

[195] A. Baba, W. Knoll, and R. Advincula, “Simultaneous *in situ* electrochemical, surface plasmon optical, and atomic force microscopy measurements: Investigation of conjugated polymer electropolymerization,” *Rev. Sci. Instrum.*, vol. 77, no. 6, p. 064101, Jun. 2006.

[196] H. Dong, X. Cao, C. M. Li, and W. Hu, “An in situ electrochemical surface plasmon resonance immunosensor with polypyrrole propylic acid film: Comparison between SPR and electrochemical responses from polymer formation to protein immunosensing,” *Biosens. Bioelectron.*, vol. 23, no. 7, pp. 1055–1062, Feb. 2008.

[197] Y. Wang and W. Knoll, “In situ electrochemical and surface plasmon resonance (SPR) studies of aniline-carboxylated aniline copolymers,” *Anal. Chim. Acta*, vol. 558, no. 1–2, pp. 150–157, Feb. 2006.

[198] F. Bender *et al.*, “Development of a combined surface plasmon resonance/surface acoustic wave device for the characterization of biomolecules,” *Meas. Sci. Technol.*, vol. 20, no. 12, p. 124011, Dec. 2009.

[199] L. A. Francis, J. M. Friedt, C. Zhou, and P. Bertrand, “In situ evaluation of density, viscosity, and thickness of adsorbed soft layers by combined surface acoustic wave and surface plasmon resonance,” *Anal. Chem.*, vol. 78, no. 12, pp. 4200–4209, 2006.

[200] E. Galopin, M. Beaugeois, B. Pinchemel, J.-C. Camart, M. Bouazaoui, and V.

Thomy, “SPR biosensing coupled to a digital microfluidic microstreaming system,” *Biosens. Bioelectron.*, vol. 23, no. 5, pp. 746–750, Dec. 2007.

[201] A. Renaudin, V. Chabot, E. Grondin, V. Aimez, and P. G. Charette, “Integrated active mixing and biosensing using surface acoustic waves (SAW) and surface plasmon resonance (SPR) on a common substrate,” *Lab Chip*, vol. 10, no. 1, pp. 111–115, Jan. 2010.

[202] J. Kim, S. Kim, T. Ohashi, H. Muramatsu, S.-M. Chang, and W.-S. Kim, “Construction of simultaneous SPR and QCM sensing platform,” *Bioprocess Biosyst. Eng.*, vol. 33, no. 1, pp. 39–45, Jan. 2010.

[203] D. Kohlheyer, G. A. J. Besselink, S. Schlautmann, and R. B. M. Schasfoort, “Free-flow zone electrophoresis and isoelectric focusing using a microfabricated glass device with ion permeable membranes,” *Lab Chip*, vol. 6, no. 3, p. 374, Feb. 2006.

[204] N. F. C. Visser, A. Scholten, R. H. H. Van Den Heuvel, and A. J. R. Heck, “Surface-plasmon-resonance-based chemical proteomics: Efficient specific extraction and semiquantitative identification of cyclic nucleotide-binding proteins from cellular lysates by using a combination of surface plasmon resonance, sequential elution and ,” *ChemBioChem*, vol. 8, no. 3, pp. 298–305, 2007.

[205] M. Du and F. Zhou, “Postcolumn Renewal of Sensor Surfaces for Plasmon Resonance Detection,” *Interface*, vol. 80, no. 11, pp. 4225–4230, 2008.

[206] E. C. A. Stigter, G. J. de Jong, and W. P. van Bennekom, “Development of an on-line SPR-digestion-nanoLC-MS/MS system for the quantification and identification of interferon-γ in plasma,” *Biosens. Bioelectron.*, vol. 24, no. 7, pp. 2184–2190, Mar. 2009.

[207] I. Roy *et al.*, “Optical tracking of organically modified silica nanoparticles as DNA carriers: a nonviral, nanomedicine approach for gene delivery.,” *Proc. Natl. Acad. Sci. U. S. A.*, vol. 102, no. 2, pp. 279–84, Jan. 2005.

[208] F. Yan and R. Kopelman, “The Embedding of Meta-tetra(Hydroxyphenyl)-Chlorin

into Silica Nanoparticle Platforms for Photodynamic Therapy and Their Singlet Oxygen Production and pH-dependent Optical Properties¶,” *Photochem. Photobiol.*, vol. 78, no. 6, pp. 587–591, May 2007.

[209] B. G. Trewyn, S. Giri, I. I. Slowing, and V. S.-Y. Lin, “Mesoporous silica nanoparticle based controlled release, drug delivery, and biosensor systems,” *Chem. Commun.*, vol. 0, no. 31, p. 3236, Aug. 2007.

[210] S. Giri and V. S. Lin, “Mesoporous Silica Nanoparticles for Drug Delivery and Biosensing Applications**,” pp. 1225–1236, 2007.

[211] S. Santra, P. Zhang, K. Wang, R. Tapec, and W. Tan, “Conjugation of Biomolecules with Luminophore-Doped Silica Nanoparticles for Photostable Biomarkers,” vol. 73, no. 20, pp. 4988–4993, 2001.

[212] H. H. Yang, S. Q. Zhang, X. L. Chen, Z. X. Zhuang, J. G. Xu, and X. R. Wang, “Magnetite-Containing Spherical Silica Nanoparticles for Biocatalysis and Bioseparations,” *Anal. Chem.*, vol. 76, no. 5, pp. 1316–1321, 2004.

[213] R. Tapec, X. J. Zhao, and W. Tan, “Development of Organic Dye-Doped Silica Nanoparticles for Bioanalysis and Biosensors,” *J. Nanosci. Nanotechnol.*, vol. 2, no. 3, pp. 405–409, Jul. 2002.

[214] T. Endo, S. Yamamura, N. Nagatani, Y. Morita, Y. Takamura, and E. Tamiya, “Localized surface plasmon resonance based optical biosensor using surface modified nanoparticle layer for label-free monitoring of antigen–antibody reaction,” *Sci. Technol. Adv. Mater.*, vol. 6, no. 5, pp. 491–500, Jan. 2005.

[215] Tatsuro Endo, Kagan Kerman, Naoki Nagatani, and Yuzuru Takamura, and E. Tamiya*, “Label-Free Detection of Peptide Nucleic Acid−DNA Hybridization Using Localized Surface Plasmon Resonance Based Optical Biosensor,” 2005.

[216] W. Stober and A. Fink, “Controlled Growth of Monodispersed Silica Spheres in the Micron Size Range,” *J. Colloid Interface Sci.*, vol. 26, pp. 62–69, 1968.

[217] R. Lindberg, G. Sundholm, G. Øye, and J. Sjöblom, “A new method for following the kinetics of the hydrolysis and condensation of silanes,” *Colloids Surfaces A Physicochem. Eng. Asp.*, vol. 135, no. 1–3, pp. 53–58, 1998.

[218] G. H. Bogush and C. F. Zukoski IV, “Uniform silica particle precipitation: An aggregative growth model,” *J. Colloid Interface Sci.*, vol. 142, no. 1, pp. 19–34, 1991.

[219] D. L. Green, J. S. Lin, Y. F. Lam, M. Z. C. Hu, D. W. Schaefer, and M. T. Harris, “Size, volume fraction, and nucleation of Stober silica nanoparticles,” *J. Colloid Interface Sci.*, vol. 266, no. 2, pp. 346–358, 2003.

[220] T. Matsoukas and E. Gulari, “Monomer-addition growth with a slow initiation step: A growth model for silica particles from alkoxides,” *J. Colloid Interface Sci.*, vol. 132, no. 1, pp. 13–21, 1989.

[221] L. Hall *et al.*, “Capture-antibody conjugate model leading to specifications for biological and marker components of immunoassay test coupon,” 2014.

[222] G. W. Tormoen, J. Drelich, and E. R. Beach, “Analysis of atomic force microscope pull-off forces for gold surfaces portraying nanoscale roughness and specific chemical functionality,” *J. Adhes. Sci. Technol.*, vol. 18, no. 1, pp. 1–17, 2004.

[223] H. S. Dhadwal, R. R. Ansari, and W. V. Meyer, “A fiber-optic probe for particle sizing in concentrated suspensions,” *Rev. Sci. Instrum.*, vol. 62, no. 12, pp. 2963–2968, 1991.

[224] V. Kestens *et al.*, “Challenges in the size analysis of a silica nanoparticle mixture as candidate certified reference material,” *J. Nanoparticle Res.*, vol. 18, no. 6, 2016.

[225] R. F. Domingos, Y. O. N. Ju-nam, M. M. Reid, N. Tufenkji, J. R. Lead, and G. G. Leppard, “Characterizing Manufactured Nanoparticles in the Environment : Multimethod Determination of Particle Sizes,” pp. 7277–7284, 2009.

[226] L. C. J. Hesselmans, A. J. Derksen, and J. A. M. Van Den Goorbergh, "Polycarbodiimide crosslinkers," *Prog. Org. Coatings*, vol. 55, no. 2, pp. 142–148, 2006.

[227] A. D. Rakić, A. B. Djurišić, J. M. Elazar, and M. L. Majewski, "Optical properties of metallic films for vertical-cavity optoelectronic devices," *Appl. Opt.*, vol. 37, no. 22, p. 5271, 1998.

[228] X. Lang, L. Qian, P. Guan, J. Zi, and M. Chen, "Localized surface plasmon resonance of nanoporous gold," *Appl. Phys. Lett.*, vol. 98, no. 9, p. 093701, Feb. 2011.

[229] N. Hardy, "What is Thin Film Deposition By Thermal Evaporation," 2013. [Online]. Available: http://www.semicore.com/news/71-thin-film-deposition-thermal-evaporation. [Accessed: 30-Jul-2018].

[230] C. Y. Tan and Y. X. Huang, "Dependence of Refractive Index on Concentration and Temperature in Electrolyte Solution, Polar Solution, Nonpolar Solution, and Protein Solution," *J. Chem. Eng. Data*, vol. 60, no. 10, pp. 2827–2833, 2015.

[231] I. Langmuir, "The adsorption of gases on plane surfaces of glass, mica and platinum," *J. Am. Chem. Soc.*, vol. 40, no. 9, pp. 1361–1403, 1918.

[232] D. G. Myszka, X. He, M. Dembo, T. A. Morton, and B. Goldstein, "Extending the Range of Rate Constants Available from BIACORE: Interpreting Mass Transport-Influenced Binding Data," *Biophys. J.*, vol. 75, no. 2, pp. 583–594, Aug. 1998.

[233] R. W. Glaser, "Antigen-antibody binding and mass transport by convection and diffusion to a surface: A two-dimensional computer model of binding and dissociation kinetics," *Anal. Biochem.*, vol. 213, no. 1, pp. 152–161, Aug. 1993.

[234] E. Pensa, E. Corte, M. H. Fonticelli, G. Benítez, A. Rubert, and R. C. Salvarezza, "The Chemistry of the Sulfur À Gold Interface : In Search of a Unified Model," vol. 45, no. 8, pp. 1183–1192, 2012.

[235] N. Aissaoui, L. Bergaoui, J. Landoulsi, and P. Vi, “Silane Layers on Silicon Surfaces : Mechanism of Interaction , Stability , and Influence on Protein Adsorption,” pp. 656–665, 2012.

[236] J. C. Maxwell Garnett, “XII. Colours in metal glasses and in metallic films,” *Philos. Trans. R. Soc. London. Ser. A, Contain. Pap. a Math. or Phys. Character*, vol. 203, no. 359–371, p. 385 LP-420, Jan. 1904.

[237] R. Landauer, “The electrical resistance of binary metallic mixtures,” *J. Appl. Phys.*, vol. 23, no. 7, pp. 779–784, 1952.

[238] M. Kanso, S. Cuenot, and G. Louarn, “Roughness effect on the SPR measurements for an optical fibre configuration: Experimental and numerical approaches,” *J. Opt. A Pure Appl. Opt.*, vol. 9, no. 7, pp. 586–592, 2007.

[239] T. Viitala, N. Granqvist, S. Hallila, M. Raviña, and M. Yliperttula, “Elucidating the Signal Responses of Multi-Parametric Surface Plasmon Resonance Living Cell Sensing: A Comparison between Optical Modeling and Drug–MDCKII Cell Interaction Measurements,” *PLoS One*, vol. 8, no. 8, p. e72192, Aug. 2013.

[240] E. Hecht, *Optics*, 4th 02. Addison-Wesley, 2002.

[241] X. Hong and E. A. H. Hall, “Contribution of gold nanoparticles to the signal amplification in surface plasmon resonance,” *Analyst*, vol. 137, no. 20, p. 4712, Sep. 2012.

[242] V. Ball and J. J. Ramsden, “Buffer Dependence of Refractive Index Increments,” no. 3, pp. 489–492, 1998.

[243] J. De Feijter, J. Benjamins, and F. Veer, “Ellipsometry as a tool to study the adsorption behavior of syntetic and biopolyers at the air water interface,” *Biopolymers*, vol. 17, no. 7, pp. 1759–1772, 1978.

[244] H. Zhao, P. H. Brown, and P. Schuck, “On the Distribution of Protein Refractive Index Increments,” *Biophysj*, vol. 100, no. 9, pp. 2309–2317, 2011.

[245] S. Kimoto, W. D. Dick, Z. Syedain, D. Y. H. Pui, and D. L. Roberts, “Effective Density of Silica Nanoparticle Size Standards,” no. 2013, p. 2014, 2014.

[246] Y. H. Tan, M. Liu, B. Nolting, J. G. Go, J. Gervay-Hague, and G. Y. Liu, “A nanoengineering approach for investigation and regulation of protein immobilization,” *ACS Nano*, vol. 2, no. 11, pp. 2374–2384, 2008.

[247] R. L. Rich and D. G. Myszka, “BIACORE J: a new platform for routine biomolecular interaction analysis,” *J. Mol. Recognit.*, vol. 14, no. 4, pp. 223–228, Jul. 2001.

[248] R. J. Whelan and R. N. Zare, “Surface plasmon resonance detection for capillary electrophoresis separations,” *Anal. Chem.*, vol. 75, no. 6, pp. 1542–1547, 2003.

[249] A. K. H. Kwan, K. W. Chan, and V. Wong, “A 3-parameter particle packing model incorporating the wedging effect,” *Powder Technol.*, vol. 237, pp. 172–179, 2013.

[250] H. Y. Sohn and C. Moreland, “The effect of particle size distribution on packing density,” *Can. J. Chem. Eng.*, vol. 46, no. 3, pp. 162–167, Jun. 1968.

[251] J. Zheng, W. B. Carlson, and J. S. Reed, “The packing density of binary powder mixtures,” *J. Eur. Ceram. Soc.*, vol. 15, no. 5, pp. 479–483, Jan. 1995.

[252] Q. M. Mao, A. Johnston, I. G. Prince, and M. T. W. Hearn, “High-Performance Liquid Chromatography of Amino Acids, Peptides and Proteins .113. Predicting the Performance of Non-Porous Particles in Affinity Chromatography of Proteins,” *J. Chromatogr.*, vol. 548 (1-2), no. 199 1, pp. 147–163, 1991.

[253] M. F. Vitha, *Chromatography: Principles and instrumentation*, vol. 185. John Wiley & Sons, 2016.

[254] P. N. Dwivedi and S. N. Upadhyay, “Particle-Fluid Mass Transfer in Fixed and Fluidized Beds,” *Ind. Eng. Chem. Process Des. Dev.*, vol. 16, no. 2, pp. 157–165, Apr. 1977.

[255] M. J. Rhodes and M. Rhodes, *Introduction to particle technology*. John Wiley &

Sons, 2008.

[256] P. H. Brown, A. Balbo, H. Zhao, C. Ebel, and P. Schuck, “Density Contrast Sedimentation Velocity for the Determination of Protein Partial-Specific Volumes,” *PLoS One*, vol. 6, no. 10, p. e26221, Oct. 2011.

[257] S. Peter and H. Zhao, “The Role of Mass Transport Limitation and Surface Heterogeneity in the Biophysical Characterization of Macromolecular Binding Processes by SPR Biosensing,” in *Methods in Molecular Biology*, vol. 627, 2010, pp. 55–73.

[258] J. D. Taylor, M. J. Linman, T. Wilkop, and Q. Cheng, “Regenerable tethered bilayer lipid membrane arrays for multiplexed label-free analysis of lipid-protein interactions on poly(dimethylsiloxane) microchips using SPR imaging,” *Anal. Chem.*, vol. 81, no. 3, pp. 1146–1153, 2009.

[259] K. Campbell *et al.*, “Use of a novel micro-fluidic device to create arrays for multiplex analysis of large and small molecular weight compounds by surface plasmon resonance,” *Biosens. Bioelectron.*, vol. 26, no. 6, pp. 3029–3036, 2011.

[260] S. E. McNamee, C. T. Elliott, P. Delahaut, and K. Campbell, “Multiplex biotoxin surface plasmon resonance method for marine biotoxins in algal and seawater samples,” *Environ. Sci. Pollut. Res.*, vol. 20, no. 10, pp. 6794–6807, Oct. 2013.

[261] Y. Chen, K. Nakamoto, O. Niwa, and R. M. Corn, “On-chip synthesis of RNA aptamer microarrays for multiplexed protein biosensing with SPR imaging measurements,” *Langmuir*, vol. 28, no. 22, pp. 8281–8285, 2012.

[262] C. Corne *et al.*, “SPR imaging for label-free multiplexed analyses of DNA N-glycosylase interactions with damaged DNA duplexes,” *Analyst*, vol. 133, no. 8, pp. 1036–1045, 2008.

[263] D. Dorokhin, W. Haasnoot, M. C. R. Franssen, H. Zuilhof, and M. W. F. Nielen, “Imaging surface plasmon resonance for multiplex microassay sensing of mycotoxins,” *Anal. Bioanal. Chem.*, vol. 400, no. 9, pp. 3005–3011, 2011.

[264] R. Slavík and J. Homola, “Ultrahigh resolution long range surface plasmon-based sensor,” *Sensors and Actuators, B: Chemical*, vol. 123, no. 1. pp. 10–12, 2007.

[265] M. Vala, S. Etheridge, J. A. Roach, and J. Homola, “Long-range surface plasmons for sensitive detection of bacterial analytes,” *Sensors Actuators, B Chem.*, vol. 139, no. 1, pp. 59–63, 2009.

[266] V. Chabot, Y. Miron, M. Grandbois, and P. G. Charette, “Long range surface plasmon resonance for increased sensitivity in living cell biosensing through greater probing depth,” *Sensors Actuators, B Chem.*, vol. 174, pp. 94–101, 2012.

[267] M. A. Kessler and E. A. H. Hall, “Multilayered structures exhibiting long-range surface exciton resonance,” *Thin Solid Films*, vol. 272, no. 1, pp. 161–169, 1996.

[268] M. Hamzaoui, B. Bestani, and N. Benderdouche, “The use of linear and nonlinear methods for adsorption isotherm optimization of basic green 4-dye onto sawdust-based activated carbon,” vol. 2508, no. 4, pp. 1110–1118, 2018.

[269] T. A. Osmari, R. Gallon, M. Schwaab, E. Barbosa-Coutinho, J. B. Severo Jr., and J. C. Pinto, “Statistical analysis of linear and non-linear regression for the estimation of adsorption isotherm parameters,” *Adsorpt. Sci. Technol.*, vol. 31, no. 5, pp. 433–458, 2013.

[270] B. Nagy, C. Mânzatu, A. Măicăneanu, C. Indolean, L. Barbu-Tudoran, and C. Majdik, “Linear and nonlinear regression analysis for heavy metals removal using Agaricus bisporus macrofungus,” *Arab. J. Chem.*, vol. 10, pp. S3569–S3579, 2017.

[271] S. Butterworth, “On the theory of filter amplifiers,” *Wirel. Eng.*, vol. 7, no. 6, pp. 536–541, 1930.

[272] J. R. Dormand and P. J. Prince, “A family of embedded Runge-Kutta formulae,” *J. Comput. Appl. Math.*, vol. 6, no. 1, pp. 19–26, Mar. 1980.

[273] L. F. Shampine and M. W. Reichelt, “The MATLAB ODE Suite,” *SIAM J. Sci. Comput.*, vol. 18, no. 1, pp. 1–22, 1997.

Appendix A MATLAB Scripts

A.1 MATLAB Functions

In this thesis, a large portion of the data plotting, numerical analysis and model simulation is done using the MATLAB software (MathWorks). Besides the basic functions that are prevalently used to import and export data, reduce noise, and to generate plots, there are a few special functions used in this thesis that are relevant to understanding some of the plots and analysis.

A.1.1 “surf”

This function creates a three-dimensional surface plot often called a heatmap. It is used extensively in this work to visualise a dependent variable that depends on two independent variables. For instance, in the simulation of attenuated total reflection (ATR) in this chapter, the reflectance is plotted against the wavelength and the incident angle. In Chapter 1, the reflectance is plotted against displacement and time. The colours on the surface plots range from blue to red and are proportional to the intensity of the signal at that point on the surface plot. Figure 6.1 shows an illustration of a 256-colour colour bar.

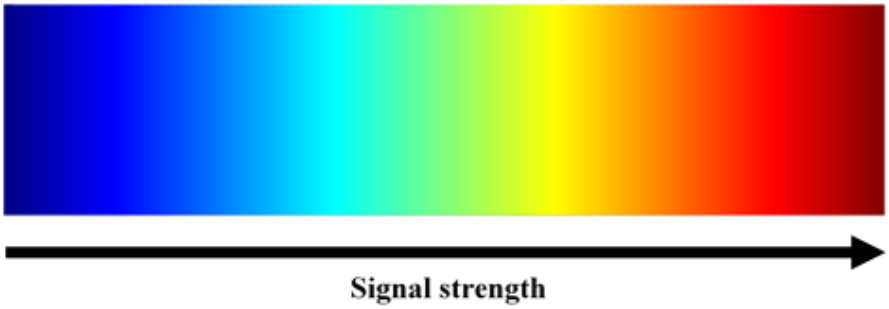

Figure 6.1 A general colour bar showing the range of colours associated with the signal strength in a surface plot. A colour point that is more to the tight on the colour pallet signifies a higher value.

A.1.2 "lsqcurvefit"

This function does nonlinear curve-fitting by minimising the square of the errors. It finds coefficients *x* that solve the problem

$$\min_{x} \|\boldsymbol{F}(\boldsymbol{x}, \boldsymbol{xdata}) - \boldsymbol{ydata}\|_2^2 = \min_{x} \sum_{i} (\boldsymbol{F}(\boldsymbol{x}, \boldsymbol{xdata_i}) - \boldsymbol{ydata_i})^2 \tag{6.1}$$

given input data *xdata*, and the observed output *ydata*. This MATLAB tool is extensively used when analysing the sensorgrams showing the adsorption kinetics. For many kinetic models mentioned in this thesis, the formulas can be manipulated such that a linear relationship is found between the derivatives of the parameter and the result. However, studies have shown that for intrinsically nonlinear adsorption processes, nonlinear least-square fitting has smaller error than linear regression fitting method [268 – 270]. Moreover, some of the more complex models such as Langmuir model with mass transfer limitation do not have linear form. Therefore, all the data-fitting in this thesis is done by a nonlinear solver to provide better fidelity.

A.1.3 “butter”

This function designs a Butterworth filter given the specified pass or stop frequencies. The filter design was first introduced by S. Butterworth [271]. In that paper, he showed that a low-pass filter can be achieved in the following frequency response

$$G(\omega) = \frac{1}{\sqrt{1+\omega^{2n}}} \tag{6.2}$$

where the cut-off frequency is normalised to 1, ω is the angular frequency in radians per second and n is the number of poles in the filter. He has also showed the way that this low-pass filter can be modified to become high-pass, band-pass and band-stop filters. In this thesis, the Butterworth filter is realised in MATLAB to filter out the periodical noise manifested in a sensorgram that is generated by the pulsation of the pump in the particle column.

A.1.4 “ode45”

`ode45` is a function that integrates a system of differential equations. It is used throughout this thesis when integrating the ordinary differential equation systems that describe the binding kinetics. The function is designed to handle the following general problem:

$$\begin{aligned} \frac{dx_1}{dt} &= f(t, x_1), \quad x_1(t_0) = x_1|_0, \\ \frac{dx_2}{dt} &= f(t, x_2), \quad x_2(t_0) = x_2|_0, \\ &\vdots \\ \frac{dx_n}{dt} &= f(t, x_n), \quad x_n(t_0) = x_n|_0, \end{aligned} \tag{6.3}$$

where t is the independent variable, x_k is a vector of dependent variables to be found and $f(t, x_k)$ is a function of t and x_k. The mathematical problem is specified when the initial conditions, $x_k = x_k|_0$ at time t_0 are given.

The algorithm of this function is based on an explicit Runge-Kutta (4,5) formular, the Dormand-Prince pair [272, 273]. It is widely used today to solve and fit systems of ODEs to experimental data.

A.2 3-Layer SPR Simulation Model

```
clear all;

c=299792458; %Speed of light
hbar=6.5822e-16; %Reduced Planck constant
lambda=632.8e-9; %Wavelength of He-Ne Laser
omega=2*pi/lambda*c; %Angular frequency of He-Ne Laser
fukso=complex(0,1); %i

thickness=50;%Thickness of Au film

%Refractive index of Prism
en(1)=1.51; %Real part
ek(1)=0;    %Im part

%Wavelength dependent RI of gold layer
indexfilename='rakic.csv.txt';
eAu=csvread(indexfilename,36,0,[36,0,85,1]);
eAu(:,3)=csvread(indexfilename,238,1,[238,1,287,1]);
en(2)=1; %Real part initialiasation
ek(2)=0; %Im part initialisation
d(2)=thickness*1E-9; %Thickness (m)

%Sensitive layer
en(3)=1; %Real part
ek(3)=0; %Im part
d(3)=0; %thickness (m)

%Substrate (water)
en(4)=1.33; %Real part
```

```
ek(4)=0; %Im part

%Angular range
Angle_first=62;
Angle_last=90;
Theta_deg=(Angle_first:.1:Angle_last);
Theta=Theta_deg/180*pi;

%calculation of dielectric constant
er=en(1)^2-ek(1)^2;
ei=2*en(1)*ek(1);
e(1)=complex(er,ei);

er=en(2)^2-ek(2)^2;
ei=2*en(2)*ek(2);
e(2)=complex(er,ei);

er=en(3)^2-ek(3)^2;
ei=2*en(3)*ek(3);
e(3)=complex(er,ei);

er=en(4)^2-ek(4)^2;
ei=2*en(4)*ek(4);
e(4)=complex(er,ei);

for jwl=1:50;
    en(2)=eAu(jwl,2);
    ek(2)=eAu(jwl,3);
    er=en(2)^2-ek(2)^2;
    ei=2*en(2)*ek(2);
    e(2)=complex(er,ei);
```

```
    for jtheta=1:length(Theta);
        theta=Theta(jtheta);
        q1=sqrt(e(1)-en(1)^2*sin(theta)^2)/e(1);
        qn=sqrt(e(end)-en(1)^2*sin(theta)^2)/e(end);
        for j=2:(length(e)-1)
            beta=d(j)*2*pi/lambda*sqrt(e(j)-
en(1)^2*sin(theta)^2);
            q=sqrt(e(j)-en(1)^2*sin(theta)^2)/e(j);
            em(j,1,1)=cos(beta);
            em(j,1,2)=-fukso*sin(beta)/q;
            em(j,2,1)=-fukso*sin(beta)*q;
            em(j,2,2)=cos(beta);
        end
        emtot=[1 0;
           0 1];
        for j=2:(length(e)-1)
            emtot1(:,:)=em(j,:,:);
            emtot=emtot*emtot1;
        end

        rp=((emtot(1,1)+emtot(1,2)*qn)*q1-
(emtot(2,1)+emtot(2,2)*qn))/...

((emtot(1,1)+emtot(1,2)*qn)*q1+(emtot(2,1)+emtot(2,2)*qn));

tp=2*q1/((emtot(1,1)+emtot(1,2)*qn)*q1+(emtot(2,1)+emtot(2,2)*
qn));
        ref=rp*conj(rp);
        tra=tp*conj(tp)/cos(theta)*en(1)*qn;
        REF(jtheta,jwl)=ref;
        TRA(jtheta,jwl)=tra;
```

```
    end
end

%Plot the heatmap
clf
figure(1)
surf(eAu(:,1)*1000,Theta_deg,REF,'EdgeColor','None','facecolor
','interp')
view(2);
title(['Simple Au Film SPR Simulation
(thinkness:',num2str(d(2)*1e9),'nm)'],'FontSize',14)
xlabel('Wavelength(nm)','FontSize',14)
ylabel('Incident Angle','FontSize',14)
zlabel('Reflectance','FontSize',14)
```

A.3 Periodic Noise Reduction Script

```
clear all;

%Read data from file
filename='test.txt';
W=readPeak(filename);

%Data treatment if there are zero values
for j = 2:length(W)
    if W(j,1)==0
        W(j,1)=W(j-1,1);
    end
end

y=W(:,1);
x=(0:0.25:(length(y)-1)/4);
yy = smooth(W(:,1),0.01,'rloess'); %Preliminary data smoothing

%Band-stop filter to eliminate pulsating signal
fc_1 = 0.01;
fc_2 = 0.1;
fs = 4;
[b,a] = butter(3,[fc_1/(fs/2) fc_2/(fs/2)],'stop');
yy = filtfilt(b,a,yy);

%Plot sensorgram
clf
figure
p = plot(x,y,x,yy,'r');
set(p,'LineWidth',2)
```

```
hold on
set(gca, 'FontSize',16)
xlabel('Time (s)')
ylabel('Peak wavelength (nm)')
legend('Raw signal', 'Filtered signal')
```

A.4 Nonlinear curve fitting to a system of ODEs

```
clear all

%Data points extracted from the sensorgram
Data = ...
  [0        0.0000
   100      0.6351
   200      1.2078
   300      1.5176
   400      1.7264
   500      1.8773
   600      1.9922
   700      2.0873
   800      2.1667
   900      2.2312
   1000     2.2820
   1100     2.3310
   1200     2.3713
   1300     2.4146
   1400     2.4539
   1500     2.4845
   1600     2.5042
   1700     2.5320
   1800     2.5550];

t = Data(:,1);
y = Data(:,2);

%Plot of the data points
plot(t,y,'r^','MarkerSize',8)
```

```
c_A = 1.7857e-6; %Analyte concentration
S = 5.55e6; %Observed sensitivity
f_s = 1/S; %Sensitivity factor

%Parameter initialisation
k_ad = 5000; %Association rate
Q_max = 3; %Max respons at equilibrium
k_d = 5E-5; %Dissociation rate
k_tr = 0.0001; %Mass transfer rate

xt0 = zeros(1,4);
xt0(1) = k_ad;
xt0(2) = Q_max;
xt0(3) = k_d;
xt0(4) = k_tr;

%Lower and upper boundary for the parameters
lb = [0,0,0,0];
ub = [1e10,1e10,1e10,1e10];

%Nonlinear curve fitting using least mean square root
[pbest,presnorm,~,exitflag,output] =
lsqcurvefit(@paramfun,xt0,t,y,lb,ub);

%Plot of the fitted model
hold on
plot(t,paramfun(pbest,t),'LineWidth',2);
set(gca, 'FontSize',14)
xlabel('Time (s)', 'FontSize',14)
ylabel('Wavelength Shift (nm)', 'FontSize',14)
```

```
legend({'Experiment','Theory'}, 'Location', 'east')
hold off

%Differential equation system solver
function pos=paramfun(x,t)

k_ad = x(1);
Q_max = x(2);
k_d = x(3);
k_tr = x(4);
c_A = 1.7857e-6;
S = 5.55e6;
f_s = 1/S;

f = @(t,xdata) [k_ad*xdata(2)*(Q_max-xdata(1))-k_d*xdata(1);
k_tr*(c_A-xdata(2))-f_s*(k_ad*xdata(2)*(Q_max-xdata(1))-
k_d*xdata(1))];

[~,pos_full] = ode45(f,t,[0, c_A]);
pos = pos_full(:,1);
end
```